NATURAL GAS COMBUSTION UNDER ENGINE-RELEVANT CONDITIONS

by

JIAN HUANG

B.Sc. Shanghai Maritime University, 1996
M.A.Sc. The University of British Columbia, 2002

A THESIS SUBMITTED IN PARTIAL FULFILLMENT OF
THE REQUIREMENTS FOR THE DEGREE OF

DOCTOR OF PHILOSOPHY

in

THE FACULTY OF GRADUATE STUDIES

(Mechanical Engineering)

THE UNIVERSITY OF BRITISH COLUMBIA

March 2006

Abstract

This thesis focuses on the study of natural gas combustion under engine relevant conditions. The work begins with the development of a detailed chemical kinetic mechanism that represents the ignition characteristics of methane with various minor additives over a wider range of operating conditions than previously existing mechanisms. The mechanism includes a NOx submechanism selected from the literature that yields good agreement with experimental data in various methane/air combustion systems.

The excessive computational load associated with detailed chemistry is alleviated using a trajectory generated low-dimensional manifold (TGLDM) method. The TGLDMs generated in this work provide a satisfactory approximation of calculation using detailed chemistry in various methane/air reaction systems with a significant reduction of the computational cost.

An innovative combustion model for simulating turbulent diffusion flames is presented at the end of this thesis. The model employs the Conditional Source-term Estimation method for the closure of the chemical source term. It obtains production/consumption rates of reaction scalars through TGLDMs generated with the new reaction mechanism. The model was used to simulate ignition and combustion of transient turbulent methane jets under engine-relevant conditions; it has achieved encouraging results in comparison with the experimental data from this work as well as the literature.

Table of Contents

List of Tables

List of Figures

Nomenclature and Acronyms

Symbol	Meaning	Units
D	Diffusivity	$m^2.s^{-1}$
E	Activation Energy	$cal.mol^{-1}$
h	Specific Enthalpy	$J.kg^{-1}$
I	Identity Matrix	
$\mathbf{J}$	Jacobian Matrix	s^{-1}
k	Reaction Rate	
p	Pressure	Pa or bar
P	Probability Density Function	
$\mathbf{P}$	Projection Matrix	
R	Universal Gas Constant	$J.mol^{-1}$
$\mathbf{V}$	Eigen(Schur) Basis Matrix	
S	Sensitivity	
T	Temperature	K
Y	Mass Fraction	
Z	Mixture Fraction	
$\langle Y|Z = \eta \rangle$	Conditional Average of Y with Condition $Z = \eta$	
$\langle Z \rangle$	Mean of Mixture Fraction	
$\langle Z''^2 \rangle$	Variance of Mixture Fraction	
CMC	Conditional Moment Closure	
CSE	Conditional Source-term Estimation	
EGR	Exhaust Gas Recirculation	
FCT	Flux Corrected Transport	
$ILDM$	Intrinsically Low Dimensional Manifold	
$TGLDM$	Trajectory-Generated Low Dimensional Manifold	

Symbol	Meaning	Units
ϵ	Dissipation Rate of Turbulent Kinetic Energy	$J.kg^{-1}.s^{-1}$
λ	Thermal Diffusivity	$m^2.s^{-1}$
Λ	Diagonal Matrix of Eigenvalues	s^{-1}
ρ	Density	$kg.m^{-3}$
ϕ	Equivalence Ratio	
φ	Relative Contribution	
τ	Ignition Delay or Time Duration	$\mu s, ms$ or s
$\dot{\omega}$	Chemical Source Term	s^{-1}
χ	Scalar Dissipation Rate	s^{-1}

Acknowledgement

Doubtlessly, the past five and half years have been the greatest and most memorable experiences in my life. For the many people who have offered me their love, friendship, support and help throughout this extraordinary journey, I would like to take this opportunity to express my thankfulness and appreciation.

I would like to thank Dr. Steve Rogak, Dr. Martin Davy and Dr. Tony Bi, who are the members of my research committee, for spending time reading through the proposal and the preliminary draft of my thesis and providing many valuable feedbacks.

I would like to thank all my colleges and friends in Rusty Hut 101 and the combustion lab as well as the students, faculties and staffs of the Mechanical Engineering Department, whose understanding, help and support have made this research project truly enjoyable.

Particular thanks are due to Dr. Philip Hill, for his everlasting enthusiasm and constant encouragement to my work, which have been a major driving force for me to pursue progress in this challenging field of study.

It is my greatest pleasure to thank my supervisor, Dr. Kendal Bushe, who has been an excellent guider and a real friend-in-need since the very first day of my arrival, for offering his great knowledge, firm support and trust that eventually lead to the accomplishment of this thesis

work.

I would like to express my special gratitude to my parents, Yongning Huang and Yanhua Chen, whose constant and unconditional love, support and encouragement have always been my greatest source of strength, and helped me through even the most difficult time in my life to reach where I am today.

Finally, I would like to thank my wife, Wen Gao, for her dedication to our family and for walking side by side with me through the course of this journey.

To My Son, James Kaiming Huang

Chapter 1
Introduction and Thesis Outline

1.1 Introduction

Natural-gas-fueled internal-combustion engines have been increasingly studied because of their potential environmental and economic benefits [1–8]. Recent technological development enables direct injection of natural gas into diesel engines [3–8]. This technology provides a practical solution for diesel engines to meet increasingly stringent emission regulations while maintaining their high thermal efficiency [4–8]. For a direct-injection natural gas engine, knowledge of ignition and combustion processes inside the combustion chamber is critical for optimizing engine design and perfecting control strategies. Despite a large amount of pioneer studies on natural gas combustion [9–25], the study of transient reactive natural gas jets under engine-relevant conditions remains a major challenge. On the experimental side, it is extremely difficult to obtain direct measurements of a reacting jet in an operating engine. On the chemistry side, only limited high-pressure experimental data are available to validate the existing reaction mechanisms so that large uncertainties exist when these mechanisms are applied to natural gas combustion in practical combustion devices. In terms of numerical simulation, to properly model a turbulent transient reactive jet with complex chemistry is still an intensely studied subject;

1

simulating the process efficiently within the capability of limited computational resources presents an extra challenge to an already complex problem. The urgent need to tackle the above issues in order to obtain a better understanding of natural gas combustion under engine-relevant conditions is what has motivated this work.

1.2 Outline

This thesis is structured so that each chapter can be viewed as a standalone paper without having to refer excessively to other chapters. Each chapter contains sections of introduction, results and discussion, and ends with conclusions. The main conclusions are recapitulated and some general remarks are given at the end of the thesis. Chapters 3 and 4 were modified from two published journal articles resulting from this thesis work. The contents of Chapters 5 to 7 have been or are to be submitted for publication.

Chapter 2 provides a comprehensive review of the subject discussed in this thesis. Discussions are given for the development of detailed chemical kinetic mechanisms for natural gas combustion and various analysis techniques. The mechanisms for formation of nitrogen oxides in natural gas flames are covered. Issues related to implementing detailed chemistry in turbulent reactive flow calculations are raised, and commonly used simplification techniques are introduced. The chapter concludes with an introduction to various closure methods for the chemical source term in turbulent combustion modeling.

In Chapter 3 a detailed chemical kinetic mechanism for the ignition of methane with minor ethane and propane additives is developed. With the establishment of a new experimental database, it is shown that the new mechanism properly predicts the ignition delay of vari-

ous synthetic natural gas fuels over a range of engine-relevant conditions. The mechanism is subject to a series of analyses which leads to the identification of the main reaction path. Further insight into the kinetics that govern the natural gas ignition process is obtained from an analytical model derived from the detailed chemistry.

In Chapter 4, the reaction mechanism is extended to simulate ignition of methane/hydrogen mixtures. It is shown from the experimental and numerical results that the effect of hydrogen on promoting methane ignition decreases with decreasing temperature; this is explained by analyzing the detailed kinetic mechanism.

In Chapter 5, several selected NO_x mechanisms are evaluated using experimental data from the literature. The NO_x mechanism with optimal performance in reproducing the experimental results when added to the new natural gas reaction mechanism is identified.

Chapter 6 introduces the basic concept of Trajectory-Generated Low-Dimensional Manifold (TGLDM) for reducing detailed chemical kinetic mechanisms. The TGLDMs generated in this work provide a satisfactory approximation of calculations using the detailed chemistry in various methane/air reaction systems with simple flow configurations.

Finally, in Chapter 7, it is demonstrated that TGLDMs can be used in conjunction with the method of Conditional Source-term Estimation (CSE) to provide closure for the chemical source terms in turbulent reactive flow calculations with relatively low computational cost. We test the CSE-TGLDM combustion model in the simulation of turbulent reactive methane jets under engine-relevant conditions. The ignition delay time obtained from the simulation agrees well with the experimental data of the current work as well as the literature.

The appendices at the end of the thesis cover some extra reference

materials and mathematical derivations that are used in this thesis.

Chapter 2
Natural Gas Combustion - A Review

2.1 Introduction

Natural gas (commercial grade methane fuel) is the cleanest fossil energy source available in large quantities on earth [26]. On an energy basis, the combustion of natural gas releases significantly lower pollutants (carbon dioxide CO_2, nitrogen oxides NO_x, sulfur dioxide SO_2 and particulates) than fossil fuels such as coal, diesel and gasoline [26]. Because of the huge economic and environmental benefits associated with using natural gas in place of these more traditional fuels, a large number of studies have investigated the combustion of natural gas in various practical and laboratory systems. In the past decades, with the rapid development of digital computer technology, numerical simulation and analysis in conjunction with experimental investigation have been increasingly used as standard approaches in these studies.

2.2 Reaction Kinetics for Natural Gas Combustion

Experimental studies of methane and natural gas combustion in well-controlled laboratory devices not only provide fundamental information regarding the characteristics of the testing fuel, but also generate valuable databases for developing and validating detailed reaction

mechanisms or complex combustion models. A common feature of laboratory setups for combustion study is that the initial and boundary conditions of the reaction system are well established, which greatly facilitates the analytical and numerical work that follows. Attributes of well-controlled reaction systems that are often measured and reported in the literature include the ignition delay time, species concentration profiles in shock tubes and flow reactors and laminar flame velocities.

2.2.1 Experimental Studies of Methane Ignition

A very important device for studying ignition in a homogeneous reaction system is the shock tube. In a shock-tube experiment, the test mixture is heated to the desired temperature and pressure instantaneously by a shock wave, which is generated by rupturing a diaphragm that separates a high-pressure driver section from a low-pressure driven section. For an ideal shock reflection [27], the testing gas in the experimental section is essentially quiescent so that fluid dynamic effects can be neglected, leaving the system governed exclusively by chemical kinetics. The ignition delay time is then measured by means of a pressure trace or optical emissions from the reacting mixture in the test section. For most hydrocarbon fuels under these conditions, including methane, the measured ignition delay time is often correlated with initial (post shock reflection) conditions using an Arrhenius-type parametric formula given by

$$\tau = A \, exp \left(\frac{E}{RT} \right) [O_2]^x [CH_4]^y, \qquad (2.1)$$

where τ is the ignition delay time, E is the global activation energy, R is the universal gas constant and T is temperature. The values of A, E, x, and y are obtained by fitting the experimental data using regression

methods. Table 2.1 lists some of the coefficient values reported in the literature along with their experimental conditions.

Table 2.1: Experimental conditions and empirical coefficients for methane ignition from the literature [28]

Source	P (atm)	T (K)	x	y	A^1	E (kcal/mol)
[9]	1.5-4	1300-1900	0.4	-1.6	7.65E-18	51.4
[10]	2-10	1500-2150	0.33	-1.03	3.62E-14	46.5
[11]	2-3	1200-2100	0.32	-1.02	2.50E-15	53.0
[12]	1-3	1600-2200	0.48	-1.94	1.19E-18	46.3
[13]	1-6	1640-2150	0.33	-1.03	4.40E-15	52.3
[29]	40-260	>1300	-0.02	-1.20	1.26E-14	32.7
[29]	40-260	<1300	-0.38	-1.31	4.99E-14	19.0

The global activation energy, E, indicates the sensitivity of ignition delay with respect to changing temperature. It can be seen from Table 2.1 that at relatively high temperature, the experimentally obtained value for E is around 50 kcal/mol, while it reduces significantly to 19 kcal/mol at temperatures below 1300 K. The reduction in the activation energy with reducing temperature implies that the reactions which are rate-limiting in methane system are different at different temperatures; it also highlights the limitation of the above empirical coefficients, which should not be used beyond the experimental ranges within which they were obtained.

While most of the earlier studies focused on ignition at high temperature and low pressure, ignition delay data at elevated pressures and moderate temperatures have become more available in the literature recently [28–30]. Petersen et al. [29, 30] conducted shock tube

---

[1]units $(s(cm^3/mol)^{x+y})$

experiments on ignition of methane/air and methane/oxygen/argon
mixtures at pressures from 40 to 260 atm and temperatures from 1040
to 1500 K. The objective of their study was to understand the methane
ignition mechanism for ram-propulsion applications so that they cov-
ered the equivalence ratios (ϕ) in the fuel-lean ($\phi = 0.4$) and fuel-rich
($\phi > 3.0$) regions. Later, Huang et al. [28] reported shock-tube igni-
tion results for undiluted methane/air mixtures at pressures from 16
to 40 bar and temperatures from 1000 to 1350 K. The equivalence ratios
ranged from slightly lean ($\phi = 0.7$) to slightly rich ($\phi = 1.3$); this is
the range of great interest for internal combustion (IC) engine applica-
tions. In the above two studies, it was found that the ignition behavior
of methane is more complex at moderate temperature than that at high
temperature; the measured ignition delay cannot be well correlated us-
ing a single empirical formula. The observed global activation energy
decreases initially with reducing temperature, but tends to increase as
the temperature drops below 1100 K. This trend is particularly promi-
nent in the stoichiometric and rich mixtures.

2.2.2 Experimental Studies of Natural Gas Ignition

When higher alkanes (ethane, propane, butane, etc.) are added to me-
thane, the ignition characteristics change significantly. In most cases,
a sharp reduction of ignition delay was observed with the presence
of minor higher alkanes [10,20,22,23,31–33]. For example, in an early
study, Higgin and Williams [33] observed a reduction of ignition de-
lay by a factor of three when 1% (by volume) of n-butane was added
to methane (at an equivalence ratio of 0.5, pressure between 200 and
300 torr and temperature between 1800 and 2500 K); the reduction
increases to a factor of ten when 10% n-butane was added. Spadac-

cini and Colket [23] provide a comprehensive review of ignition of methane/hydrocarbon fuels (natural gas). For mixtures of methane enriched with 2-20% higher-molecular-weight hydrocarbons, the measured ignition delay time in the literature can be well correlated using the formula

$$\tau = 1.77 \times 10^{-14} exp(18693/T)[O_2]^{-1.05}[CH_4]^{0.66}[HC]^{-0.39}, \qquad (2.2)$$

where [HC] is the concentration of higher hydrocarbon in the fuel. The negative exponential coefficient on [HC] indicates that the overall effect of hydrocarbon additives is to reduce the ignition delay.

Lifshitz et al. [10] studied the ignition delay of methane/oxygen-/Ar mixtures enriched by a small fraction of hydrogen and propane using the reflected shock technique. They suggested that the ignition promoting effect of minor additives can be accounted for using a simple thermal theory, which treats the base fuel and additive as kinetically decoupled. They attribute the reduction in ignition delay time to the increase of temperature caused by the more rapid oxidation of the additive. Crossley et al. [20] examined the thermal theory with shock tube experiments in methane-oxygen-argon mixtures with addition of several higher alkanes (ethane, propane, iso-butane) at temperatures from 1430 to 2000 K. They found significant differences between the predicted ignition delay using the thermal theory and that from the measurements under certain experimental conditions, particularly with a relatively large fraction of higher alkanes. They concluded that the chemical coupling of the oxidation reactions between the base fuel and the additive is an important factor in explaining the reduced ignition delay time. Zellner et al. [34] investigated the ignition of methane-/air mixtures with 10% ethane, propane and n-butane additions. The

results show that these higher alkanes are similarly effective at reducing the ignition delay time of methane. A later study conducted by Eubank et al. [32] for ignition in a 1% methane, 99% air mixture enriched with C2-C4 alkanes shows that the effects of the hydrocarbons are cumulative. They suggested that each alkane additive should be considered to characterize the ignition of the fuel mixture. Griffiths et al. [35] conducted a comparison study of the ignition temperature of various methane-based fuels using a spherical reactor. They found that the change of ignition temperature is most sensitive to a hydrocarbon addition below 10% by volume. Beyond this fraction, the incremental sensitivity decreases.

It is interesting to note that among the numerous experimental results of methane with higher alkane ignition reported in the literature, reliable experimental data under engine-relevant conditions are rare. The lack of experimental data has become a major issue in the study of natural gas ignition in this particularly important region, which has motivated the work in this thesis.

2.2.3 Ignition Chemistry of Methane

Higgin and Williams [33] were among the first to study the ignition process of methane using a detailed chemical kinetic mechanism. They investigated the ignition of a lean methane/oxygen/argon mixture behind the reflected shock using a 16-step mechanism. The results from their theoretical model agree reasonably well with their experimental data. Seery and Bowman [9] developed an eighteen-step reaction mechanism; they obtained the rate constants of most reactions from reliable experimental values. The mechanism was used to study methane-/oxygen/argon ignition under temperatures from 1350 to 1900 K and

pressures from 1.5 to 4 atm. For mixtures with equivalence ratios between 0.5 to 2, the agreement between their experimental and numerical results is within 30 percent. Following these pioneer efforts, more complex reaction mechanisms were developed and used in the studies of methane ignition in recent years. Table 2.2 lists some of the methane-/natural gas mechanisms in the literature. The ignition mechanism for methane under a wide range of initial conditions has been fairly well established.

Figure 2.1 gives an example of the main reaction paths of methane during the induction period obtained by analyzing a detailed reaction mechanism [28]. Similar results can be found in the work of Petersen et al. [29]. These reaction paths are typical for methane ignition under moderate temperature conditions.

Following Frenklach and Bornside [22], we can divide the induction period of methane into three phases. In the initiation phase, methane decomposes into methyl (CH_3) and hydrogen (H) radicals via reaction

$$CH_4 + M \rightleftharpoons CH_3 + H + M. \tag{R1}$$
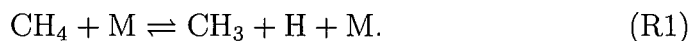
The hydrogen radical is rapidly consumed in the chain branching reactions

$$H + O_2 \rightleftharpoons OH + O, \tag{R2}$$

$$O + CH_4 \rightleftharpoons OH + CH_3. \tag{R3}$$
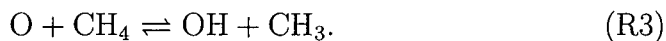
The two hydroxyl (OH) radicals formed in this process accelerate the decomposition of methane through

$$OH + CH_4 \rightleftharpoons CH_3 + H_2O. \tag{R4}$$
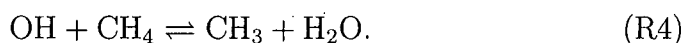
In parallel to the above path, hydroxyl radicals can be also generated through

$$HO_2 + CH_4 \rightleftharpoons CH_3 + H_2O_2, \tag{R5}$$
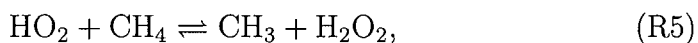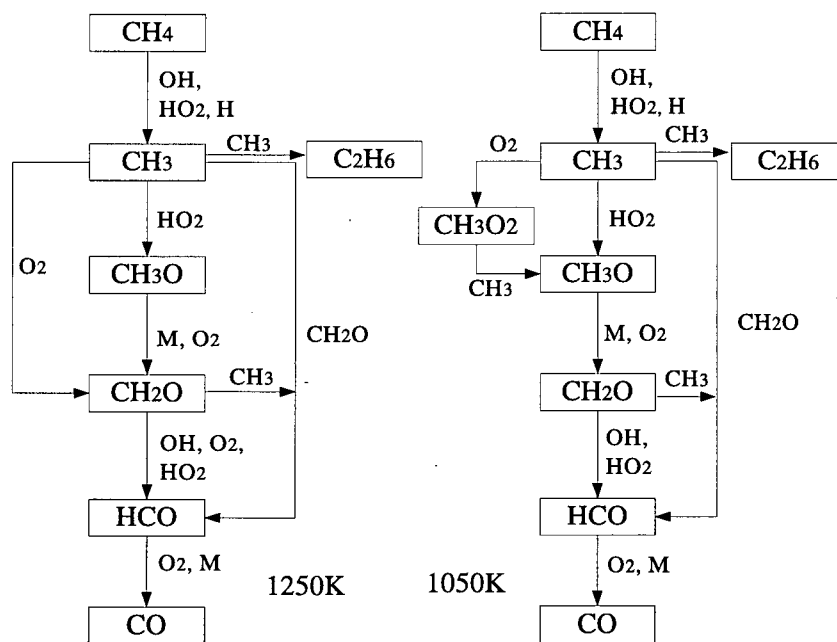
Figure 2.1: Main reaction paths during ignition in a stoichiometric methane/air mixture at 40 bar [28]. Results are based on integral reaction flow analysis.

$$H_2O_2 + M \rightleftharpoons OH + OH + M. \qquad\qquad (R6)$$
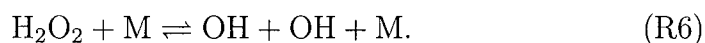
Spadaccini and Colket [23] pointed out that reaction R5 is more important for ignition below 1500 K, where more HO_2 radicals are generated through the reaction between hydrogen radicals and molecular oxygen. Reaction $H + O_2 \rightleftharpoons HO_2$ has a negative activation energy; thus the contribution of HO_2 becomes more significant at lower temperature. Similar to the effect of H radicals, for each hydroperoxyl (HO_2) radical consumed, two hydroxyl radicals are generated in the initiation phase. This makes OH a major radical in the reaction path of methane during the induction period.

Table 2.2: Mechanisms for natural gas combustion in the literature

Source	Species	Reactions	C_3[2]	NO_x[3]
Higgin and Williams [33]	10	16		
Seery and Bowman [9]	11	18		
Frenklach and Bornside [22]	34	140	✓	
Li and Williams [36]	45	177	✓	✓
Hughes et al. [37]	37	351[4]		
Hunter et al. [38]	40	207	✓	
GRI-Mech 1.2 [39]	32	177		
GRI-Mech 2.11 [40]	49	279		✓
GRI-Mech 3.0 [41]	53	325	✓	✓

The second phase of ignition is characterized by the competition between two methyl oxidation reactions

$$CH_3 + O_2 \rightleftharpoons CH_3O + O, \qquad (R7)$$

$$CH_3 + HO_2 \rightleftharpoons CH_3O + OH, \qquad (R8)$$
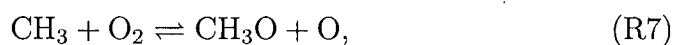
and a chain termination reaction

$$CH_3 + CH_3 \rightleftharpoons C_2H_6. \qquad (R9)$$
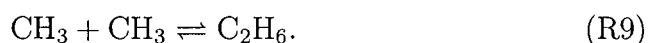
This is the longest phase in the induction period and the ignition delay time is very sensitive to the rates of key reactions in this phase [22]. It is also the phase during which the most significant differences between the high and low temperature ignition mechanisms occur. First, the

----

[2]Includes C_3 submechanism
[3]Includes NO_x submechanism
[4]Irreversible reactions

rate of formation of methylperoxy radical (CH_3O_2) increases for temperatures below 1300 K [28], which opens an extra oxidation path for methyl radicals:

$$CH_3 + O_2 \rightleftharpoons CH_3O_2. \tag{R10}$$

$$CH_3O_2 + CH_3 \rightleftharpoons 2CH_3O. \tag{R11}$$
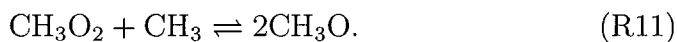
Ranzi et al. [42] pointed out that the conversion from methylperoxy to methoxy radicals can also proceed through

$$CH_3O_2 + CH_3O_2 \rightleftharpoons 2CH_3O + O_2, \tag{R12}$$

$$CH_3O_2 + HO_2 \rightleftharpoons CH_3O_2H + O_2, \tag{R13}$$

$$CH_3O_2H \rightleftharpoons CH_3O + OH. \tag{R14}$$
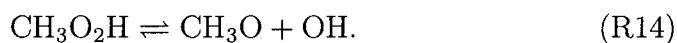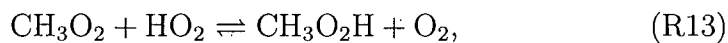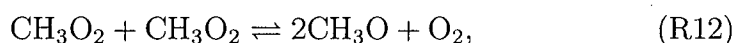
The rising significance of methylperoxy chemistry at relatively low temperatures is also indicated by other modeling studies [29,38]. This mechanism explains the observed reduction in the global activation energy with reducing temperature. The sensitivity of the ignition delay time to the formation of ethane in reaction R9 is higher in stoichiometric and rich mixtures compared to that in lean mixtures due to the higher methyl concentration. Consequently, the effect of methylperoxy chemistry is more prominent in the stoichiometric and rich regions where a greater reduction of the activation energy has been observed [28,29].

At even lower temperatures (T<1100 K), the reduction in the rates of key OH generation reactions such as R6 leads to a depletion of the OH radical, which becomes a new rate-limiting mechanism [28]. The activation energy changes from decreasing to increasing with the switch in the sensitization reactions although the formation rate for methylperoxy remains high.

The third phase of ignition is characterized by a rapid increase of radical concentrations accompanying strong thermal feedbacks. The auto-catalytic oxidation [22] proceeds through

$$CH_3O + M \rightleftharpoons CH_2O + H + M, \qquad (R15)$$

$$CH_2O + OH \rightleftharpoons HCO + H_2O, \qquad (R16)$$

$$HCO + M \rightleftharpoons H + CO + M, \qquad (R17)$$

and

$$HCO + O_2 \rightleftharpoons HO_2 + CO. \qquad (R18)$$
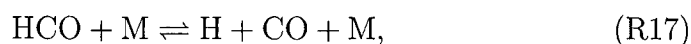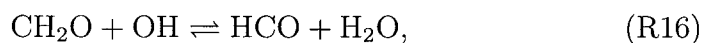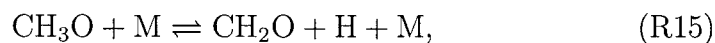
Reactions R17 and R18 restore the concentration of active radicals, i.e. H, HO_2; these two reactions are also highly exothermic, which makes them very effective in bringing the system to ignition.

2.2.4 Ignition Chemistry of Natural Gas

For methane ignition with higher alkanes, the modeling work of Westbrook [21,43] and Eubank [32] show that the reduction in ignition delay time is caused by the early generation of radical pools by the more active hydrocarbon additives. For ignition in methane/ethane mixtures, Westbrook [43] pointed out that H abstractions of ethane and subsequent decomposition of the resulting ethyl radicals are more efficient in producing hydrogen radicals than methane and methyl. At high temperatures, the extra hydrogen radicals lead to a quick chain initiation via reactions R2, R3 and R4, which accounts for the faster ignition. Frenklach and Bornside [22] studied the ignition delay in 9.5% methane, 19% oxygen, 71.5%argon mixtures enriched with 0.19 to 1.9% propane using a 140 step reaction mechanism. They attribute the ignition-promotion effectiveness of propane to its rapid decomposition

$$C_3H_8 \rightleftharpoons CH_3 + C_2H_5 \qquad (R19)$$

followed by

$$C_2H_5 \rightleftharpoons C_2H_4 + H. \qquad\qquad (R20)$$

Similar to ethane, an extra hydrogen radical is generated in this process that leads to buildup of radical pools in the early phase of ignition.

While the kinetic interaction between higher alkanes and methane during ignition is relatively well established for temperatures above 1400 K, it is less understood at moderate to low temperatures. As introduced above, the sensitization reactions in the pure methane system change with reducing temperature. Similarly, the low-temperature mechanism of methane/hydrocarbon systems is likely to be significantly different from that at high temperatures. For example, Hunter et al. [44] studied ethane oxidation at pressures from 3 to 10 atm and temperatures from 915 to 966K using a continuous flow reactor. The reaction process was modeled using a 277 step reaction mechanism. It was found that a large fraction of ethane at these temperatures is converted to ethylperoxy ($C_2H_5O_2$) in the early phase of reaction, while ethylperoxy is not included in many well-known reaction mechanisms because its concentration is insignificant at high temperatures. Thus there is a need to evaluate and improve the existing reaction mechanisms for modeling methane/hydrocarbon interactions at moderate temperature conditions, which are particularly relevant for practical combustion devices.

2.2.5 Ignition Studies of Methane with Hydrogen

Hydrogen enriched methane fuels are being increasingly studied due to their economic and environmental benefits. Experimental and computational results reported recently [45–50] show that by extending the lean-burn limit or increasing the fraction of exhaust gas recircu-

lation (EGR) with hydrogen addition, a significant reduction of NO_x and hydrocarbon emissions from natural-gas-fueled internal combustion engines can be achieved with unaffected or slightly higher engine efficiency. Potential applications of premixed methane/hydrogen fuels are also found in the aerospace [51] and gas turbine [52] industries. An understanding of the autoignition behavior of these mixtures is clearly needed.

Shock tube studies of high-temperature ignition in CH_4-H_2-O_2 mixtures have been reported by Lifshitz et al. [10] as well as by Cheng and Oppenheim [10]. In both cases, the reactants were diluted with 90 percent argon. The data of Lifshitz et al. [10] measured at a fixed pressure of 185 torr and covered temperatures from 1600 to 1800K. A thermal-based-promotion theory was proposed to account for the effects of hydrogen addition. Cheng and Oppenheim [12] conducted experiments for temperatures from 800 to 2000 K and pressures from 1 to 3 atm. They correlated the ignition delay of pure methane, pure hydrogen and their mixtures with the formula

$$\tau = \tau_{CH_4}^{(1-\epsilon)} \tau_{H_2}^{\epsilon},\qquad(2.3)$$

where ϵ is the mole fraction of hydrogen in the total fuel and τ_{CH_4} and τ_{H_2} are the ignition delay times of pure methane and pure hydrogen under the same conditions. Fotache et al. [53] investigated the ignition delay of hydrogen-enriched methane by heated air using a counterflow reactor. They identified three ignition regimes depending on the mole fractions of hydrogen. Methane ignition was found to benefit from hydrogen addition mainly due to the kinetic interactions between the two fuels. The modeling study shows that the promoting effect is enhanced by the spatial separation of the branching and termination

18

steps resulting from the high diffusivity of atomic and molecular hydrogen. Ju and Niioka [51] conducted a numerical study of hydrogen-/methane ignition in a supersonic mixing layer. They found a reduction of ignition delay proportional to the fraction of hydrogen addition. They suggested that the extra H and O radicals from H_2 oxidation was the main reason for the increased reaction rate.

2.2.6   Species Concentration Profile

In contrast to ignition delay, which is a result of the integrated effect of elementary reactions over a period of time, species concentration measurements provide instantaneous information of a reaction system. These data are particularly valuable for determining rates of elementary reactions as well as for developing and validating detailed chemical kinetic mechanisms. Davidson et al. [54] studied the decomposition rate of methane in a shock tube facility using state-selective laser absorption by CH_3. The methyl concentration as a function of time was obtained by measuring the attenuation of a laser beam passing through the homogeneous mixture in the test section. Yu et al. [55] measured fuel-lean mixtures of methane and oxygen diluted in argon behind the reflected shock at temperatures from 1550 to 2200 K. The reaction progress was determined in situ by laser absorption of OH radicals and CO molecules. The rate coefficient of the $CH_3 + O_2$ reaction were determined using GRI-Mech 1.2 [39] and theoretical calculation based on Rice-Ramsperger-Kassel-Marcus (RRKM) [56] master equation formalism. In the development of detailed chemical kinetic mechanisms such as GRI-Mech 3.0 [41], the species profiles obtained from the above experiments were used as targets for optimizing elementary reaction rates.

One drawback of shock tubes in combustion study is that the experimental time is relatively short. Typically, the ideal experimental conditions behind a reflected shock last from a few hundred microseconds to a few milliseconds. The observation period is followed by rapid cooling with the arrival of the rarefaction wave generated coincide with the incident shock [27]. For pure methane/air systems, ignition occurs only rarely for temperatures below approximately 1000 K in a shock tube because the chemical induction time is longer than the maximum experimental time. For studying combustion processes with longer time scales, continuous flow reactors are often used. In such a system, fuel and oxidizer are introduced independently into a mixing chamber which is followed by a measurement section. With the introduction of strong turbulence by means of jets or mixing fans, the mixing time scale is kept considerably shorter than the reaction time scale so that local mixtures can be considered to be homogeneous. At various points along the measurement section, the composition of the mixture is determined by optical, thermal or other methods. Given the mass flow rate, the species concentration profile can be obtained as a function of time.

Hunter et al. [38, 44] investigated the oxidation of methane and ethane at elevated pressures using a jet-mixing flow reactor at temperatures from 930 to 1000 K. The gas samples were extracted from ten equally-spaced points along the test section using a stainless probe. The concentrations of methane (CH_4), carbon dioxide (CO_2), carbon monoxide (CO), water (H_2O), methanol (CH_3OH), ethane (C_2H_6) and ethene (C_2H_4) were measured using gas chromatography, while the concentration of formaldehyde (CH_2O) was measured using a gas chromatograph equipped with a mass spectrometer (GC/MS). The mea-

sured species profiles were used to optimize a detailed kinetic mechanism. The maximum residence time was around 280 ms, which is significantly longer than that achievable in shock tubes. Compared to shock tubes, the drawback of continuous flow reactors mainly comes from their finite mixing time, which makes the facility unsuitable for studying reaction systems with a time scale less of than one millisecond [57].

2.2.7 Laminar Premixed Flame

Experimentally measured laminar flame velocities can be used to validate combustion models that incorporate detailed kinetic mechanisms and species transport properties.

Measurements of laminar burning velocity of methane/air mixtures in the literature cover pressures from 0.1 to 30 atm, unburned-mixture temperatures from 298 to 600 K and equivalence ratio from 0.4 to 1.7 [58–61]. For pressure above 1 atm, the commonly used methods are counter flow flames [58] and constant-volume combustion bombs [59–61]. Warnatz [62] compared measured laminar flame velocity of methane with C_2-C_6 hydrocarbons at 298K and 1 bar. The methane flame was shown to have the lowest velocity under identical conditions. The measured laminar flame velocity peaks between $\phi = 1.0$ and $\phi = 1.1$ with a value around 39 cm/s; it drops to around 9 cm/s at $\phi = 0.6$ and 11 cm/s at $\phi = 1.5$ [58].

The classical laminar premixed flame propagation theory based on Zel'dovich's analysis [63] suggests that the laminar flame velocity v_L depends on the diffusivity D of mass and energy, and the characteristic time of reaction τ. The formula

$$v_L = \sqrt{\frac{D}{\tau}} \tag{2.4}$$

indicates a balance between the rate of species transport as a physical process and the rate of chemical reactions. Mathematically v_L is the eigenvalue of a set of partial differential equations (PDEs) that govern the steady-state mass and energy conservations of a reaction system. According to the theory of gas diffusion [57], species diffusivity has an inverse first-order dependence on pressure. The pressure dependence of the chemical time scale is related to reaction order n by

$$\tau \propto P^{1-n}. \tag{2.5}$$

Thus the laminar flame velocity has an overall pressure dependence of order $n/2 - 1$. For methane/natural gas combustion, the main reactions are mostly second-order so that one can expect the laminar flame velocity to be roughly proportional to $P^{0.5}$. For a single-step reaction with an Arrhenius rate expression, the temperature dependence of the laminar burning velocity would then be

$$\tau \propto exp\left(\frac{E}{2RT_b}\right), \tag{2.6}$$

where E is the activation energy and T_b is the temperature of the burned gas. Warnatz [62] compared calculated laminar flame velocities using the above correlations for methane/air mixtures with measurements from the literature and reported good agreement over a wide range of temperature and pressure.

Using advanced digital computing technology, the contemporary method of solving for the laminar flame velocity has changed significantly from the classical approaches introduced above. Solutions can now be obtained by solving energy and species mass conservation equations with detailed chemistry [57,62]. For a one-dimensional premixed diffusion flame, the governing equation of species mass conser-

vation is given by

$$\rho \frac{\partial Y_i}{\partial t} + \rho u \frac{\partial Y_i}{\partial x} = -\frac{\partial}{\partial x}(\rho Y_i V_i) + \dot{\omega}_i, \qquad (2.7)$$

where ρ is the density, Y is the mass fraction, t is time, u is the bulk convection velocity, V is the diffusion velocity, and $\dot{\omega}$ is the rate change of mass fraction due to chemical reactions. The subscript i indicates the ith species. The mixture averaged diffusion velocity V_i, which incorporates both mass diffusion and thermal diffusion velocities, can be obtained from the Fickian formula [57]

$$V_i = -\frac{1}{X_i} D_i \nabla X_i - \frac{D_i^T}{\rho Y_i T} \nabla T, \qquad (2.8)$$

where D is the mixture-averaged diffusion coefficient, X is the mole fraction, and D^T is the thermal diffusivity at temperature T. The energy conservation equation is given by

$$\rho C_p \frac{\partial T}{\partial t} + \rho u C_p \frac{\partial T}{\partial x} = \frac{\partial}{\partial x}\left(\lambda \frac{\partial T}{\partial x}\right) + \sum_{i=1}^{N} \dot{\omega}_i \Delta h_{fi}^o - \rho \sum_{i=1}^{N} C_{p,i} Y_i V_i \frac{\partial T}{\partial x}, \qquad (2.9)$$

where C_p is the specific heat at constant pressure, λ is the thermal conductivity, and Δh_f^o is enthalpy of formation. The boundary conditions are

$$Y_i = Y_{u,i}, \qquad T = T_u \qquad at \qquad x = 0, \qquad (2.10)$$

and

$$\frac{\partial Y_i}{\partial x} = 0, \qquad \frac{\partial T}{\partial x} = 0 \qquad at \qquad x \to \infty. \qquad (2.11)$$

The subscript u indicates unburned mixture. The above n+1 (n species conservation and one energy) partial differential equations (PDEs) can be solved numerically, and the laminar flame velocity can be obtained from the steady-state solution of the convection velocity u. Detailed species and temperature profiles across a laminar flame, i.e. the structure of flame front, can also be extracted from the solution of the above PDEs.

Bernstein et al. [64] performed numerical calculations for the spatial profiles of key intermediate species (O, H, OH, CH, CO, HCO, and CH_3) in a premixed methane/air flame at low pressures. The model results are in good agreement with their experimental measurements obtained using two laser-based diagnostic methods. Heard et al. [65] measured the OH, CH, and NO radicals in slightly rich methane/air flames burning at 30, 70, and 120 torr using the Laser-Induced Fluorescence (LIF). Absolute NO and OH concentrations were determined using separate calibration experiments. They performed a simulation of the flame using a numerical model similar to that introduced above. The predicted profiles of the radical concentrations as a function of height above the burner agree well with the experimental results.

2.3 NOx **Chemistry**

Nitrogen oxides (NOx) are the main pollutant emissions from combustion processes. Severe environmental and health issues can be caused by an elevated level of NOx in the atmosphere. Nitrogen oxides are critical components of photochemical smog; Nitrogen dioxides cause damage to the mechanisms that protect the human respiratory tract and can increase a person's susceptibility to, and the severity of, respiratory infections and asthma. Long-term exposure to high levels of nitrogen dioxide can cause chronic lung disease. Because internal combustion engines and gas turbines are a significant source of NOx emissions, stringent regulations have been imposed by government agencies worldwide to control NOx emissions from these devices. Consequently, the formation of NOx and its reduction have become and remain to be a major focus of combustion studies by researchers from both industry and academia.

NO and NO_2 are the main nitrogen oxides generated in IC engines. Experimental data on NO and NO_2 formation in methane/air mixtures in stirred reactors or in laminar premixed flames are readily available in the literature [66–69]. Detailed discussion of NOx formation mechanisms can be found in combustion books [57,62]. In general, for the formation of NO, three major mechanisms have been identified: the thermal NO (Zel'dovich mechanism), the prompt NO (Fenimore mechanism) and the fuel-bound nitrogen mechanism.

2.3.1 Thermal NO

The Zel'dovich [63] mechanism for NO formation involves three major steps[5]

$$O + N_2 \rightleftharpoons NO + N, \qquad (R21)$$

$$O_2 + N \rightleftharpoons NO + O, \qquad (R22)$$

and

$$N + OH \rightleftharpoons NO + H. \qquad (R23)$$

The rate of reaction R21, the rate-limiting step in the Zel'dovich mechanism, has a very high activation energy: around 318 kJ/mol [70]. As a result, the Zel'dovich mechanism is very sensitive to temperature change. That is why the mechanism is also called thermal NO route. As a rule-of-thumb, the contribution from the Zel'dovich mechanism becomes significant only when the temperature is above 1800 K [57]. In internal combustion engines, the rate of reaction R21 is significantly lower than the rate of fuel oxidation and change of engine conditions, which makes the formation of NO a kinetically-controlled

---

[5]This is often called the "extended" Zel'dovich mechanism. Reactions 21 and 22 were initially suggested by Zel'dovich [63]. Reaction R23 was added by Lavoie et al. [63].

slow process [71]. The rate expression of the formation of NO from the Zel'dovich mechanism is

$$\frac{d[NO]}{dt} = k_{21}^f[O][N_2] + k_{22}^f[N][O_2] + k_{23}^f[N][OH] \qquad (2.12)$$
$$- k_{21}^b[NO][N] - k_{22}^b[NO][O] - k_{23}^b[NO][H],$$

where k denotes reaction rates; the square bracket denotes molar concentrations; superscript f denotes forward reactions; superscript b denotes backward reactions. Simplification of the rate expression for NO can be achieved by applying the quasi-steady-state assumption to the nitrogen atom, which leads to

$$\frac{d[NO]}{dt} = 2k_{21}^f[O][N_2]\frac{1 - [NO]^2/(K[O_2][N_2])}{1 + k_{21}^b[NO]/(k_{22}^f[O_2] + k_{23}^f[OH])}. \qquad (2.13)$$

where $K = k_{21}^f k_{22}^f/(k_{21}^b k_{22}^b)$. In an IC engine, the amount of NO formed in the postflame gas is usually much higher than that in the flame front due to the short residence time of the latter [71]. For thermal NOx, it is thus reasonalbe to approximate the concentration of O, O_2, OH, H and N_2 using the equilibrium values at the local pressure and temperature. The validity of the equilibrium assumption has been proven by Kuo [57] and Warnatz [62]. Warnatz reported that the equilibrium assumption yields a reasonable approximation to detailed chemistry for temperatures above 1700 K [62]. For conditions when the concentration of NO is significantly lower than it equilibrium concentration, the fractional term on the r.h.s of Eq. 2.13 reduces to unity. Correspondingly, the rate of NO formation reduces to

$$\frac{d[NO]}{dt} = 2k_{21}^f[O]_e[N2]_e. \qquad (2.14)$$

where subscript e denotes equilibrium properties.

2.3.2 Prompt NO

Fenimore [72, 73] measured the NO concentration in a flat premixed hydrocarbon flame; he found that the NO concentration close to the unburned mixture side is significantly higher than that predicted by the Zel'dovich mechanism. He thus postulated a new mechanism for the prompt formation of NO in a flame with the presence of hydrocarbon radicals. First, nitrogen-containing radicals are formed, via:

$$CH + N_2 \rightleftharpoons HCN + N, \tag{R24}$$

$$CH_2 + N_2 \rightleftharpoons HCN + NH, \tag{R25}$$

$$CH_2 + N_2 \rightleftharpoons H_2CN + N, \tag{R26}$$

$$C + N_2 \rightleftharpoons CN + N. \tag{R27}$$
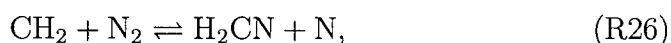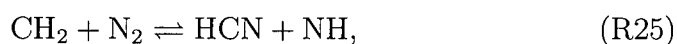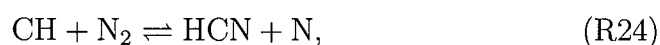
According to Glarborg et al. [74], reaction R24 is the most important initiation step in the prompt mechanism. The activation energy of this reaction reported in the literature ranges from 57 kJ/mol [75, 76] to 87 kJ/mol [77], which is significantly smaller than that of R21 in the thermal mechanism. This is the main reason for the dominance of the prompt NO in low temperature zones in hydrocarbon flames.

In lean and slightly rich flames, the hydrocyanic acid (HCN) and nitrogen radical formed in the above reactions are quickly converted to NO via

$$HCN + O \rightleftharpoons NCO + H, \tag{R28}$$

$$NCO + H \rightleftharpoons NH + CO, \tag{R29}$$

$$NH + H \rightleftharpoons N + H_2, \tag{R30}$$

$$N + OH \rightleftharpoons NO + H. \tag{R31}$$
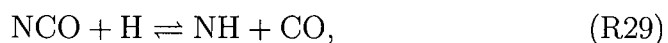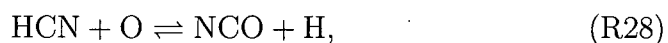
Miller and Bowman [78] reported that for equivalence ratios greater than 1.2, the rate of conversion from HCN to NO decreases due to:

1. recycling of NO to HCN by C, CH and CH_2 radicals, and

2. the shift of direction in reaction $N + NO \rightleftharpoons N_2 + O$:

The most important hydrocarbon radical in the formation of prompt NO is CH, whose concentration is established through

$$CH_3 + X \rightleftharpoons CH_2 + HX, \tag{R32}$$

$$CH_2 + X \rightleftharpoons CH + HX, \tag{R33}$$

$$CH + X \rightleftharpoons C + HX, \tag{R34}$$
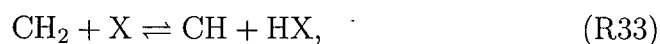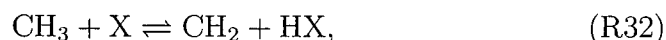
were X denotes H or OH radicals.

Figure 2.2 shows the main reaction path for the formation of prompt NO in methane flames. For methane/air premixed flames at ambient pressure, Miller and Bowman [78] showed that CH and total fixed nitrogen (TFN) both peak at $\phi = 1.4$. Beyond this equivalence ratio, the concentration of CH decreases due to the depletion of H and OH radicals, which leads to a reduction in prompt NO. The prompt mechanism contributes most significantly to NO formation at T < 2000K, while the thermal mechanism dominates for T > 2500K [57].

2.3.3 NO Formation from Fuel-Bound Nitrogen

Nitrogen compounds contained in natural gas may be released in a combustion process to form NOx. Studies have shown that in the gas phase, fuel-bound nitrogen (FBN) converts quickly into hydrogen cyanide (HCN) and ammonia (NH_3) [57], which then proceed along their respective reaction paths to form NO. In general, FBN is not a major issue in natural gas combustion since most natural gas contains very low concentrations of chemically bound nitrogen; it is much more important for coal combustion since the FBN mass fraction can be as high as a few percent in coal [62].

$$CH_3 \xrightarrow{\text{H, OH}} CH_2 \xrightarrow{\text{H, OH}} CH \xrightarrow{\text{H, OH}} C$$

$$N_2 \longrightarrow HCN \xrightarrow{\text{O}} NCO \xrightarrow{\text{H}} NH \xrightarrow{\text{H}} N$$
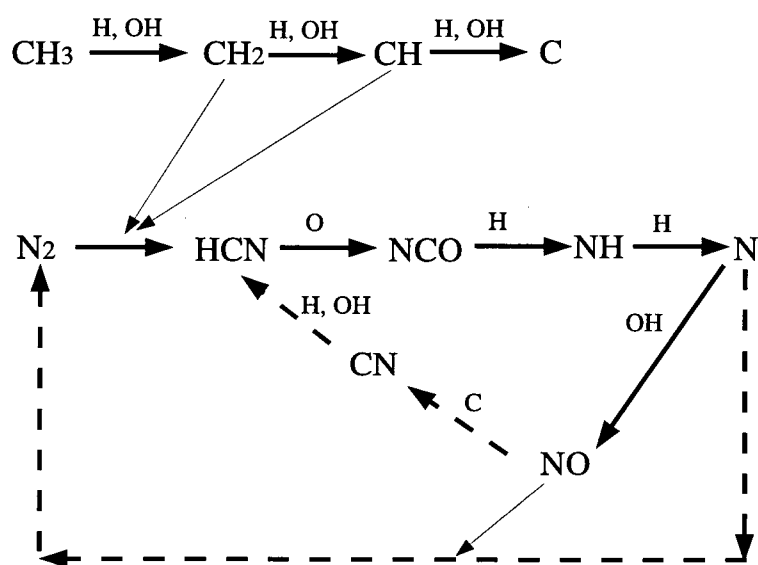
Figure 2.2: Main reaction paths of prompt NO in methane flame. The paths marked by dashed lines are more important in the fuel-rich region.

2.3.4 Formation of NO_2

In typical engine exhaust gas, the majority of NOx emissions is in the form of NO; however, for conditions where the flame temperature is low (such as in engines with significant fractions of recirculated exhaust gas), a considerable fraction of NO can be converted to NO_2 through

$$NO + HO_2 \rightleftharpoons NO_2 + OH, \qquad (R35)$$

$$NO_2 + H \rightleftharpoons NO + OH, \qquad (R36)$$

$$NO_2 + O \rightleftharpoons NO + O_2. \qquad (R37)$$
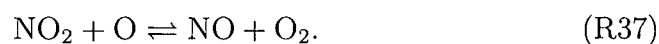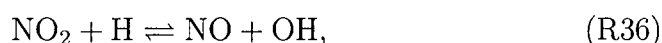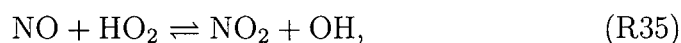
Reaction R35 is the dominating reaction in this process because of the high concentration of HO_2 in low temperature flames. Reaction R35 can be enhanced by the migration of H radicals from high-temperature regions to low-temperature ones in a diffusion flame. The hydrogen radicals can be readily combined with molecular oxygen to form HO_2 in

$$H + O_2 + M \rightleftharpoons HO_2 + M. \qquad (R38)$$

Reaction R38 is a third-order reaction, which implies that the conversion from NO to NO_2 has a higher rate at higher pressures, which makes this mechanism more relevant to combustion in IC engines.

2.3.5 In-flame NOx Reduction Strategies

Various in-flame NOx reduction technologies have been developed in the past decades for internal combustion engines and gas turbines to address increasing environmental concerns. Technologies such as lean combustion, staged combustion and exhaust gas recirculation (EGR) [79] have been widely adopted in the design of modern combustion devices. For example, in direct-injection natural gas engines, recent stud-

ies by McTaggart-Cowan et al. [5,6] show that up to an 80% reduction of NOx in the engine exhaust can be achieved with a high fraction of EGR compared with baseline results under identical load conditions.

While these techniques are mainly based on the concept of thermal NOx reduction by lowering the flame temperature, their kinetic impact should also be considered. Li and Williams [36,80] studied the effects of H_2O, CO_2 and N_2 addition in a two-stage methane/air counterflow flame. Water was found to be the most effective agent for reducing flame temperature due to its high specific heat, which led to the greatest reduction in thermal NOx. Although CO_2 and N_2 have similar specific heats, CO_2 is more effective than N_2 in suppressing NOx formation. This can be attributed to the kinetic interaction between CO_2 and CH through reaction

$$CH + CO_2 \rightleftharpoons CHO + CO. \qquad (R39)$$

Similarly, kinetic benefits can be obtained with water addition due to reaction

$$CH + H_2O \rightleftharpoons CH_2O + H. \qquad (R40)$$
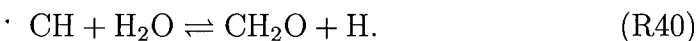
The high concentration of CO_2 or H_2O shifts the directions of R39 and R40, which reduces the rate of CH production, and consequently, the prompt NO formation.

NOx reburning is another effective technology for reducing NOx emission. Reburning is a chemically complex process in which NO is reduced in a hydrocarbon flame. Experimental studies of NOx reburning by doping reaction mixtures with NO, NO_2 and N_2O in plug-flow reactors or premixed flames have been reported by numerous researchers [68,81–83]. The consumption of NO in a reburning process is found to be strongly related to temperature, equivalence ratio and

residence time. Fuel-rich mixtures were found to favor NO reduction in most studies.

Miller and Bowman [78] postulated a mechanism for NOx reburning in hydrocarbon flames. It is believed that during reburning, nitric oxide is converted into hydrogen cyanide (HCN) and cyano (CN) by hydrocarbon radicals through

$$CH_2 + NO \rightleftharpoons HCNO + H, \qquad (R41)$$

$$HCNO + H \rightleftharpoons HCN + OH, \qquad (R42)$$

$$CH + NO \rightleftharpoons HCN + O, \qquad (R43)$$

$$C + NO \rightleftharpoons CN + O. \qquad (R44)$$
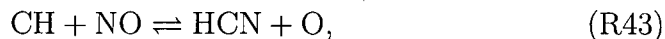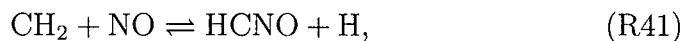
Their numerical study shows that the concentrations of CH_2 and CH radicals peak in slightly fuel-rich flames so that the reduction efficiency is the highest in this region. This is consistent with the experimental observations introduced above.

For flame temperatures between 800 and 1500 K, Glarborg et al. [84] suggested that the most important reactions in the reburning mechanism are those related to HCCO + NO and CH_3 + NO. Specifically, reactions

$$CH_3 + NO(+M) \rightleftharpoons CH_3NO(+M), \qquad (R45)$$

$$CH_3 + NO \rightleftharpoons H_2CN + OH, \qquad (R46)$$

and

$$CH_3 + NO \rightleftharpoons HCN + H_2O \qquad (R47)$$
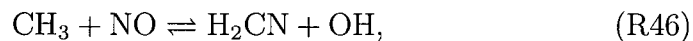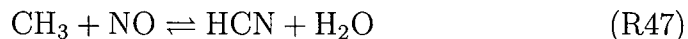
are dominant reactions for NO reburning in CH_4/air flames. Reaction

$$HCCO + NO \rightleftharpoons HCNO + CO \qquad (R48)$$
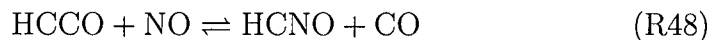
dominates NO reburning in natural gas/C_2 flames because of the relatively high concentration of acetylene (C_2H_2) in these flames. Acetylene is a main precursor for the formation of HCCO radicals. Hydrogen cyanide formed in the above reactions is partially recirculated back to N_2 via reactions

$$O + HCN \rightleftharpoons NCO + H, \tag{R49}$$

$$NCO + H \rightleftharpoons NH + CO, \tag{R50}$$

$$NH + H \rightleftharpoons N + H_2, \tag{R51}$$

$$N + NO \rightleftharpoons N_2 + H. \tag{R52}$$
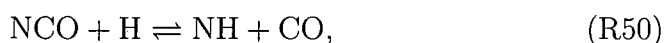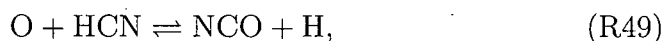
Although the NOx-formation mechanisms in hydrocarbon flames have been studied intensively, the uncertainties in the rate constants of some important elementary reactions remain high (e.g. HCCO + NO reaction [84]). Much research work is still necessary for us to fully understand the formation of NOx in practical combustion systems.

2.4 Analysis and Reduction of Detailed Chemistry

As shown in the reference cited in Table 2.2, a typical detailed reaction mechanism for natural gas combustion may contain dozens of species and hundreds of reactions. Depending on the combustion system, the thermal and kinetic contributions from some reactions are more significant than others. Numerical analyses help to identify the most significant reactions. They also serves as valuable tools for the reduction of detailed reaction mechanisms, whose implementation may be otherwise beyond the reach of the available computational resource. Sensitivity analysis, reaction flow analysis and eigenvalue-based analysis are three categories of analysis methods which are extensively used in

studying reaction mechanisms. Sensitivity analyses identify the rate-limiting reaction steps. Reaction flow analyses investigate the main reaction paths and integrated contribution of elementary reactions in any time period of interest. Eigenvalue/eigenvector analyses determine the characteristic time scales and directions of the chemical reactions [62].

2.4.1 Sensitivity Analysis

For a reaction system with defined initial and boundary conditions, the rate at which the system changes its state is a function of the species concentrations and the rates of elementary reactions involved. Mathematically, for a system with n species and m reactions, the above statement can be expressed as

$$\frac{\partial \xi}{\partial t} = f(c_1...c_n, k_1...k_m),$$ (2.15)

where ξ denotes a state variable of the reaction system (e.g. temperature, pressure, individual species mass fraction, etc.), c is the species concentration and k is the reaction rate. Some of the elementary reactions have nearly no effect on the solution of ξ, while others are more significant in determining the state of the system [62]. The rate-determining or rate-limiting reaction steps can be identified by examining the dependence of the solution of ξ on the parameter k_i by means of two definitions. One, the absolute sensitivity is

$$S_j = \frac{\partial \xi}{\partial k_j}.$$ (2.16)

in which the subscript j denotes the jth reaction. The second definition is the relative sensitivity

$$S_j = \frac{k_j}{\xi} \frac{\partial \xi}{\partial k_j} = \frac{\partial \ln \xi}{\partial \ln k_j}.$$ (2.17)

The differential equation governing the change of S_j can be derived by differentiating Eq. 2.15 with respect to k_j

$$\frac{\partial}{\partial t}\frac{\partial \xi}{\partial k_j} = \frac{\partial}{\partial k_j}\frac{\partial \xi}{\partial t} \tag{2.18}$$

$$\frac{\partial S_j^m}{\partial t} = \frac{\partial f}{\partial k_j} + \sum_{i=1}^{n}\left(\frac{\partial f}{\partial c_i}\frac{\partial c_i}{\partial k_j}\right),$$

in which the superscript i denotes the ith species. If one is interested in the sensitivity of concentration of species m with respect to the rate constant k_j, Eq. 2.18 reduces to

$$\frac{\partial S_j^m}{\partial t} = \left(\frac{\partial f}{\partial k_j}\right) + \sum_{i=1}^{n}\left[\left(\frac{\partial f}{\partial c_i}\right)S_j^i\right]. \tag{2.19}$$

Equation 2.18 or 2.19 can be integrated numerically to obtain the value of the sensitivity as the reaction system evolves.

An approximate evaluation of Eq. 2.18, which has the merit of simplicity in application, is given by

$$S_j = \frac{k_j}{\xi}\frac{\partial \xi}{\partial k_j} \approx \frac{k_j}{\xi}\frac{\xi(nk_j) - \xi(k_j/n)}{(n - 1/n)k_j}, \tag{2.20}$$

where n is a multiplication factor, which is typically given a value of two in the literature [22, 29]. Equation 2.20 is sometimes referred as a "brute-force" sensitivity analysis. Figure 2.3 presents an example of brute-force sensitivity analysis [28]. It shows that at the higher temperature, the recombination of two methyl radicals to form an ethane molecule is a main rate-limiting step in the induction period; while at the lower temperature, reactions that are related to the formation and consumption of OH radicals are more important in determining the ignition delay.

2.4.2 Reaction Flow Analysis

Sensitivity analyses provide important information regarding the rate-limiting steps of a reaction system; however, the information is usually
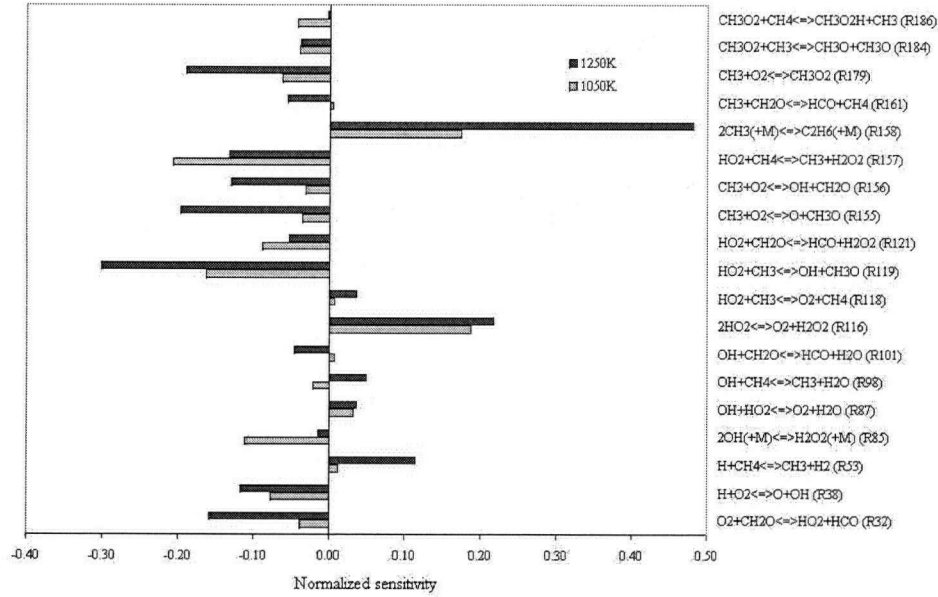
Figure 2.3: Sensitivity of ignition delay in methane/air mixture with respect to elementary reaction rates

insufficient to determine the main reaction path the system takes to evolve from one state to another. Such information can be obtained from reaction flow analyses. For a reaction process involving n species and m elementary reactions, the rate of change of species mass fraction at any moment t can be written in matrix form as

$$\mathbf{G}_i = \frac{d\mathbf{y}_i}{dt} = \mathbf{S}_{i,j}\mathbf{F}_j, \tag{2.21}$$

where $\mathbf{y}$ is the rate array of mass fractions of n species; $i = 1...n$; $\mathbf{S}$ is a $n \times m$ matrix of stoichiometric coefficients; $j = 1...m$, and $\mathbf{F}$ is the rate array of m reactions. The relative contribution, φ, of reaction l to the formation of species k can be obtained from the integral equation

$$\varphi_k^l = \int_{t_1}^{t_2} \frac{\mathbf{S}(k,l)\mathbf{F}(l)}{\sum_{j=1}^{m}\mathbf{S}(k,j)\mathbf{F}(j)}dt, \tag{2.22}$$

where t_1 and t_2 are the start and end times of interest, for example, the induction period. The integral reaction flow analysis was used to identify the key reaction steps during the ignition delay of methane/air mixtures as shown in Fig 2.1 in section 2.2.3.

A reaction flow analysis can also be performed locally. Reactions are unimportant if their contribution to the reaction system is insignificant at any time of interest. This criterion is often used in generating reduced reaction mechanisms from more detailed ones.

Frenklach [85] and Wang et al. [86] studied the reduction of a detailed methane/air mechanism which contains 163 steps and 32 species. The criteria they applied to identify non-contributing reactions are:

$$|F_j| < \epsilon_F |F_{ref}| \tag{2.23}$$

$$|F_j \Delta H_j| < \epsilon_Q \dot{Q}_{max}. \tag{2.24}$$

where F_j is the rate of reaction j; F_{ref} is the rate of a reference reaction (usually a rate-limiting step); ΔH_j is the enthalpy change of reaction j; $\dot{Q}_{max}$ is the maximum rate of change of enthalpy among all reactions; ϵ_F and ϵ_Q are two selected parameters which are significantly less than unity. For a value of 0.01 assigned to both ϵ_F and ϵ_Q, Wang et al. [86] reported that, based on the above criteria, nearly half of the reactions in the detailed mechanism can be removed while maintaining good agreement with calculated species profiles and laminar flame velocities using the full chemistry.

2.4.3 Chemical Time Scale and Eigenvalue Analysis

It is well known that the rate of reaction involved in a combustion system varies drastically from reaction to reaction. The characteristic time scales associated with different reactions can easily differ by several

orders of magnitude. The large difference between the minimum and maximum time scales of governing ODEs for a reaction system leads to a high *stiffness* in the mathematical model. For an explicit numerical solution to be stable, the smallest time scale must be resolved even if the rate-limiting reactions are usually those with longer time scales. This causes the solution procedure to be highly inefficient.

The local characteristic time scales of a reaction system can be obtained by analyzing the Jacobian matrix of the rate of change of species mass fraction. The Jacobean matrix is defined as

$$\mathbf{J}_{i,j} = \frac{\partial F(Y)_i}{\partial Y_j},$$

(2.25)

where Y denotes the mass fractions of species and the $F(Y)$ denotes the reaction rates of Y. It can be seen that each entry of $\mathbf{J}$ represents the inverse of a time scale indicating the rates at which species approach depletion. The eigenvalues of the Jacobean matrix represent the inverse of the characteristic (linearly independent) time scales in the composition space, and the corresponding eigenvectors determine the direction in which the reaction system evolves.

An important feature resulting from the large separation of time scales is that the species associated with fast reactions tend to approach a quasi-steady state rapidly. The consumptions of such species are much faster than the generations so that their concentrations remain low compared with those of the major species. Consequently, their rates of change are small, i.e. $d\dot{y}/dt \approx 0$. For species in quasi-steady state, one can replace the governing differential equations with algebraic expressions using the concentrations of slower species, which effectively simplifies the reaction mechanism [57, 62]. The main drawback of the quasi-steady-state assumption (QSSA) is that, in order to apply the me-

thod, the modeler must have some *a priori* knowledge about the reaction system; the assumptions are usually valid only over a limited range of conditions and thus may not be suitable for general mechanism reduction.

Computational Singular Perturbation

Lam and Goussis [87,88] proposed an efficient method for solving stiff ODE systems of chemical reactions based on the quasi-steady state concept but using a more rigorous mathematical approach. As shown in Eq. 2.21, a chemical reaction system evolves in an N dimensional hyperspace (called composition space) where N is the number of species involved in the reaction mechanism. Because of the separation of reaction time scales, the composition space can be split into a m-dimensional fast subspace and a n dimensional slow space, where $m + n = N$. The reaction vector G can be represented in the above two subspaces

$$\mathbf{G} = \mathbf{G}_{fast} + \mathbf{G}_{slow} = \mathbf{a}_i\mathbf{f}^i + \mathbf{G}_{slow}, \tag{2.26}$$

where $\mathbf{a}_i$ is an $N \times m$ matrix whose columns are the basis vectors span the fast subspace; $\mathbf{f}$ is an $m \times m$ diagonal matrix representing the magnitude of the projected G vector on the fast subspace. The notation

$$\mathbf{a}_i\mathbf{f}^i = \sum_{i=1}^{m} a(i,j)f(i). \tag{2.27}$$

The ith diagonal entry of $\mathbf{f}$ can be calculated from

$$\mathbf{f}^i = \mathbf{b}^i \cdot \mathbf{G}_{fast}, \tag{2.28}$$

where $\mathbf{b}^i$ is the dual of the basis vector $\mathbf{a}^i$. A differential equation can be derived for the evolution of f^i based on Eq. 2.26 and Eq. 2.28.

$$\frac{d\mathbf{f}}{dt} = (\mathbf{BJA} + \frac{d\mathbf{B}}{dt}\mathbf{A})\mathbf{f}, \tag{2.29}$$

where $\mathbf{J}$ is the Jacobian matrix; $\mathbf{A}$ is a transformation matrix whose ith columns is $\mathbf{a}_i$, and $\mathbf{B}$ is a dual matrix whose jth row is $\mathbf{b}_j$. A detailed derivation of Eq. 2.29 is given in Appendix A.

As stated above, the eigenvalue of the Jacobian matrix represents the inverse of the characteristic time scale. Thus the eigenvectors corresponding to large negative eigenvalues span the fast subspace. The right eigenvectors of $\mathbf{J}$ are defined as

$$\mathbf{J}\beta = \lambda\beta, \tag{2.30}$$

where β is a $n \times n$ matrix whose columns are the right eigenvectors; λ is a $n \times n$ diagonal matrix of eigenvalues. Similarly, the left eigenvectors are defined as

$$\alpha\mathbf{J} = \lambda\alpha. \tag{2.31}$$

The basis vectors that span the fast subspace and their duals are the right and left eigenvectors that correspond to the m largest negative eigenvalues. The dimension of the fast subspace may change as the reaction system evolves. The value of m can usually be determined by comparing the characteristic time scale with the desired time resolution of the numerical solutions; an eigenvalue is large if

$$|\lambda\Delta t| > 1. \tag{2.32}$$

The CSP method solves the stiff ODE system of chemical reactions using the following procedure:

1. Integrate the governing equation 2.21 using sufficiently small time steps.

2. Compute the Jacobian matrix numerically (this is where the name of the method comes from). Decompose the Jacobian matrix to

find the eigenvalues and corresponding eigenvectors. Determine the dimension of the fast subspace and its basis vectors.

3. Solve Eq. 2.29 for **f**.

4. Repeat Steps 1 to 3 until G^m_{fast} in the fast subspace becomes trivial.

5. Bypass reactions related to the fast mode and integrate Eq. 2.21 using large time steps; update the Jacobian matrix and its eigenvalues at each time step.

6. Whenever the dimension of the fast subspace changes, return to step 1.

The CSP method resolves the stiffness problem in the governing ODEs of a reaction system by separating the time scales. In this way, the efficiency of integration is greatly increased. Because the reactions in the fast subspace are eliminated only when the projections in G^m_{fast} become insignificant, the accuracy of the detailed reaction mechanism is well preserved. Lu et al. [89] compared model results using CSP with direct numerical integration for premixed CH_4/air and H_2/air flames. They reported very good agreement in terms of flame velocity and flame structure.

Intrinsically Low-Dimensional Manifold

The eigenvalues of the Jacobian matrix give the characteristic time scale of a reaction system. The number of large negative eigenvalues determines the dimension of the fast subspace. For a typical combustion system, Maas and Pope [90] have shown that most of the eigenvalues of the Jacobian matrix are large and negative, which implies that the
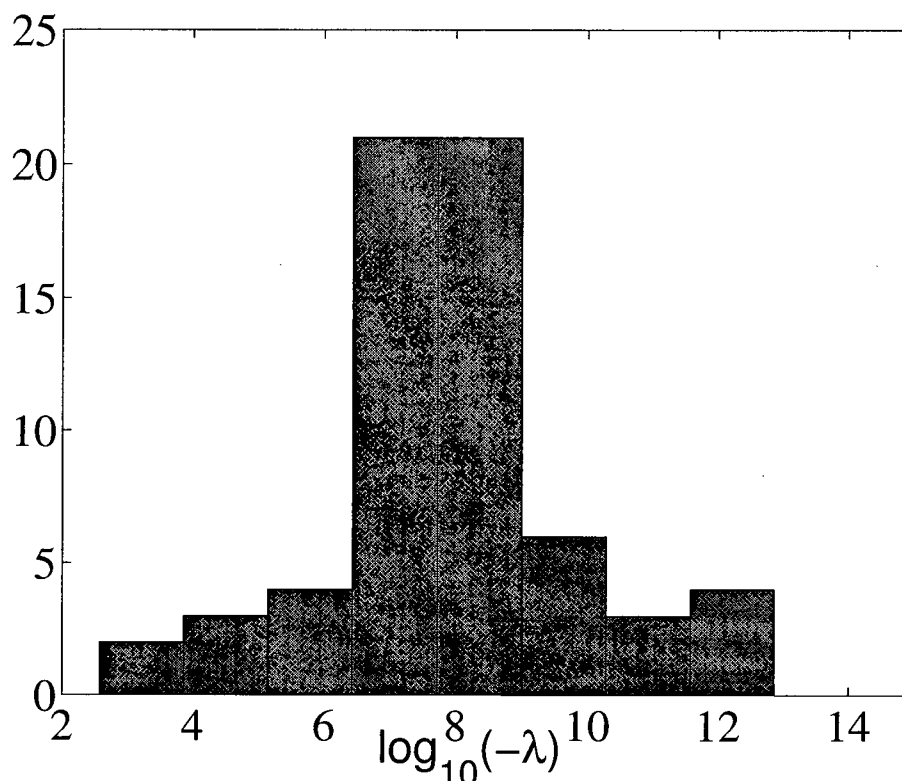
Figure 2.4: Histogram of eigenvalues of natural gas - air combustion system at 2100 K, $\phi = 1$. The system contains 71 species, 5 elements. There are five zero eigenvalues corresponding to the element mass conservations that are not shown in the graph.

rate of the system is controlled by a small number of slow reactions. Figure 2.4 shows an example of the histogram of eigenvalues in a homogeneous, constant pressure natural gas - air reaction system. It can be seen that for the conditions investigated, a majority of eigen modes have very short time scales ($\tau < 1e - 4s$). In other words, a constrained reaction system tends to converge to a low-dimensional manifold (attractive subspace) as the reactions in the fast subspace exhaust rapidly. A *constrained system* is one that conserves elements and has defined boundary conditions, which lead to a unique equilibrium state, e.g. a constant-pressure, adiabatic reaction system. Figure 2.5 shows the con-
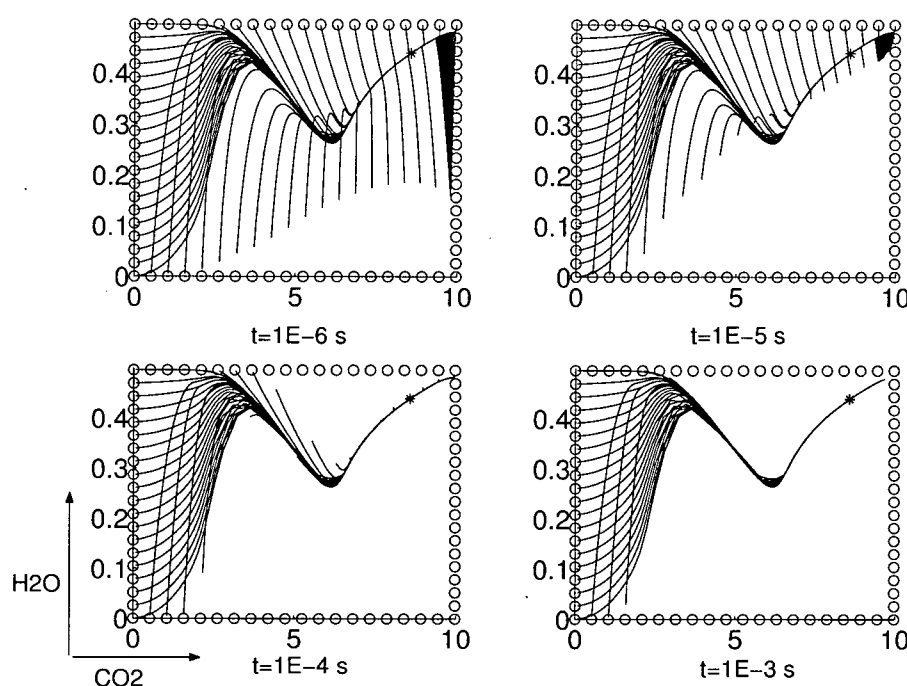
Figure 2.5: Convergence of reaction trajectories onto a one-dimensional ILDM. The reaction system is a stoichiometirc $H_2 - CO -$ air system containing 13 species [90].The manifold is projected onto $\phi_{H2O} - \phi_{CO2}$ plane; ϕ denotes specific mole number

vergence of trajectories starting from various initial conditions in the composition space onto a manifold by progressively truncating a given reaction time. This important feature forms the basis of the intrinsically low-dimensional manifold (ILDM) [90] as an effective method for automatic mechanism reduction. Since the manifold is *intrinsically low-dimensional,* it is possible to tabulate all the rate and concentration profiles on the manifold using a small number of progress variables so that the solution can be retrieved quickly in a reactive flow calculation.

Maas and Pope [90] proposed a mathematical formula to compute the ILDM of a constrained reaction system. The ideal is to locate points in the composition space where the projection of the reaction vector on the fast subspace vanishes. Naturally, following the concept of CSP

as introduced above, one would tend to use the eigenvectors corresponding to the large negative eigenvalue as the basis for the projection. However, due to the Jacobian matrix being ill-conditioned (rows of the Jacobian matrix could exhibit a nearly linear dependence), the numerical approach of eigen decomposition could fail occasionally. Instead of using eigenvectors, Maas and Pope [90] suggest using Schur factorization [6] of the Jacobian matrix

$$\mathbf{J} = \mathbf{V}\Lambda\widetilde{\mathbf{V}}, \tag{2.33}$$

where $\mathbf{V}$ is the right Schur vector matrix of the Jacobian $\mathbf{J}$; Λ is an upper-triangular matrix whose diagonal entries are the eigenvalues of $\mathbf{J}$, which represent the inverse of the characteristic time scales; $\widetilde{\mathbf{V}}$ denotes inverse matrix of $\mathbf{V}$. The eigenvalues and corresponding Schur vectors in Λ, $\mathbf{V}$ and $\widetilde{\mathbf{V}}$ are sorted in descending order with the negative eigenvalues of greatest magnitude representing the fastest process at the bottom of Λ. Such a decomposition always exists and can be computed readily with robust numerical methods [91].

If there exists a distinct difference between time scales associated with the n_sth and n_s+1th process, i.e. $\|\Lambda(n_s, n_s)\| << \|\Lambda(n_s+1, n_s+1)\|$, the fast processes corresponding to $n - n_s$ large negative eigenvalues quickly relax to quasi-steady state, leading to the convergence of the reaction system onto a n_s-dimensional manifold. Mathematically, the low-dimensional manifold is expressed as a n_s-dimensional subspace of the composition space which satisfies

$$\widetilde{\mathbf{V}}_f\mathbf{F}(\mathbf{Y}) = 0, \tag{2.34}$$

where $\widetilde{\mathbf{V}}_f$ is an $(n - n_s)$ by n matrix taken from the last $n - n_s$ rows of $\widetilde{\mathbf{V}}$. The physical meaning of Eq. 2.34 is that the projection of the re-

---

[6]See Appendix B for details

action vector along the slow manifold onto the fast subspace vanishes. Eq. 2.34 can be solved by adding n_s parametric equations representing system constrains (i.e. element mass conservation, etc.) and a small number of progress variables. The final form of the ILDM equations can be written as

$$G(\mathbf{Y}, \tau) = \begin{pmatrix} \tilde{\mathbf{V}}_f \mathbf{F}(\mathbf{Y}) \\ P(\mathbf{Y}, \tau) \end{pmatrix} = 0, \tag{2.35}$$

where P denotes n_s parameter equations, and τ denotes the values of parameters. Equations 2.35 form a constrained optimization problem, where the constraints are defined by the parametric equations.

Due to the highly non-linear nature of reaction rates, Eqs. 2.35 are very difficult to solve even with dedicated non-linear solvers [90]. In addition, Nafe and Maas [92] identified three issues associated with computing ILDMs using Eq. 2.35. First, there is no guarantee that a converged solution exists everywhere in the realizable domain. Second, in the region where eigenvalues cross each other (i.e. when the separation between fast and slow time scales vanishes), the manifold may become discontinuous. Finally, the ILDM is not an inertial manifold unless the time scale separation approaches infinity. To improve the construction of the ILDM, Nafe and Maas proposed a method based on the Fraser algorithm [93]. The method is based on a pseudo-unsteady equation, which evolves the manifold towards a steady state solution representing the slow manifold. The governing equation is given by

$$\frac{\partial \mathbf{Y}}{\partial \tau} = (I - \mathbf{Y}_\theta \mathbf{Y}_\theta^+)\mathbf{F}(\mathbf{Y}), \tag{2.36}$$

where $\mathbf{Y}$ is a n-dimensional vector of system variables (e.g. species mass fraction and temperature); θ is a m-dimensional vector that parameterizes the manifold; $\mathbf{Y}_\theta$ is the partial derivative of $\mathbf{Y}$ with respect

to θ; $\mathbf{Y}_\theta^+$ is the Moore-Penrose pseudo-inverse which is given by

$$\mathbf{Y}_\theta^+ = (\mathbf{Y}_\theta^T \mathbf{Y}_\theta)^{-1} \mathbf{Y}_\theta^T; \tag{2.37}$$

$\mathbf{F}$ is the rate vector of system variables. The pseudo time scale τ is introduced to stabilize the calculation to achieve a steady state solution, which satisfies

$$(I - \mathbf{Y}_\theta \mathbf{Y}_\theta^+)\mathbf{F}(\mathbf{Y}) = 0. \tag{2.38}$$

The manifold generated using Nafe and Maas algorithm has the merit of being continuous and differentiable, which overcome the problems associated with the original ILDMs.

Trajectory Generated Low-Dimensional Manifold

In general, the construction and implementation of an optimal ILDM is mathematically complex. In order to simplify the calculation, Pope [94] proposed the Trajectory-Generated Low-Dimensional Manifold (TG-LDM) method. The manifold is defined in terms of reaction trajectories, which are generated by simply integrating Eq. 2.21. The initial points of the trajectories, which define the boundary of the manifold, are computed from the realizable composition space C_R. For a 2-D manifold, the manifold generator is a closed curve G, which should be as large as possible to maximize the overlap between the TGLDM and intrinsic (attracting) manifold. Pope and Maas [94] computed the trajectory generator G using the *extreme-value-of-major-species* method. For example, if a two-dimensional manifold is to be generated, $n_e + 2$ major species were selected based on the global balance equation of the reaction system. Here n_e is the number of elements involved. The linear equation system that satisfies element mass conservation was constructed using

$$\sum_{i=1}^{n_e+2} Y_c(j,i)Y(i) = Y_e(j) \qquad j = 1, n_e, \tag{2.39}$$

where $Y_c(j,i)$ is the mass fraction of element j in species i; $Y(i)$ is the mass fraction of species i; $Y_e(j)$ is the mass fraction of element j in the mixture. This equation system is under-determined with 2-degree of freedom in the solution space. The boundary of the solution space can be readily calculated using simple linear programming techniques [95].

Once the manifold is constructed, its projection in the parameter space can be computed for tabulation. For a two-dimensional manifold, the rate of change of species mass fraction Φ on the manifold is a function of two parameters u and v:

$$\frac{d\Phi}{dt} = \frac{\partial\Phi(u,v)}{\partial u}\frac{\partial u}{\partial t} + \frac{\partial\Phi(u,v)}{\partial v}\frac{\partial v}{\partial t}, \qquad (2.40)$$

where Φ is the species mass fraction on the manifold. The values of Φ, u and v are tabulated. In a reactive flow, the chemical reactions are perturbed by mass transport in the flow field through diffusion and convection. The perturbation alters the direction of reactions from the tangent plane on the manifold. Thus the value of $d\Phi/dt$ is usually different from that of dY/dt. It is necessary to project the perturbation into the manifold space. According to Pope and Maas [94], parameter u evolves following

$$\frac{\partial u}{\partial t} = \mathbf{P^u} \cdot (\mathbf{S} + \mathbf{F}), \qquad (2.41)$$

where $\mathbf{S}$ is the chemical source term and $\mathbf{F}$ is the perturbation; $\mathbf{P}^u$ is a projection vector for u, which is given by

$$\mathbf{P}^u = \frac{(\Phi_v \cdot \Phi_v)\Phi_u \cdot \mathbf{P} - (\Phi_u \cdot \Phi_v)\Phi_v \cdot \mathbf{P}}{(\Phi_u \cdot \Phi_u)(\Phi_v \cdot \Phi_v) - (\Phi_u \cdot \Phi_v)^2}, \qquad (2.42)$$

where Φ_u is $\partial\Phi/\partial u$; Φ_v is $\partial\Phi/\partial v$, and $\mathbf{P}$ is a specified $n \times n$ projection matrix. Similar equations apply to the evolution of v. Ideally, the projection matrix should be based on the eigenvectors of the Jacobian matrix [94]; however, perpendicular projection in the composition space

is sometimes used to simplify computation. This means that the projection matrix is reduced to an identity matrix. An important feature of the TGLDM is that the reaction vector **S** is in the tangent plane of the manifold so that the selection of a projection matrix only affects the perturbation term **F** but not the chemical source term **S**.

The difference between the ILDM and the TGLDM with tailored initial states can be examined by considering the following hypothetical reaction system:

$$S_1 \xrightarrow{k_1} S_2 \xrightarrow{k_2} S_3, \tag{2.43}$$

with the initial conditions

$$Y_{S1,t=0} = 1, Y_{S2,t=0} = Y_{S3,t=0} = 0. \tag{2.44}$$

Here S_2 is an intermediate species, and $k_1 \ll k_2$. The global reaction is

$$S_1 \rightarrow S_3. \tag{2.45}$$

The Jacobian matrix of this reaction system is given by

$$\mathbf{J} = \begin{pmatrix} -k_1 & 0 & 0 \\ k_1 & -k_2 & 0 \\ 0 & k_2 & 0 \end{pmatrix}. \tag{2.46}$$

The three right eigenvalues of **J** are $-k_2$, $-k_1$ and 0. The corresponding eigenvector matrix is written as

$$\mathbf{V} = \begin{pmatrix} 0 & 1 & 0 \\ -1 & \frac{k_1}{k_2-k_1} & 0 \\ 1 & -\frac{k_2}{k_2-k_1} & 1 \end{pmatrix}. \tag{2.47}$$

The matrix inverse of **V** gives

$$\widetilde{\mathbf{V}} = \begin{pmatrix} \frac{k_1}{k_2-k_1} & -1 & 0 \\ 1 & 0 & 0 \\ 1 & 1 & 1 \end{pmatrix}. \tag{2.48}$$

The first row of $\widetilde{V}$ designates the projection vector to the fast subspace. Based on eigenvectors corresponding to fast eigen modes, a one-dimensional IDLM is given by

$$\frac{dY_{S_2}}{dt} - \frac{k_1}{k_2 - k_1} \frac{dY_{S_1}}{dt} = 0, \tag{2.49}$$

whose solution is given by

$$Y_{S_2} = \frac{k_1}{k_2 - k_1} Y_{S_1}, \tag{2.50}$$

which is the same as one would get from the quasi-steady-state analysis assuming $d[S_2]/dt = 0$. The projection of the constrain due to mass conservation in the $Y_{S_1} - Y_{S_2}$ plane is a straight line intersecting both axes at unity. The final ILDM subject to this constraint is shown in Fig. 2.6. For demonstration, the ratio of k_2/k_1 is set at 10 to emphasize the difference between fast and slow processes. It can be seen that, along the section of the ILDM defined by the linear constraint, the direction of the projected reaction vector is given by

$$\frac{\partial \dot{Y}_{S_2}}{\partial \dot{Y}_{S_1}} = \frac{k_2}{k_1 Y_{S_1}} - \frac{k1 + k2}{k_1}, \tag{2.51}$$

which is apparently not in the tangent plane of the ILDM. Thus a back projection is required to return the solution to the manifold.

For the TGLDM, the initial state can be obtained based on the species involved in the global reaction. The linear system given by Eq. 6.5 is used to obtained the manifold generator [94] that defines the initial state of the trajectories. In order to solve Eq. 6.5, the number of major species to be involved in the global reactions should be equal to $n_c + n_p$, ie. the total number of elements plus the dimension of the manifold. For the current simple system with a one-dimensional manifold, the initial state is defined by

$$\begin{pmatrix} 1 & 1 \\ 1 & 0 \end{pmatrix} \begin{pmatrix} Y_{S_1} \\ Y_{S_3} \end{pmatrix} = \begin{pmatrix} 1 \\ 1 \end{pmatrix}. \tag{2.52}$$
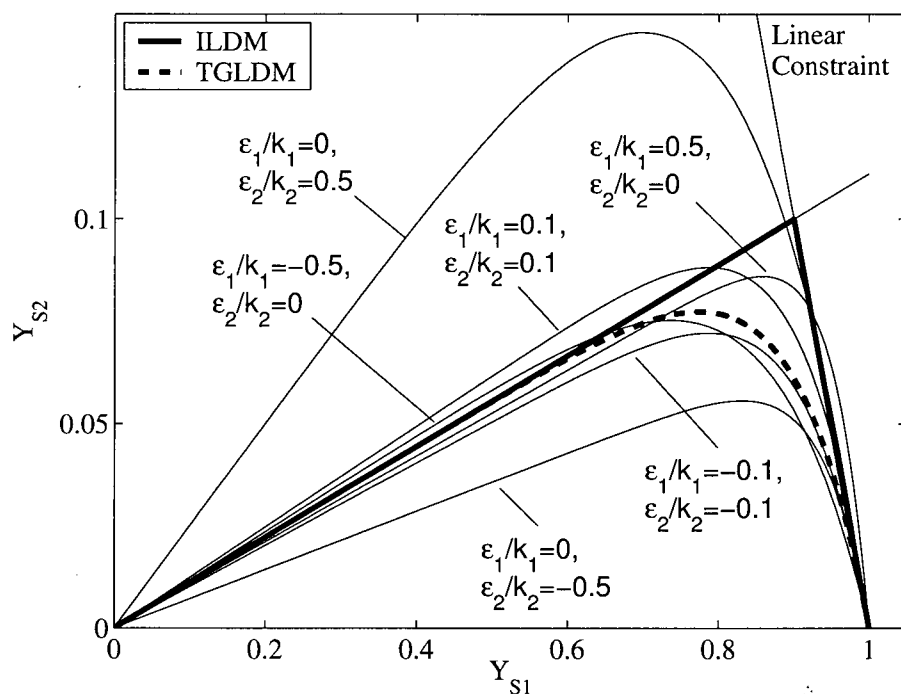
Figure 2.6: Comparison of 1-D ILDM and TGLDM calculated for a hypothetical reaction system. The ratio of reaction rate between the fast and slow processes is 10. The manifolds are projected into Y_{S_1} - Y_{S_2} plane. The thin lines represent trajectories subject to perturbations of various time scales.

In forming Eq. 2.52, the *a priori* knowledge that $Y_{S_1} = 1$ at $t = 0$ has been used. In reactive flow calculations, such information is usually available from initial conditions. The resulting TGLDM, which represents the trajectory of an unperturbed reaction system, is shown in Fig. 2.6.

When the system is perturbed by some physical process, such as mass transport by diffusion and convection, the Jacobian matrix takes the form

$$
\mathbf{J} = \begin{pmatrix} -k_1 + \epsilon_1 & 0 & 0 \\ k_1 & -k_2 + \epsilon_2 & 0 \\ -\epsilon_1 & k_2 - \epsilon_2 & 0 \end{pmatrix}, \tag{2.53}
$$

where ϵ_1 and ϵ_2 represent arbitrary time scales associated with the perturbations. We assume the perturbations occur in the same subspace as defined in Eq. 6.5. The assumption is consistant with that of identical diffusivity and unity Lewis number adopted by many turbulent combustion models [96,97]. The three eigenvalues of this perturbed system are 0, $-k_2 + \epsilon_2$, $-k_2 + \epsilon_1$. The closed form solution is given by

$$
Y_{S_1} = exp\left[-(k_1 - \epsilon_1)t \right] \tag{2.54}
$$
$$
Y_{S_2} = \frac{k_1 Y_{S_1}}{k_2 - \epsilon_2 - (k_1 - \epsilon_1)} \left\{ 1 - exp\left[-(k_2 - \epsilon_2) \right] \right\}
$$
$$
Y_{S_3} = 1 - Y_{S_1} - Y_{S_3}.
$$

Under conditions when $\epsilon_1 \ll k_1$ and $\epsilon_2 \ll k_2$, the solution converges to TGLDM. In fig. 2.6, it is shown that the trajectories of the sample reaction system subject to various levels of perturbation. It can be seen that when the time scale of perturbation is larger or comparable to that of the slow process $(1/k_1)$, the TGLDM with tailored initial condition provides a reasonable approximation to the analytical solution. A large deviation from both manifolds occurs when the physical time scale is comparable to that of the fast process $(1/k_2)$ of the reaction system.

2.5 Modeling of Turbulent Reactive Flow

One fundamental issue in turbulent reactive flow modeling is to properly represent the effect of turbulent fluctuations on chemical reaction rates. For most practical turbulent flow problems, direct numerical simulations (DNS) that fully resolve the smallest turbulent scales are still beyond the reach of the current computational resources. In practice, the mean or filtered values of the flow field are often obtained by solving the Reynolds-averaged or spatially-filtered Navier-Stokes equations as in Reynolds-Averaged Navier-Stokes (RANS) models and Large Eddy Simulation (LES). The effect of unresolved fluctuations on the mean flow field is often accounted for through turbulent viscosity models. For a turbulent reactive flow, the mean value of the chemical source term is required to close the conservation equations. However, as illustrated by Warnatz [62], the averaged chemical reaction rate is strongly affected by the details of the fluctuations in the flow field, and thus cannot be computed from the mean values directly. That is, in a turbulent reactive flow

$$\bar{\omega}\big(p(x,t), T(x,t), \mathbf{Y}(x,t)\big) \neq \omega\big(\bar{p}, \bar{T}, \bar{\mathbf{Y}}\big), \qquad (2.55)$$

where $\bar{\omega}$ is the mean reaction rate. One fundamental approach to address the closure problem in the chemical source term is to calculate the mean value from a statistical description of the reaction system using the probability density function (PDF). If the PDF of the turbulent flow field is known, the mean reaction rate can be integrated from the conditional reaction rates weighted by their local PDFs, i.e.

$$\bar{\omega} = \int \dots \iiint \omega(p, T, \mathbf{Y}) P(\mathbf{v}, \tau, T, \mathbf{Y}; \mathbf{x}, t) dv_x dv_y dv_z dT dY_1 \dots dY_n,$$
$$(2.56)$$

where p is pressure, T is temperature, τ is a characteristic time scale of turbulence, $\mathbf{v}$ is the velocity vector, Y is the mass fraction of species, and P is the probability density function. The probability density function is typically assumed to be a joint PDF of velocity, turbulent frequency, and thermochemical composition [98]. A model transport equation is solved, typically by Lagrangian particle method, to obtain the instantaneous value of the joint PDF [98]. The merit of PDF method is that the effect of turbulent convection on non-linear chemical reaction is captured exactly. The PDF method has been successfully applied to model various turbulent combusting flows [99–101]. Nevertheless, as implied by Eq. 2.56, the PDF-transport equation is a high-dimensional equation; numerical approaches used to solve the joint PDF, such as Monte-Carlo methods or hybrid methods, are very time consuming even for systems with a relatively small number of species [62].

A significant simplification of the PDF-transport equation can be achieved if the PDF is assumed to take on the form of a generic function (e.g. a β function or a clipped Gaussian), which is fully determined by a limited number of parameters, such as the mean and variance. In that case, the PDF can be constructed based on certain conserved scalar whose mean and variance can be solved from their transport equations. Ideally, such a conserved scalar should have some physical meaning that is related to the fluctuation in the reaction rates. For non-premixed or partially premixed combustion problems, the mixture fraction (Z) is often used as such a scalar. One definition of mixture fraction is

$$Z = \frac{Y_i - Y_{i,1}}{Y_{i,2} - Y_{i,1}}, \tag{2.57}$$

where Y_i denotes the mass fraction of element i in the mixture; $Y_{i,1}$ denotes the mass fraction of i in stream 1; $Y_{i,2}$ denotes the mass frac-

tion of i in stream 2. Mixture fraction is a measure of the element mass fraction, which originates from the fuel (or oxidizer) stream. If all the species are assumed to have the same diffusivity, the mixing process can be characterized using the mixture fraction alone. For each mixture fraction with given density or pressure, there is a defined equilibrium state subject to the boundary conditions. If we make further assumptions that the thermal diffusivity is identical to the species diffusivity (unity Lewis number) and the chemical time scale is significantly shorter than the physical time scale (fast chemistry), all the scalar variables in a turbulent combustion problem become a known function of mixture fraction [62].

As introduced in the previous section, due to the large separation of chemical time scales, the fast chemistry assumption is not valid in many combustion systems. Various finite-rate turbulent combustion models have been developed to address the non-equilibrium effects. Among them, the Laminar Flamelet (LF) model and the Conditional Moment Closure (CMC) model have received the most recent attention. They are discussed in the following sections. An introduction of the Conditional Source-term Estimation (CSE) method is given at the end of the chapter. This is the key combustion model used in this work. All three models are based on the two-parameter representation of the PDF of mixture fraction using its mean and the variance.

2.5.1 Laminar Flamelet Model

The fundamental assumption of the laminar flamelet model is that the reacting interface of a non-premixed turbulent flame can be viewed as an ensemble of locally laminar diffusion flamelets. The model formulation was formally introduced by Peters [96], who performed a
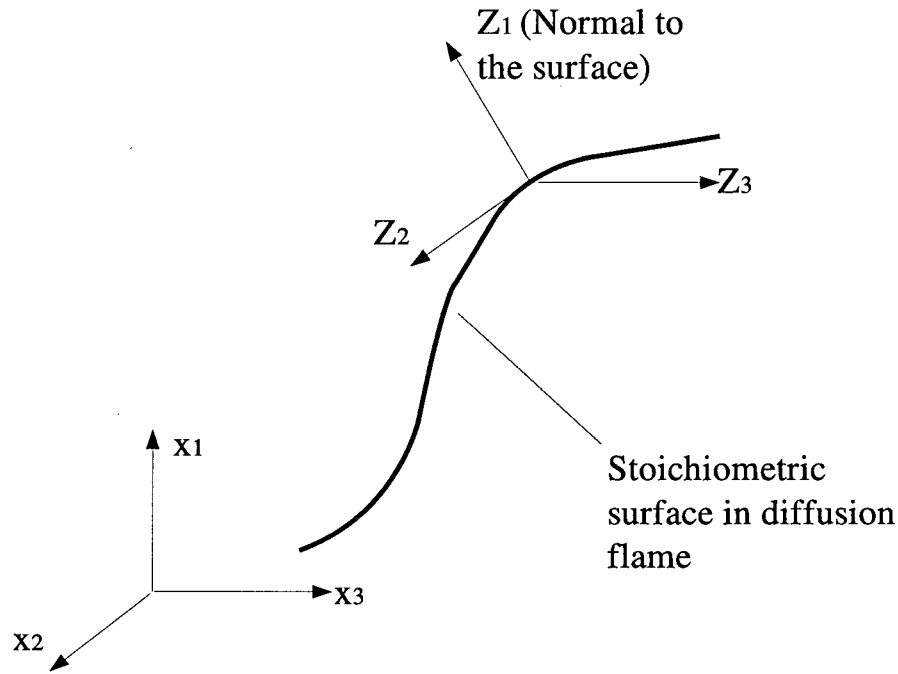
Figure 2.7: Coordinate transformation in laminar flamelet model

Crocco-type coordinate transformation to the conservation equations of species and enthalpy using following rules

$$\frac{\partial}{\partial t} = \frac{\partial}{\partial \tau} + \frac{\partial Z}{\partial t}\frac{\partial}{\partial Z} \qquad (2.58)$$
$$\frac{\partial}{\partial x_1} = \frac{\partial Z}{\partial x_1}\frac{\partial}{\partial Z}$$
$$\frac{\partial}{\partial x_i} = \frac{\partial}{\partial Z_i} + \frac{\partial Z}{\partial x_i}\frac{\partial}{\partial Z} \qquad i = 2, 3,$$

where t denotes time; $x_1...x_3$ denote the spatial coordinates; Z denotes a new coordinate normal to the stoichiometric surface of the mixing field; $Z_i(i = 2, 3)$ are the two other components of the transformed spatial coordinates; τ is the transformed time coordinates given by $\tau = t$. A schematic of original and transformed spatial coordinates is given in Fig. 2.7. The function of this transformation is to move the coordinates from a Lagrangian frame to an Eulerian frame attached to the flame

front. The transformed conservation equations are written as

$$\rho\frac{\partial Y_i}{\partial \tau} = \rho D\frac{\partial Z}{\partial x_j}\frac{\partial Z}{\partial x_j}\frac{\partial^2 Y_i}{\partial Z^2} + \dot{w}_i - R(Y_i) \qquad (2.59)$$

$$\rho\frac{\partial T}{\partial \tau} = \rho D\frac{\partial Z}{\partial x_j}\frac{\partial Z}{\partial x_j}\frac{\partial^2 T}{\partial Z^2} + \sum_{i=1}^{n}\frac{h_i}{c_p}\dot{w}_i - R(T),$$

where D is the mass/thermal diffusivity (where it has been assumed that all the species have the same diffusivity and the Lewis number is unity); $\dot{w}_i$ is the mass production rate of species i; h_i is the enthalpy of species i; and c_p is the mixture-averaged specific heat. The radiation and pressure fluctuation terms in the energy equation have been omitted. The operators $R(Y_i)$ and $R(T)$ contain the derivatives of Y_i and T with respect to Z_2 and Z_3; they are considered as being of lower order compared with the first term on the r.h.s. of Eq. 2.59, and are neglected in the final form of the flamelet equations [96]. The above transformation and assumptions yield a one-dimensional flamelet equation which is normal to the stoichiometric surface. The instantaneous scalar dissipation rate, which is defined by

$$\chi = 2D\frac{\partial Z}{\partial x_j}\frac{\partial Z}{\partial x_j} \qquad (2.60)$$

describes the non-equilibrium effect in diffusion flames. A higher value of χ leads to a more rapid removal of species and heat from the flame; at a certain critical value, χ_q, where the chemical reaction cannot sustain the heat loss due to turbulent mixing, a quenching of the flame occurs. In turbulent flame calculations, it is preferable to represent the profile of χ with a single parameter. Following Law and Chung [102], Peters [96] proposed using the scalar dissipation at the stoichiometric surface, i.e. $\chi_{st} = \chi(Z_{st})$ as the representative parameter. Assuming flamelets of the mixing layer type are predominant in turbulent diffusion flames, Peters chose to use the counter-flow geometry to describe

the Z dependence of the χ profile. From the analytical solution, it can be shown that

$$\chi(Z) = \frac{a}{\pi} exp\{-2[\text{erfc}^{-1}(2Z)]^2\}, \qquad (2.61)$$

where erfc^{-1} is the inverse of the complementary error function. The functional dependence of $\chi(Z)$ on χ_{st} can be derived from Eq. 2.61

$$\chi(Z) = \chi_{st} f(Z)/f(Z_{st}), \qquad (2.62)$$

where $f(Z)$ is the exponential term in Eq. 2.61. In RANS turbulence models, the mean value of scalar dissipation can be related to turbulent fluctuation through [96, 103]

$$\tilde{\chi} = c_x \frac{\tilde{\epsilon}}{\tilde{k}} \widetilde{Z''^2}, \qquad (2.63)$$

where ϵ is the dissipation rate of turbulent kinetic energy; k is the turbulent kinetic energy; $\widetilde{Z''^2}$ is the variance of the mixture fraction; c_x is a scaling coefficient with a standard value of 2.0 [103]. The $\tilde{}$ indicates that the variable is a Favre-averaged quantity. The representing parameter, χ_{st} in Eq. 2.62 is often equated its Favre-average, which can be calculated from the integral equation

$$\chi_{st} = \widetilde{\chi_{st}} = \frac{\tilde{\chi} f(Z_{st})}{\int_0^1 f(Z)P(Z)dZ}. \qquad (2.64)$$

Once the χ profile in the flow filed is solved, the mean value of a species mass fraction can be computed from the joint PDF of Z and χ

$$\widetilde{Y_i} = \int_0^\infty \int_0^1 Y_i(Z;\chi)P(Z,\chi)dZd\chi. \qquad (2.65)$$

Further simplification can be achieved if Z and χ are assumed to be statically independent. In that case, Eq. 2.65 is reduced to

$$\widetilde{Y_i} = \int_0^\infty \int_0^1 Y_i(Z;\chi)P(Z)P(\chi)dZd\chi. \qquad (2.66)$$

In the most direct implementation of the laminar flamelet model, the steady-state flamelet equations with various profiles of the scalar dissipation are solved numerically. The solutions are then tabulated to form a flamelet library with Z and χ as the table dimensions. The mean mass fractions can then be obtained by solving the conservation equations of various moments of Z and χ, and substituting the resulting PDF and conditional reaction rates from the pre-computed flamelet library into Eq. 2.66.

The steady-state flamelet model relaxes the fast chemistry assumption significantly; however, experimental and theoretical studies have shown that the flamelet structure cannot respond instantaneously to changes in scalar dissipation [104–106]. Hence, the steady-state flamelets are not suitable for modeling processes where the chemical time scale is comparable to or longer than the flow time scale. To address this issue, various unsteady flamelet models have been developed and tested with different levels of success.

Coelho and Peters [107] studied a piloted methane/air diffusion flame using an Eulerian particle flamelet model. The unsteady calculations were performed in the post-processing stage by transporting fluid particles that trace the temporal evolution of the scalar dissipation rate and solve the unsteady flamelet equation with the varying χ value. The results show an improvement in the predicted species concentration profile compared with the steady-state model. A similar approach, called the representative interactive flamelet model(RIF) proposed by Barths et al. [108], solves the unsteady flamelet equations interactively with the solution of the flow field. This method has been implemented in simulating combustion and pollutant formation in diesel engines [108–111] where the transient process dominates. Rao and Rut-

land [112] proposed a flamelet time scale model, which features lower computational cost compared with the RIF model. The model takes a first-order expansion of the steady-state flamelet solution. A chemical time scale determined from the Jacobian matrix is used to compute the rate of change of species mass fraction from the steady-state solution.

Although the laminar flamelet model and its various derivatives are being used extensively in modeling turbulent combustion, it is important to realize their inherent limitations. The underlying assumption of flamelet models is that the turbulent flame is an ensemble of laminar flamelets. For this assumption to be valid, the structure of the flame front must remain locally laminar. In other words, the thickness of the flame must be thinner than the smallest length scale of turbulence - the Kolmogorov length scale. It is now generally accepted that the flamelet assumption is only valid in the region of large turbulent Damköhler number, Da, which is defined by

$$D_a = \frac{\tau_p}{\tau_L} = \frac{l_p/v'}{l_L/v_L}, \qquad (2.67)$$

where τ_p is the macroscopic time scale of the flow field; τ_L is the characteristic time scale of the laminar flame; l_p is the largest turbulent eddy length scale; v' is the turbulence intensity ; l_L is the laminar flame thickness, and v_L is the laminar burning velocity. When the physical time scale approaches the chemical time scale, or the value of Da is small, the suitability of the flamelet assumption becomes questionable [62, 113].

2.5.2 Conditional Moment Closure

The conditional moment closure (CMC) model was proposed independently by Klimenko [114] and Bilger [115, 116], and was described in

details in their joint review [97]. Although the final form of the CMC equations are unified, the mathematical methods and model assumptions adopted by Klimenko and Bilger in their derivations are quite different. Klimenko started his derivation from the transport equation of a two-dimensional joint PDF, P(**Z**)

$$\frac{\partial \langle \rho | \mathbf{Z} \rangle P}{\partial t} + div(\langle \rho v | \mathbf{Z} \rangle P) \tag{2.68}$$
$$+ \frac{\partial^2}{\partial Z_i \partial Z_j}(\langle \rho D(\nabla Y_i \cdot \nabla Y_j) | \mathbf{Z} \rangle P)$$
$$= -\frac{\partial}{\partial Z_1}(\langle W_1 \rho | \mathbf{Z} \rangle P).$$

The above equation follows the convention used by Klimenko [97] where Z is the sample space variable for Y, $\mathbf{Z} \equiv (Z_1, Z_2)$, W_1 is the chemical source term; the expression $\langle a|c \rangle$ is short for $\langle a|b = c \rangle$ which is the conditional expectation of a conditioned on the variable b being equal to c. Equation 2.68 is multiplied by Z and integrated over all Z to get

$$\frac{\partial \langle \rho | \eta \rangle \langle Y | \eta \rangle P(\eta)}{\partial t} + div\big(\langle \rho | \eta \rangle \langle vY | \eta \rangle P(\eta)\big) \tag{2.69}$$
$$= \langle \rho | \eta \rangle \langle W | \eta \rangle P(\eta) + \frac{\partial J_Y}{\partial \eta},$$

where

$$J_Y \equiv 2\langle \rho | \eta \rangle \langle D(\nabla Y \cdot \nabla \xi | \eta \rangle P(\eta) - \frac{\partial \langle \rho | \eta \rangle \langle NY | \eta \rangle P(\eta)}{\partial \eta}. \tag{2.70}$$

Here $N \equiv D(\nabla \xi)^2$ is the dissipation rate of the conserved scalar; the variable $\xi = \eta \equiv Z_2$. Closure of the last term on the r.h.s, J_Y, which is the reaction scalar flux in conserved scalar space, was achieved through a diffusion approximation with the form

$$J_Y = A\langle Y | \eta \rangle + B\frac{\partial \langle Y | \eta \rangle}{\partial \eta}. \tag{2.71}$$

Here A and B are the drift coefficient and diffusion turbulent coefficient respectively. This closure assumption leads to the final form of the basic CMC equation which governs the evolution of the conditional values of reaction scalars;

$$\frac{\langle Y|\eta\rangle}{\partial t} + \langle v|\eta\rangle \cdot \nabla\langle Y|\eta\rangle + \frac{div\big(\langle\rho|\eta\rangle\langle v''Y''|\eta\rangle P(\eta)\big)}{P(\eta)\langle\rho|\eta\rangle} - \langle N|\eta\rangle\frac{\partial^2\langle Y|\eta\rangle}{\partial\eta^2}$$

$$= \langle W|\eta\rangle,$$

(2.72)

where $v'' \equiv v - \langle v|\eta\rangle$ is the velocity fluctuation about the conditional mean; similarly, Y'' is the fluctuation of species mass fraction. The physical meaning of the second and third terms on the l.h.s. of Eq. 2.72 are the convection of the conditional value of the reaction scalar; the forth term on the l.h.s. represents the effect of turbulent diffusion on the conditional expectation; the term on the r.h.s. is the conditional source term.

In Bilger's derivation of the CMC equation [115, 116], the conditional value of the reaction scalar is decomposed into its mean and fluctuation, which are substituted into the transport equation. After taking the conditional average, the equation becomes

$$\langle\rho|\eta\rangle\frac{\partial\langle Y|\eta\rangle}{\partial t} + \langle\rho|\eta\rangle\langle v|\eta\rangle \cdot \nabla\langle Y|\eta\rangle + \langle\rho|\eta\rangle\langle N|\eta\rangle\frac{\partial^2\langle Y|\eta\rangle}{\partial\eta^2}$$

(2.73)

$$= \langle\rho|\eta\rangle\langle W|\eta\rangle + e_Q + e_Y$$

with

$$e_Q \equiv \langle div(\rho D\nabla\langle Y|\eta\rangle) + \rho D\nabla\xi \cdot \nabla\frac{\partial\langle Y|\eta\rangle}{\partial\eta}|\eta\rangle,$$

(2.74)

$$e_Y \equiv -\langle\rho\frac{\partial Y''}{\partial t} + \rho v \cdot \nabla Y'' - div(D\rho\nabla Y'')|\eta\rangle.$$

(2.75)

For large Reynolds numbers, the value of e_Q is small and can be neglected. The unconditional average of e_Y can be calculated from the

integral equation

$$\int e_Y P(\eta) d\eta = - \int div(\langle \rho | \eta \rangle \langle v'' Y'' | \eta \rangle P(\eta) d\eta. \tag{2.76}$$

Closure for the unclosed term e_Y is realized through the assumption

$$e_Y P(\eta) d\eta = -div(\langle \rho | \eta \rangle \langle v'' Y'' | \eta \rangle P(\eta) d\eta, \tag{2.77}$$

which leads to the same CMC equation as Eq. 2.72. The Closure of the conditional source term in the CMC equation is usually achieved by neglecting the effect of the conditional fluctuations, i.e.

$$\langle W_i(\mathbf{Y}, h) | \eta \rangle \approx \langle W_i(\langle Y | \eta \rangle \langle h | \eta \rangle) | \eta \rangle. \tag{2.78}$$

A close examination of Eq. 2.72 shows that the conditional expectation of the reactive scalar is transported in a four-dimensional space: three spatial coordinates and one conditional variable (i.e. the mixture fraction). Thus the computational cost for solving the CMC equation for a complex flow is likely to be substantial.

A further simplification of Eq. 2.72 can be obtained by assuming homogeneous turbulence with uniform and constant density. In that case, the basic equation reduces to

$$\frac{\partial \langle Y | \eta \rangle}{\partial t} - \langle N | \eta \rangle \frac{\partial^2 \langle Y | \eta \rangle}{\partial \eta^2} = \langle W | \eta \rangle. \tag{2.79}$$

It is interesting to note that this form of the CMC equation closely resembles the unsteady flamelet equation discussed in the previous section; however, the subtle difference between the two models must be emphasized. The fundmental assumption of the flamelet model constrains its application in the flamelet regime, while the model assumption of CMC is more general. It is also possible to achieve closures at higher moments with CMC, thus the method has potential to describe

flames with significant conditional fluctuations (such as those during quenching and reignition) with higher accuracy.

The CMC model has been applied with considerable success in predicting reactive scalars (species mass fraction and temperature) in attached jet flames [117–120], lifted flames [121] and bluff-body flames [122, 123]. It was also used in predicting soot formation in a turbulent methane/air reactive jet [124]. More recently, second-order closure methods have been developed and implemented to improve the performance of CMC in predicting jet flames [125], especially regions with significant local extinction and reignition [126].

2.5.3 Conditional Source Term Estimation

The Conditional Source-term Estimation (CSE) method [127] seeks closure of the chemical source term using the conditional average of the reaction scalars in a manner which is essentially identical to the first-order CMC. The conditional values, however, are not obtained by solving a transport equation such as that in Eq. 2.72. Based on the *a priori* knowledge from DNS calculations that the conditional averages of scalars do not vary rapidly in space, Bushe and Steiner proposed a method to obtain the conditional averages of the reactive scalars through inverting an integral equation using the unconditional averages of an ensemble of discrete points on a computational domain [127]. Mathematically, the unconditional mean at any spatial location x and time t is

$$\langle Y(x,t)\rangle = \int_0^1 P(x,t;\eta)\langle Y(x,t)|\eta\rangle d\eta. \qquad (2.80)$$

For a selected spatial ensemble of N points, the CSE method assumes that the conditional average is uniform within the ensemble:

$$\langle Y^n(x,t)|\eta\rangle = \langle Y|\eta\rangle_{A,t}, \qquad (2.81)$$

where the superscript n is the nth point in the ensemble, and the subscript A denotes the ensemble. This leads to a discrete set of N integrals:

$$\langle Y^n(x,t) \rangle = \int_0^1 P(x,t;\eta) \langle Y|\eta \rangle_{A,t} d\eta. \qquad (2.82)$$

Equation 2.82 can be approximated using a numerical quadrature with M quadrature points (M<N),

$$\langle Y^n(x,t) \rangle = \sum_{m=1}^M P(x,t;\eta) \langle Y|\eta_m \rangle_{A,t} \delta\eta_m, \qquad (2.83)$$

where $n = 1...N$. The least-square solution of the conditional averages of interested scalars can be computed by inverting Eq. 2.83.

The CSE method was initially implemented in a large eddy simulation of a piloted methane/air diffusion flame with encouraging success in predicting the experimental measurements [128]. Later, the concept of CSE was tested in conjunction with the unsteady laminar flamelet model, in which the conditional averages of reaction scalars are calculated using a linear combination of flamelet solutions [129]. The appropriate weighting factors for the flamelet solutions are determined by inverting the integral equation of the unconditional mean temperature field. The method was then used in the context of a RANS model to study turbulent methane jet ignition under engine-relevant conditions with some success [130, 131].

In order to address the issue of ill-posedness in Eq. 7.3, as well as to provide temporal continuity in the solution, Grout [131] proposed a regularization method for the inverting process. The modified equation system for solving conditional scalars is

$$min\left\{ \|\mathbf{\Omega}\langle \mathbf{Y}|\eta \rangle^t - \langle \mathbf{Y} \rangle^t\| + \lambda\|\langle \mathbf{Y}|\eta \rangle^t - \langle \mathbf{Y}|\eta \rangle^{t-dt}\| \right\}, \qquad (2.84)$$

where Ω is the original coefficient matrix for the discrete integral equations; the superscripts t and $t - dt$ is the times at which the scalars

are evaluated; λ is a weighting coefficient specified by the modeler. In Grout's [131] implementation, λ was chosen to add just enough *a priori* information to produce a well-behaved solution. The regularization term $\lambda \| \langle \mathbf{Y} | \eta \rangle^t - \langle \mathbf{Y} | \eta \rangle^{t-dt} \|$ limits the change of conditional average between two consecutive time steps and acts to stabilize the solution.

A main advantage of the CSE method is that the computational cost is substantially lower than that of CMC. Meanwhile, it does not involve constraining assumptions such as those employed by the laminar flamelet model, and is thus applicable to a wide range of turbulent non-premixed flames.

2.6 Summary

This chapter has reviewed experimental and kinetic studies on natural gas combustion. The chemical kinetic mechanisms that govern the oxidation of pure methane and methane with additions of higher alkanes and hydrogen have been discussed. The need for reliable experimental data on natural gas ignition under engine-relevant conditions has been established. The main mechanisms for nitric oxide formation in hydrocarbon flames and several useful techniques for in-flame NOx reduction have been introduced. Numerical techniques and mathematical methods that are used frequently in analyzing and reducing detailed reaction mechanisms have been discussed. Finally, the closure problem in turbulent combustion modeling has been introduced, and three popular methods for closing the chemical source term using two-parameter representation of the PDF of reactive scalar have been discussed.

Chapter 3

Ignition of Methane with Higher Alkane Additives[7]

3.1 Introduction

Ethane and propane are two non-methane alkanes often present in natural gas; in combustion studies, they are often added to methane to represented typical natural gas [15]. The variation of ethane and propane concentration in natural gas can significantly change the ignition characteristics of the base fuel; this is particularly relevant to the performance of HCCI engines [17, 132] as well as to forced-ignition natural-gas engines and gas turbines in the sense of controlling autoignition [16, 18]. The issue is especially important for mobile applications since natural gas composition can vary significantly from place to place. Previous researchers have conducted a large number of experimental and numerical studies to understand the ignition behavior in homogeneous methane/ethane or methane/propane mixtures [10, 15, 17–25, 43]; however, most of these studies—particularly the experimental ones—were focused on systems at near atmospheric pressures and very high temperatures. Our knowledge of natural gas ignition

---

[7]A version of this chapter has been accepted for publication. Huang. J. and Bushe, W. K. (2005) Experimental and kinetic study of autoignition in methane/ethane/air and methane/propane/air mixtures under engine relevant conditions, Combust. Flame, In Press

66
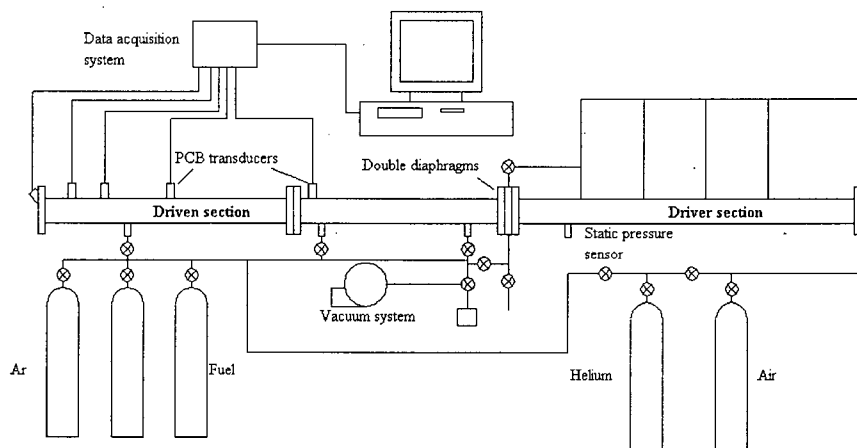
Figure 3.1: Schematic of the shock tube facility used in premixed experiments

under conditions relevant to practical combustion devices (such as IC engines or gas turbines) is still insufficient. Thus, the first objective of the work described in this chapter was to obtain reliable experimental data that extend the ignition database of various methane/ethane, methane/propane and simulated natural gas mixtures burning in air under engine-relevant conditions. The second was to obtain a better understanding of the kinetic interaction between methane and the two higher alkanes when undergoing ignition in air.

3.2 Experimental Apparatus

The experiments were conducted in a shock tube facility previously described in detail [28]. A schematic of the shock tube facility is shown in Fig. 3.1. The stainless-steel shock tube has a circular cross section with an inner diameter of 59 mm. The length of the driver section is 3.18m,

and length of the driven section is 4.25m. Five PCB dynamic pressure transducers were flush mounted along the driven section to measure the incident shock velocity. The ignition is indicated by the rise of the pressure signal from the transducer mounted at the end plate of the driven section. A double-diaphragm technique was used to guarantee the rupture of diaphragms at the desired pressure ratio. The pressure and temperature behind the reflected shock were calculated using standard normal shock relations [133] incorporating temperature-dependent thermodynamic properties and the ideal gas state equation. Peterson et al. [29] have shown that the difference between the experimental conditions calculated based on the ideal gas state equation and those based on a real gas state equation is not significant in the pressure range covered by this study.

In order to measure the long ignition delay times associated with relatively low temperatures, tailored interface conditions [133] were obtained by tuning the thermodynamic properties of the driver gas using different mixtures of air and helium. The result is that only a Mach wave is generated at the contact surface when the reflected shock wave passes across; for an ideal shock reflection, the conditions in the experimental region remain unaffected until the arrival of the rarefaction wave [133]. In this study, undiluted air-fuel mixtures were used as the driven gas for the best simulation of conditions in IC engines. Since the driven gas is not monoatomic, interactions between the reflected shock wave and the boundary layer could lead to reflected-shock bifurcations. It has been reported that streams of cold driven gas emerging from the bifurcated shock can arrive at the end plate along the wall of the shock tube and eventually surround a core of hot gas [134]. The effect of this cooling flow in the current experiments was examined
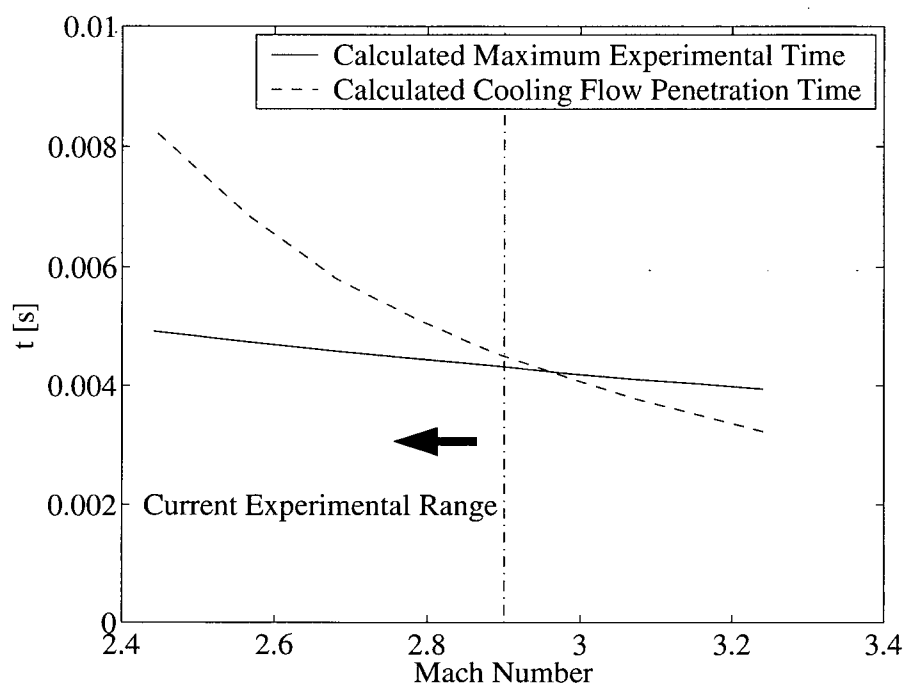
Figure 3.2: Determination of experimental time by comparing calculated time for tailored interface conditions and the time for cooling flow to reach the end plate due to the reflected-shock/boundary-layer interaction. The dotted line indicates the upper limit of Mach number of the incident shock in the current study.

numerically using models proposed by Mark [135] and Davis [136]. In Fig. 3.2, a comparison is made between the typical time scale for the cooling gas to reach the end plate and the experimental time scale determined by the arrival of the rarefaction fan. It can be seen that for the current shock-tube configuration and experimental conditions, the cooling flow from the bifurcated shock foot cannot affect the experimental conditions before the arrival of the rarefaction wave.

The contact surface instability as a result of the reflected shock passage is another phenomenon, which could lead to a premature termination of the experiment. This is because an unstable contact surface can promote mixing between the cold driver gas and hot driven gas.

Markstein [137] applied the interface stability theory of Taylor [138] to the shocked contact surface to show that the perturbation velocity at the contact surface can be expressed by the formula

$$u(x,y) = \Delta U k A \frac{\rho_2 - \rho_3}{\rho_2 + \rho_3} e^{k(\pm x + iy)} \tag{3.1}$$

Here, ΔU is the difference in velocities of driver gas immediately behind the incident and reflected shocks; $k = 2\pi/\lambda$ where λ is the wavelength; A is the amplitude of the perturbation; and ρ_2 and ρ_3 are densities of driven and driver gas behind the incident shock respectively. The sign of this perturbation velocity depends on the sign of $\rho_2 - \rho_3$. Using this formula, it can be shown that the direction of the perturbation under the current experimental conditions is towards the driver gas side so that its effect on the test mixture is small. To minimize the uncertainty in the experimental temperature, the actual experimental time was limited below 50 percent of the valid tailored interface period, which is determined from the pressure trace measured at the end plate.

The experimental uncertainty was calculated using a standard error analysis procedure [139] based on the uncertainty in measured incident shock velocities and correcting for attenuation in both incident and reflected shock velocities. The root-mean-square of the temperature uncertainty behind the reflected shock is 14 K, which agrees with the uncertainty calculated from measured reflected-shock Mach numbers using a method suggested by Skinner [140].

Research-grade or ultra-high purity gases (methane-99.97%, ethane-99.999%, propane-99.99%) were used for testing mixtures, which were prepared in a stainless steel vessel using the partial pressure method. The uncertainty of ethane/propane concentration in the final mixture is less than 5% of the target concentration.

3.3 Kinetic Model

For the autoignition of CH_4-air mixtures in high pressure and moderate temperature, recent kinetic studies reported by Petersen et al. [29] and Huang et al. [28] show an increased significance of methylperoxy (CH_3O_2) chemistry for temperatures below 1100K, which causes the global activation energy to change. The proposed kinetic mechanisms in the above two studies show good agreement with the experimental ignition delay for a wide range of initial conditions. GRI mechanism (v1.2) was taken as the base mechanism as in our previous work [28]. Due to the importance of alkylperoxy chemistry in the low-medium temperature range, reactions related to the formation of methylperoxy, ethylperoxy and propylperoxy were added. The reaction rates were taken from the work of Tsang et al. [141]. Unfortunately, there has been no experimental measurement reported for these reactions at conditions close to those of this study and the rates reported in the literature show a relatively large uncertainty. The rate coefficients of some reactions were thus optimized based on the experimental results in this work.

Hunter et al. [44] developed a detailed kinetic mechanism for the oxidation of ethane at elevated pressures (3–10 bar) and moderate temperatures (916–966K) based on experimental data from their flow reactor. An important reaction path identified in their analysis includes the formation and oxidation of ethylperoxy ($C_2H_5O_2$). The extended C2 reactions in the new mechanism were mostly taken from Hunter et al. [44] . The C3 sub-mechanism was based on the work of Frenklach et al. [22]. Reactions between iso/normal propylperoxy and major alkane species were taken from Curran et al. [142]. The final mechanism con-

tains 55 species and 278 elementary reactions. The extended reactions and their rate coefficients are listed in Table 3.1.

Table 3.1: Modified and extended reactions in the model (based on GRI-Mech 1.2)

No	Reaction	A	B	E(cal)	Ref.
157	$HO_2 + CH_4 \rightleftharpoons CH_3 + H_2O_2$	4.48E+13	0.0	24629.0	[38]
174	$C_2H_5 + O2 \rightleftharpoons HO_2 + C_2H_4$	2.90E+11	0.0	6856.0	[44]
177	$CH_3 + OH \rightleftharpoons CH_2O + H_2$	8.00E+12	0.0	0.0	[29]
178	$CH_3 + O_2 \rightleftharpoons CH_3O_2$	8.52E+58	-15.0	17018.0	[141]
179	$CH_3O + HO_2 \rightleftharpoons CH_2O + H_2O_2$	1.20E+13	0.0	0.0	[29]
180	$CH_3O + CH_3 \rightleftharpoons CH_2O + CH_4$	2.41E+13	0.0	0.0	[29]
181	$CH_3O_2H \rightleftharpoons CH_3O + OH$	4.00E+15	0.0	42920.0	[143]
182	$CH_3O_2 + CH_3 \rightleftharpoons CH_3O + CH_3O$	3.00E+13	0.0	-1200.0	[29]
183	$CH_3O_2 + CH_4 \rightleftharpoons CH_3O_2H + CH_3$	5.40E+11	0.0	18580.0	[141], a
184	$CH_3O_2 + H_2O_2 \rightleftharpoons CH_3O_2H + HO_2$	2.40E+12	0.0	9942.0	[29]
185	$CH_3O_2 + CH_2O \rightleftharpoons CH_3O_2H + HCO$	2.00E+12	0.0	11663.0	[29]
186	$CH_3O_2 + HO_2 \rightleftharpoons CH_3O_2H + O_2$	4.60E+10	0.0	-2600.0	[29]
187	$CH_3O_2 + CH_3O_2 \rightleftharpoons O_2 + CH_3O + CH_3O$	3.70E+11	0.0	2200.0	[44]
188	$CH_3O_2 + CH_3CHO \rightleftharpoons CH_3O_2H + CH_3CO$	2.80E+12	0.0	13592.0	[44]
189	$C_2H_5 + O_2 \rightleftharpoons C_2H_5O_2$	1.10E+47	-10.6	14830.0	[44]
190	$C_2H_5 + O_2 \rightleftharpoons C_2H_5O + O$	1.10E+13	-0.2	27926.0	[44]
191	$C_2H_5 + O_2 \rightleftharpoons CH_3CHO + OH$	1.60E+14	-1.2	10392.0	[44]
192	$C_2H_5 + HO_2 \rightleftharpoons C_2H_5O + OH$	1.15E+13	0.0	0.0	[44]

Continued on next page

Table 3.1 – continued from previous page

No	Reaction	A	B	E(cal)	Ref.
193	$C_2H_5 + CH_3 \rightleftharpoons C_2H_4 + CH_4$	7.94E+11	0.0	0.0	[44]
194	$C_2H_5 + CH_3O_2 \rightleftharpoons CH_3O + C_2H_5O$	2.40E+13	0.0	0.0	[44]
195	$C_2H_5 + C_2H_5 \rightleftharpoons C_2H_6 + C_2H_4$	1.45E+12	0.0	0.0	[44]
196	$C_2H_4 + CH_3O_2 \rightleftharpoons C_2H_4O + CH_3O$	2.82E+12	0.0	17104.0	[44]
197	$C_2H_4O \rightleftharpoons CH_3 + HCO$	3.40E+13	0.0	57788.0	[44]
198	$C_2H_4O \rightleftharpoons CH_3CHO$	5.48E+11	0.0	52341.0	[44]
199	$C_2H_4O + H \rightleftharpoons C_2H_3O + H_2$	7.90E+13	0.0	9795.0	[44]
200	$C_2H_4O + OH \rightleftharpoons C_2H_3O + H_2O$	1.78E+13	0.0	3607.0	[44]
201	$C_2H_5O \rightleftharpoons CH_2O + CH_3$	1.00E+15	0.0	21600.0	[44]
202	$C_2H_5O \rightleftharpoons CH_3CHO + H$	2.51E+14	0.0	23387.0	[44]
203	$C_2H_5O + O_2 \rightleftharpoons CH_3CHO + HO_2$	6.03E+10	0.0	1648.0	[44]
204	$C_2H_5O_2 + CH_2O \rightleftharpoons C_2H_5O_2H + HCO$	2.00E+12	0.0	11663.0	[44]
205	$C_2H_5O_2 + HO_2 \rightleftharpoons C_2H_5O_2H + O_2$	1.75E+11	0.0	-1696.0	[44]
206	$C_2H_5O_2 + CH_4 \rightleftharpoons CH_3 + C_2H_5O_2H$	8.10E+11	0.0	18580.0	[44],a
207	$C_2H_5O_2 + C_2H_4 \rightleftharpoons C_2H_4O + C_2H_5O$	2.82E+12	0.0	17105.0	[44]
208	$C_2H_5O_2 + C_2H_4 \rightleftharpoons C_2H_3 + C_2H_5O_2H$	1.12E+12	0.0	30411.0	[44]
209	$C_2H_5O_2 + C_2H_6 \rightleftharpoons C_2H_5 + C_2H_5O_2H$	1.70E+13	0.0	20450.0	[44]
210	$C_2H_5O_2 + C_3H_8 \rightleftharpoons nC_3H_7 + C_2H_5O_2H$	1.70E+13	0.0	20450.0	[44]
211	$C_2H_5O_2 + C_3H_8 \rightleftharpoons iC_3H_7 + C_2H_5O_2H$	1.70E+13	0.0	20450.0	[44]
212	$C_2H_5O_2H \rightleftharpoons C_2H_5O + OH$	4.00E+15	0.0	42920.0	[143]

Continued on next page

Table 3.1 – continued from previous page

No	Reaction	A	B	E(cal)	Ref.
213	$C_2H_5O_2 \rightleftharpoons C_2H_4O_2H$	2.86E+11	0.0	30005.0	[44]
214	$C_2H_4O_2 \rightarrow C_2H_4O + OH$	3.16E+11	0.0	19494.0	[44]
215	$C_2H_3 + O_2 \rightleftharpoons C_2H_3O + O$	6.61E+06	1.9	979.0	[44]
216	$C_2H_3 + O_2 \rightleftharpoons C_2H_2 + HO_2$	8.40E+05	1.9	2246.0	[44]
217	$C_2H_3 + O_2 \rightleftharpoons HCO + CH_2O$	2.05E+13	-0.3	1553.0	[44]
218	$C_2H_6 + HO_2 \rightleftharpoons H_2O_2 + C_2H_5$	4.00E+12	0.0	14940.0	[141],a
219	$C_2H_6 + O_2 \rightleftharpoons C_2H_5 + HO_2$	3.98E+13	0.0	59883.0	[44]
220	$C_2H_6 + CH_3O_2 \rightleftharpoons C_2H_5 + CH_3O_2H$	4.00E+12	0.0	14940.0	[141],a
221	$CH_3 + C_2H_5(+M) \rightleftharpoons C_3H_8(+M)$[8]	9.43E+12	0.0	0.0	[41]
222	$OH + C_3H_8 \rightleftharpoons iC_3H_7 + H_2O$	7.08E+06	1.9	158.9	[144]
223	$OH + C_3H_8 \rightleftharpoons nC_3H_7 + H_2O$	3.16E+07	1.8	993.9	[144]
224	$C_3H_8 + CH_3O_2 \rightleftharpoons nC_3H_7 + CH_3O_2H$	9.03E+13	0.0	19380.0	[141],a
225	$C_3H_8 + CH_3O_2 \rightleftharpoons iC_3H_7 + CH_3O_2H$	2.98E+13	0.0	17050.0	[141],a
226	$nC_3H_7 + O_2 \rightleftharpoons nC_3H_7O_2$	1.63E+19	-2.7	0.0	[142]
227	$iC_3H_7 + O_2 \rightleftharpoons nC_3H_7O_2$	6.62E+12	0.0	0.0	[142]
228	$nC_3H_7O_2H \rightleftharpoons nC_3H_7O + OH$	1.50E+16	0.0	42500.0	[142]
229	$iC_3H_7O_2H \rightleftharpoons iC_3H_7O + OH$	9.45E+15	0.0	41600.0	[142]
230	$nC_3H_7O_2 + CH_2O \rightleftharpoons nC_3H_7O_2H + HCO$	5.60E+12	0.0	13600.0	[142]
231	$nC_3H_7O_2 + CH_3CHO \rightleftharpoons nC_3H_7O_2H + CH_3CO$	2.80E+12	0.0	13600.0	[142]

Continued on next page

[8]The low-pressure rate coefficients and third-body enhancement coefficients are identical to those in the reference

Table 3.1 – continued from previous page

No	Reaction	A	B	E(cal)	Ref.
232	$iC_3H_7O_2 + CH_2O \rightleftharpoons iC_3H_7O_2H + HCO$	5.60E+12	0.0	13600.0	[142]
233	$iC_3H_7O_2 + CH_3CHO \rightleftharpoons iC_3H_7O_2H + CH_3CO$	2.80E+12	0.0	13600.0	[142]
234	$nC_3H_7O_2 + HO_2 \rightleftharpoons nC_3H_7O_2H + O_2$	1.75E+10	0.0	-3275.0	[142]
235	$iC_3H_7O_2 + HO_2 \rightleftharpoons iC_3H_7O_2H + O_2$	1.75E+10	0.0	-3275.0	[142]
236	$C_2H_4 + nC_3H_7O_2 \rightleftharpoons C_2H_3 + nC_3H_7O_2H$	1.13E+13	0.0	30430.0	[142]
237	$C_2H_4 + iC_3H_7O_2 \rightleftharpoons C_2H_3 + iC_3H_7O_2H$	1.13E+13	0.0	30430.0	[142]
238	$CH_3OH + nC_3H_7O_2 \rightleftharpoons CH_2OH + nC_3H_7O_2H$	6.30E+12	0.0	19360.0	[142]
239	$CH_3OH + iC_3H_7O_2 \rightleftharpoons CH_2OH + iC_3H_7O_2H$	6.30E+12	0.0	19360.0	[142]
240	$CH_4 + nC_3H_7O_2 \rightleftharpoons CH_3 + nC_3H_7O_2H$	8.10E+11	0.0	18580.0	[142]
241	$CH_4 + iC_3H_7O_2 \rightleftharpoons CH_3 + iC_3H_7O_2H$	8.10E+11	0.0	18580.0	[142]
242	$H_2 + nC_3H_7O_2 \rightleftharpoons H + nC_3H_7O_2H$	3.01E+13	0.0	26030.0	[142]
243	$H_2 + iC_3H_7O_2 \rightleftharpoons H + iC_3H_7O_2H$	3.01E+13	0.0	26030.0	[142]
244	$iC_3H_7O_2 + C_2H_6 \rightleftharpoons iC_3H_7O_2H + C_2H_5$	1.70E+13	0.0	20460.0	[142]
245	$nC_3H_7O_2 + C_2H_6 \rightleftharpoons nC_3H_7O_2H + C_2H_5$	1.70E+13	0.0	20460.0	[142]
246	$nC_3H_7O_2 + C_3H_8 \rightleftharpoons nC_3H_7O_2H + nC_3H_7$	1.70E+13	0.0	20460.0	[142]
247	$nC_3H_7O_2 + C_3H_8 \rightleftharpoons nC_3H_7O_2H + iC_3H_7$	2.00E+12	0.0	17000.0	[142]
248	$iC_3H_7O_2 + C_3H_8 \rightleftharpoons iC_3H_7O_2H + nC_3H_7$	1.70E+13	0.0	20460.0	[142]
249	$iC_3H_7O_2 + C_3H_8 \rightleftharpoons iC_3H_7O_2H + iC_3H_7$	2.00E+12	0.0	17000.0	[142]
250	$C_3H_8 + C_2H_5 \rightleftharpoons iC_3H_7 + C_2H_6$	5.01E+10	0.0	10272.3	[22]
251	$C_3H_8 + C_2H_5 \rightleftharpoons nC_3H_7 + C_2H_6$	5.01E+10	0.0	10272.3	[22]

Continued on next page

Table 3.1 – continued from previous page

No	Reaction	A	B	E(cal)	Ref.
252	$C_3H_8 + CH_3 \rightleftharpoons iC_3H_7 + CH_4$	1.29E+13	0.0	18633.5	[22]
253	$C_3H_8 + CH_3 \rightleftharpoons nC_3H_7 + CH_4$	1.55E+14	0.0	21261.0	[22]
254	$C_3H_8 + O_2 \rightleftharpoons iC_3H_7 + HO_2$	2.00E+13	0.0	55900.0	[22]
255	$C_3H_8 + O_2 \rightleftharpoons nC_3H_7 + HO_2$	6.03E+13	0.0	55900.0	[22]
256	$C_3H_8 + HO_2 \rightleftharpoons iC_3H_7 + H_2O_2$	9.77E+11	0.0	12422.4	[22],a
257	$C_3H_8 + HO_2 \rightleftharpoons nC_3H_7 + H_2O_2$	2.95E+12	0.0	14811.3	[22],a
258	$C_3H_8 + H \rightleftharpoons iC_3H_7 + H_2$	1.95E+13	0.0	7883.0	[22]
259	$C_3H_8 + H \rightleftharpoons nC_3H_7 + H_2$	8.13E+13	0.0	10750.0	[22]
260	$C_3H_8 + O \rightleftharpoons iC_3H_7 + OH$	2.57E+13	0.0	4539.0	[22]
261	$C_3H_8 + O \rightleftharpoons nC_3H_7 + OH$	3.02E+13	0.0	5733.0	[22]
262	$iC_3H_7 \rightleftharpoons CH_3 + C_2H_4$	1.00E+12	0.0	34400.0	[22]
263	$nC_3H_7 \rightleftharpoons CH_3 + C_2H_4$	6.31E+13	0.0	33206.0	[22]
264	$iC_3H_7 \rightleftharpoons H + C_3H_6$	2.00E+14	0.0	41328.0	[22]
265	$nC_3H_7 \rightleftharpoons H + C_3H_6$	6.31E+13	0.0	37984.0	[22]
266	$iC_3H_7 + O_2 \rightleftharpoons C_3H_6 + HO_2$	1.00E+12	0.0	2867.0	[22]
267	$nC_3H_7 + O_2 \rightleftharpoons C_3H_6 + HO_2$	1.00E+12	0.0	5734.0	[22]
268	$C_3H_6 + M \rightleftharpoons CH_3 + C_2H_3 + M$	1.00E+18	0.0	74056.0	[22]
269	$C_3H_6 \rightleftharpoons H + C_3H_5$	1.00E+15	0.0	87912.0	[22]
270	$C_3H_6 + C_2H_5 \rightleftharpoons C_3H_5 + C_2H_6$	1.00E+11	0.0	8122.3	[22]
271	$C_3H_6 + C_2H_3 \rightleftharpoons C_3H_5 + C_2H_4$	1.00E+11	0.0	6928.0	[22]

Continued on next page

Table 3.1 – continued from previous page

No	Reaction	A	B	E(cal)	Ref.
272	$C_3H_6 + CH_3 \rightleftharpoons C_3H_5 + CH_4$	2.00E+13	0.0	14094.0	[22]
273	$C_3H_6 + H \rightleftharpoons C_3H_5 + H_2$	2.51E+12	0.0	1194.0	[22]
274	$C_3H_6 + O \rightleftharpoons C_2H_5 + HCO$	1.51E+12	0.0	0.0	[22]
275	$C_3H_6 + OH \rightleftharpoons C_3H_5 + H_2O$	7.94E+12	0.0	0.0	[22]
276	$C_3H_6 + OH \rightleftharpoons C_2H_5 + CH_2O$	7.94E+12	0.0	0.0	[22]
277	$C_3H_5 \rightleftharpoons C_2H_2 + CH_3$	3.02E+13	0.0	36311.0	[22]
278	$C_3H_4 + H \rightleftharpoons C_3H_5$	2.40E+11	0.0	0.0	[22]

a. Rate constant A modified in this work.

Optimization of the rate constants in key reactions was performed to improve the agreement between the model and experiments. This was done by first identifying the most significant reactions using the sensitivity and reaction flow analyses described in Chapter 2. The rate constants of some of these reactions were then adjusted within the uncertainty limits reported in the literature to improve the performance of the mechanism. It should be noted that the C2/C3 sub-mechanisms involved in the new mechanism do not completely describe the ignition and oxidation of these fuels; thus the mechanism should not be used to model combustion of pure C2/C3 fuels.

The boundary conditions behind the reflected shock were modeled as being adiabatic and constant-volume. The thermodynamic properties of the species in the mechanism were obtained from the NASA thermodynamic database [145] as well as from the latest database of Burcat [146]. The reaction rates were calculated using Chemkin II [147] and the solution of a system of ODEs for species and energy conservation was obtained using DVODE [148].

3.4 Results and Discussion

3.4.1 Experimental and Model Results

A list of gas mixtures investigated in this study is given in Table 3.2.

Table 3.2: Molar fractions of main constituents in the test mixtures ($\phi = 1$ for all mixtures, balanced by air ($79\%N_2$, $21\%O_2$))

No	X_{CH_4}	$X_{C_2H_6}$	$X_{C_3H_8}$
1	96.3%	3.7%	0%
2	93.0%	7.0%	0%
3	90.0%	10.0%	0%
4	98.75%	0%	1.25%
5	97.5%	0%	2.5%
6	95.0%	0%	5.0%
7	95.05%	3.7%	1.25%

The concentrations of ethane and propane are selected so that they represent the most typical constituents of natural gas from various resources [23]. The measured ignition delay time together with the calculated initial conditions are summarized in Table 3.3.

Table 3.3: Experimental conditions and ignition delay results for methane/ethane and methane/propane mixtures

Mix. No	T (K)	P (bar)	$\tau(\mu s)$	Mix. No	T (K)	P (bar)	$\tau(\mu s)$
3	1013	34.3	1560	5	1129	38.7	710
3	1102	40.2	740	5	1093	39.5	900
3	1044	39.5	1190	5	1059	40.8	1190
3	1004	40.4	2650	5	994	39.5	1640
3	967	38.8	1707	5	985	40.9	2510
3	911	39.1	4900	6	1116	37.8	790
3	943	39.3	2840	6	1094	39.8	1020
3	1221	38.9	318	6	1043	39.2	1240
2	1100	40.0	720	6	1008	40.5	1500
2	1025	38.0	1130	6	978	39.4	2040
2	988	39.1	1630	6	1104	40.3	940
2	950	40.0	1730	6	998	39.8	1780
2	920	40.0	2230	6	976	40.1	1540
1	986	38.8	2060	6	970	41.9	2290
1	1076	39.7	790	6	1060	40.8	1000
1	1088	36.2	710	6	1004	40.3	1100
1	1191	38.1	530	4	1168	15.1	780
1	1249	38.1	343	4	1135	15.6	960
1	960	36.6	3081	4	1075	15.2	1240
3	1231	13.2	410	4	1064	16.5	1580
3	1182	16.9	620	4	1058	16.8	2280
3	1239	17.1	365	4	1260	16.2	580
3	1084	15.5	978	5	1249	16.1	710
3	1014	15.1	2010	5	1184	15.7	930
3	1143	15.5	929	5	1091	14.3	1500
3	1211	15.8	657	5	1173	16.7	930
3	1064	16.5	1257	5	1114	16.4	1100
3	1057	16.8	1564	5	1096	16.8	1590
1	1271	15.8	528	5	1036	16.8	2500
1	1227	16.2	692	7	1197	39.8	400
1	1080	13.7	1529	7	1094	39.6	830
1	983	14.8	4800	7	1048	39.8	1590
1	1060	17.4	1755	7	928	33.9	3220

Table 3.3 – continued from previous page

Mix. No	T (K)	P (bar)	$\tau(\mu s)$	Mix. No	T (K)	P (bar)	$\tau(\mu s)$
1	1008	16.6	2373	7	985	38.8	1570
1	1307	16.3	383	7	1187	39.2	560
1	1181	13.2	857	7	1096	39.7	749
1	1139	15.2	1291	7	1059	40.8	1150
4	1095	39.6	900	7	1019	41.7	1690
4	1077	41.4	1060	7	960	41.0	2560
4	1032	41.1	1160	7	927	40.2	4010
4	991	41.0	2350				
4	1037	43.3	1310				
4	1141	39.3	580				

They are also presented graphically in Figs. 3.3 through 3.5. Note that the data for $7\%C_2H_6$, $93\%CH_4$ - which basically collapse on the data for $10\%C_2H_6$, $90\%CH_4$ - are not presented in Fig. 3.3 for the reason of clarity.

It is clear that the effects of ethane/propane additive on methane ignition in this study are significantly different from those reported in the literature at high-temperature and low-pressure conditions. For instance, most of the earlier results [20, 23] show that the factor of reduction in ignition delay for a given ethane/propane fraction is nearly constant in a range of temperature, so that the results can be approximated with a simple Arrhenius-type correlation. In this study, much more complex effects were observed. For mixtures with ethane, the reduction in ignition delay appears to have a minimum at around 1100K, and it increases as the temperature deviates from this point (which is more clearly seen at 40 bar). For mixtures with propane, the promoting effect is more prominent at lower temperatures. For example, at 40 bar, the reduction of ignition delay time with 1.25% to 5% propane
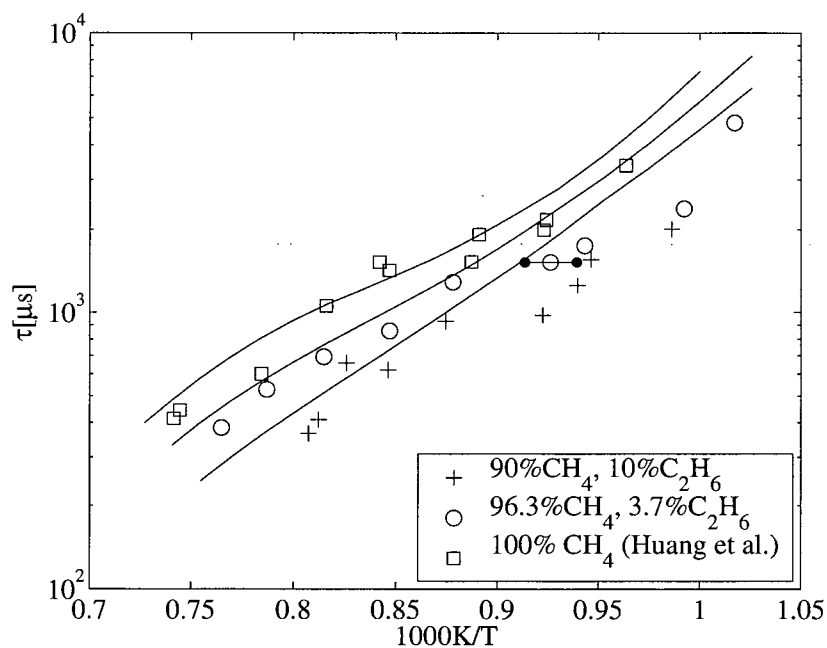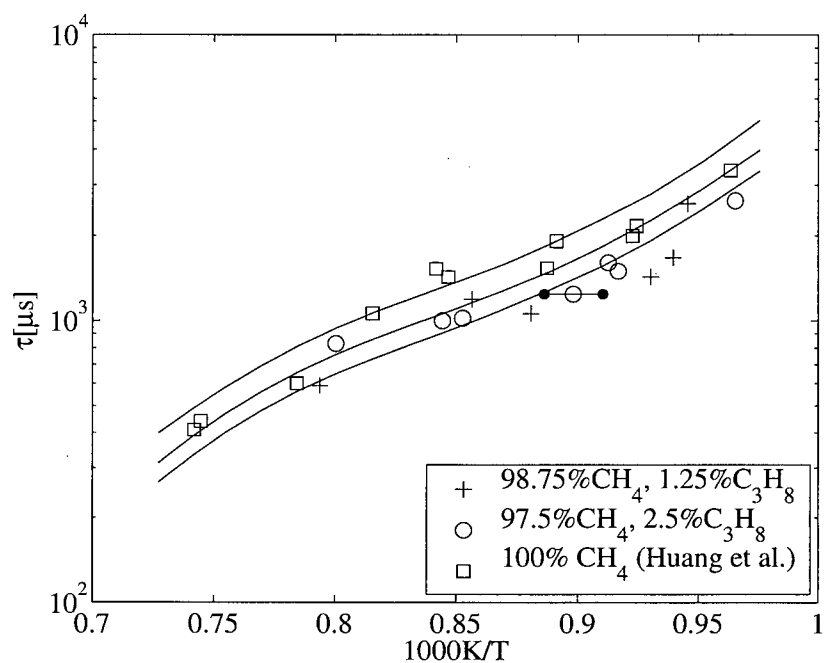
(a) $CH_4 - C_2H_6$, 16 bar
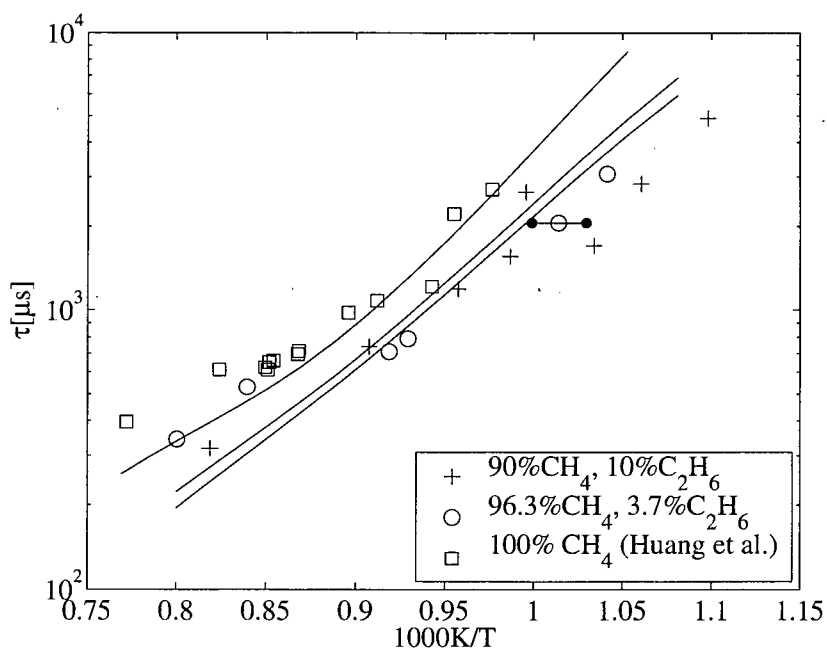
(b) $CH_4 - C_2H_6$, 40 bar

Figure 3.3: Ignition delay in methane/ethane mixtures. The horizontal error bar shows the characteristic uncertainty of experimental temperature. The lines represent the model results. Experimental data for 100% CH_4 are from Huang et al. [28]

(a) $CH_4 - C_3H_8$, 16 bar
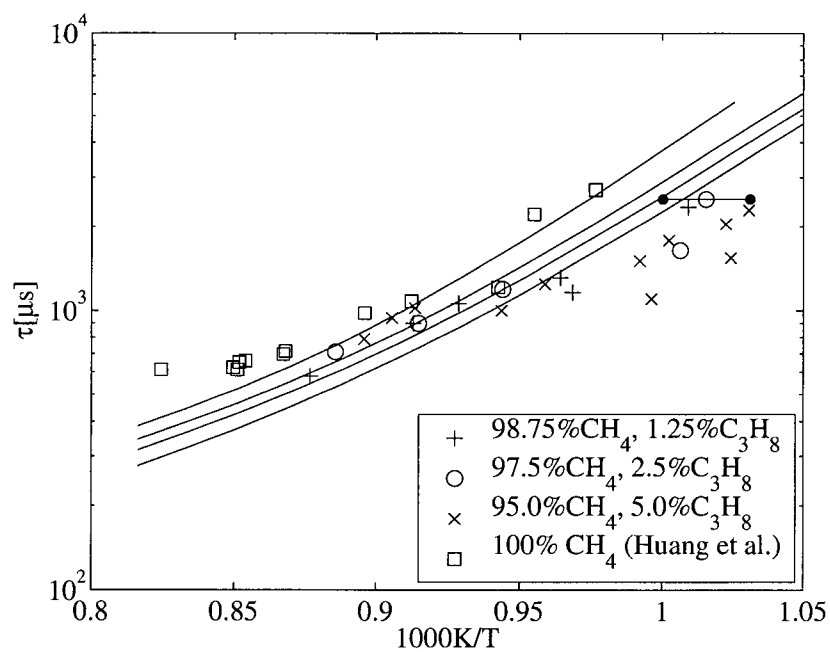
(b) $CH_4 - C_3H_8$, 40 bar

Figure 3.4: Ignition delay in methane/propane mixtures. The lines represent the model results. Experimental data for 100% CH_4 are from Huang et al. [28]
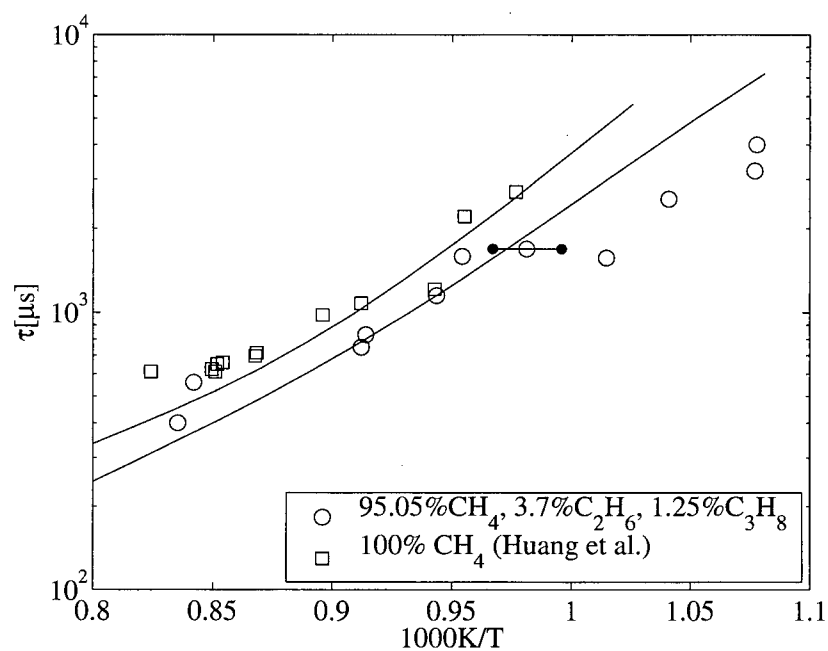
Figure 3.5: Ignition delay in methane/ethane/propane mixtures.The lines represent the model results. Experimental data for 100% CH_4 are from Huang et al. [28]

addition at temperatures around 1100K is approximately 10% to 15%; however, it increases to over 50% near 1000K. Also noticeable is that the reduction in ignition delay is not proportional to the concentrations of ethane or propane. In general, the promoting efficiency, which is the reduction in ignition normalized by the additive concentrations, reduces with increasing concentration for both additives. Such a reduction in the promoter efficiency has been well documented by earlier researchers [23,43].

The ignition delay time predicted by the numerical model with the detailed kinetic mechanism is also shown in Figs. 3.3 to 3.5. The agreement between the model and experimental data is good in general. It is encouraging that the model is able to capture some details of the unique characteristics of the test mixtures. For example, at 16 bar, the experimental results show that the difference between ethane-enriched fuel and pure methane increases noticeably for temperature higher than 1100K; at 40 bar, the difference between 3.7% and 10% ethane mixtures is less significant compared with that between pure methane and 3.7% ethane mixtures - which indicates a reduced efficiency of ethane with increasing concentration. These details are correctly predicted by the new mechanism. The model also shows an increased promoting effect of the two hydrocarbons at lower temperatures.

3.4.2 Kinetic Analysis—Methane/Ethane Mixtures

Fig. 3.6 shows the sensitivity of ignition delay with respect to the change of forward rate constants of elementary reactions for the fuel mixture of 3.7% ethane and 96.3% methane at 40 bar and two different temperatures. It is well known that the formation of ethane from the recombi-
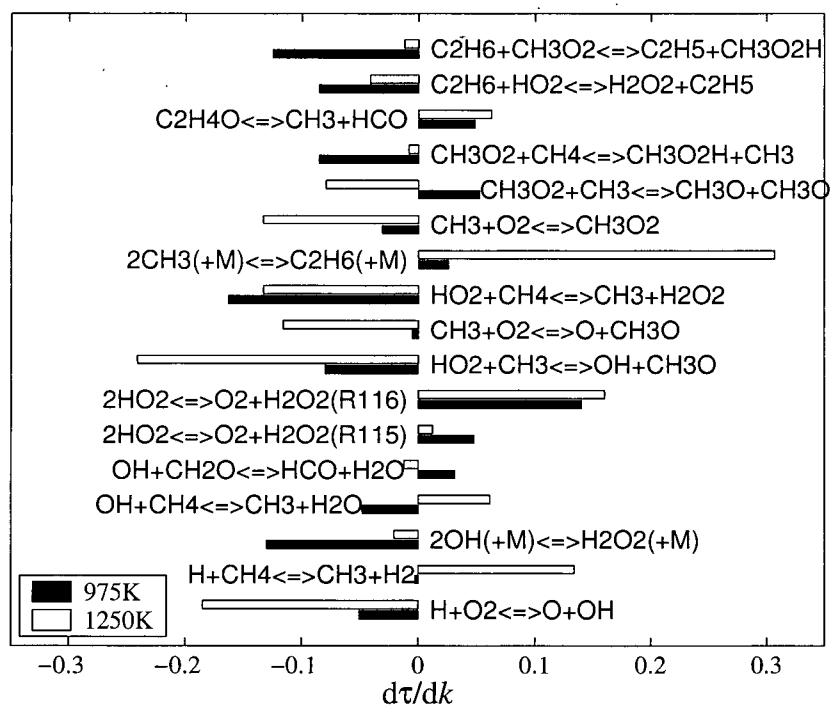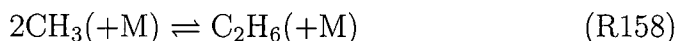
Figure 3.6: Sensitivity of ignition delay with respect to rates of elementary reactions for the 3.7% C_2H_6/96.3% CH_4 mixture

nation of two methyl radicals

$$2CH_3(+M) \rightleftharpoons C_2H_6(+M) \qquad \text{(R158)}$$

is a main chain termination step at high temperatures [149]. The presence of ethane addition at the beginning of reaction shifts the equilibrium of R158 so that less methyl is consumed in this reaction. More importantly, as shown by Westbrook et al. [150], the H-atom abstraction from ethane and the subsequent decomposition of ethyl radical is very efficient in producing H atoms, which lead to a rapid chain branching through

$$H + O_2 \rightleftharpoons OH + O. \qquad \text{(R38)}$$

This mechanism is supported by Fig. 3.6, which shows that the sensitivity to R38 increases drastically with increasing temperature. While the ignition-promoting effect of ethane at high temperatures is relatively well understood, the above mechanism does not account for the enhanced effect of ethane at lower temperatures, since the sensitivities to both R158 and R38 decrease significantly at lower temperatures. Previous work [28] shows that at temperatures below 1100K, the rate of methylperoxy formation

$$CH_3 + O_2 \rightleftharpoons CH_3O_2 \qquad \text{(R179)}$$

rises rapidly. Reaction 179 starts to compete with R158 for methyl radicals. Since the reaction channel formed by R179 and

$$CH_3O2 + CH3 \rightleftharpoons 2CH_3O \qquad \text{(R182)}$$
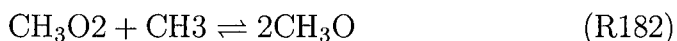
is very efficient in accelerating the oxidation of methyl, R158 becomes less rate-limiting at low temperatures. In this regime, the overall reaction rate is mainly limited by the depletion of OH radicals. This trend

can be seen from Fig. 3.6 which shows a higher (negative) sensitivity with respect to a main OH formation step

$$2OH(+M) \rightleftharpoons H_2O_2(+M) \qquad (R85)$$
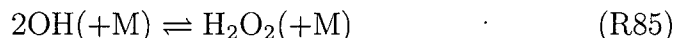
at 975K compared with the sensitivity at 1250K.

The increasing promoting effect of ethane appears to coincide with the increasing formation rate of methylperoxy with reducing temperature. Correspondingly, the ignition delay shows an increased sensitivity to

$$C_2H_6 + CH_3O_2 \rightleftharpoons C_2H_5 + CH_3O_2H \qquad (R193)$$
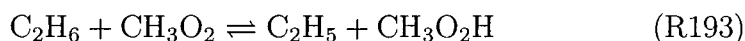
at the lower temperature. As reported by Tsang et al. [141], the rate of R193 is significantly higher than the rate of reaction

$$CH_4 + CH_3O_2 \rightleftharpoons CH_3 + CH_3O_2H, \qquad (R183)$$

thus more methylhydroperoxide (CH_3O_2H) is produced through reaction with ethane. Subsequent reaction following R183 and R193 involves the decomposition of CH_3O_2

$$CH_3O_2H \rightleftharpoons OH + CH_3O, \qquad (R181)$$
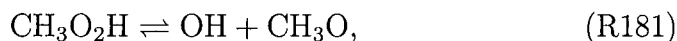
which forms an OH radical. To see whether this mechanism is sufficient to account for the enhanced effect of ethane at reduced temperature, a series of reaction flow analyses was conducted to examine the contribution from elementary reactions to OH generation at various stages of the induction period. As shown in Fig. 3.7, although the overall contribution from R181 is significantly less than R85 and R119

$$CH_3 + HO_2 \rightleftharpoons CH_3O + OH, \qquad (R119)$$
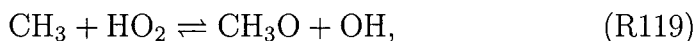
it does dominate the OH formation in the initial stage of the ignition process. The species involved in the R179-R193-R181 branch are all
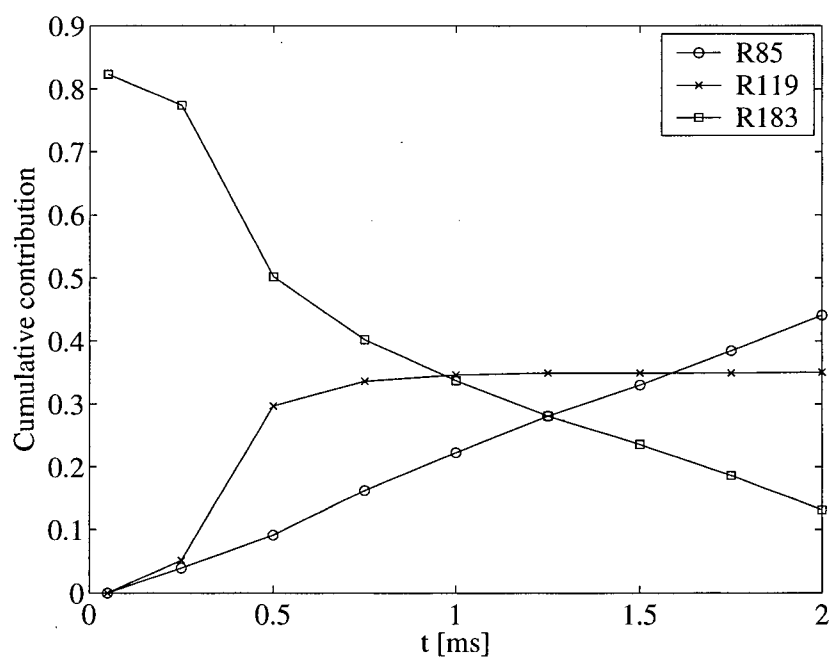
Figure 3.7: Cumulative contribution to OH formation. The analysis was carried out for the fuel mixture of 3.7% C_2H_6 and 96.3% CH_4 (mixture No. 1) at 40 bar and 975K.

present in the upper portion of the main reaction path, which explains the higher efficiency of this branch at the beginning of the reaction. In the later stage, the concentration of hydroperoxy (HO_2) radicals increases, which leads to a faster accumulation of hydrogen peroxide (H_2O_2) through

$$2HO_2 \rightleftharpoons O_2 + H_2O_2. \qquad\qquad (R115, R116)$$

Subsequently, R85 catches up and replaces R181 as a main source for OH radicals. Another way to examine the contribution of R179-R193-R181 path is to reduce the reaction rate of R193 to be identical to that of R183. It is found that the reduction in ignition delay disappears at temperatures below 1100K as this accelerating mechanism is turned off. It should be noted that the formation and decomposition of ethylhydroperoxide ($C_2H_5O_2H$) has a similar effect of generating OH radical as that of CH_3O_2H; however, the overall contribution from $C_2H_5O_2H$ is less significant than CH_3O_2H due to the relatively low concentration of ethane present in this work.

The above analysis shows that the sensitization mechanism for methane ignition with minor ethane addition changes with temperature. At higher temperatures (T 1100K), the H-atom abstraction of ethane leads to a quicker chain branching that accelerates ignition; at lower temperatures, the presence of ethane leads to a more efficient production of CH_3O_2H and $C_2H_5O_2H$ than reactions with methane. The subsequent decomposition of these alkylhydroperoxide species enhances the production of OH radicals at the early stage of the induction period, which significantly promotes the overall reaction rate. The transition from the high-temperature to the low-temperature mechanism occurs with the rise of CH_3O_2 formation at around 1100K. This could account
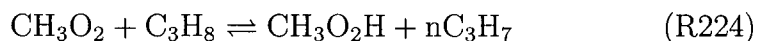
for the change of efficiency with changing temperature that has been observed in this study.

3.4.3 Kinetic Analysis—Methane/Propane Mixtures

A comprehensive kinetics study of methane ignition with propane addition at high temperatures was reported by Frenklach et al. [22]. The ignition-promoting effect of propane is mainly attributed to its rapid decomposition:

$$CH_3 + C_2H_4 + (M) + H \rightleftharpoons C_3H_8(+M), \qquad (R221 + R74)$$
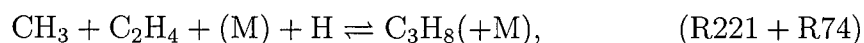
which provides active H radicals leading to the chain branching. The efficiency of propane, however, is lower than that of ethane because H-atom abstraction of propane forms propyl radicals which can decompose to produce methyl radicals [150] as that shown in Eq. R221+R74. As stated above, the recombination of two methyl radicals (Eq. R158) leads to the chain termination immediately. Similar to ethane, it is found that the reaction between propane and methylperoxy needs to be taken into account to address the enhanced promoting effect at lower temperatures:

$$CH_3O_2 + C_3H_8 \rightleftharpoons CH_3O_2H + nC_3H_7 \qquad (R224)$$

and

$$CH_3O_2 + C_3H_8 \rightleftharpoons CH_3O_2H + iC_3H_7. \qquad (R225)$$
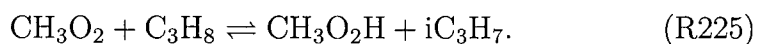
The rates of R224 and R225 are comparable to that of R193 so that propane shows a similar promoting effect to that of ethane at lower temperatures.

3.4.4 Analytical Model

Figure 3.8 presents the main reaction path during the ignition in a methane/ethane/propane mixture, which is identified based on sensitivity and integrated reaction flow analyses. Figure 3.8 reveals two facts regarding the ignition mechanism of methane with minor ethane-/propane additives:

1. The presence of small fractions of C_2H_6-C_3H_8 does not modify the main reaction path of methane (this is also true at higher temperatures [22]).

2. The ignition of methane fuel in this study is dominated by a limited number of key elementary reactions.

It is thus possible to describe the current reaction system with a relatively simple analytical model. One advantage of analytical models comes from the explicit description of the relation between an integrated system and individual factors. It allows a deeper insight into the general nature of the system that are otherwise hard to identify with numerical approaches. In the past, such analytical models based on skeletal mechanisms for methane ignition have been reported by several researchers [149, 151, 152]; however, none of the previous models has taken into account the alkylperoxy chemistry, which is essential under the conditions of this study. In this work, this new mechanistic feature was included to address the transitional behavior of natural gas at intermediate temperature.

The derivation of an analytical model requires further simplification from the main reaction path identified in Fig. 3.8. Following the description of Fig. 3.8 and the previous analysis, the key reactions in the methane oxidation path can be sorted into three main steps:
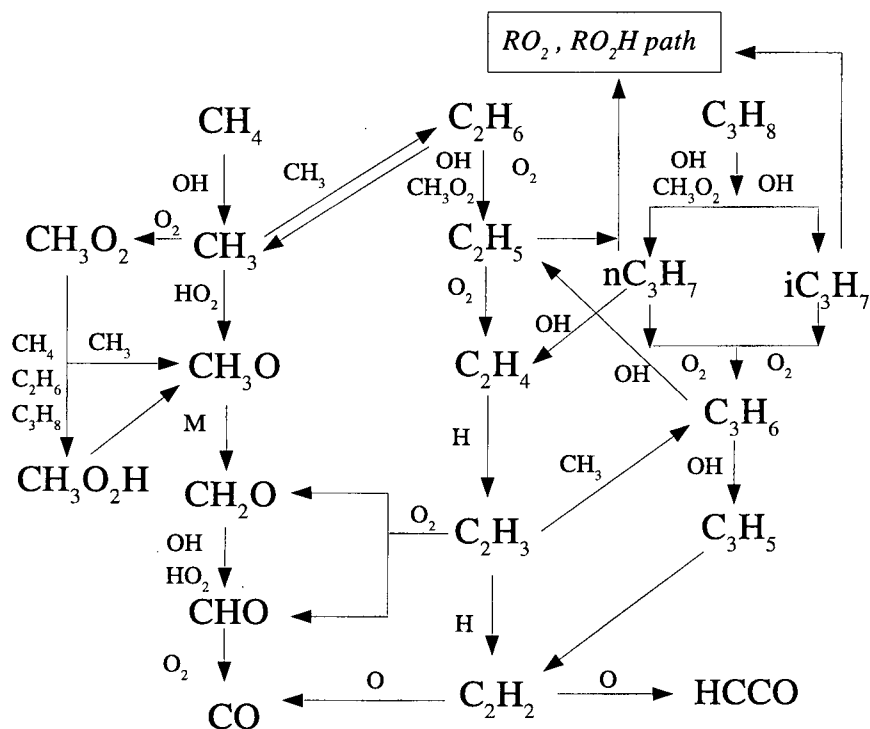
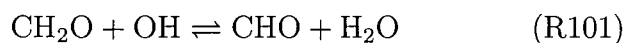Figure 3.8: Main reaction path for methane oxidation during the induction period with the presence of minor ethane and propane additives. The "RO_2, RO_2H path" represents reactions related to the formation and decomposition of $C_2H_5O_2, C_2H_5O_2H, C_3H_7O_2$ and $C_3H_7O_2H$ radicals.

1. Chain initiation

$$CH_4 + O_2 \rightleftharpoons CH_3 + HO_2 \qquad \text{(R118)}$$

2. Chain propagation

   (a) Main propagation path:

$$CH_4 + OH \rightleftharpoons CH_3 + H_2O \qquad \text{(R98)}$$

$$CH_3 + HO_2 \rightleftharpoons CH_3O + OH \qquad \text{(R119)}$$

$$CH_3O + O_2 \rightleftharpoons CH_2O + HO_2 \qquad \text{(R170)}$$

$$CH_2O + OH \rightleftharpoons CHO + H_2O \qquad \text{(R101)}$$

$$CH_2O + HO_2 \rightleftharpoons CHO + H_2O_2 \qquad \text{(R121)}$$

$$CHO + O_2 \rightleftharpoons CO + HO_2 \qquad \text{(R168)}$$
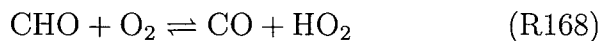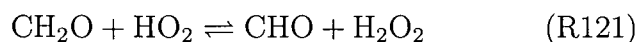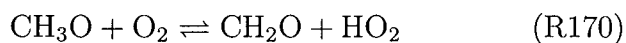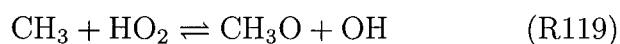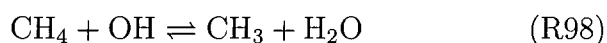
The oxidation of CH_3O radicals occurs at a significantly faster rate than their formation; R119 and R170 can be essentially written as

$$CH_3 + O_2 \rightleftharpoons CH_2O + OH. \qquad \text{(S3)}$$
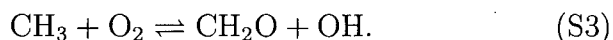
In the lower part of the reaction chain, hydrogen peroxide from R121 rapidly decomposes to OH radicals via R85. The conversion between the HO_2 and OH radicals occurs through the path of R115, R116 and R85. These radical-radical conversions have much higher rates than the main chain propagation steps, so that R101, R121 and R168 can be readily approximated with a one-step reaction

$$CH_2O + \frac{3}{4}O_2 \rightleftharpoons CO + \frac{1}{2}H_2O + OH. \qquad \text{(S4)}$$

95

(b) Methylperoxy chemistry:

$$CH_3 + O_2 \rightleftharpoons CH_3O_2 \qquad\qquad (R179)$$

$$CH_3O_2 + CH_3 \rightleftharpoons 2CH_3O. \qquad\qquad (R182)$$
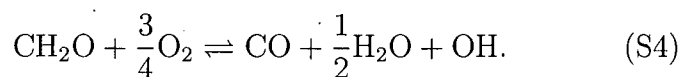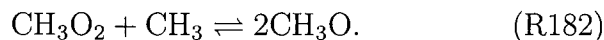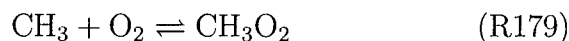
Interestingly, a one-step approximation of R179, R182 (with the consideration of R119 and R170) takes the same form as that of S3.

3. Chain termination

$$2CH_3 \rightleftharpoons C_2H_6. \qquad\qquad (R158)$$

In summary, the pre-ignition reactions of methane can be simplified into five steps (with some reactions renumbered):

$$CH_4 + O_2 \rightarrow CH_3 + HO_2 \qquad\qquad (S_1)$$

$$CH_4 + OH \rightarrow CH_3 + H_2O \qquad\qquad (S_2)$$

$$CH_3 + O_2 \rightarrow CH_2O + OH \qquad\qquad (S_3)$$

$$CH_2O + \frac{3}{4}O_2 \rightarrow CO + \frac{1}{2}H_2O + OH \qquad\qquad (S_4)$$

$$2CH_3 \rightarrow C_2H_6. \qquad\qquad (S_5)$$
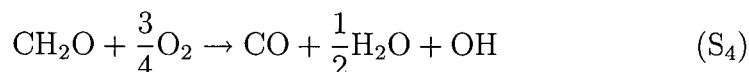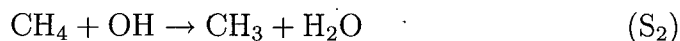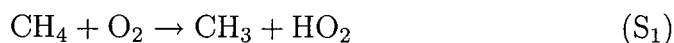
For simplicity, all the reactions are assumed to be non-reversible.

The rate laws for intermediate species concentrations in the reduced mechanism are given by

$$\frac{d[OH]}{dt} = -k_2[CH_4][OH] + k_3[CH_3][O_2] + k_4[CH_2O][O_2]^{3/4} \qquad (3.2)$$

$$\frac{d[CH_3]}{dt} = k_2[CH_4][O_2] - k_3[CH_3][O_2] - 2k_5[CH_3]^2 \qquad (3.3)$$

$$\frac{d[CH_2O]}{dt} = k_3[CH_4][O_2] - k_4[CH_2O][O_2]^{3/4}, \qquad (3.4)$$

where k_1 to k_5 are the rate constants of reactions S_1 to S_5 respectively. As stated above, the rate k_3 represents a combined effect of the main propagation steps and the branch through methylperoxy.

Some "conventional" simplifications for the ignition analysis can be applied to the current system [151, 152]. During the induction period, the temperature and pressure in the reaction system do not change significantly so that constant reaction rates can be used. Meanwhile, the concentrations of methane and oxygen remain nearly unchanged prior to ignition [153]; one can approximate the concentration of methane and oxygen with their initial values.

Because OH is an active radical, its rate of consumption is significantly faster than major intermediates, while its net concentration is much lower. One can readily apply the steady state assumption [62] to OH radicals so that their concentration can be calculated from

$$[OH] \approx \frac{k_3[CH_3][O_2] + k_4[CH_2O][O_2]^{3/4}}{k_2[CH_4]}. \tag{3.5}$$

Strictly speaking, the steady assumption can only be applied to CH_2O when its consumption rate is significantly higher than that of its generation (this implies a large coefficient, k_4, for the stabilization term.) This is not the case in the early phase of ignition delay because the conversion from methoxy to formaldehyde occurs at a relatively high rate (since R170 does not rely on radicals). In the latter phase, with the increase of OH and HO_2 radicals, the concentration of CH_2O does level off rapidly. Since the initiation phase represents a relatively small portion of the induction period, one can roughly assume partial-equilibrium between the generation and consumption of CH_2O for most of the induction period. With the above assumptions and simplifications, the rate law of methyl radicals is given by

$$\frac{d[CH_3]}{dt} \approx k_1[CH_4][O_2] + k_3[CH_3][O_2] - 2k_5[CH_3]^2. \qquad (3.6)$$

Since rate change of CH_3 concentration best reflects the rate of consumption of methane, it can be used to characterize the system progress in the induction period. A close look at Eq. 3.6 shows that it well represents the first and second phases of ignition [22] prior to thermal explosion. The terms on the right hand side of Eq. 3.6 designate the initiation, propagation and termination steps respectively. It is interesting to note that Eq. 3.6 resembles the characteristic equation reported by Zamansky for non-branching reactions system with no promoters [151]; the main difference is the presence of the second term in the current equation, which represents the self-promoting (feedback) mechanism in the chain propagation steps. A similar equation is also reported by Frenklach [22] for methyl radicals at higher temperatures and lower pressures, although the derivation is slightly different from this work. Mathematically, Eq. 3.6 is a first-order Ricatti's differential equation with constant coefficients (see Appendix C for details); its closed form solution is given by

$$[CH_3] = \frac{1}{-\frac{b}{a} + \left(\frac{1}{c} + \frac{b}{a}\right)e^{-at}} - c, \qquad (3.7)$$

where

$$a = \left[(k_3[O_2])^2 + 8k_1k_5[CH_4][O_2]\right]^{1/2}; \qquad (3.8)$$

$$b = -2k_5; \qquad (3.9)$$

$$c = \frac{k_3[O_2] - \left[(k_3[O_2])^2 + 8k_1k_5[CH_4][O_2]\right]^{1/2}}{-2k_5}. \qquad (3.10)$$

The asymptotic (or equilibrium) concentration, which is a steady state solution of Eq. 3.7, can be found from

$$[CH_3]_{equi} = \frac{k_3[O_2] + \left[(k_3[O_2])^2 + 8k_1k_5[CH_4][O_2]\right]^{1/2}}{4k_5}, \qquad (3.11)$$
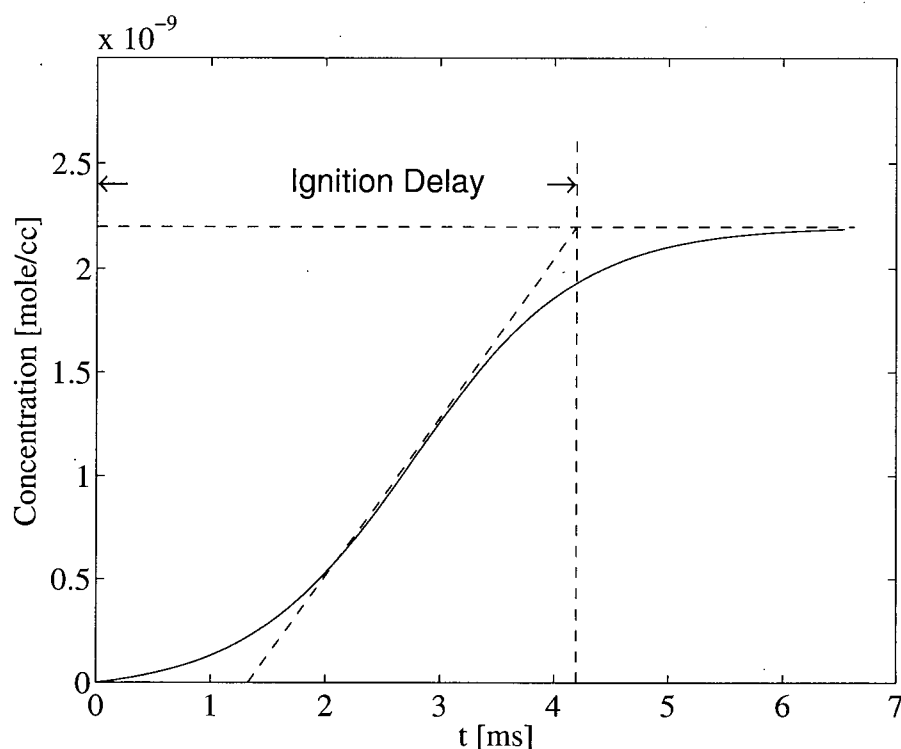
Figure 3.9: Definition of ignition delay in the analytical model.

The system approaches this concentration at the end of the second phase of the induction period, which represents a quasi-steady state where the kinetic growth of methyl is balanced by the second-order recombination step. A breakthrough from this state with the presence of thermal feedback leads to the third phase of ignition - the chain explosion. The third phase, although important, takes only a small portion of the induction period [22]. It thus seems reasonable to approximate the ignition delay time with a characteristic time scale that represents the kinetic delay up to the end of the second phase. In this work, this time scale is defined by extrapolating the maximum growth rate of CH_3 to the asymptotic concentration as shown in Fig. 3.9. With this definition, the ignition delay can be calculated from the formula

$$\tau = \frac{ln - \frac{b}{a}\left(\frac{1}{c} + \frac{b}{a}\right)}{-a} + \frac{2}{a}. \tag{3.12}$$

Table 3.4 lists the rate coefficients of reactions involved in the above skeletal mechanism.

Table 3.4: The skeletal mechanism used in the analytical model

No	Reaction	A	B	E(cal)
1	$CH_4 + O_2 \rightarrow CH_3 + HO_2$	4.04E13	0.0	56807
2	$CH_4 + OH \rightarrow CH_3 + H_2O$	2.00E06	1.6	3120
3	$CH_3 + O_2 \rightarrow CH_2O + OH$	1.08E12	0.0	22000
4	$CH_2O + \frac{3}{4}O_2 \rightarrow CO + \frac{1}{2}H_2O + OH$	$5.00E12[O_2]^{0.25}$	0	40000
5	$2CH_3 \rightarrow C_2H_6$	4.24E14	-1.0	620
6(C_2H_6)	$C_2H_6 \rightarrow 2CH_3$	6.64E42	-8.24	93553
6(C_3H_8)	$C_3H_8 \rightarrow C_2H_5 + CH_3$	5.50E16	0.0	84416
7	$C_2H_6 + CH_4 + \frac{5}{4}O_2 \rightarrow C_2H_5 + CH_3O_2H + \frac{1}{2}H_2O$	$1.20E14[M]^9$	0.0	14931
8	$CH_3O_2H + \frac{1}{2}O_2 \rightarrow CH_2O + 2OH$	$1.10E13/[O_2]^{0.5}$	0.0	42996
9(C_2H_6)	$C_2H_6 + OH \rightarrow H_2O + C_2H_5$	3.54E05	2.1	870
9(C_3H_8)	$C_3H_8 + OH \rightarrow H_2O + nC_3H_7$	3.16E06	1.8	994

[9]total mixture concentration

They are mostly taken from the rate-limiting reactions in the detailed mechanism. The pre-exponential coefficients of these reactions are adjusted to account for factors such as changing reaction order or effects from reverse-reactions. The activation energy and the temperature exponents are unchanged to maintain the characteristic temperature responses of the reaction rates. A comparison of the ignition delay calculated from Eq. 3.12 and that from predicted by the detailed mechanism is shown in Fig. 3.10.

Fig. 3.11 shows a comparison of species concentrations prior to ignition based on the analytical model with the results from the detailed chemistry at 1000 and 1300K. It can be seen that the analytical solutions predict both the ignition delay and the methyl concentration very well. As expected, the agreement for the concentration of CH_2O radicals is very good at the end of the second phase where the partial-equilibrium assumption becomes more valid, but less good in the earlier phase.

When ethane is present in the system, four skeletal steps need to be added to address the two promoting mechanisms aforementioned. The first is the decomposition of ethane to form methyl radicals:

$$C_2H_6 \rightarrow 2CH_3 \qquad \text{(SE6)}$$

To model the reactions between methylperoxy and ethane, the formation of methylperoxy is approximated with a one-step reaction by combining the effects of R118, R85, R98 and R179:

$$CH_4 + \frac{5}{4}O_2 \rightarrow CH_3O_2 + \frac{1}{2}H_2O;$$
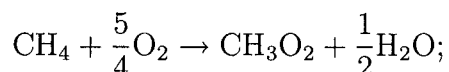
further combining this reaction with R193 froms CH_3O_2H

$$C_2H_6 + CH_4 + \frac{5}{4}O_2 \rightarrow C_2H5 + CH_3O_2H + \frac{1}{2}H_2O. \qquad \text{(SE7)}$$
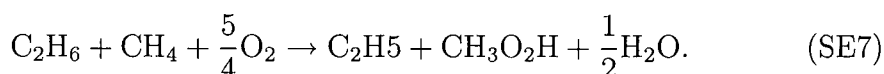
Figure 3.10: Comparison of ignition delay calculated from the model with that from the detailed chemistry at 16 bar (upper lines) and 40 bar (lower lines).
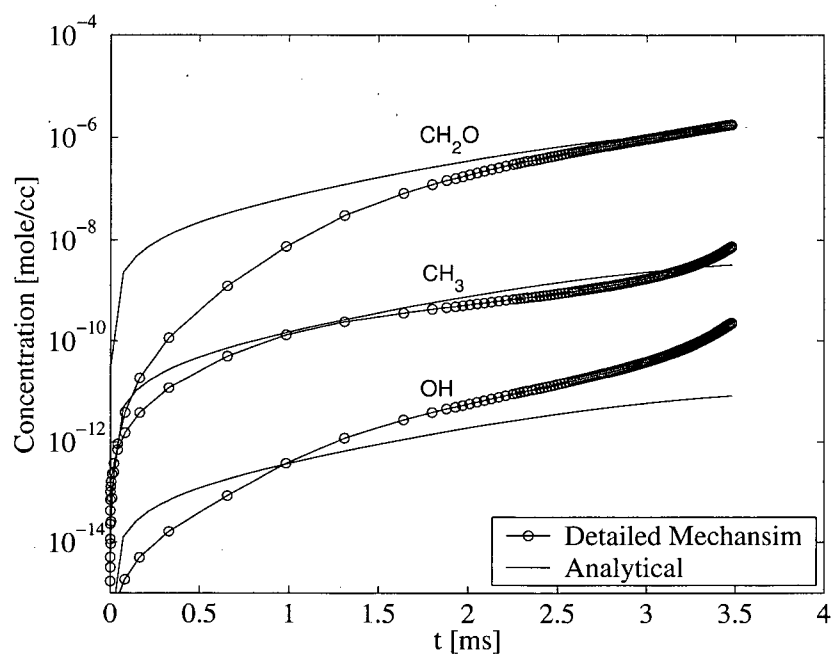
(a) 40 bar, 1000K
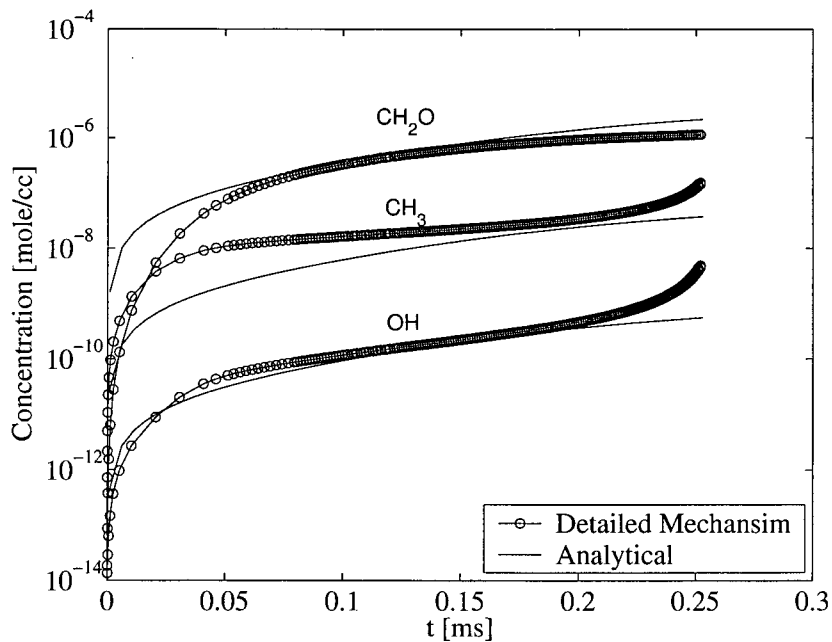
(b) 40 bar, 1300K

Figure 3.11: Species concentrations predicted by the analytical model compared with the calculation from the detailed kinetic model for the stoichiometric methane/air mixture.

This is followed by a series of decomposition and oxidation reactions (R181, R170 and R85), which can be approximated by

$$CH_3O_2H + \frac{1}{2}O_2 \rightarrow CH_2O + 2OH. \tag{S8}$$
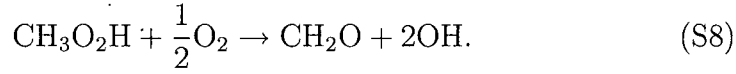
Finally, the oxidation of ethane mainly goes through the reaction with OH radicals:

$$C_2H_6 + OH \rightarrow C_2H_5 + H_2O. \tag{SE9}$$
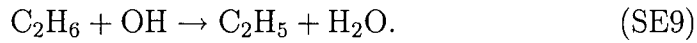
With these extended reactions, the updated rate laws for the intermediate species are

$$\frac{d[OH]}{dt} = -k_2[CH_4][OH] + k_3[CH_3][O_2] + k_4[CH_2O][O_2]^{3/4} \tag{3.13}$$
$$+ 2k_8[CH_3O_2H][O_2]^{1/2} - k_9[C_2H_6][OH]$$

$$\frac{d[CH_3]}{dt} = k_1[CH_4][O_2] + k_2[O_2][OH] - k_3[CH_3][O_2] \tag{3.14}$$
$$- 2k_5[CH_3]^2 + 2k_6[C_2H_6]$$

$$\frac{d[CH_2O]}{dt} = k_3[CH_3][O2] - k_4[CH_3][O_2]^{3/4} + 2k_8[CH_3O_2H][O_2]^{1/2}$$
$$\tag{3.15}$$

$$\frac{d[CH_3O_2H]}{dt} = k_7[CH_4][C_2H_6][O_2]^{5/4} - k_8[O_2]^{1/2}. \tag{3.16}$$

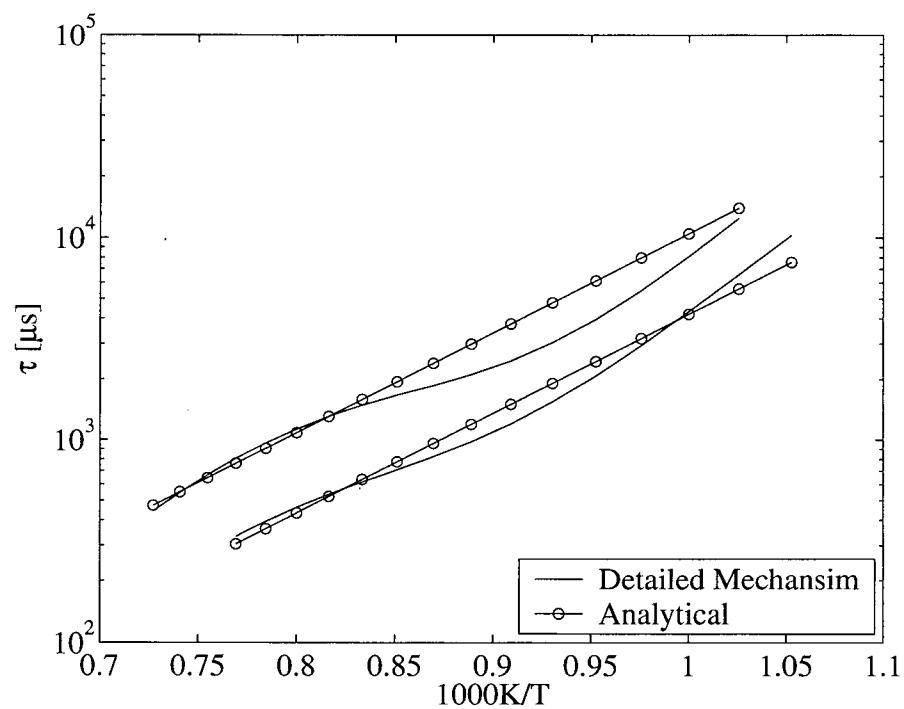It should be noted that, unlike methane, the concentration of ethane changes significantly during the induction period [153]. The detailed kinetic model shows that more than 70% of added ethane has decomposed or been oxidized compared to around 10% of methane prior to ignition at 1300K. It is thus not appropriate to simplify the calculation with a constant ethane concentration. Instead, the concentration of ethane must be calculated from its rate expression

$$\frac{d[C_2H_6]}{dt} = -(k_7[CH_4][O_2]^{5/4} + k_6 + k_9[OH])[C_2H_6] + k_5[CH_3]^2. \tag{3.17}$$

The contribution from the second term of Eq. 3.17 is negligible compared with that of the first term for the concentration of ethane present

in this study. An approximate solution of Eq. 3.17 can be obtained through asymptotic analysis. The change of ethane concentration is given by

$$[C_2H_6] = [C_2H_6]_0 \exp\left\{-\left(k_7[CH_4][O_2]^{5/4} + k_6 + 2\frac{k_3[O_2]}{k_2[CH_4]}[CH_3]_{equi}\right)t\right\}$$

(3.18)

where $[C_2H_6]_0$ is the initial concentration of C_2H_6. Subsequently, a differential equation for CH_3O_2H can be solved to get its concentration at time t

$$[CH_3O_2H] = \frac{m[C_2H_6]}{n-k}e^{-nt}[e^{(n-k)t} - 1],$$

(3.19)

where

$$k = k_7[CH_4][O_2]^{5/4} + k_6 + 2\frac{k_3[O_2]}{k_2[CH_4]}[CH_3]_{equi};$$

$$m = k_6[CH_4][O_2]^{5/4};$$

$$n = k_8[O_2]^{1/2}.$$

The solution to this equation indicates that the concentration of CH_3O_2H should experience an initial growth followed by an exponential decay with the depletion of ethane.

With the C_2H_6 and CH_3O_2H concentrations known, one can process Eq. 3.13 using a similar steady-state assumption technique as that introduced earlier. This leads to a new rate law for the methyl concentration:

$$\frac{d[CH_3]}{dt} = \left(k_1[CH_4][O_2] + 2k_6[C_2H_6] + \frac{4k_8[CH_3O_2H][O_2]^{1/2}}{k_2[CH_4] + k_9[C_2H_6]}\right)$$

(3.20)

$$+ \left(k_3[O_2] - \frac{k_9[C_2H_6]}{k_2[CH_4] + k_9[C_2H_6]}\right)[CH_3] - 2k_5[CH_3]^2.$$

Comparing Eq. 3.20 with Eq. 3.6, one can find that the initiation term (the terms in the parentheses on the right hand side) of Eq. 3.6 is en-

hanced through the decomposition of ethane and methylhydroperoxide. The large rate constant k_8 at low temperatures accounts for the higher promoting effect in that regime. However, ethane shows a negative effect on the propagation term. It can be seen that if the concentration of ethane is significantly lower than that of methane, the second part of the propagation term becomes negligible, i.e.

$$\frac{k_9[C_2H_6]}{(k_2[CH_4] + k_9[C_2H_6])k_3[O_2]} \ll 1, \tag{3.21}$$

and the promoting effect from the initiation term dominates. With an increase in ethane concentration, the ignition promoting efficiency of ethane starts to decrease due to the increasing negative effect of its concentration on the propagation term. The physical meaning of this reduction is related to the competition between ethane and methane for OH radicals. A maximum reduction is achieved when the positive and negative effects of ethane are balanced. This trend in the change of ethane efficiency found by simply analyzing Eq. 3.20 agrees with the experimental results from this work as well as those reported in the literature. Also, since the concentrations of C_2H_6 and CH_3O_2H are two exponential functions which vanishes as they approach infinity, the asymptotic concentration of methyl does not change with ethane addition.

The above characteristics revealed by the analytical equation are consistent with the numerical analyses presented earlier regarding the promoting mechanism of ethane. First, the kinetic effect of ethane primarily comes from its contribution to the initiation phase of the induction period. Second, while additional ethane does not change the main reaction path of methane ignition (ethane does not lower the critical concentration of methyl required for the transition to the third phase),

it does change the rate of progress of different phases in the induction period.

The skeletal mechanism for propane addition is very similar to that for ethane addition. For propane/methane mixtures, reaction SE7 is replaced by

$$C_3H_8 + CH_4 + \frac{5}{4}O_2 \rightarrow nC_3H_7 + CH_3O_2H + \frac{1}{2}H_2O \qquad \text{(SP7)}$$
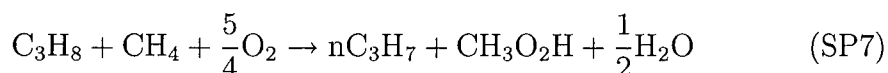
The decomposition of propane replaces that of ethane in SE6

$$C_3H_8 \rightarrow C_2H_5 + CH_3. \qquad \text{(SP6)}$$
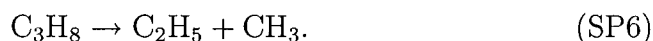
The oxidation of propane goes through

$$C_3H_8 + OH \rightarrow nC_3H_7 + H_2O. \qquad \text{(SP9)}$$
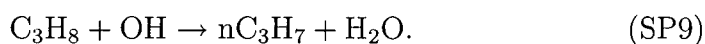
The governing equation for methyl concentration with additional propane takes a form analogous to that with ethane. Note that the decomposition reaction of propane contributes only one methyl radical compared with two of ethane; this could partially account for the weaker promoting effect of propane at relatively high temperatures. Fig. 3.12 presents the ignition delay calculated from the analytical model for two methane/ethane and methane/propane mixtures at 40 bar. Figures 3.13 and 3.14 compare the predicted species concentrations of ethane/propane and methylhydroperoxide by the analytical model with those calculated from the detailed chemistry. It can be seen that, despite the simplicity of the analytical model, the results agree reasonably well with the detailed chemistry and the experiments. The key features of the ignition system with the presence of ethane/propane are well captured by the analytical model. In particular, the model reproduces the transition of the promoting mechanism in the correct temperature range.
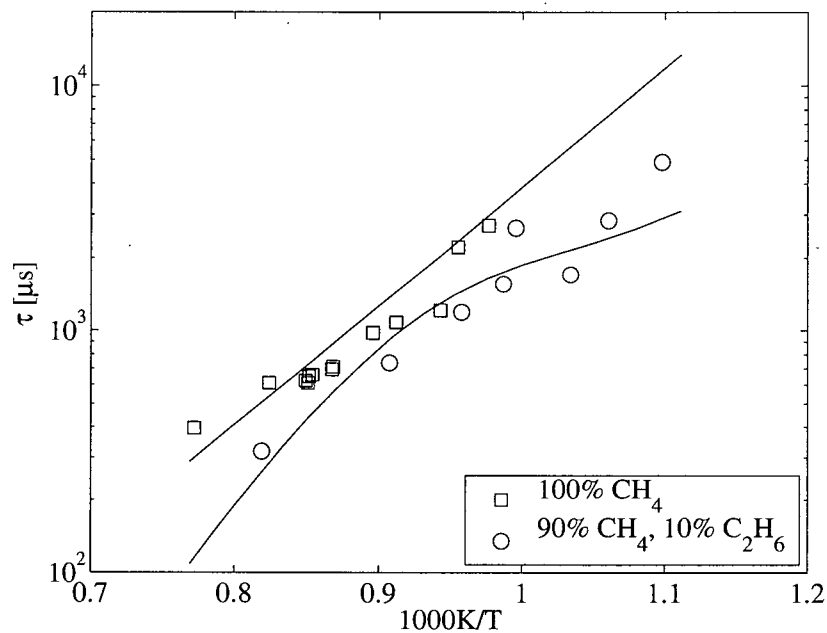
(a) 10% C_2H_6, 90% CH_4, 40 bar
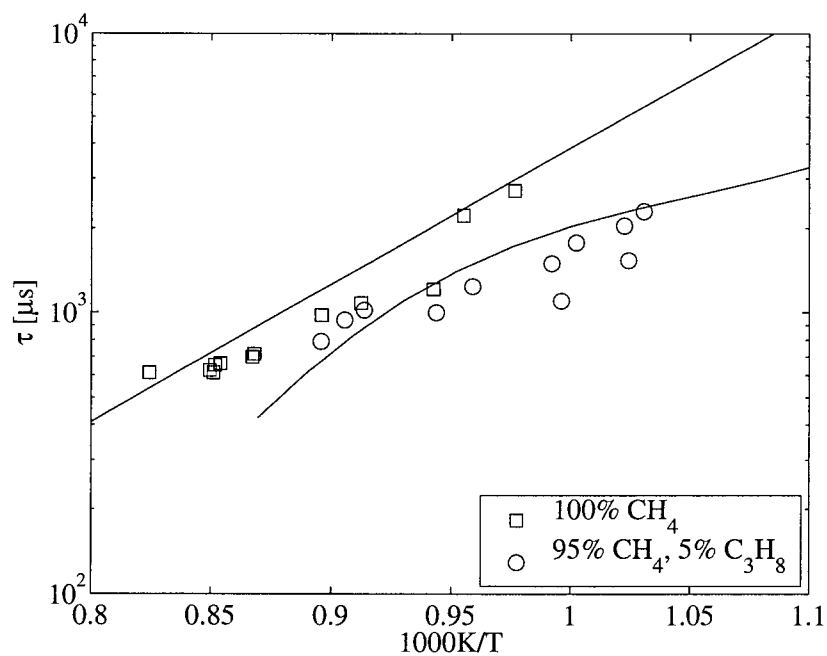
(b) 5% C_3H_8, 95% CH_4, 40 bar

Figure 3.12: Ignition delay with ethane/propane additives: comparison of analytical model and experimental results.
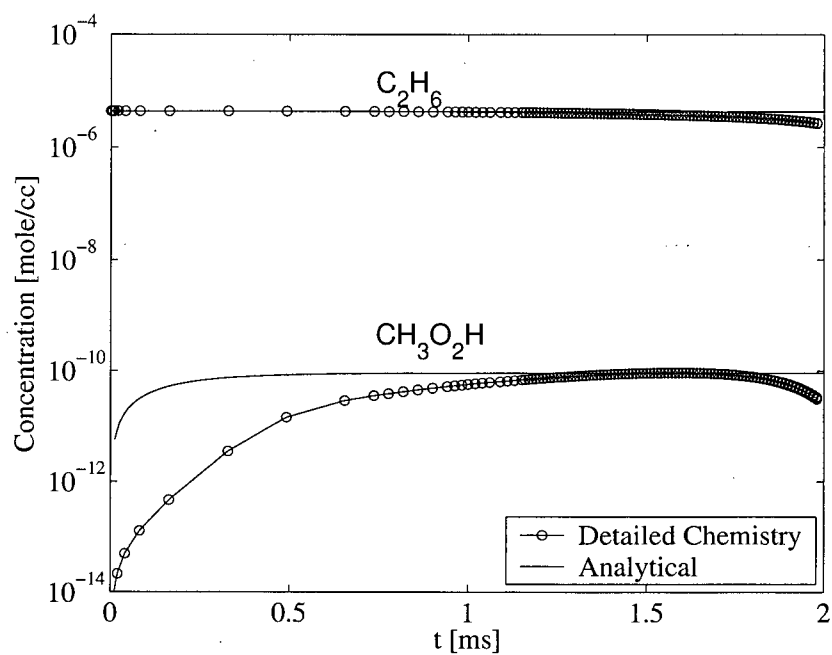
(a) 40 bar, 1000K
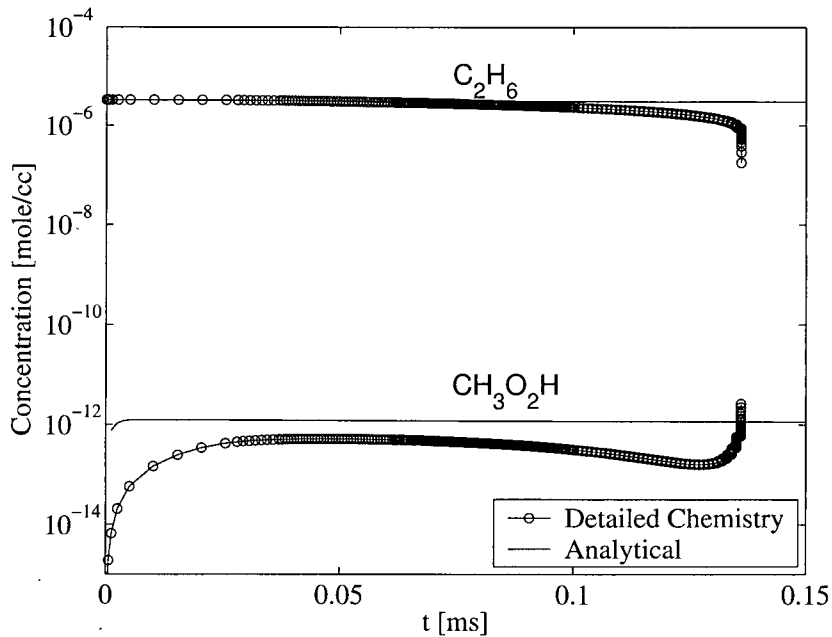
(b) 40 bar, 1300K

Figure 3.13: Species concentrations predicted by the analytical model compared with the calculation from the detailed kinetic model for mixture No.3 (90% CH_4, 10% C_2H_6).
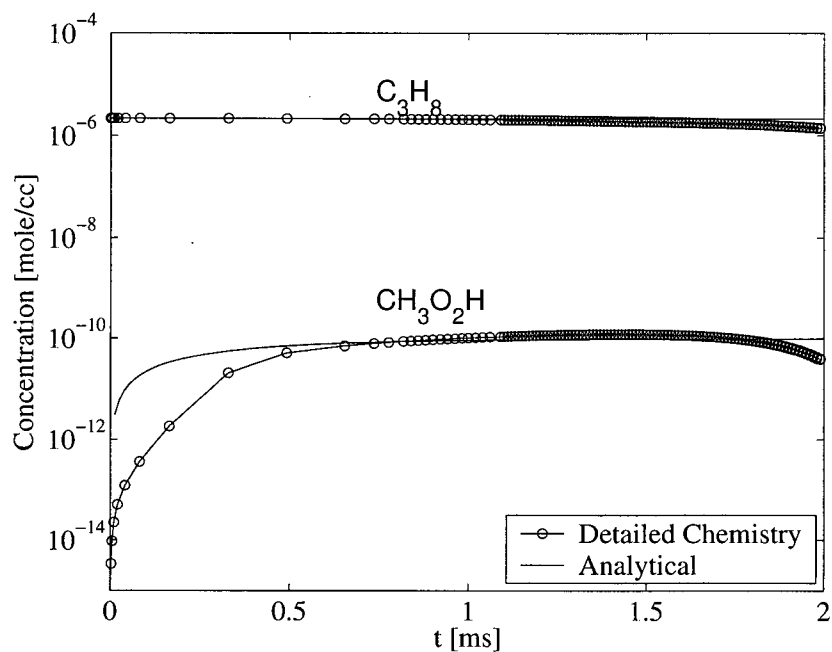
(a) 40 bar, 1000K
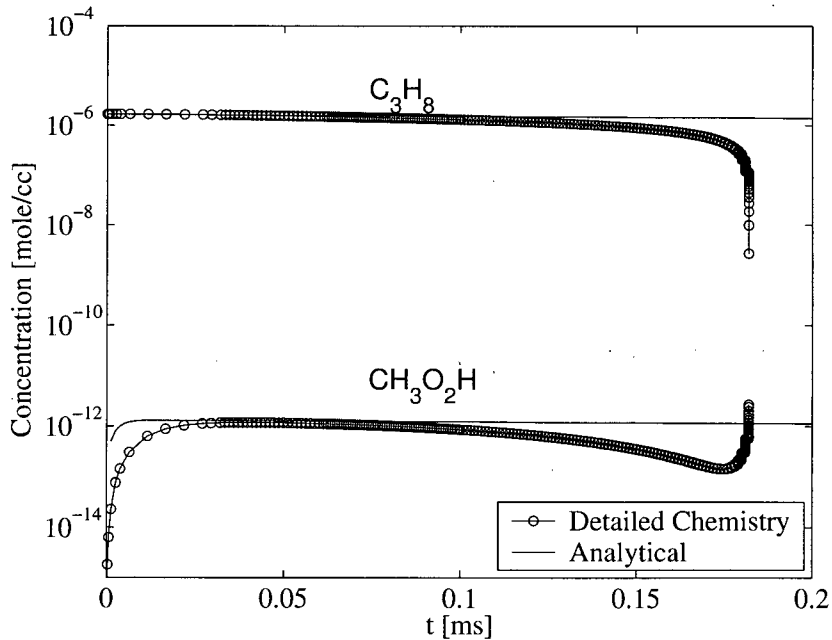
(b) 40 bar, 1300K

Figure 3.14: Species concentrations predicted by the analytical model compared with the calculation from the detailed kinetic model for mixture No.6 (95% CH_4, 5% C_3H_8).

3.5 Conclusions

Experimental and analytical studies have been conducted on the ignition of homogeneous methane/ethane/air and methane/propane/air mixtures at conditions relevant to practical combustion devices, particularly IC engines and gas turbines. A complex behavior has been observed for the promoting effect of ethane/propane, which varies significantly with temperature and pressure. A detailed chemical kinetic model, which includes elementary reactions between ethane/propane and methylperoxy, have been used to study the new reaction system. The predicted ignition delay time based on this mechanism agrees well with the experimental results. The kinetic study reveals a switch of the dominant ignition-promoting mechanism for ethane/propane with changing temperature. The enhanced promoting effect of ethane and propane at low temperatures (T<1100K) is attributed to the increasing significance of methylperoxy and methylhydroperoxide chemistry.

An analytical solution was obtained for the ignition delay of methane enriched with ethane and/or propane by systematically reducing the skeletal mechanism identified from the reaction-flow analysis using the steady state assumption. The analytical model agrees well with the detailed-kinetic model for both ignition delay and the concentrations of main intermediate species. Both the analytical model and kinetic analysis of the detailed mechanism show that the addition of ethane/propane does not change the main reaction path of pure methane during ignition. The promotion of ignition is realized through accelerating the initiation phase in the induction period.

Chapter 4
Ignition of Methane with Hydrogen Addition[10]

4.1 Introduction

Hydrogen enriched methane fuels are being increasingly studied due to their economic and environmental benefits. Experimental and computational results reported recently [45–50] show that by extending the lean-burn limit or increasing the fraction of exhaust gas recirculation (EGR) with hydrogen addition, a significant reduction of NO_x and hydrocarbon emissions from natural-gas-fueled internal combustion engines can be achieved with unaffected or slightly higher engine efficiency. The gain in combustion efficiency mainly comes from the enhanced reaction rate and the higher flame velocity. Potential applications of premixed methane/hydrogen fuels are also found in the aerospace [51] and gas turbine [52] industries. An understanding of the autoignition behavior of these mixtures is clearly needed.

Shock tube studies of high-temperature ignition in CH_4 - H_2 - O_2 mixtures have been reported by Lifshitz et al. [10] as well as by Cheng and Oppenheim [10]. In both cases, the reactants were diluted with

---

[10]A version of this chapter has been accepted for publication. Huang. J., Hill, P. G., Bushe, W. K. and Munshi, S. R. (2005) Experimental and kinetic study of shock initiated ignition in homogeneous methane-hydrogen-air mixtures at engine-relevant conditions, Int. J. Chem. Kine., In Press

90 percent argon. The data of Lifshitz et al. [10] measured at a fixed pressure of 185 torr and covered temperatures from 1600 to 1800K. A thermal-based-promotion theory was proposed to account for the effects of hydrogen addition. Cheng and Oppenheim [12] conducted experiments for temperatures from 800 to 2000 K and pressures from 1 to 3 atm. They correlated the ignition delay of pure methane, pure hydrogen and their mixtures with the formula

$$\tau = \tau_{CH_4}{}^{(1-\epsilon)}\tau_{H_2}{}^{\epsilon} \qquad (4.1)$$

where ϵ is the mole fraction of hydrogen in the total fuel and τ_{CH_4} and τ_{H_2} are the ignition delay times of pure methane and pure hydrogen under the same conditions. Fotache et al. [53] investigated the ignition delay of hydrogen-enriched methane by heated air using a counter-flow reactor. They identified three ignition regimes depending on the mole fractions of hydrogen. Methane ignition was found to benefit from hydrogen addition mainly due to the kinetic interactions between the two fuels. The modeling study shows that the promoting effect is enhanced by the spatial separation of the branching and termination steps resulting from the high diffusivity of atomic and molecular hydrogen. Ju and Kiioka [51] conducted a numerical study of hydrogen-/methane ignition in a supersonic mixing layer. They found a reduction of ignition delay proportional to the fraction of hydrogen addition. They suggested that the extra H and O radicals from H_2 oxidation was the main reason for the increased reaction rate.

In reviewing the literature, it is clear that most of the prior work on the ignition of methane/hydrogen/air or methane/hydrogen/oxygen mixtures was at relatively low pressures (≤ 8 atm) [10, 12, 53] and was focused on high temperatures [10, 12]; systematic studies of methane-

hydrogen-air ignition and the underlining chemical kinetics under conditions pertinent to internal combustion engines have rarely been reported. In this work, experimental and computational investigations have been conducted to address this specific issue. This study focuses on ignition in homogeneous, quiescent methane/hydrogen/air mixtures behind a reflected shock [133] so that fluid dynamic effects can be isolated from chemical kinetics to simplify the analysis.

4.2 Experiments

The experiments were conducted in a shock tube facility introduced in detail previously [28]. The stainless-steel shock tube has a circular cross section with an inner diameter of 59 mm. The length of the driver section is 3.18 m; the driven section is 4.25 m long. Ignition is initiated behind the reflected shock. A PCB pressure transducer mounted at the end plate and two photomultipliers (one equipped with a 427 nm interference filter) were used to detect the ignition based on pressure and optical emission signals. The experimental temperature was calculated using the incident shock velocity, which is measured by 5 flush-mounted PCB pressure transducers with a minimum response time of $2\,\mu$ s. The uncertainty in the calculated temperatures is around 15K. To extend the experimental time for ignition to lower temperatures, the tailored-interface technique [27] was adopted; this technique allows a maximum experimental time of up to 5 ms to be achieved with the current facility.

The compositions of gas mixtures in this work are presented in Table 4.1.

Table 4.1: Molar fractions of main constituents in the test mixtures ($\phi = 1$ for all mixtures, balanced by air (79%N_2, 21%O_2))

Mixture #	X_{H_2}	X_{CH_4}
1	15%	85%
2	35%	65%

The focus of this work was on stoichiometric fuel-air mixtures so that the equivalence ratio was fixed at unity. The test gases had the following purities: methane (99.95%), hydrogen (99.995%) and air (99.9%; 21%O_2, 79%N_2). Ignition was defined by extrapolating the maximum value of dP/dt (measured at the end plate of the driven sections) back to the pressure right after shock reflection; this method has been widely adopted in shock tube ignition studies [9,30].

4.3 Kinetic Model

In the range of intermediate temperature (1000–1300K) and high pressure (16–230bar), previous studies show that the alkylperoxy chemistry, especially reactions related to the formation and consumption of CH_3O_2, are important to better describe the ignition characteristics of methane [28,29]. In this work, a mechanism from a previous work [28] was adopted; it is a modified version of a mechanism proposed by Petersen et al. [29]. The main part of the mechanism is identical to that of GRI-Mech 1.2 [39] with major CH_3O_2 and $C_2H_5O_2$ chemistry included. The numerical models based on this mechanism are able to reproduce experimental ignition delay results of methane/oxygen-/argon and methane/oxygen/nitrogen mixtures over a wide range of

conditions [28].

It should be noted that the hydrogen subset of this mechanism is identical to that in GRI-Mech 1.2, which has been validated substantially using low-pressure, high-temperature experimental data, but not optimized for conditions similar to those of this study. A recent investigation conducted by Akbar et al. [154] shows a significant discrepancy between the numerical results calculated using various hydrogen mechanisms and experimental data for hydrogen/air ignition at pressures above 1 atm. To improve the performance of the new mechanism at higher pressures, rate coefficients of several reactions key to hydrogen ignition were updated using recent values reported in the literature. These reactions were identified based on the results of preliminary sensitivity and reaction flow analyses. Among the changes, the rates of reactions related to

$$H + O_2 + M \rightleftharpoons HO_2 + M$$
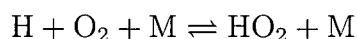
(reactions R36–R38) were replaced using values proposed by Baulch et al. [70]. The reaction with methane as a third body (R37) was added to the mechanism. For the rate of reaction

$$CH_4 + H \rightleftharpoons CH_3 + H_2, \tag{R54}$$
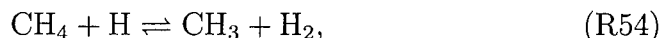
the experimentally obtained values by Sutherland [155] were used. The rate constants of reaction

$$OH + H_2 \rightleftharpoons O + H_2O \tag{R85}$$

were adopted from the work of Isaacson [156]; his rate coefficients were supported by latest kinetic experiments of Smith and Crim [157]. Due to the significance of CH_3O_2 chemistry in the low-intermediate temperature range, reactions between hydrogen and methylperoxy were

added:

$$CH_3O_2 + H \rightleftharpoons CH_3O + H \qquad\qquad (R194)$$

and

$$CH_3O_2 + H_2 \rightleftharpoons CH_3O_2H + H. \qquad\qquad (R195)$$
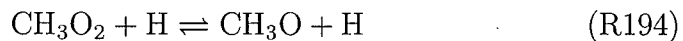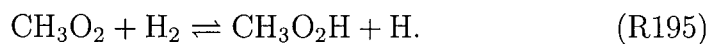
The rate coefficients of these reactions were taken from Tsang et al. [141]. The final mechanism includes 40 species and 195 reversible reactions. A list of reactions extended or modified, including their rate coefficients and source, is given in Table 4.2.

Table 4.2: Modified and extended reactions in the new model (based on GRI-Mech 1.2)

Rx #	Reaction	A	B	E(cal)	Ref.
R1–R33	R1–R33, GRI-Mech 1.2	-	-	-	[39]
R34	$H + 2O_2 \rightleftharpoons HO_2 + O_2$	1.41E+18	-0.8	0.0	[70]
R35	$H + O_2 + H_2O \rightleftharpoons HO_2 + H_2O$	9.38E+18	-0.8	0.0	[70]
R36	$H + O_2 + N_2 \rightleftharpoons HO_2 + N_2$	2.20E+18	-0.8	0.0	[70]
R37	$H + O_2 + CH_4 \rightleftharpoons HO_2 + CH_4$	4.40E+18	-0.8	0.0	[11]
R38	$H + O_2 + AR \rightleftharpoons HO_2 + AR$	7.00E+17	-0.8	0.0	[70]
R39–R53	R38–R52, GRI-Mech 1.2	-	-	-	[39]
R54	$H + CH_4 \rightleftharpoons CH_3 + H_2$	3.99E+03	3.2	8760.0	[155]
R55–R84	R54–R83, GRI-Mech 1.2	-	-	-	[39]
R85	$OH + H_2 \rightleftharpoons H + H_2O$	1.81E+09	1.2	4707.0	[156]
R86–R157	R85–R156, GRI-Mech 1.2	-	-	-	[39]
R158	$HO_2 + CH_4 \rightleftharpoons CH_3 + H_2O_2$	4.48E+13	0.0	24629.0	[38]
R159–R178	R158–R177, GRI-Mech 1.2	-	-	-	[39]
R179	$CH_3 + OH \rightleftharpoons CH_2O + H_2$	8.00E+12	0.0	0.0	[29]
R180	$CH_3 + O_2 \rightleftharpoons CH_3O_2$	2.13E+58	-15.0	17018.0	[28]
R181	$C_2H_5O \rightleftharpoons CH_2O + CH_3$	1.00E+15	0.0	21606.0	[29]
R182	$CH_3O + HO_2 \rightleftharpoons CH_2O + H_2O_2$	1.20E+13	0.0	0.0	[29]

Continued on next page

[11]Rate estimated in this work

Table 4.2 – continued from previous page

Rx #	Reaction	A	B	E(cal)	Ref.
R183	$CH_3O + CH_3 \rightleftharpoons CH_2O + CH_4$	2.41E+13	0.0	0.0	[29]
R184	$CH_3O_2H \rightleftharpoons CH_3O + OH$	4.00E+15	0.0	42996.0	[143]
R185	$CH_3O_2 + CH_3 \rightleftharpoons CH_3O + CH_3O$	3.00E+13	0.0	-1200.0	[29]
R186	$CH_3O_2 + H_2O_2 \rightleftharpoons CH_3O_2H + HO_2$	2.40E+12	0.0	9942.0	[29]
R187	$CH_3O_2 + CH_2O \rightleftharpoons CH_3O_2H + HCO$	2.00E+12	0.0	11663.0	[29]
R188	$CH_3O_2 + CH_4 \rightleftharpoons CH_3O_2H + CH_3$	1.80E+11	0.0	18475.0	[29]
R189	$C_2H_5 + O_2 \rightleftharpoons C_2H_5O_2$	1.00E+12	0.0	0.0	[29]
R190	$C_2H_5O_2 + CH_2O \rightleftharpoons C_2H_5O_2H + HCO$	2.00E+12	0.0	11663.0	[29]
R191	$C_2H_5O_2H \rightleftharpoons C_2H_5O + OH$	1.00E+16	0.0	42977.0	[29]
R192	$CH_3O_2 + HO_2 \rightleftharpoons CH_3O_2H + O_2$	4.60E+10	0.0	-2600.0	[29]
R193	$CH_3O_2 + CH_3O_2 \rightleftharpoons O_2 + CH_3O + CH_3O$	3.70E+11	0.0	2200.0	[29]
R194	$CH_3O_2 + H \rightleftharpoons CH_3O + OH$	9.60E+13	0.0	0.0	[141]
R195	$CH_3O_2 + H_2 \rightleftharpoons CH_3O_2H + H$	1.50E+14	0.0	26030.0	[141]

The forward rate constant k_f is calculated using the formula $k_f = AT^\beta \exp(E/RT)$; A, E are in cgs units. The reverse rate constant k_r is calculated from the forward rate constant and the equilibrium constant K_{eq} using $k_r = k_f/K_{eq}$. All the reactions in the mechanism are reversible.

The numerical simulation of ignition behind the reflected shock was performed using a zero-dimensional model with constant-density and adiabatic boundary conditions. A system of ordinary differential equations (ODEs) containing mass and energy conservation equations was solved using VODE [148]. To be consistent with the base mechanism, the thermodynamic properties of reactants were mostly taken from the GRI thermo database; species properties not available in the GRI database were taken from those of Burcat [146] and Curran et al. [158]. The gas-phase reaction rates and mixture properties were calculated using Chemkin II [147].

To validate the modification to the base mechanism, computations were performed for hydrogen/oxygen/argon and hydrogen/air ignitions at various pressures. Figure 4.1 presents the results of calculated ignition delay time using the modified mechanism together with experimental data from the literature [30, 159–161]. The results from the base mechanism (GRI-Mech 1.2) are also presented for comparison. It can be seen that the modified mechanism basically maintains or slightly improves the accuracy of GRI-Mech 1.2 in predicting ignitions in hydrogen/oxygen/argon mixtures, while it significantly improves the agreement between numerical and experimental results for ignitions in hydrogen/air mixtures. A sensitivity analysis shows that the improvement can be largely attributed to the slightly higher rate of

$$H + O_2 + N_2 \rightleftharpoons HO_2 + N_2 \qquad \text{(R36)}$$
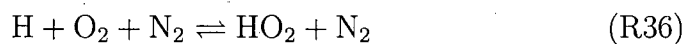
in the new mechanism at intermediate temperatures compared with the original rate. As we will show later, R36 is a main H-scavenging step for hydrogen ignition; the increase in the rate of R36 typically leads to a reduction in the overall reaction rate. To examine if the modi-
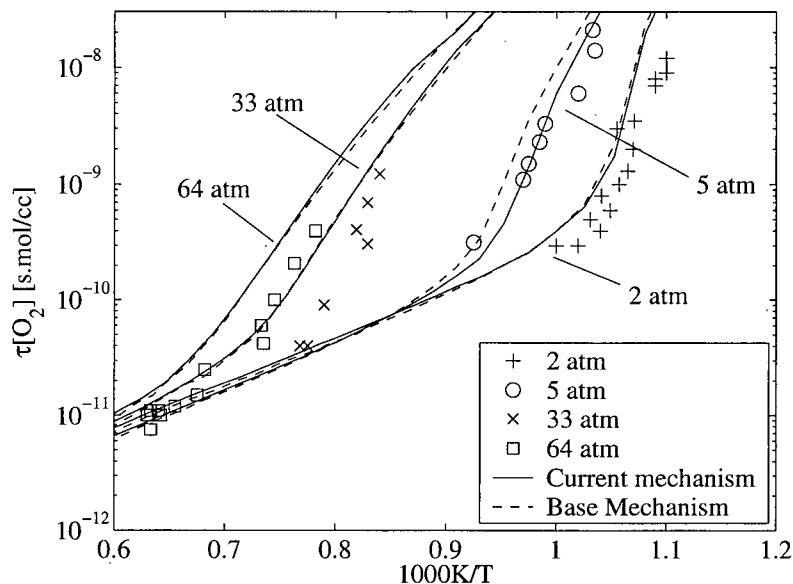
(a) Ignition Delay in $H_2/O_2/Ar$ Mixtures
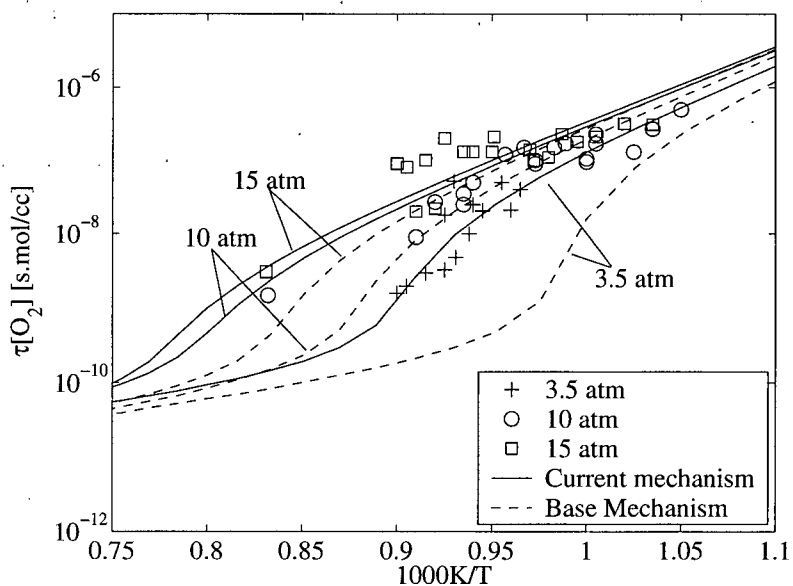
(b) Ignition Delay in H_2/Air Mixtures

Figure 4.1: Calculated ignition delay of hydrogen/oxygen/argon mixtures with experimental data from the literature. Symbols designate experimental data. In plot a: + - $2\%H_2 + 1\%O_2 + 97\%Ar$ [159]; o - $8\%H_2 + 2\%O_2 + 90\%Ar$ [160]; × - $2\%H_2 + 1\%O_2 + 97\%Ar$ [30];□ - $2\%H_2 + 1\%O_2 + 97\%Ar$ [30]. In plot b: $15\%H_2 + 85\%Air$ [161] for all mixtures. Lines designate calculated delay.

fication has caused any significant deterioration of the base mechanism in the regime where it has been extensively optimized, extra computations have been performed for the ignition of methane under a variety of conditions and compared results with the experimental data from the literature as well as the predictions using GRI-Mech1.2 and GRI-Mech 3.0 [41]. It was found that above modifications did not significantly affect the calculated methane ignition results as demonstrated in Fig. 4.2, given as an example.

4.4 Results and Discussion

Table 4.3 lists the experimental conditions and measured ignition delay time; the results are also presented graphically in Figure 4.3.
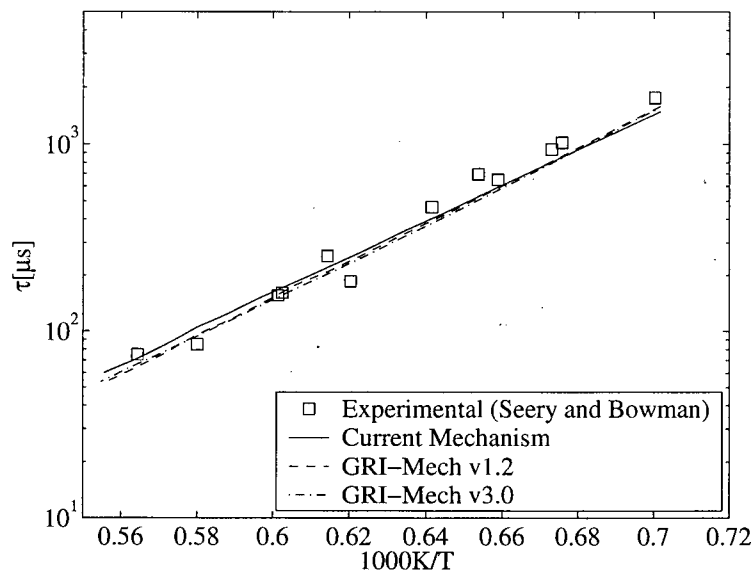
(a) Low-pressure CH_4 Ignition Delay
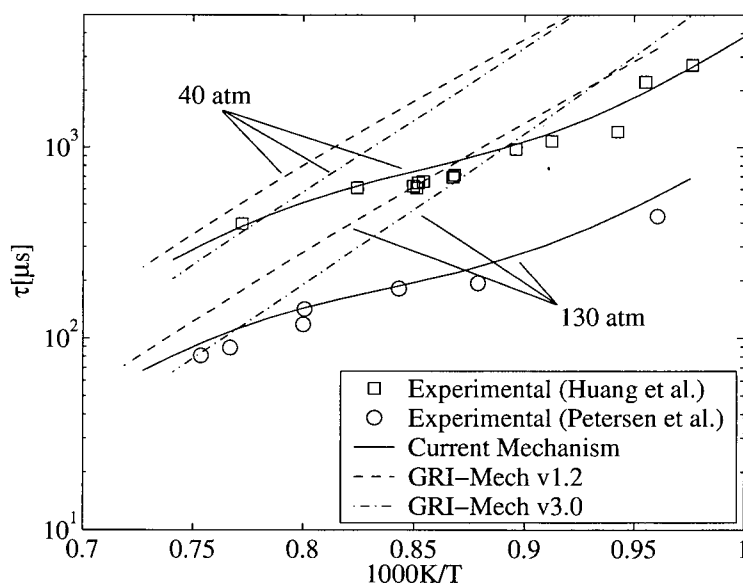
(b) High-pressure CH_4 Ignition Delay

Figure 4.2: Predicted methane ignition delay using the new mechanism. In plot a, the experimental data were taken from Seery and Bowman [9] for a $CH_4 - O_2 - Ar$ (9.1%-18.2%-72.7%) mixture with a concentration of 14.6 mol/m3 (1.8-2.1 atm). In plot b, the experimental data were taken from Huang et al. [28] for a CH_4-air mixture at 40 atm ($\phi = 1$) and Petersen et al. [29] for a $CH_4 - O_2 - Ar$ mixture at 130 atm ($\phi = 6$)

Table 4.3: Experimental conditions and ignition delay
results for methane/hydrogen mixtures

$\mathrm{mol_{H_2}/mol_{fuel}}$	T (K)	P (bar)	$\tau(\mu s)$	$\mathrm{mol_{H_2}/mol_{fuel}}$	T (K)	P (bar)	$\tau(\mu s)$
0.15	1297	36.4	332	0.15	1307	17.0	462
0.15	1259	40.2	405	0.15	1284	17.2	552
0.15	1212	40.3	588	0.15	1239	16.0	738
0.15	1183	42.7	672	0.15	1213	16.4	840
0.15	1116	39.2	752	0.15	1178	17.2	1170
0.15	1083	39.4	1164	0.15	1155	14.8	1014
0.15	1056	33.4	1356	0.15	1146	17.5	1152
0.15	1028	37.5	1614	0.15	1096	18.8	1676
0.35	1318	37.4	158	0.35	1318	17.0	260
0.35	1276	39.8	264	0.35	1276	15.9	372
0.35	1235	40.2	390	0.35	1201	16.9	876
0.35	1201	41.1	726	0.35	1134	15.6	1098
0.35	1156	41.1	759	0.35	1134	15.9	864
0.35	1103	37.6	1056	0.35	1103	15.9	1044
0.35	1072	36.0	882	0.35	1079	16.6	1736
0.35	1045	36.6	1500	0.35	1051	16.8	2189
0.35	1043	38.3	1986	0.35	1036	16.2	2016
0.35	1035	39.2	2166	0.35	1032	16.8	1822
				0.35	1019	16.0	3250

For the mixture with a high hydrogen fraction (mixture #2), the promoting effect of hydrogen addition is more evident at high temperatures; however, a rapid reduction in the difference between pure-methane and methane/hydrogen mixtures is observed as the temperature decreases. Specifically, at 1300K and 40 bar, the hydrogen addition in mixture #2 reduces the ignition delay time of pure methane by a factor of 1.5, but the difference is hardly distinguishable for temperatures below 1200K. A similar trend is observed at 16 bar but the overall difference between the two mixtures is more evident. For a low hydrogen fraction (in mixture #1), the effect of hydrogen appears to be largely
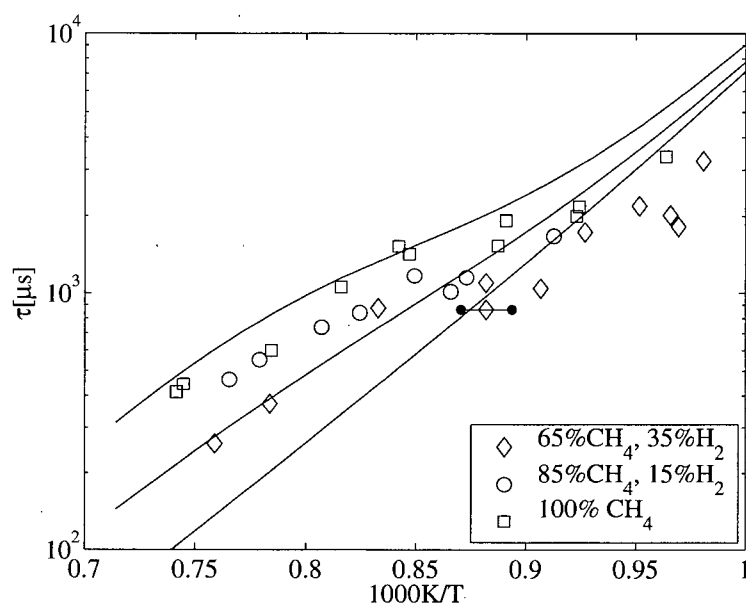
(a) 16 bar
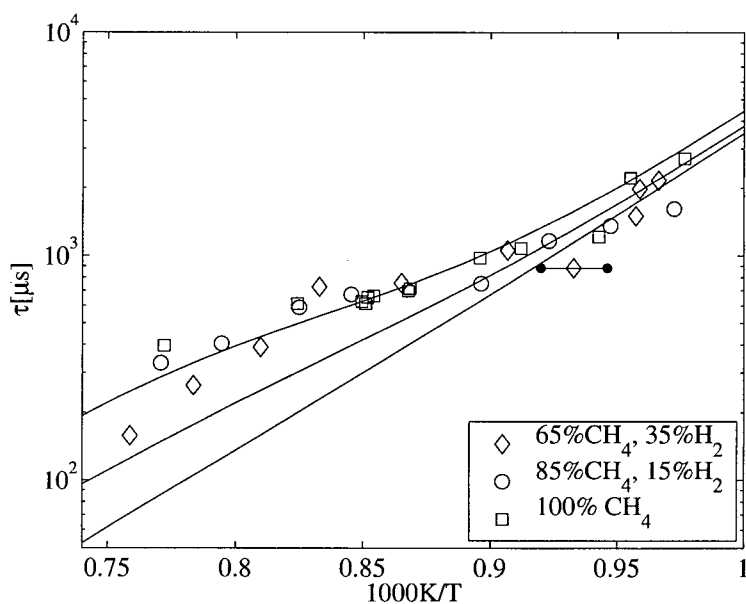
(b) 40 bar

Figure 4.3: Measured and calculated ignition delay of test mixtures. Symbols designate experimental results: □ - Pure methane (Φ=1); o - Mixture #1 ($85\%CH_4, 15\%H_2$); ◊ - Mixture #2 ($65\%CH_4, 35\%H_2$). Lines represent calculated ignition delay from the new model. A horizontal error bar represents the typical uncertainty in the experimental temperature.

inhibited. The reduction in ignition delay time with hydrogen in mixture #1 is small at 16 bar and can be barely seen at 40 bar.

The agreement between the numerical results and experimental data is less than ideal; the new mechanism under-predicts the ignition delay of methane/hydrogen mixtures at relatively high temperatures, which highlights the need to further refine the elementary reaction rates. Despite the discrepancy, the new model shows a reduction in the promoting effect with decreasing temperature, which is in agreement with the experimental observation described above. The model also predicted the slightly stronger effect of hydrogen addition at 16 bar compared to that at 40 bar.

An empirical correlation with the form

$$\tau = A[CH_4]^a[O_2]^b[H_2]^c exp(E/RT) \tag{4.2}$$

was fit to the experimental results of this work (see Fig.4.4). Table 4.4 lists the coefficients in Eq. 4.2 obtained by a linear regression method.

Table 4.4: Correlation coefficients for Eq. 4.2

$A(s.(cc/mol)^{a+b+c})$	a	b	c	E(kcal/mol)
2.10E-8	2.31	-2.83	-0.0055	19.06

The activation energy E of the current correlation is 19.06 kcal/mol, which is consistent with value of 19.0 kcal/mol reported by Petersen et al. [29] for pure methane ignition under similar temperature conditions. The overall effect of hydrogen on methane ignition observed in this work is weak as indicated by a small, negative value of the coefficient c in the above correlation (note that $c < a$).
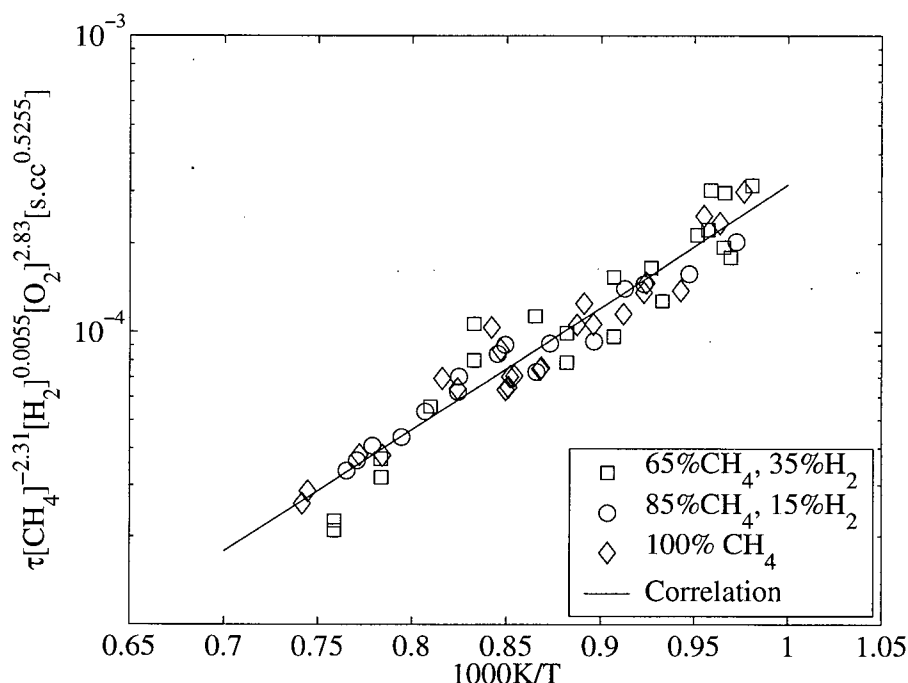
Figure 4.4: Comparison of measured ignition delay with formula 4.2

Fotache et al. [53] attribute the significantly stronger effect of hydrogen on methane/air ignition in a diffusive system to the separation of hydrogen from other species due to its high diffusivity. In a homogeneous system, the scavenging effect of methane on hydrogen radicals can be much stronger, leading to the lesser effect of hydrogen addition on the reaction system. For a methane/air mixture with a high hydrogen mole fraction, Fotache et al. [53] report that the ignition is effected through radical rather than thermal explosion. To confirm this point, we removed reaction heat of all elementary reactions from the energy equation. The results show an increase of ignition delay for both methane and methane/hydrogen mixtures; however, the relative difference between mixtures does not change significantly. This suggests that the thermal feedback in the current mixtures, being important to the overall reaction rate, has similar contributions to the oxidation of methane

and hydrogen. In other words, the global activation energy of pure methane and methane/hydrogen systems may be similar under the current conditions. The promoting effect from hydrogen appears to be mainly kinetic based.

A "brute force" sensitivity analysis was conducted to investigate the significance of elementary reactions to the overall reaction rate. The normalized sensitivity is calculated using the formula

$$S_{k_i} \approx \frac{\tau(2k_i) - \tau(0.5k_i)}{2k_i - 0.5k_i}\frac{k_i}{\tau(k_i)} = \frac{\tau(2k_i) - \tau(0.5k_i)}{1.5\tau(k_i)} \qquad (4.3)$$

The results are presented in Fig. 4.5 for pure methane and $65\%CH_4 - 35\%H_2$ mixtures respectively.

Comparing the results between the two mixtures, one immediately observe that the sensitivities to reactions

$$2CH_3(+M) \rightleftharpoons C_2H_6(+M) \qquad (R159)$$

and

$$HO_2 + CH_3 \rightleftharpoons OH + CH_3O \qquad (R120)$$
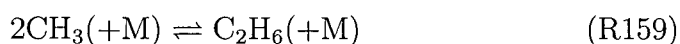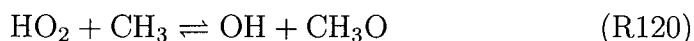
are reduced significantly with the presence of hydrogen at 1300K, while, the sensitivities to reactions

$$OH + H_2 \rightleftharpoons H + H_2O \qquad (R85)$$

and

$$H + O_2 \rightleftharpoons O + OH \qquad (R39)$$

increase drastically. The recombination of two methyl radicals in R159 is a well-known chain termination reaction at high temperatures. Reaction R120 is a main competitor of R159 for methyl radicals; it also generates an active hydroxyl radical which is a crucial species in the
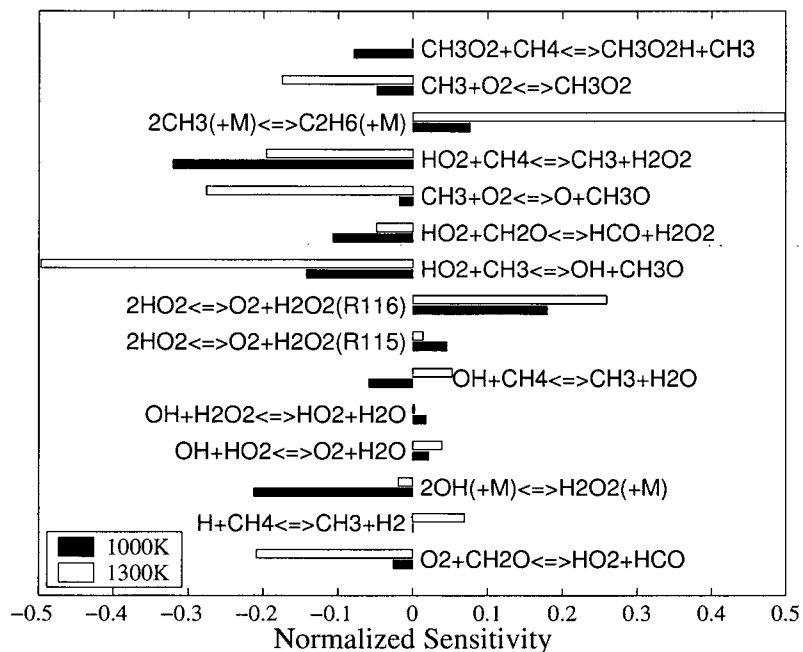
(a) 100%CH$_4$
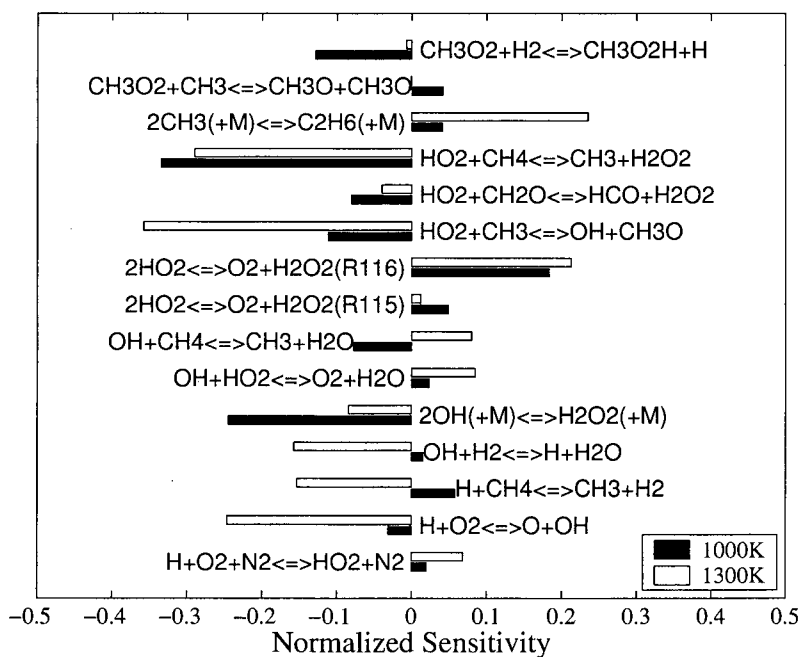
(b) 65%CH$_4$, 35%H$_2$

Figure 4.5: Normalized sensitivity of ignition delay with respect to individual reaction rate for methane and methane/hydrogen mixtures at 40 bar.

main oxidation path of methane. With the presence of hydrogen, the production rate of hydrogen radical through

$$OH + H_2 \rightleftharpoons H + H_2O \tag{R85}$$

increases. Hydrogen radicals are more active than OH radicals, they branch through

$$H + O_2 \rightleftharpoons O + OH, \tag{R39}$$

which rapidly increases radical concentrations and hence promotes the ignition.

At 1000K, the rate limiting mechanism changes. As shown in our previous study [28], with the reduction of temperature, the total reaction rate is increasingly limited by the depletion of hydroxyl. This trend is demonstrated by the increased sensitivity to a main OH generating path through

$$HO_2 + CH_4 \rightleftharpoons CH_3 + H_2O_2 \tag{R158}$$

and

$$2OH + (M) \rightleftharpoons H_2O_2(+M). \tag{R86}$$
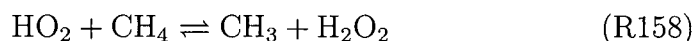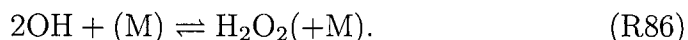
At 1000K, the rate of H radical production through R85 is low, as is the branching efficiency of R39, which leads to a reduced effect of hydrogen on methane ignition. However, the sensitivity to the reaction rate of

$$CH_3O_2 + H_2 \rightleftharpoons CH_3O_2H + H \tag{R195}$$
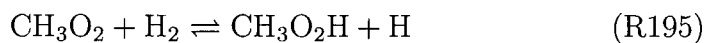
is higher at 1000K due to the increased concentration of CH_3O_2. Reaction R195 produces an H radical directly; also the subsequent decomposition of methylhydroperoxide (CH_3O_2H) species generates an OH radical which is key to intermediate-temperature methane ignition. The rate of R195 is higher than the rate of

$$CH_3O_2 + CH_4 \rightleftharpoons CH_3O_2H + CH_3 \tag{R188}$$
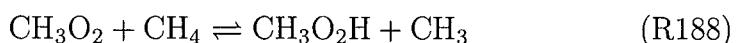
so that the overall production rate of CH_3O_2H is higher with hydrogen replacing some of methane. Compared with the branching-dominated promoting mechanism at higher temperature, the low-temperature promoting mechanism is much weaker. This accounts for the reduced difference between pure methane and hydrogen-enriched mixtures at low temperatures.

It is interesting to note the sign change of sensitivity to reaction

$$H + CH_4 \rightleftharpoons CH_3 + H_2 \qquad (R54)$$
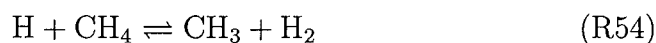
in the two different mixtures. Reaction R54 is usually considered a major H-scavenging step in methane/hydrogen systems [51,53]. However, in this work, R54 shows a promoting effect on ignition at 1300K when a high fraction of hydrogen presents. This is because the high H_2 concentration in the system changes the equilibrium of R54 and leads to a reverse of it primary direction. This reaction is beneficial for increasing the overall reaction rate in two ways. First, it produces an active H radical that leads to chain branching; second, it reduces the termination efficiency of R159 (combination of two methyl) by competing for CH_3 radicals. It should be noted that the shift in direction of R54 can only occur when the concentration of hydrogen molecule is sufficiently high. This appears to be consistent with the much weaker effect when a smaller fraction of hydrogen is present.

By comparing the sensitivity analyses between pure methane and methane/hydrogen mixtures, one can identify several reactions whose uncertainties in their rate coefficients could be responsible for the discrepancy between the new model and experimental results. We shift our attention away from those reactions with rates to which pure methane or pure hydrogen ignition (for which the delay time is relatively

well predicted) are sensitive and focus instead on the rates that to which only the ignition in methane/hydrogen mixtures is sensitive. The new numerical model over-predicts the reduction of ignition delay in methane/hydrogen mixtures at high temperature. It is clear that at 1300K, the ignition delay with hydrogen addition is sensitive to the rate of R54 ($CH_4 + H \rightleftharpoons CH_3 + H_2$), but the ignition of pure methane is less sensitive to this reaction. Since the reaction involves both methane and hydrogen, it cannot affect the pure-hydrogen submechanism either. A review of the literature related to the rate of this reaction shows that the data (experimental or theoretical) reported by different authors vary by a factor of 3, which could account for a change of 20% to 30% in the calculated delay time. At lower temperatures, the uncertainty in the rate of R195 ($CH_3O_2 + H_2 \rightleftharpoons CH_3O_2H + H$) could be responsible for the under-predicted effect of hydrogen. There are no experimental measurements of the rate of this reaction in the temperature range of this study, and the data reported in the literature shows an uncertainty of a factor of ten.

The sensitivity analysis reveals that the effect of hydrogen on methane ignition is closely tied to the production and consumption of hydrogen radicals. In Fig. 4.6, the concentrations of hydrogen radicals during the induction period in two different mixtures are presented at 1000K and 1300K respectively. It can be seen that, for both temperatures, the concentration of H radicals increases significantly with hydrogen replacing some methane in the fuel; as expected, the difference is more prominent at higher temperatures, where a stronger promoting effect is observed. Further insight into the function of hydrogen can be obtained by tracking the contribution of elementary reactions to the generation and consumption of hydrogen radicals during the induc-
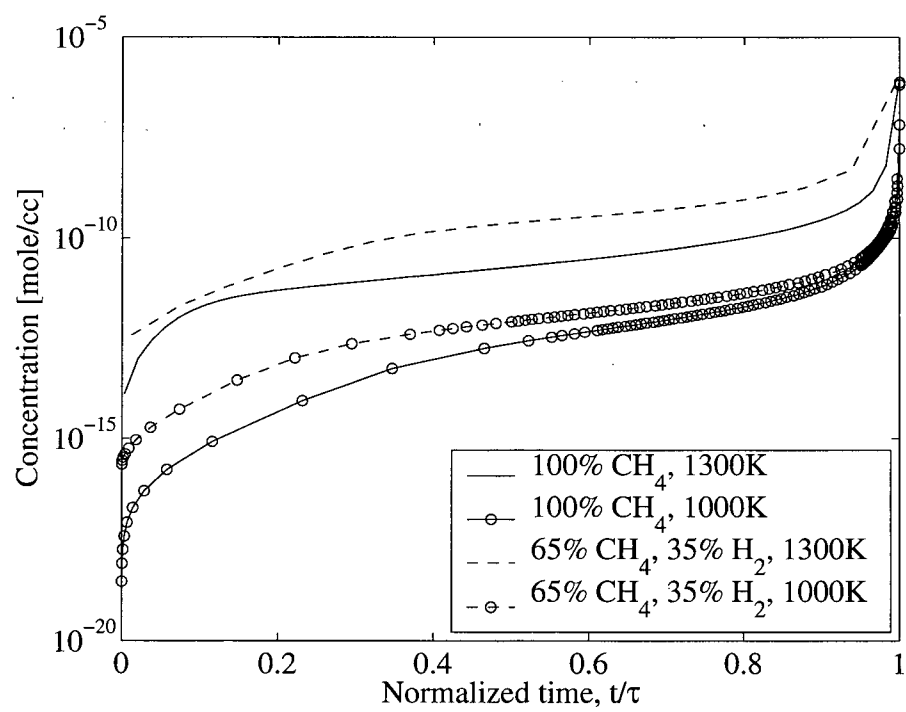
Figure 4.6: H concentration during the induction period in different mixtures
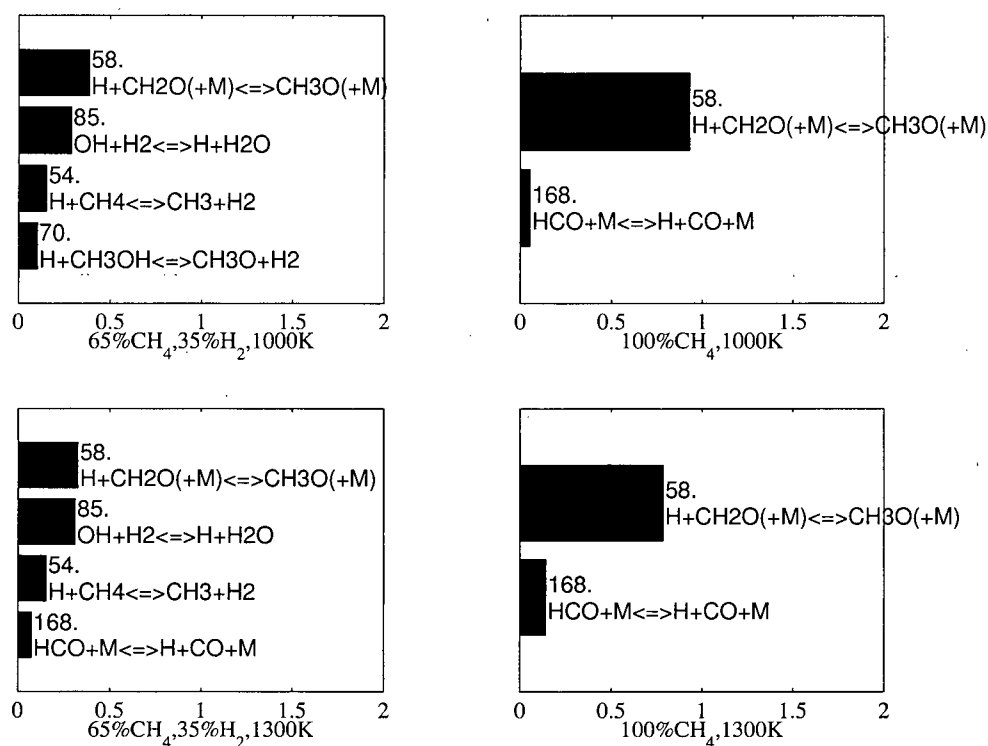
Figure 4.7: Integrated contribution of major H-generation reactions for methane and methane/hydrogen mixture at 1000K and 1300K respectively. The analysis was performed at P=40 bar.

tion period.

As shown in Figs.4.7 and 4.8, for the temperatures investigated, the third-order reactions

$$H + O_2 + M \rightleftharpoons HO_2 + M$$
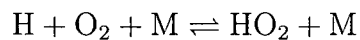
(R33–R38) are mainly responsible for the consumption of H radicals. But in the methane/hydrogen mixture at 1300K, a relatively higher fraction of hydrogen radicals is consumed in the branching reaction

$$H + O_2 \rightleftharpoons O + OH, \tag{R39}$$

which indicates that this is the main promoting mechanism. It is also noticeable that, in agreement with the sensitivity analysis, R54 (hydr-
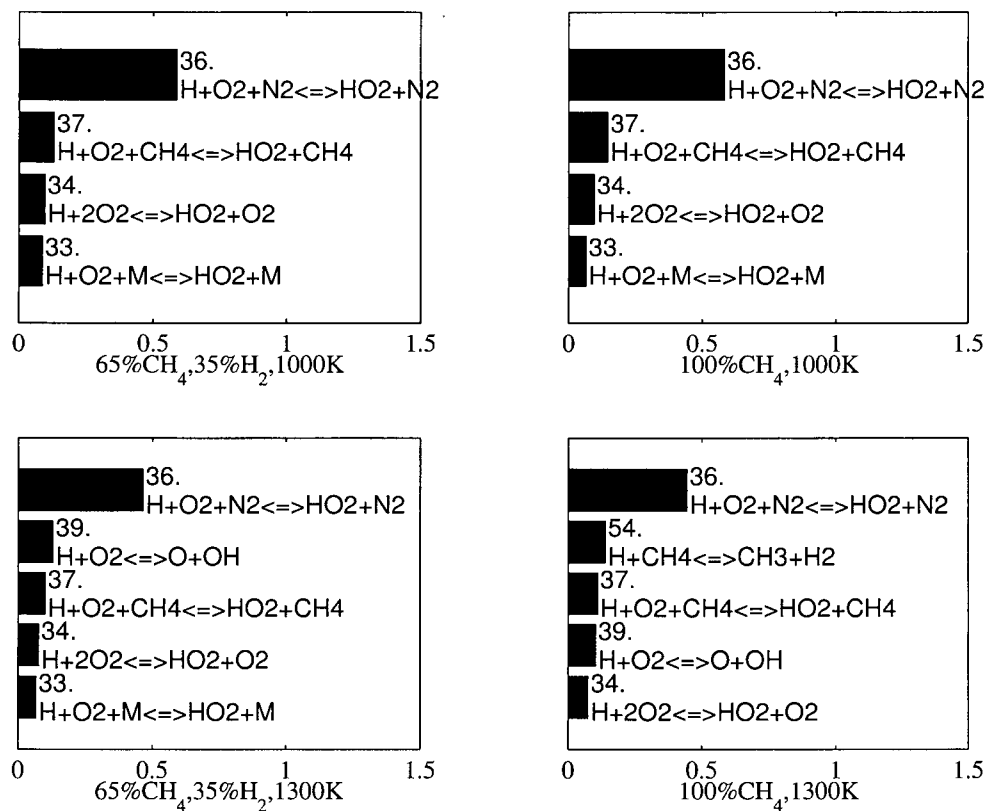
Figure 4.8: Integrated contribution of major H-consumption reactions for methane and methane/hydrogen mixture at 1000K and 1300K respectively. The analysis was performed at P=40 bar.
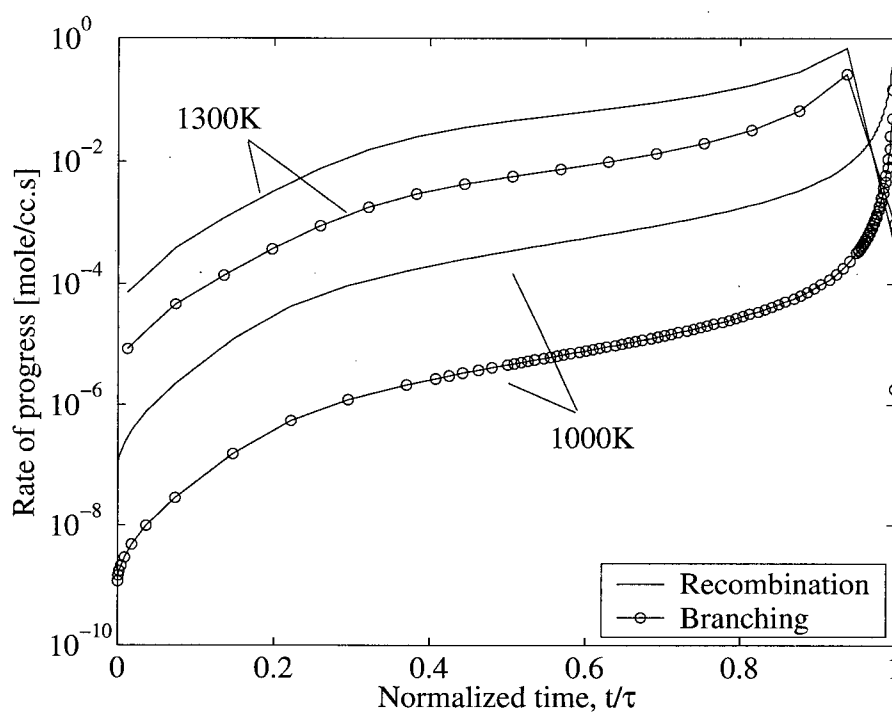
Figure 4.9: Comparison of rates of progress of recombination reactions (sum of R33–R38) and the chain branching reaction (R39) in the $0.35H_2/0.65CH_4$ mixture at 40 bar during the induction period.

ogen reacting with methane) is a secondary reaction for the consumption of hydrogen radicals in pure methane mixtures at 1300K, but appears as a major H generating reaction with the presence of a large initial H_2 concentration. Figures 4.7 and 4.8 suggest that the competition between chain termination (R33–R38) and chain branching (R39) reactions is key to the effect of hydrogen in methane ignition. As shown in Fig.4.9, at 1000K, the recombination reactions dominate. As a result, branching through R39 is largely suppressed. At 1300K, the difference between the rate of chain branching and that of recombination decreases significantly, which leads to a stronger promoting effect.

Figure 4.10 presents the main oxidation path during the induction period for the hydrogen/methane mixture based on integral reaction

flow analyses [62]. It shows that the oxidation of hydrogen is mainly through the path

$$H_2 \rightarrow H \rightarrow HO_2 \rightarrow H_2O_2 \rightarrow OH \rightarrow H_2O.$$
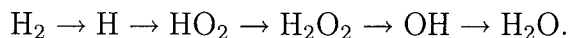
Two of the most important intermediate species for methane oxidation – OH and HO_2 – are among the main intermediates in the reaction pathway of hydrogen; however, the presence of hydrogen addition in the system does not change the fundamental reaction path of methane discussed in previous work [28,29], except for an additional CH_3O oxidation channel through reaction

$$H + CH_3OH \rightleftharpoons CH_3O + H_2. \tag{R66}$$

This new branch,

$$CH_3O \rightarrow CH_3OH \rightarrow CH_2OH \rightarrow CH_2O,$$
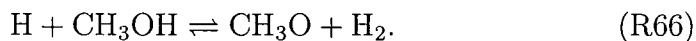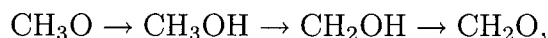
is in parallel with the main oxidation path through

$$H + CH_2O(+M) \rightleftharpoons CH_3O(+M) \tag{R58}$$

and

$$CH_3O + O_2 \rightleftharpoons HO_2 + CH_2O. \tag{R171}$$
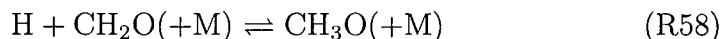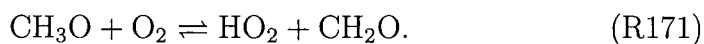
The significance of this extra path to the overall reaction rate is only secondary, because the oxidation of CH_3O is not a main rate-limiting step for methane ignition [28].

Since the third order reactions R33–R38 are more sensitive to the change of concentration than the second-order reaction R39, it is reasonable to believe that to reduce the pressure in the reaction system should favor the chain branching and thus more rapid ignition. This is consistent with the experimental observation. A slightly stronger promoting effect was observed at 16 bar compared with that at 40 bar. To
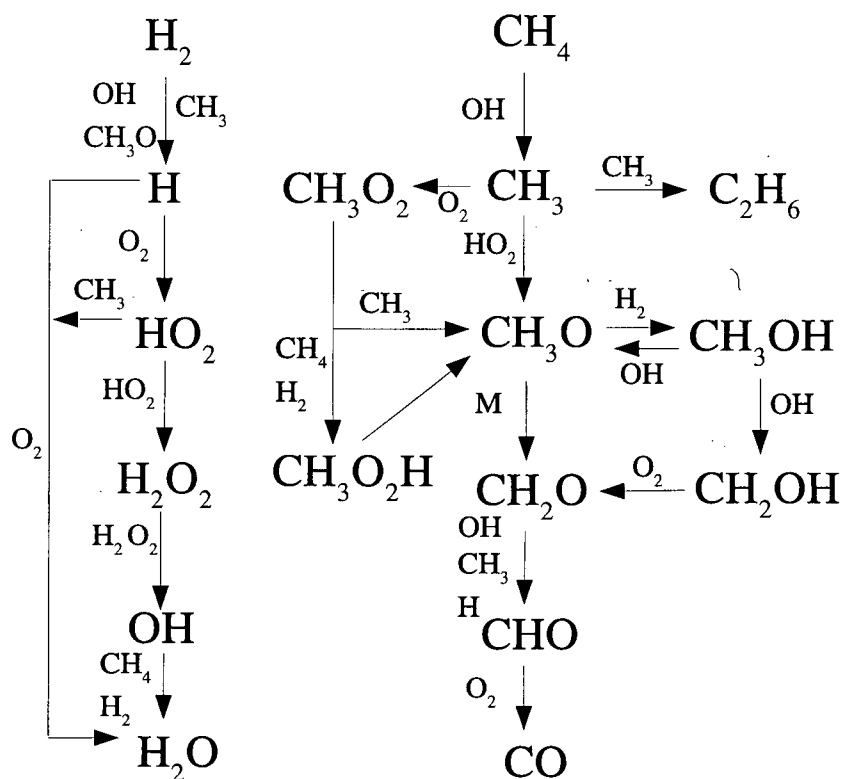
Figure 4.10: Integral reaction flow analysis showing main reaction pathway for mixture #2 at 1300k and 40 bar. Smaller-font letters designate main intermediate species participating the reaction steps.
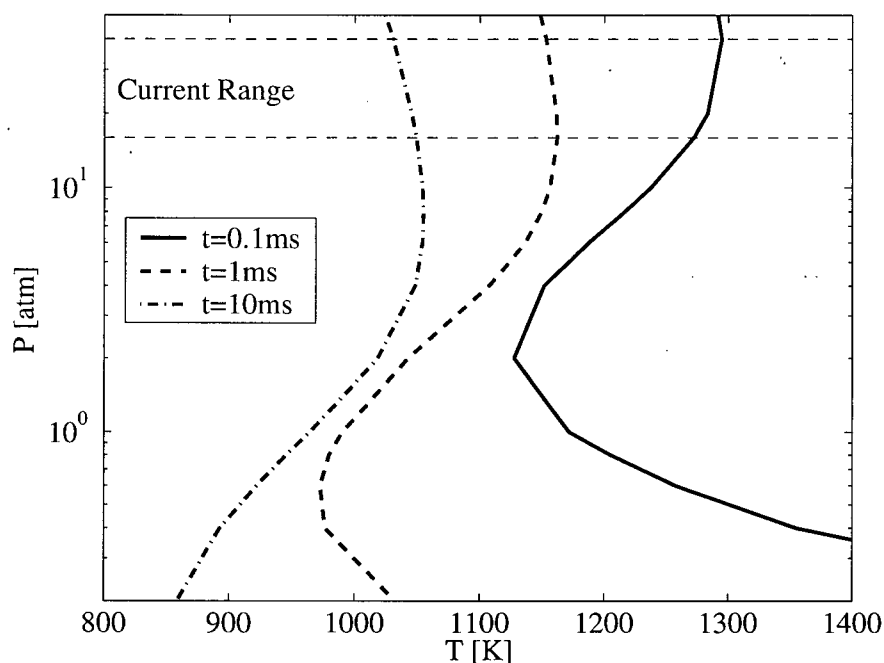
Figure 4.11: Calculated ignition limit of hydrogen for a given ignition delay in this work. The thin dash lines indicate the pressure range studied in this work.

clearly illustrate the pressure dependence of hydrogen, a traditional "ignition limit" calculation has been performed for mixture #2 with methane treated as an inert gas (rates of reactions related to methane were set to zero). Figure 4.11 shows the pressure and temperature conditions required by the hydrogen-only systems to obtain ignition at a given delay time. The well-defined reversed S curves are observed, which show the (three) classical ignition limits of hydrogen. Figure4.11 shows that, over the experimental range of this work, particularly for ignitions with a delay time below one millisecond, we are primarily at the second ignition limit where the ignition temperature shows a negative pressure dependence. Namely, the third-order recombination reactions (R33–R38) are the rate-limiting steps in this region. This leads to a more discernible difference in ignition delay between the pure me-

thane and methane/hydrogen mixtures at the lower pressure.

4.5 Conclusions

Shock tube experiments on the ignition of two stoichiometric methane hydrogen air mixtures under high pressure and moderate temperature conditions have been conducted. It has been observed that the promoting effect of hydrogen decreases with decreasing temperature. The difference between pure methane and methane/hydrogen mixtures is more prominent at 16 bar than that at 40 bar. A low fraction of hydrogen addition shows only weak effects on the ignition delay of methane under the conditions explored.

A numerical study of methane/hydrogen/air ignition under the experimental conditions has been conducted using a detailed chemical kinetic mechanism. The mechanism was modified to obtain an improved agreement between the model and experimental results. The effect of hydrogen on methane ignition was primarily related to the generation and consumption of H radicals. At high temperatures, the rapid oxidation of hydrogen molecules through R85 ($OH + H_2 \rightleftharpoons O + H_2O$) and the fast branching reaction R39 ($H + O_2 \rightleftharpoons O + OH$) are mainly responsible for the stronger ignition promoting effect. The rates of both R85 and R39 decrease rapidly with decreasing temperature. At lower temperatures, reactions between H_2 and CH_3O_2 account for a weak effect of hydrogen on methane ignition due to the production of extra H radicals. The effect of hydrogen in the current system exhibits a negative pressure dependence, which implies that the third-order recombination reactions (R33-R38) are rate-limiting steps under the conditions of this work.

Further experimental and kinetic studies are necessary to improve

our understanding of the ignition characteristics of methane/hydrogen mixtures under high-pressures and intermediate-temperatures. This should include studies on key elementary reactions such as R54 and R195 as well as ignition studies at other equivalence ratios and with a wider range of hydrogen concentrations.

Chapter 5

Evaluation of Detailed Nitrogen Oxides Mechanisms in Methane Flames[12]

5.1 Introduction

Computational studies of the formation of oxides of nitrogen (NOx) in natural gas fueled internal combustion engines using detailed kinetic mechanisms have been reported recently in the literature [162–164]. The agreement between the numerical results and experimental data is sometimes compromised by the under-performance of the underlying detailed kinetic mechanism for combustion, which has often not been sufficiently validated under engine-relevant conditions [162]. Although the results under certain operating conditions can possibly be improved by empirically adjusting the key reaction rate constants, this approach is clearly questionable given the lack of justification on scientific grounds, and could lead to reduced credibility of the detailed mechanism.

In our earlier work, we have developed a detailed reaction mechanism for the ignition of methane including minor higher hydrocarbons

---

[12]A version of this chapter has been submitted for publication. Huang, J. and Bushe, W. K. Evaluation of detailed nitrogen oxides mechanisms in methane/air flames, Submitted to Combust. Flame

(C2 and C3). The mechanism has been validated against the shock tube ignition data for methane and various synthetic natural gas fuels over a wide range of pressure and temperature conditions [28, 165], particularly under conditions relevant to practical combustion devices. Unfortunately, the earlier versions of the mechanism do not contain sub-models for NOx, which are considered important pollutants from combustion processes; given that, in most practical applications, natural gas is burned in air, it is important to include a sub-model for NOx.

The objective of the work described in this chapter is to find an appropriate sub-model for NOx to supplement our existing mechanism, which would make the resulting mechanism capable of predicting ignition, combustion and pollutant formation for all major gas-phase species considered to be pollutants under engine-relevant conditions. In the work described in this paper, we evaluate detailed NOx mechanisms from the literature used in conjunction with our natural gas reaction mechanism in predicting experimental data for NOx formation in methane/air combustion systems.

5.2 Experimental Data

Two sets of experimental data on NOx formation have been selected in this study: the measurement of NOx and N_2O profiles in a stirred reactor by Steele et al. [66] and the measurement of the NO profile in a methane/air two-stage counterflow flame by Li and Williams [36]. Three reasons are behind the selection of the above two data sets:

1. They represent typical premixed and non-premixed reaction systems.

2. The premixed experiment [66] focused on fuel-lean conditions

($\phi = 0.41 - -0.67$) with relatively low temperature ($T = 1415 - -1845K$), conditions which are closely related to those found in HCCI engines. The counter-flow diffusion flame experiment [36] is more relevant to combustion in direct-injection natural gas engines.

3. The NOx control techniques studied in both experiments – lean combustion, staged flame and H_2O/CO_2 addition – are among the most important and widely used in practical combustion devices.

5.3 NOx Mechanisms

A set of five NOx mechanisms chosen from the literature has been tested in this work. Information regarding these mechanism is provided in Table 5.1

Table 5.1: Selected NOx mechanisms from the literature

Source	Nitro Componds	NOx Related Reactions
Glarborg1 [74]	17	78
Glarborg2 [84]	24	207
Li and Williams [36]	16	52
GRI-Mech 2.11 [40]	17	102
GRI-Mech 3.0 [41]	19	105

It should be emphasized that the above mechanisms are subsets of the detailed hydrocarbon reaction mechanisms from which they were taken. The intent of this work is to examine their performance when used in conjunction with our mechanism for natural gas combustion,

not to judge the accuracy of the individual NOx mechanisms, which cannot be justified without referring to their parent mechanisms.

5.4 Results and Discussion

A perfectly stirred reactor (PSR) model was used to simulate the experiment of Steele et al. [66]. The experimentally measured reactor temperature was used as an input to the PSR model. Figures 5.1 and 5.2 show the comparison between the experimental data and model results using the detailed chemistry with the different NOx mechanisms introduced above. The mass fraction of NOx is the sum of the mass fraction of NO and that of NO_2. It can be seen that the model results using the Glarborg2 mechanism show the best agreement with the experimental data for both NOx and N_2O mass fractions. The Li and Williams mechanism and GRI-Mech 2.11 give reasonable prediction for NOx but underpredict the mass fraction of N_2O, while the predictions from the Glarborg1 mechanism and GRI-Mech 3.0 deviate significantly from the experimental results for both NOx and N_2O.

The counter flow diffusion flame was modeled using FlameMaster [166], which solves the transformed conservation equations of a two-dimensional potential flow in similarity coordinates. The fuel and oxidizer inlet temperatures are constant at 300K. The fuel stream contains methane/air mixtures at different equivalence ratios. Figures 5.3 and 5.4 present the numerical results incorporating different NOx sub-mechanisms compared with the experimental data.

The predicted temperature profiles agree fairly well with the experimental measurements. The fact that all the temperature profiles calculated with the different NOx sub-mechanisms collapse into one line shows that the NOx reactions have little influence on the original
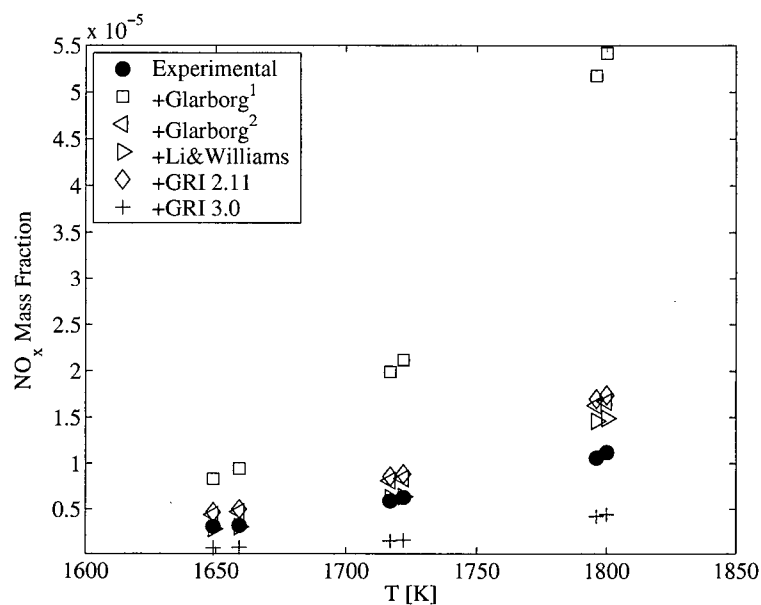
(a) $\bar{\tau} = 3.42$ms
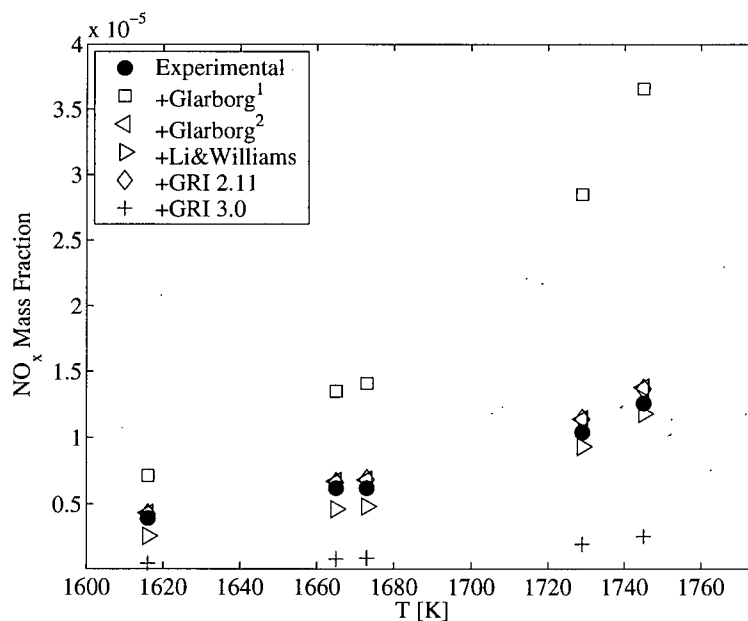
(b) $\bar{\tau} = 6.49$ms

Figure 5.1: NOx prediction in simulated PSR in comparison with experimental data [66]. In subplot (a), the average residence time is 3.42 ms; in subplot (b), the average residence time is 6.49 ms. $\Phi \approx 0.517 - 0.673$.
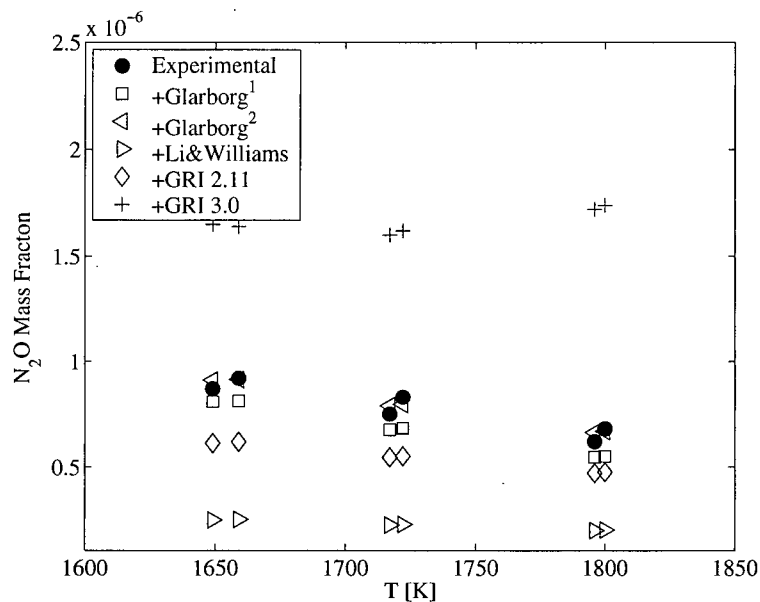
(a) $\bar{\tau} = 3.42$ms
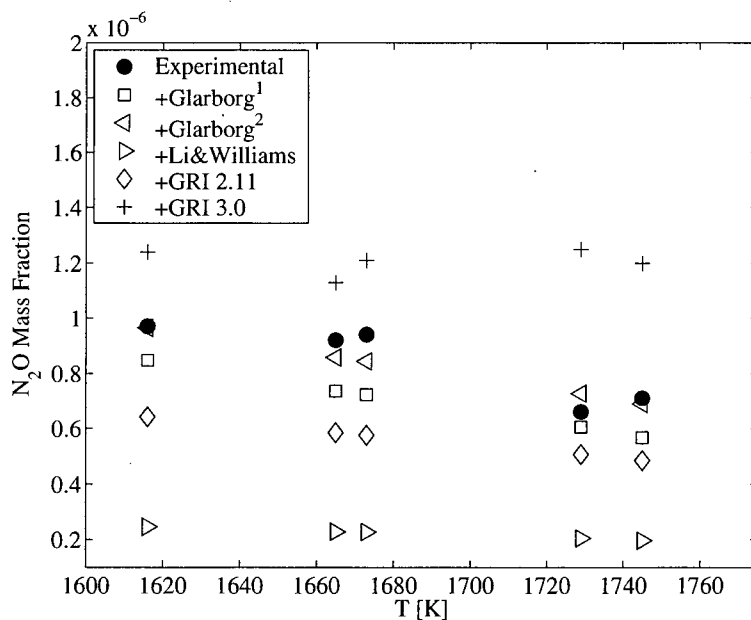
(b) $\bar{\tau} = 6.49$ms

Figure 5.2: N_2O prediction in simulated PSR in comparison with experimental data [66]. In subplot (a), the average residence time is 3.42 ms; in subplot (b), the average residence time is 6.49 ms. $\Phi \approx 0.517 - 0.673$.

(a) NO
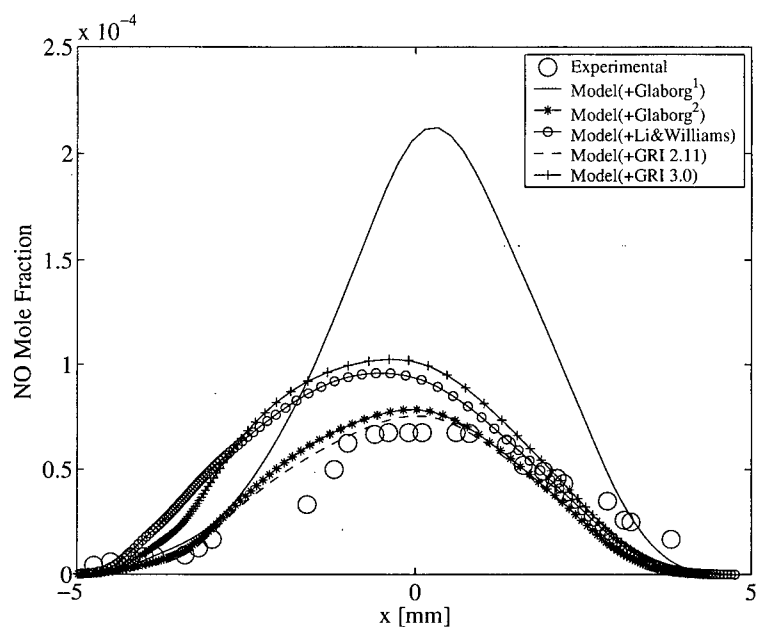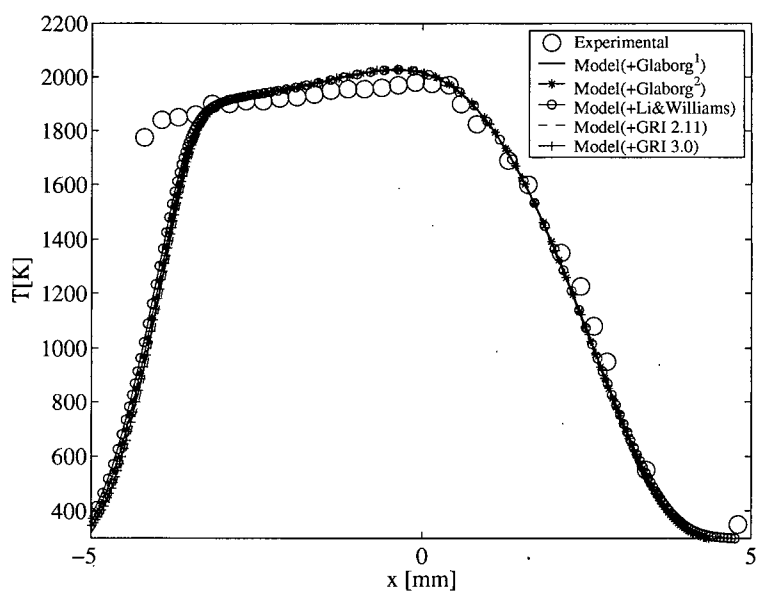
(b) Temperature

Figure 5.3: NO prediction in a laminar counterflow diffusion flame in comparison with experimental data [36]. In subplot (a), the predicted NO profile; in subplot (b), the predicted temperature profile. The equivalence ratio in the fuel stream is 1.5.

(a) NO
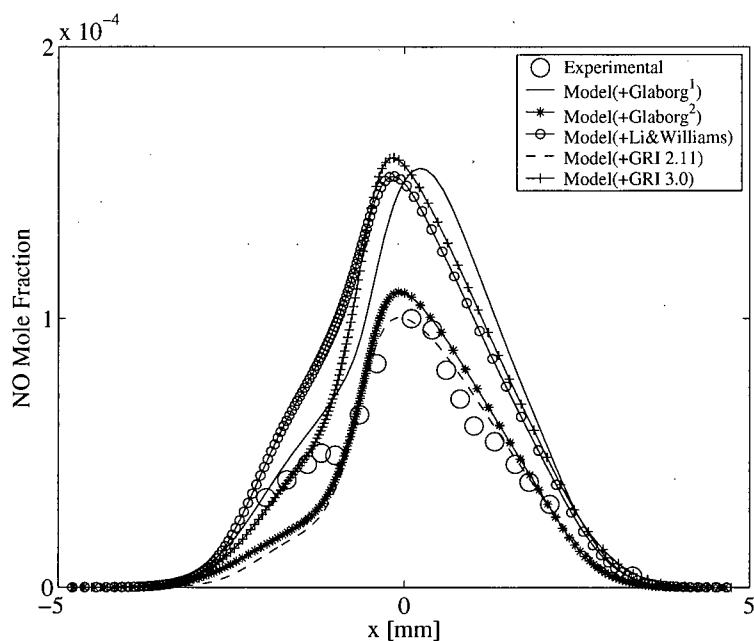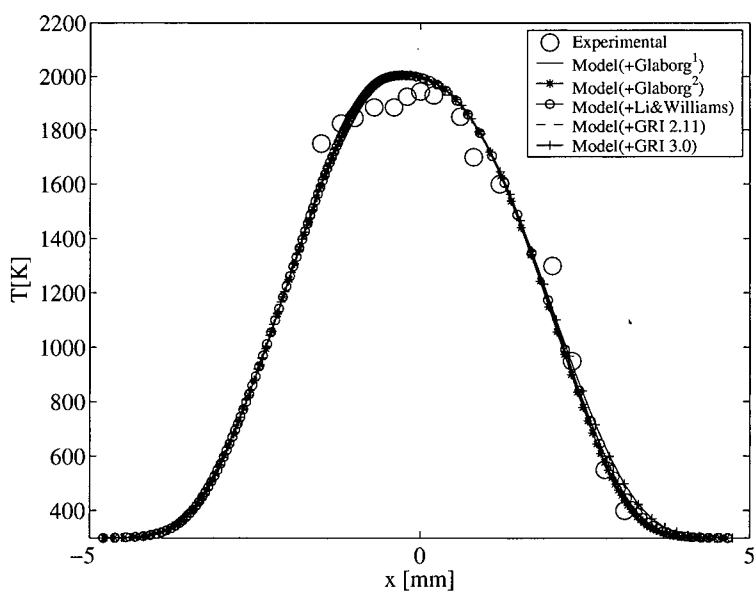
(b) Temperature

Figure 5.4: NO prediction in a laminar counterflow diffusion flame in comparison with experimental data [36]. In subplot (a), the predicted NO profile; in subplot (b), the predicted temperature profile. The equivalence ratio in the fuel stream is 2.5.

methane/air reaction system. As for the predicted NO profile, the results from GRI-Mech 2.11 and Glagborg[2] show the best agreement with the experimental data. The other three mechansms tend to overpredict the NO mole fraction in the flame.

Since the main reactions in the thermal and prompt NOx routes have been well established in the past decades [63,72], it is intuitive to examine the rates of these reactions for the possible cause of the different performance among the tested NOx mechanisms. In Table 5.2, a comparison is made for the forward reaction rates of several key NOx formation steps at 1600 and 2000K respectively. An immediate observation is that the rates of key reactions from the two Glarborg mechanisms are very similar; the only significant difference is that the main NO reburn reaction [84]

$$NO + CH_3 \rightleftharpoons HCN + H_2O \qquad (R_{R1})$$
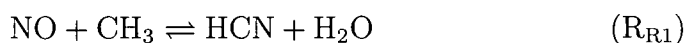
in methane/air flames is not involved in the Glarborg1 mechanism. Under the experimental conditions of Steele et al. [66], a high concentration of methyl radicals exists in the reactor, thus the absencence of key reburn reactions could lead to a significant over-prediction of NO concentration. In the counterflow diffusion flame, the peak flame temperature is around 2000K. The reaction rate of the key prompt NO formation step

$$CH + N_2 \rightleftharpoons HCN + N, \qquad (R_{T1})$$
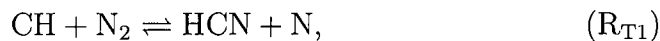
calculated from Li and Williams mechanism and GRI-Mech 3.0 is significantly higher than the rates from Glarborg2 mechanism and GRI-Mech 2.11, which could contribute to the over-prediction of NO mole fraction by the former mechanisms.

Table 5.2: Comparison of key reaction rates at 1600 and 2000K

T[K]	Reaction[13]	Glagborg1	Glarborg2	Li&Williams	GRI 2.11	GRI 3.0
1600	R_{T1}	3.02E+14	3.02E+14	6.99E+03[14]	3.15E+13	2.41E+13
	R_{T2}	1.42E+12	1.42E+12	1.42E+12	3.54E+11	1.86E+12
	R_{T3}	3.80E+13	3.80E+13	3.80E+13	5.15E+13	2.98E+13
	R_{P1}	2.63E+09	1.93E+09	4.36E+09	1.57E+09	3.65E+09
	R_{P2}	8.40E+11	8.40E+11	1.09E+10	6.64E+11	1.22E+12
	R_{R1}	N/A	8.53E+09	5.27E+09	1.11E+10	1.11E+10
2000	R_{T1}	3.23E+14	3.23E+14	8.52E+05	3.22E+13	2.47E+13
	R_{T2}	2.63E+12	2.63E+12	2.63E+12	5.29E+11	3.50E+12
	R_{T3}	3.80E+13	3.80E+13	3.80E+13	5.53E+13	3.05E+13
	R_{P1}	6.19E+09	9.78E+09	1.74E+10	7.23E+09	1.58E+10
	R_{P2}	2.07E+12	2.07E+12	2.57E+10	1.64E+12	3.00E+12
	R_{R1}	N/A	2.40E+10	1.45E+10	6.82E+10	6.82E+10

---

[13]Reactions $R_{T1} - -R_{T3}$ designate thermal NOx route. R_{T1} $N + NO \rightleftharpoons O + N_2$, R_{T2} $O_2 + N \rightleftharpoons NO + O$, R_{T3} $N + OH \rightleftharpoons NO + H$. Reactions $R_{P1} - R_{P2}$ designate prompt NOx route. R_{P1} $CH + N_2 \rightleftharpoons HCN + N$, R_{P2} $HCN + O \rightleftharpoons HCO + H$. Reaction R_{R1} is a main reburn reaction $NO + CH_3 \rightleftharpoons HCN + H_2O$.

[14]Reverse reaction rate

5.5 Conclusions

NOx formation mechanisms selected from the literature in conjunction with a natural gas reaction mechanism from our previous work have been examined to predict experimental NOx data from a stirred reactor [66] and a counterflow diffusion flame [36]. The numerical results using the mechanism proposed by Glarborg et al. [84] and GRI-Mech 2.11 show the best agreement with the experimental data. The reburn of NO by methyl radicals is found to be important in reaction systems at relatively low temperatures such as those in this work. A consistent trend has been identified between higher predicted NO concentration and higher rate of a key reaction for prompt NO formation, which suggests that the prompt NO mechanism is important under the conditions of this study.

Chapter 6

Trajectory Generated Low Dimensional Manifold in CH_4 - Air Combustion Systems[15]

6.1 Introduction

Combustion simulations incorporating detailed chemical kinetic mechanisms are being increasingly used in studying reactive flow problems; however, for many practical combustion systems, the increase of CPU load as a result of using detailed chemistry could be prohibitively high. A detailed chemical kinetic mechanism for a combustion process typically involves tens or even hundreds of reactive scalars with hundreds or thousands of chemical reactions, each with their own different time scales, which give rise to stiffness in the governing ordinary differential equations (ODEs). To solve such a stiff system of ODEs is very time-consuming since the smallest time scale must be resolved for the numerical solution to be stable [57,62]. Therefore, there is clearly a need to reduce the dimensionality and the stiffness in the detailed chemistry to reduced the computatonal time for combustion simulations.

The intrinsically low-dimensional manifold (ILDM) method pro-

posed by Maas and Pope [90] reduces the detailed chemistry from an n-dimensional composition space $\Re^n$ to a n_s-dimensional ($n_s < n$) manifold governed by the slow processes based on the concept of local time-scale separation. Following Warnatz et al. [62], the governing ODEs of a conserved chemical reaction system (i.g. a constant-pressure, isoenthalpic reactor) can be written in general vector form

$$\frac{d\mathbf{Y}}{dt} = \mathbf{F}(\mathbf{Y}), \tag{6.1}$$

where $\mathbf{Y}$ denotes an n-element vector of species mass fractions. The local time scales of the reaction system can be obtained by performing a Schur decomposition of the Jacobian matrix as in

$$\mathbf{J} = \frac{dF_i}{dY_j} = \mathbf{V}\mathbf{\Lambda}\widetilde{\mathbf{V}}, \tag{6.2}$$

where $\mathbf{V}$ is the right Schur vector matrix of the Jacobian $\mathbf{J}$; $\mathbf{\Lambda}$ is an upper triangular matrix whose diagonal entries are the eigenvalues of $\mathbf{J}$, which represents the inverse of the characteristic time scales; $\widetilde{\mathbf{V}}$ denotes inverse matrix of $\mathbf{V}$. The eigenvalues and corresponding Schur vectors in $\mathbf{\Lambda}$, $\mathbf{V}$ and $\widetilde{\mathbf{V}}$ are sorted in descending order with the negative eigenvalues of greatest magnitude representing the fastest process at the bottom of $\mathbf{\Lambda}$. If there exists a distinct difference between time scales associated with the n_sth and $n_s + 1$th process, i.e. $\|\Lambda(n_s, n_s)\| << \|\Lambda(n_s + 1, n_s + 1)\|$, the fast processes corresponding to $n - n_s$ large negative eigenvalues quickly relax to quasi-steady state, leading to the convergence of the reaction system onto a n_s-dimensional manifold. Mathematically, the low-dimensional manifold is expressed as a n_s-dimensional subspace of $\Re^n$ which satisfies

$$\widetilde{\mathbf{V}}_f \mathbf{F}(\mathbf{Y}) = 0, \tag{6.3}$$

where $\widetilde{\mathbf{V}}_f$ is an $(n - n_s) \times n$ matrix taken from the last $n - n_s$ rows of $\widetilde{\mathbf{V}}$. The physical meaning of Eq. 6.3 is that the projection of the reaction vector along the slow manifold onto the fast subspace vanishes. Eq. 6.3 can be solved by adding n_s parametric equations representing system constrains (i.e. element mass conservation, energy conservation, etc.) and a small number of progress variables. The final form of the ILDM equations can be written as

$$G(\mathbf{Y}, \tau) = \begin{pmatrix} \widetilde{\mathbf{V}}_f \mathbf{F}(\mathbf{Y}) \\ \Psi(\mathbf{Y}, \tau) \end{pmatrix} = 0, \tag{6.4}$$

where Ψ denotes n_s parametric equations, and τ denotes the values of parameters. A particularly attractive feature of the ILDM is that the species mass fractions and the reaction rates on the low-dimensional manifold can be tabulated prior to the reactive flow calculation; they can be quickly retrieved from the table based on the values of progress variables from the flow calculation to provide closure for the chemical source term. In this way, an orders-of-magnitude reduction in computational time can be achieved, which makes the ILDM method an excellent choice for complex turbulent combustion models. Another advantage of the ILDM method over other mechanism reduction techniques, particularly the quasi-steady-state-assumption (QSSA) method, is that the reduction can be performed automatically; the modeller is not required to have *a priori* knowledge of the reaction mechanism. Considerable success has been achieved in implementing the ILDM method in direct numerical simulation (DNS) and probability-density-function (PDF) modeling of premixed and non-premixed turbulent flames [167–169]. A variety of extensions of the original ILDM model to address the dynamic effects from the flow field on the construction of manifold has also been reported in the literature [170–172].

Nafe and Maas [92] discussed several issues associated with the original ILDM model. Besides the numerical difficulties associated with obtaining a converged solution using Eq. 6.4, the ILDM calculated using Maas and Pope method represents an inertial manifold only when the time scale separation approaches infinity. Hence, the reaction vectors along the ILDM are mostly not in the tangent plane of the manifold. Singh et al. [173] used the analysis of Davis and Skodje [174] to show that the ILDM of a reaction system is only an approximation of the more fundamental slow invariant manifold (SIM). An improvement of the ILDM using a modified Fraser algorithm proposed by Davis and Skodje [174] has been studied by Nafe and Maas [92]. In that case, the ILDM calculated using the method of Maas and Pope [90] was used as an initial guess for the calculation of the SIM for the same system.

An alternative approach to obtain an inertial manifold is to use the Trajectory Generated Low-Dimensional Manifold (TGLDM) method developed by Pope and Maas [94]. The TGLDM method generates the manifold by simply integrating Eq.6.1 from selected initial states in the composition space, therefore a converged solution is guaranteed. Since the manifold is generated along the trajectory, the reaction vector is always in the tangent plane of the manifold, which eliminates the need for back projection as required by the original ILDM method [94]. Theoretically, if an attractive manifold does exist in a dynamic system, the trajectory whose initial state is on the manifold stays on the manifold. Thus, such a trajectory will be equivalent to a SIM. Therefore, for the TGLDM method, the global optimization problem is reduced to one of local optimization, i.e. to locate the optimal initial state for each trajectory.

For a conserved reaction system, the initial state exists in a subspace of $\Re^n$ defined by the linear equations

$$\begin{pmatrix} M(i,j) \\ P(k,j) \end{pmatrix} Y(j) = \begin{pmatrix} Y_c(i) \\ Y_p(k) \end{pmatrix}; \quad i = 1...n_e, j = 1...n_s, k = 1...n_p. \quad (6.5)$$

where $M(i,j)$ denotes the mass fraction of the ith element in the jth species; P denotes a coefficient matrix for the parametric equations; $Y_c(i)$ denotes the mass fraction of ith element, $Y_p(k)$ denotes the assigned value of the kth parameter; n_e denotes the total number of elements in the system; n_s denotes the total number of species; n_p denotes the total number of parameters, ie. the dimension of the TGLDM. The *attractive point* is naturally the equilibrium state in this subspace. Such a constrained equilibrium state can be calculated readily using the method of Lagrange multipliers [175, 176] or Gibbs function continuation [177]. Thus, the constrained-equilibrium state is proposed in this work as the initial point for the trajectories in building a TG-LDM. Figure 6.1 shows a comparison between the resulting TGLDM and an ILDM calculated using the Maas and Pope [90] method for a CO/H$_2$/air reaction system. In this case, the agreement between the two manifolds is very good.

For trajectories starting from a region where the slowest chemical time scale in the fast subspace is comparable to or longer than the physical time scale – ie. during the induction period of a fuel jet in IC engines – constrained equilibrium or the original ILDM method can lead to significant transient state error [173]. The error can be reduced by using a higher dimensional manifold, but the task of storing a high dimensional table or switching ILDM dimensions during the flow calculation is very complex. A compromise is to use TGLDM with initial conditions that resemble the possible states in the flow field, for
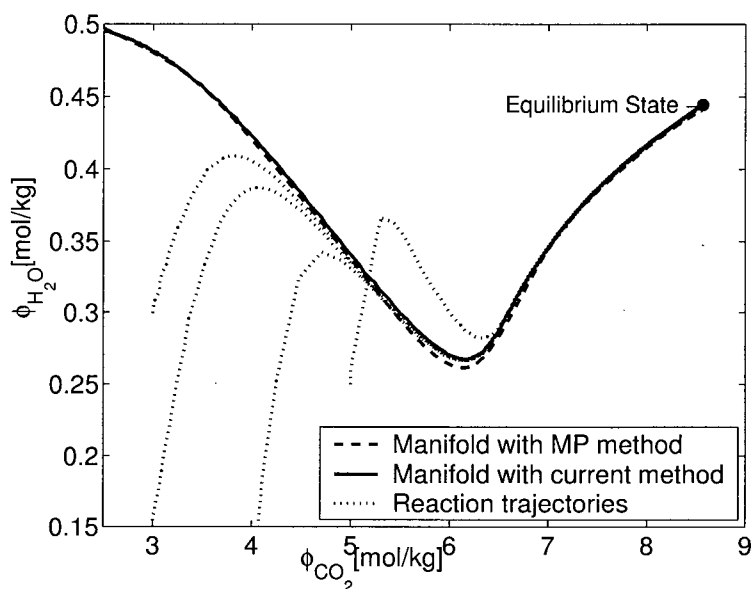
(a) $H_2O - CO_2$
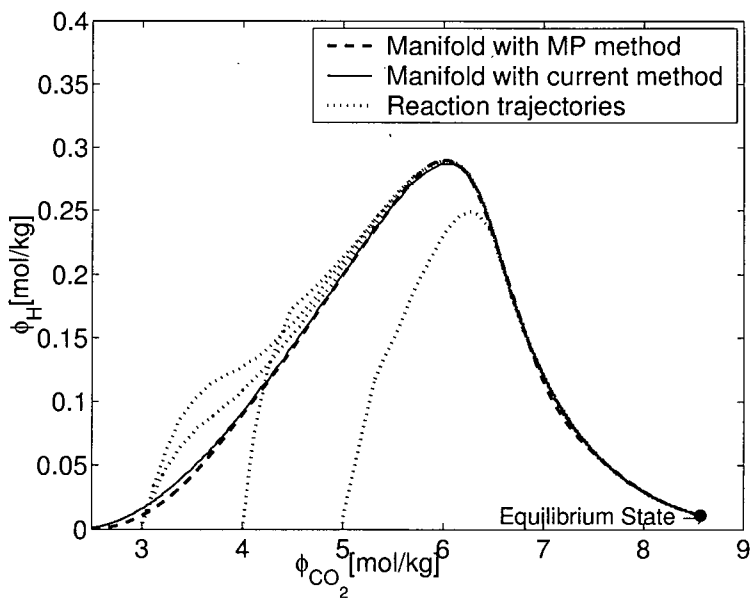
(b) $H - CO_2$

Figure 6.1: Comparison of a one-dimensional TGLDM with optimal initial states and a conventional ILDM. The manifold is projected onto H2O-CO2 and H-CO2 planes; ϕ designates specific mole number. The reaction system and detailed mechanism are identical to those described by Maas and Pope [90].

instance, the initial states of unburned mixtures of fuel and oxidizer. This approach was adopted in this work to generate TGLDMs for the testing reaction system.

6.2 Construction of TGLDM

The detailed reaction mechanism for methane combustion used in this work was taken from our previous work [28]. The mechanism contains 55 species and 278 elementary reactions. Three elements, O, H and C were involved in the reactions. To construct a two-dimensional manifold, five major species were selected: CH_4, O_2, CO, CO_2 and H_2O. Species CO_2 and H_2O were taken as the two progress variables because their formation time scales are similar to each other and are relatively long compared with other species. As a result, the projected manifold has a less skewed resolution throughout the domain. Constraints in the two parameter equations were set so that $Y_{H_2O} \geq Y_{u,H_2O}$ and $Y_{CO_2} \geq Y_{u,CO_2}$, where Y_{u,H_2O} and Y_{u,CO_2} designates the mass fraction of H_2O and CO_2 in the unreacted mixture. This guarantees that the trajectories starting from the initial mixing states are included in the manifold. The reaction rates were calculated using Chemkin II [147], and the governing ODE systems were solved using a stiff ODE solver [148].

As pointed out by Pope and Maas [94], the procedure of constructing a TGLDM introduces a natural parameterization, i.e. the trajectories can be defined using the normalized length r_t and angle of the initial point, θ_t, with respect to the equilibrium state. The domain of the TGLDM in parameter space thus becomes a circle with unit radius. Each trajectory is transformed into a straight line starting from the edge of this circle and evolving towards the center, which is the equilibrium state. The implementation of the manifold parameterized

in this way is still difficult, particularly when it comes to transforming a perturbation in the physical coordinates defined by the progress variables to the $r_t - \theta_t$ coordinates. This is because, in the physical coordinates, the trajectories bunch as they approach the equilibrium state, but in the $r_t - \theta_t$ coordinates, they remain separated. This leads to a singularity in the transformation matrix – the transformation from a low dimensional space to a high dimensional space is not uniquely defined. In this work, two progress variables, Y_{CO_2} and Y_{H_2O}, have been used as the table entry directly rather than parameterizing the TGLDM in transformed coordinates. The perturbation and reaction vectors are projected onto the same plane. Since there is no parameterization of the TGLDM, the table lookup is realized through a subprogram which performs a Delaunay triangulation, an interior point search and a surface interpolation on a two-dimensional unstructured grid [178]. Figure 6.2 presents an example of the triangulated TGLDM projected into the $Y_{CO_2} - Y_{H_2O}$ plane. One advantage of the TGLDM is that the density of mesh varies naturally with the change of stiffness in the reaction system since the stiff ODE solver used to generate the trajectories can respond to such a change by providing more solution points locally. Thus the mesh has an adaptive resolution which provides a higher accuracy in terms of rate interpolation.

6.3 Results and Discussion

The performance of the TGLDM in three different methane/air reaction systems has been investigated: a unstrained premixed laminar flame, a non-premixed flamelet, and a perfectly stirred reactor. Depending on the reaction system, the savings in CPU time by using the TGLDM method range from two to three orders of magnitude when
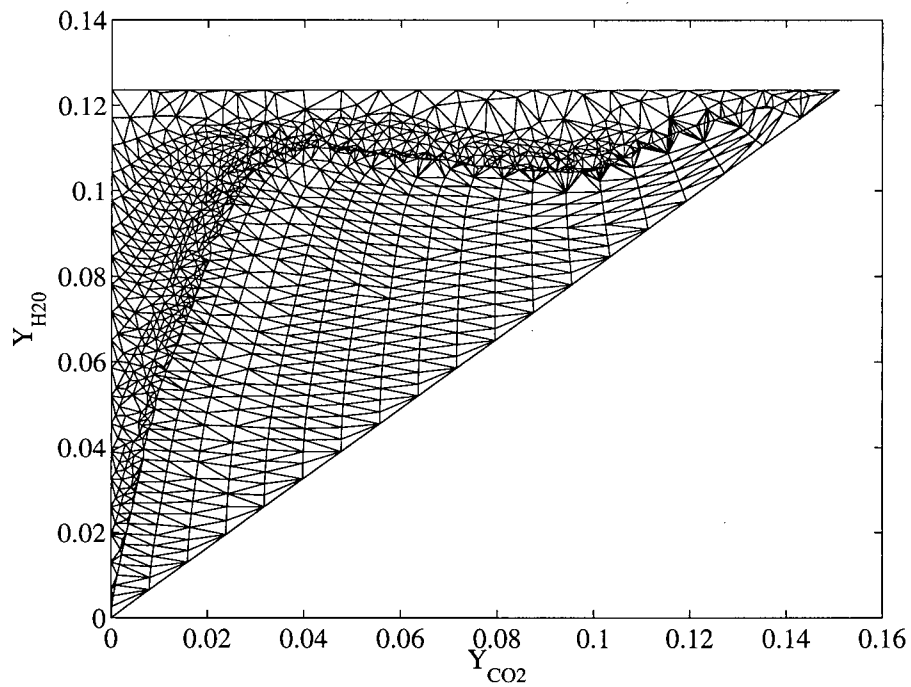
Figure 6.2: Delaunay-triangulated TGLDM in Y_{CO_2} - Y_{H_2O} plane. The unburned CH_4/air mixture temperature (at the lower-left corner) is 400K, $P = 1atm$, and $\Phi = 1$. The mesh density is reduced for the purpose of demonstration.

compared with the method of direct integration using the detailed chemistry.

6.3.1 Unstrained Premixed Laminar Flame

The governing equation for the species mass conservation of a one-dimensional, premixed, free laminar flame is given by

$$\rho \frac{\partial Y_i}{\partial t} + \rho u \frac{\partial Y_i}{\partial x} = -\frac{\partial}{\partial x}(\rho Y_i V_i) + \dot{\omega}_i, \tag{6.6}$$

where u designates the bulk convection velocity, V designates the diffusion velocity, and $\dot{\omega}$ designates the rate change of mass fraction due to chemical reactions. For the mixture averaged diffusion velocity V_i, which incorporates both mass diffusion and thermal diffusion velocities, one can assume Fickian diffusion [57]:

$$V_i = -\frac{1}{X_i} D_i \nabla X_i - \frac{D_{T_i}}{\rho Y_i T} \nabla T. \tag{6.7}$$

where D is the mixture averaged diffusion coefficient, X is the mole fraction, and D_T is the thermal diffusivity at temperature T. The energy conservation equation is given by

$$\rho C_p \frac{\partial T}{\partial t} + \rho u C_p \frac{\partial T}{\partial x} = \frac{\partial}{\partial x}\left(\lambda \frac{\partial T}{\partial x}\right) + \sum_{i=1}^{N} \dot{\omega}_i \Delta h_{fi}^o - \rho \sum_{i=1}^{N} C_{p,i} Y_i V_i \frac{\partial T}{\partial x}, \tag{6.8}$$

where C_p is the specific heat at constant pressure, λ is the thermal conductivity, and Δh_f^o is the enthalpy of formation. The boundary conditions are

$$Y_i = Y_{u,i}, \qquad T = T_u \qquad at \qquad x = 0, \tag{6.9}$$

and

$$\frac{\partial Y_i}{\partial x} = 0, \qquad \frac{\partial T}{\partial x} = 0 \qquad at \qquad x \to \infty. \tag{6.10}$$

The subscript u designates the unburned mixture. The above governing equations are solved using a Strang operator splitting [179] scheme

that separates the solution of chemical source terms from the convection/diffusion term. Each numerical time step is split into a convection-/diffusion time step and a chemical time step. In the physical time step, the convection/diffusion terms in the governing PDEs are first solved with the reaction source term suppressed. In the chemical time step, the flow field obtained from the physical time step is frozen and each computational cell is treated as being spatially homogeneous; the ODE system that governs the chemical reactions is then solved. Since the TGLDM is an inertial manifold, the solution in the chemical time step stays on the manifold so that no projection is required. The physical perturbation caused by the convection/diffusion terms, on the other hand, is not confined by the low-dimensional manifold. In this work, orthogonal projection [94] is used to return the solution to the manifold at the end of the physical time step.

Figure 6.3 compares the steady-state solutions of the flame structure for a premixed methane/air laminar flame obtained using detailed chemistry and the TGLDM method respectively. For the profiles of temperature and major species, the agreement between the TGLDM and detailed chemistry is very good. For minor species, the peak hydrogen radical mass fraction in the flame front is over-predicted by about 15 percent, while the peak OH radical mass fraction is over-predicted by around 65 percent. One factor that could contribute to the over-prediction of these minor radicals is their high diffusivity, which leads to a higher mass-transport rate from the flame. In the current TGLDM method, differential diffusion effects are cannot be accounted for, as was mentioned earlier. Away from the flame front, the agreement between TGLDM and detailed chemistry for minor species improves quickly as the burned mixture approaches the equilibrium state.
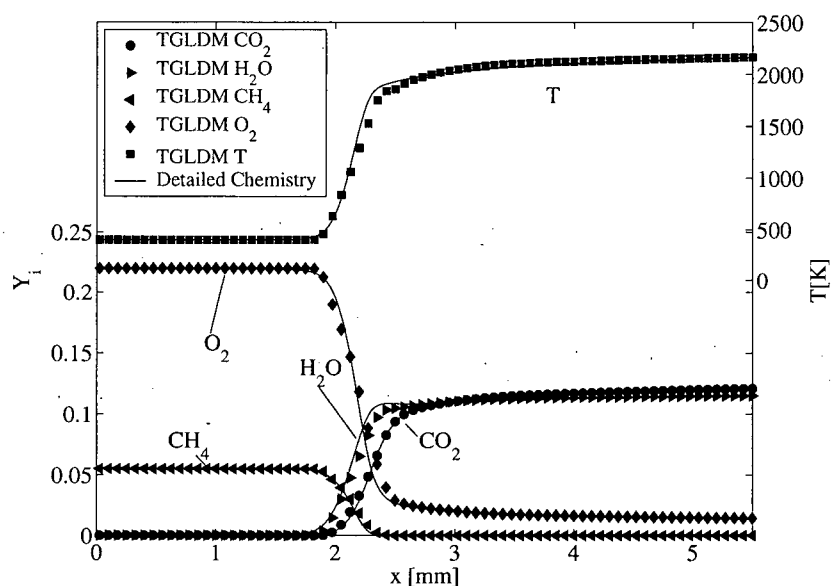
(a) Temperature and Major Species
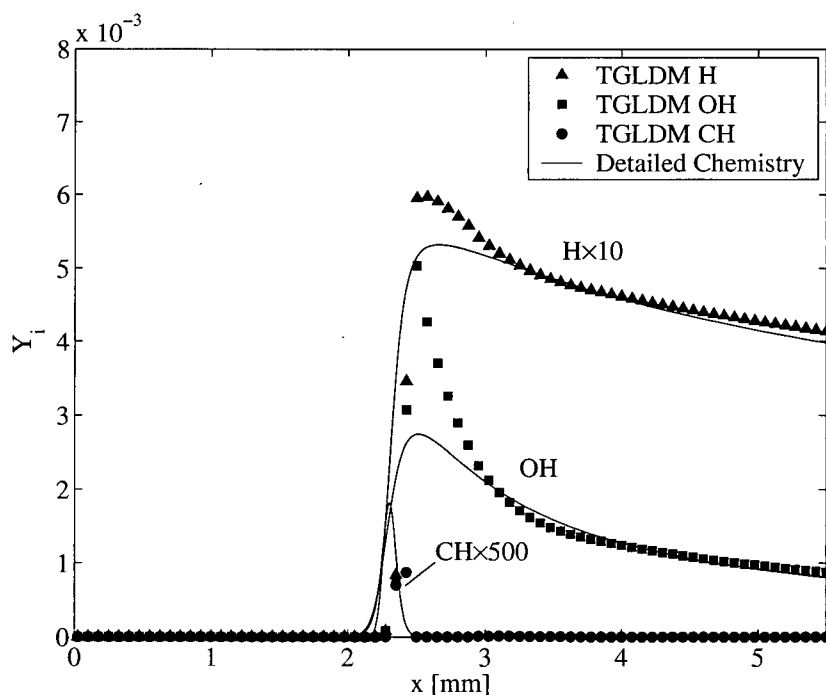
(b) Minor Species

Figure 6.3: Comparison of calculated flame structure of a one-dimensional premixed laminar methane/air flame. The flame propagates from right to left into an unburned CH_4/air mixture at 400K. $P = 1atm, \Phi = 1$.
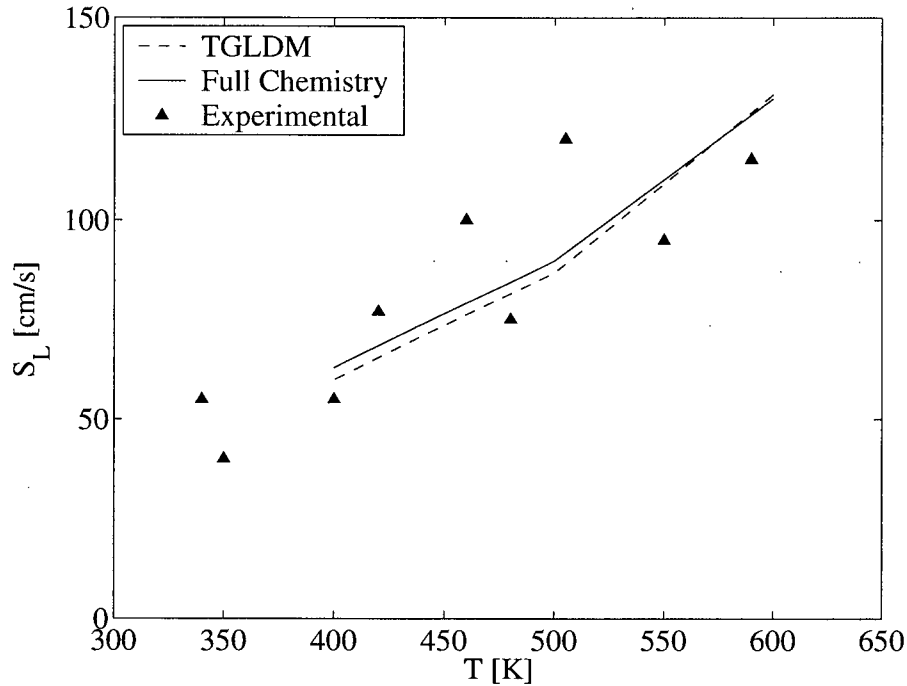
Figure 6.4: Laminar flame velocity of a stoichiometric methane/air mixture calculated using TGLDM method. The experimental data shown are those of Warnatz et al. [62].

Figure 6.3.1 shows the laminar burning velocities calculated using the TGLDM for the same mixture as a function of unburned mixture temperature. It can be seen that the agreement between the detailed chemistry and TGLDM is satisfactory for the conditions investigated and both give reasonable predictions of the experimentally measured values.

6.3.2 Laminar Flamelet

The basic flamelet equations [96] in mixture fraction space are

$$\rho\frac{\partial Y_i}{\partial \tau} = \rho\frac{\chi}{2}\frac{\partial^2 Y_i}{\partial Z^2} + \dot{w}_i \qquad (6.11)$$

$$\rho\frac{\partial T}{\partial \tau} = \rho\frac{\chi}{2}\frac{\partial^2 T}{\partial Z^2} + \sum_{i=1}^{n}\frac{h_i}{c_p}\dot{w}_i,$$

where Z denotes the mixture fraction, and χ denotes the instantaneous scalar dissipation rate, which is defined by

$$\chi = 2D(\frac{\partial Z}{\partial x_j})^2, \qquad (6.12)$$

where x_j denotes the direction normal to the flame interface. The scalar dissipation describes the mixing time scale in a diffusion flame. A larger value of χ indicates more rapid turbulent mixing. Law and Chung [102] and Peters [96] proposed using the scalar dissipation at the stoichiometric surface, $\chi_{st} \equiv \chi(Z_{st})$, as the representative parameter for diffusion flames. From the analytical solution of a steady-state counter flow configuration, it can be shown that

$$\chi(Z) = \frac{a}{\pi}exp\{-2[\text{erfc}^{-1}(2Z)]^2\}, \qquad (6.13)$$

where erfc^{-1} designates the inverse of the error function. The functional dependence of $\chi(Z)$ on χ_{st} can be derived from Eq. 6.13

$$\chi(Z) = \chi_{st}f(Z)/f(Z_{st}), \qquad (6.14)$$

where f(Z) designates the exponential term in Eq. 6.13.

Unlike the premixed flame, which corresponds to a single manifold at one equivalence ratio, the solution of the flamelet equations requires a complete spectrum of low-dimensional manifolds that spans the full range of mixture fraction. In this work, a discrete set of TGLDMs were generated at fifty two points in mixture fraction from zero to unity. The distribution of node points was made dense in the lean and stoichiometric regions where the gradients in reactive scalars are high.

Figs. 6.5 and 6.6 show a comparison of steady-state flamelet solutions obtained using the detailed chemistry and the TGLDM at $\chi_{st} = 100s^{-1}$ and $\chi_{st} = 300s^{-1}$ respectively. The oxidizer temperature at the

left boundary ($Z = 0$) is 1400K, and the fuel temperature at the right boundary ($Z = 1$) is 300K. The pressure is 30 bar throughout the domain. The two values of scalar dissipation selected represent moderate perturbation and high (near-quenching) perturbation cases for this system.

In general, for $\chi_{st} = 100s^{-1}$, the predictions of temperature, major and minor species profiles using the TGLDM method agree well with the results from the detailed chemistry, but some deviations of temperature and methane mass fraction on the rich side of stoichiometric can be observed. For mixtures with high equivalence ratios, the chemical time scales associated with the consumption of methane are long due to the relatively low mixture temperature and the high methyl concentration. The reduction in the separation of chemical and physical time scales could be a major factor that leads to the under-prediction of methane by the TGLDM. The improved agreement of minor species in the flame zone compared to that in the premixed flame is partially attributed to our having neglected differential diffusion: the same scalar dissipation used for all the species in the flamelet equations.

For the high scalar dissipation case at $300s^{-1}$, an increase in the deviation between the TGLDM results and those from detailed chemistry is observed, although the overall agreement remains reasonably good. In particular, the peak flame temperature and peak CO_2 mass fraction is slightly under-predicted. It appears that the flame profile obtained from the detailed chemistry is more "resistant" to a high level of perturbation than that obtained from the low-dimensional manifold.
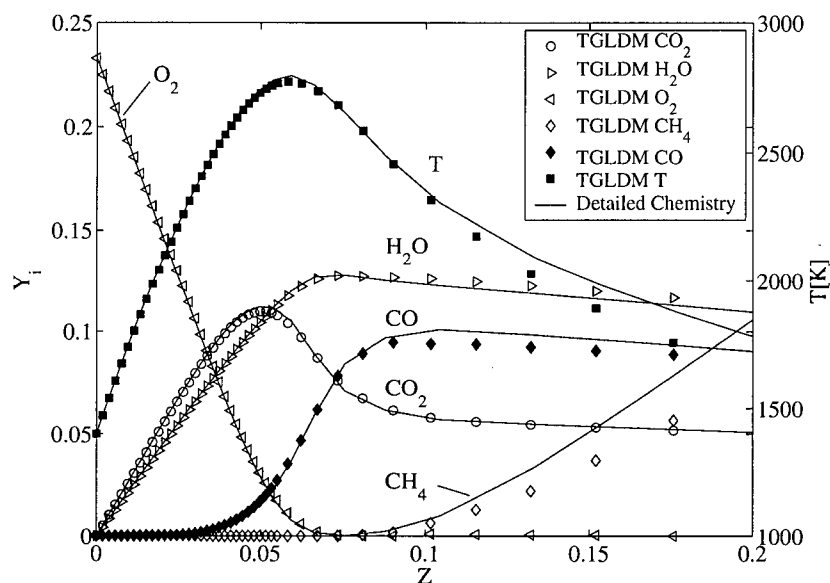
(a) Temperature and Major Species
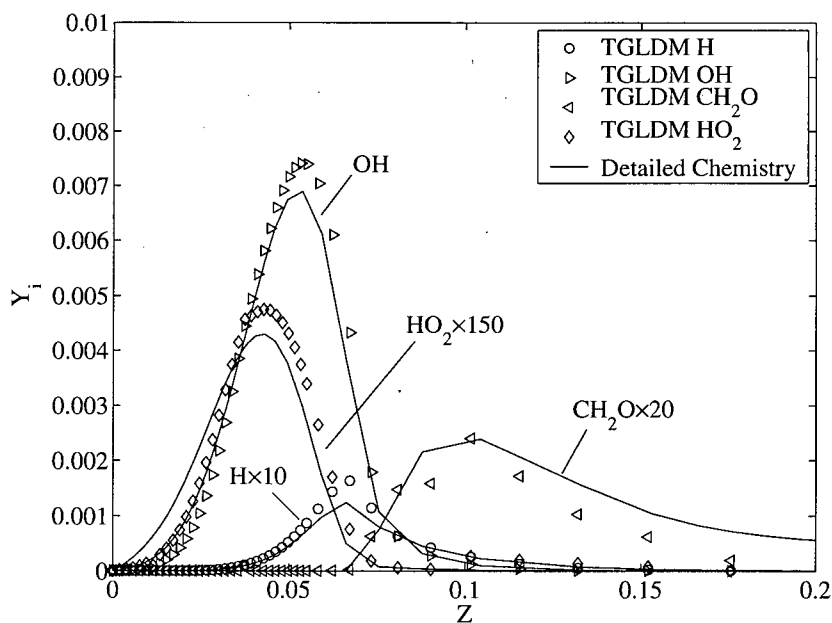
(b) Minor Species

Figure 6.5: Comparison of calculated temperature and species profile of a steady state methane/air flamelet at 30 bar in the mixture fraction space. $\chi_{st} = 100s^{-1}$
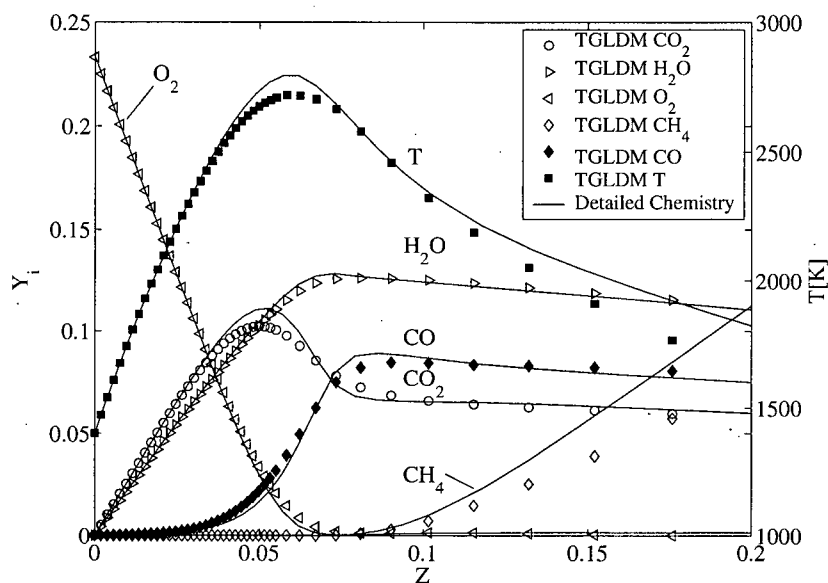
(a) Temperature and Major Species
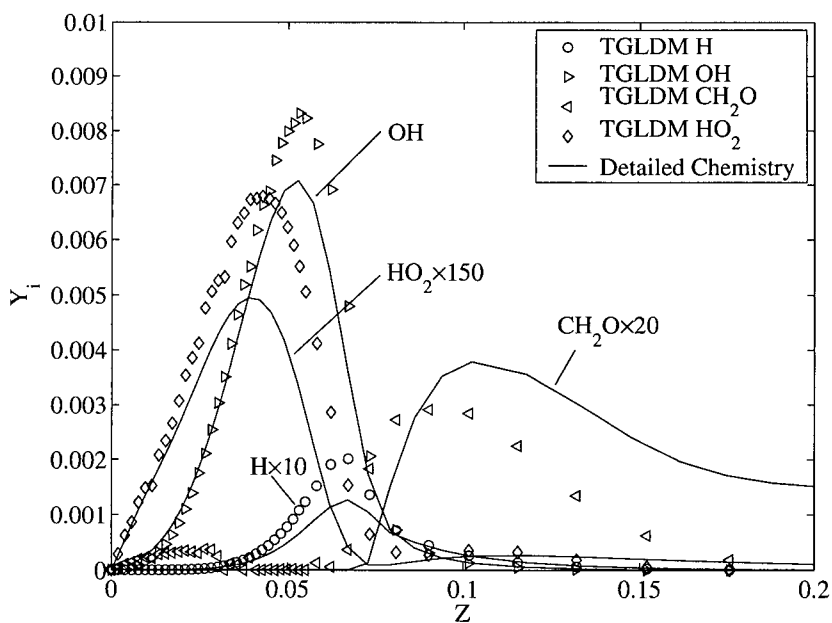
(b) Minor Species

Figure 6.6: Comparison of calculated temperature and species profile of a steady state methane/air flamelet at 30 bar in the mixture fraction space. $\chi_{st} = 300s^{-1}$

6.3.3 Perfectly Stirred Reactor

Using a TGLDM to model transient process such as ignition and flame quenching is more challenging than the previous two cases tested because more chemical time scales are in a range comparable to the physical time scales under these conditions. The perfectly stirred reactor (PSR) model was chosen to test performance under transient conditions because, in the PSR, the physical time scale can be specified explicitly.

The governing equation for a perfectly stirred reactor is given by

$$\frac{d\mathbf{Y}}{dt} = \mathbf{F}(\mathbf{Y}) - \omega \left(\mathbf{Y} - \mathbf{Y}_i \right), \qquad (6.15)$$

where $\mathbf{Y}_i$ designates the mass fraction vector of the flow entering the PSR, and ω is the inverse of residence time which represents the physical time scale. In this work, the PSR model for a stoichiometric methane-/air system at 30 bar constant pressure was investigated.

Figure 6.7 presents the change in temperature and species mass fraction during the induction period of the reactants in the PSR. Two inflow temperatures, 1229K and 1024K, were examined. They are equivalent to the temperatures when stoichiometric mixtures are formed with methane at 300K and air at 1400K and 1150K, respectively. The traces marked $\omega = 0$ represents an un-perturbed reaction system. The slight phase difference between the results with the TGLDM and those from the detailed chemistry in this case is mostly due to interpolation errors in getting the instantaneous reaction rate. When an inflow of unreacted mixture is introduced as a perturbation, the ignition delay time is retarded. For a moderate perturbation, the phase shift predicted by the TGLDM method is in reasonable agreement with detailed chemistry. For instance, at an inflow temperature of 1229K, the error in the

predicted phase shift is about 10 percent for a retard in ignition delay of nearly 100 percent. The error is larger for the case with lower in-flow temperature. Reasonable predictions of phase retard are only obtained for relatively small perturbations, as shown in Fig.6.7(a). Note that the value of ω in Fig.6.7(a) is significantly smaller than that of that in Fig.6.7(b). This is clearly due to the larger number of long chemical time scales associated with lower temperatures which leads to a significant deviation of reaction trajectories subject to large perturbations from the low-dimensional manifold.

A combustion system can be quenched when the physical perturbation is such that the chemical reaction rate cannot be sustained due to an excessive heat and radical loss. Figure 6.3.3 shows the prediction of temperature and species mass fraction history during a quenching process using the TGLDM method. In simulating the quenching process, an unperturbed reaction system is first evolved to the equilibrium state; the perturbation term is then introduced with a large value of ω. It can be seen that the calculated results using the TGLDM method essentially match those obtained with detailed chemistry. However, it has been noticed in this work that the performance of TGLDM in the near quenching region is not ideal. In particular, the current TGLDM tends to under-predict the quenching limit: the model employing the TGLDM will predict quenching at a lower level of perturbation than is observed with detailed chemistry. Future work on improving the performance of manifold methods in the region of competing chemical and physical time scales is clearly warranted.
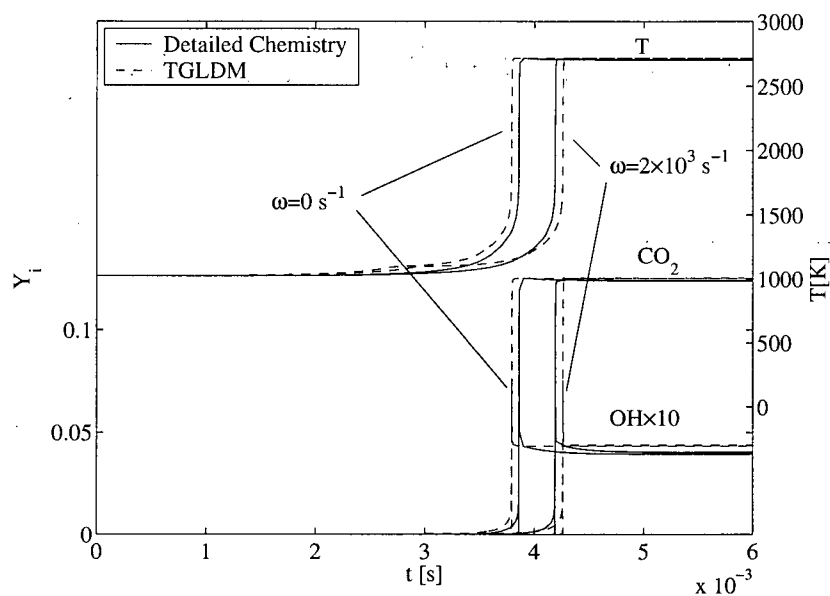
(a) T$_{in}$=1024K
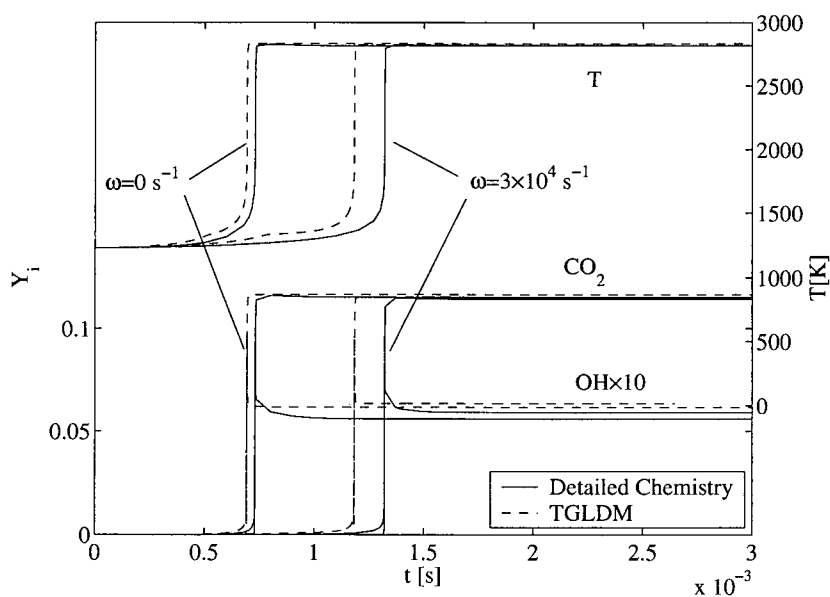
(b) T$_{in}$=1229K

Figure 6.7: Calculated temperature and species mass fraction history during the induction period for a stoichiometric methane/air mixture in a PSR. The solid line designates results from detailed chemistry; the dash line designates results from the TGLDM.
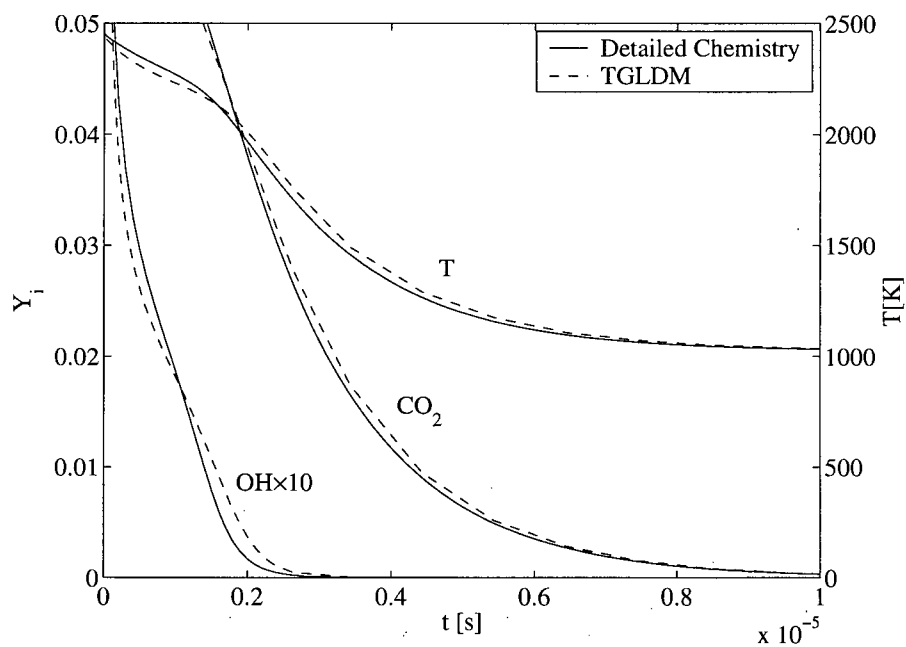
Figure 6.8: Calculated temperature and species mass fraction history during a quenching process of a stoichiometric methane/air mixture in a PSR. The inverse of the characteristic residence time, ω, is set at $6 \times 10^6 s^{-1}$; the inflow mixture temperature is 1024K.

6.4 Conclusions

An improved TGLDM method [94] that uses optimized initial states for the trajectories has been discussed. The difference between the resulting TGLDM and the ILDM generated using the method of Maas and Pope [90] has been investigated. Several merits of the TGLDM method have been identified: the construction of the manifold is less mathematically involved than the conventional ILDM method; the reaction vector of a TGLDM is always in the tangent plane of the manifold. An alysis of a hypothetical reaction system showed that if the initial state of the reaction system is known, the TGLDM with optimized initial conditions gives a better approximation of detailed chemistry than the ILDM.

The performance of the TGLDM in predicting reactive scalar profiles for a methane/air mixture has been investigated in modeling laminar premixed flames, laminar flamelets, and the transient processes in a perfectly stirred reactor. In general, reasonable agreement between the results with the TGLDM and those from detailed chemistry has been found. When the physical time scales approaches the chemical time scales in the fast subspace, relatively large errors occur using the TGLDM. Further study on improving the performance of manifold methods in these regions has been suggested.

Chapter 7

Simulation of Turbulent Reactive Methane Jets Under Engine Relevant Conditions

7.1 Introduction

Direct-injection natural gas (DING) engines offer a combined benefit of low pollutant emissions and high thermal efficiency [4–8]. The combustion process in a DING engine, particularly that of a transient turbulent natural gas jet, is a subject under intense study. Thanks to progress in the study of the chemical kinetics that are important to natural gas combustion at elevated pressures and reduced temperatures, the combustion chemistry for natural gas under engine relevant conditions is now better understood [28, 29, 38]. However, the implementation of detailed chemistry in a multi-dimensional simulation of a turbulent reactive natural gas jet remains a challenging task. In particular, two fundamental problems have to be addressed in order to simulate turbulent combustion using detailed chemistry. First, for any computational fluid dynamic (CFD) models that do not resolve all of the turbulence scales, a turbulent combustion model is required to account for the effects of turbulent fluctuations on the chemical reaction rates. Second, the combustion system described by detailed chemistry

is usually very stiff: the chemical time scales associated with different reaction scalars vary drastically. To solve such a stiff system directly in most practical turbulent reactive flow simulations is still beyond the reach with the existing computational power. Thus methods to reduce the CPU time required for computing the reaction rates from detailed chemistry must be used.

In this work, a combustion model is proposed that provides solutions to the above two problems. The model incorporates the Conditional Source-term Estimation (CSE) [127] and Trajectory Generated Low-Dimensional Manifold (TGLDM) [94] methods, which can provide a closure for the chemical source term at the level of the first moment with a relatively low computational cost. The model is applied to simulate the ignition and combustion of experimental methane jets under engine relevant conditions. The simulation results are validated using experimental data obtained from a high-pressure shock tube facility as well as data reported in literature.

7.2 CSE-TGLDM Combustion Model

7.2.1 Conditional Source-term Estimation

The Conditional Source-term Estimation (CSE) method [127] seeks closure of the chemical source term using the conditional average of the reactive scalars in a manner similar to the first-order Conditional Moment Closure (CMC) method. The solution for the conditional averages, however, is not obtained by solving transport equations as is done in CMC. Based on the assumption that the conditional averages of scalars have very low gradients in space, Bushe and Steiner proposed a method to obtain the conditional averages of reactive scalars by inverting an integral equation for an ensemble of discrete points on

177

a computational grid [127]. Mathematically, the unconditional average of a random event can be calculated from its conditional average if the local probability density function (PDF) is known.

$$\langle Y(x,t) \rangle = \int_0^1 P(x,t;\eta) \langle Y(x,t) | \eta \rangle d\eta. \tag{7.1}$$

For a selected spatial ensemble of N points, it is assumed that

$$\langle Y(x^{(n)}, t) | \eta \rangle = \langle Y | \eta \rangle_{A,t} \tag{7.2}$$

where the superscript n denotes the nth point in the ensemble; the subscript A indicates that the average is taken over the ensemble of A discrete grid points in space. Thus a discrete set of N integrals

$$\langle Y(x^{(n)}, t) \rangle = \int_0^1 P(x,t;\eta) \langle Y | \eta \rangle_{A,t} d\eta. \tag{7.3}$$

By approximating the integral using a numerical quadrature, one obtains a linear system of equations which can be inverted for the conditional average of the scalar of interest using a method such as linear regularization.

The CSE method was initially implemented in a Large Eddy Simulation of a piloted methane/air diffusion flame with encouraging success in predicting experimental measurements [128]. Later, the concept of CSE was tested in conjunction with the unsteady laminar flamelet model, in which the conditional averages of reaction scalars were calculated using a linear combination of flamelet solutions [129]. In this incarnation of CSE, one decomposes the conditional average into a linear combination of laminar flamelets; one then inverts an integral equation to determine the optimal linear combination of flamelets for each ensemble. The method has been used in the context of RANS model to study turbulent methane jet ignition under engine-relevant conditions with some success [130,131]. In order to address the issue raised

by ill-posedness in Eq. 7.3 as well as to provide temporal continuity in the solution, Grout [131] proposed using a general Tikhonov regularization method for the inverting process, given by

$$min\left\{\|\Omega\langle Y|\eta\rangle^t - \langle Y\rangle^t\| + \lambda\|\langle Y|\eta\rangle^t - \langle Y|\eta\rangle^{t-\Delta t}\|\right\}, \qquad (7.4)$$

where Ω is the original coefficient matrix for the discrete integral equation; the superscripts t and $t - \Delta t$ are the times when the scalars are evaluated; λ is a weighting coefficient specified by the modeler. The regularization term $\lambda\|\langle Y|\eta\rangle^t - \langle Y|\eta\rangle^{t-\Delta t}\|$ was added to limit the change of conditional average between two consecutive time steps as well as to stabilize the solution. In Grout's work, λ was set to the ratio of the trace of Ω to the trace of an identity matrix with the same size.

In this work, efforts have been made to further improve the regularization method by including spatial continuity for the conditional scalar field. The incremental limiter, $\|\langle Y|\eta\rangle^t - \langle Y|\eta\rangle^{t-\Delta t}\|$ in Eq. 7.4 is replaced by $\|\langle Y|\eta\rangle^t - \langle Y^*|\eta\rangle^t\|$ where $\langle Y^*|\eta\rangle^t$ is calculated from the transport equation

$$\frac{\langle Y^*|\eta\rangle^t - \langle \mathbf{Y}|\eta\rangle^{t-\Delta t}}{\Delta t} \approx -\frac{\partial \bar{\rho}\langle u_{i,x}|\eta\rangle\langle Y|\eta\rangle}{\partial x_i}^{t-\Delta t}. \qquad (7.5)$$

It has been reported from experimental studies and DNS simulations that for steady, axi-symmetric jet flames, the cross-stream variations of conditional means are not significant [127, 180, 181]. Thus the convection of the conditional means described in Eq. 7.5 is only considered in the axial direction of the jet. The conditional mean velocity at the axial location x, $\langle u_x|\eta\rangle$, is obtained by cross-stream averaging along the isopleth

$$\langle u_x|\eta\rangle = \frac{\int_0^R \langle u(x,r)\rangle P(\eta; x, r)dr}{\int_0^R P(\eta; x, r)dr} \qquad (7.6)$$

where R denotes the radius of the jet.

The main advantage of the CSE method is that the computational cost is substantially lower than that of CMC. In addition, it does not involve constraining assumptions such as those employed in laminar flamelet models, and is thus applicable to a wide range of turbulent flames.

7.2.2 Trajectory Generated Low-Dimensional Manifold

Manifold methods for reducing detailed chemistry are based on the separation of chemical time scales associated with different reaction scalars. If the time scale separation is large enough, fast processes with short time scales approach a quasi-steady state rapidly; these can be decoupled from slow processes to reduce the total dimensionality of the reaction system. The remaining low-dimensional manifold can be used to approximate the detailed chemistry with a high degree of accuracy. For a two-dimensional manifold, for example, the instantaneous rates of reaction scalars Y can be obtained from the manifold using the formula

$$\frac{dY}{dt} = \frac{\partial Y(u,v)}{\partial u}\frac{\partial u}{\partial t} + \frac{\partial Y(u,v)}{\partial v}\frac{\partial v}{\partial t} \tag{7.7}$$

where u and v are progress variables used to parameterize the manifold. Maas and Pope [90] proposed a mathematical model for computing the Intrinsic Low-Dimensional Manifold (ILDM) by minimizing the reaction vector projected into the fast subspace, which is defined by eigenvectors associated with large negative eigenvalues of the Jacobian matrix. The manifold generated by this method is somewhat optimal globally; however, the implementation of the method is very involved.

In the TGLDM method proposed by Pope and Maas [94], the manifold is generated along reaction trajectories so that the construction of

the manifold is significantly simpler than that of the ILDM. The boundary formed by the initial states of the trajectories, which is called the manifold generator, can be obtained using the extreme-value-of-major-species method [94] to achieve a maximum overlap between the TGLDM and ILDM. It should be note that the initial states of TGLDMs can be tailored to match the initial mixture compositions in the flow field to provide a better approximation of detailed chemistry.

The parameterization of the TGLDM can be realized using the normalized trajectory length and the initial locations of the trajectory with respect to some reference. However, in locations where the reaction trajectories bunch, the projecting matrix which maps the perturbation from physical space to the manifold space becomes nearly singular. To avoid this problem in this study, two reaction scalars, Y_{CO_2} and Y_{H_2O}, are used as progress variables for the manifold without parameterization. The projected TGLDM in the $Y_{CO_2} - Y_{H_2O}$ plane is triangulated using the Delaunay method to form an unstructured mesh. A subprogram is then used to perform the interior point search and interpolation on the manifold surface based on the instantaneous value of Y_{CO_2} and Y_{H_2O}.

7.3 Experiments

An experimental study of the ignition and combustion of a transient turbulent methane jet has been conducted in a shock tube facility; detailed experimental results have been reported by Sullivan et al. [182]. A schematic of the experimental setup used in this study is shown in Fig. 7.1.

The shock tube has a circular cross section with an inner diameter of 59 mm. The lengths of the driver and driven section are 3.11 m
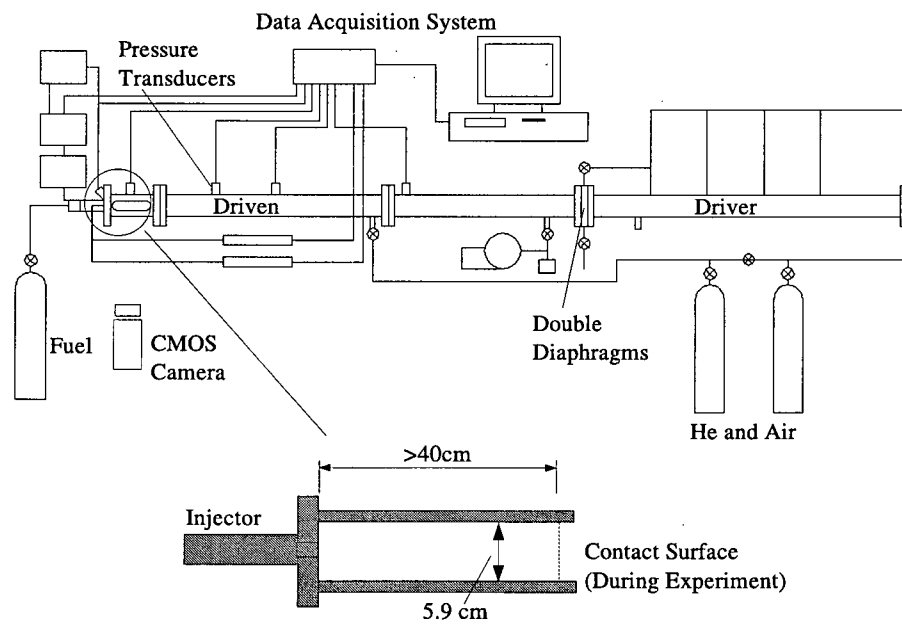
Figure 7.1: Schematic of the shock tube facility

and 4.79 m respectively. The incident shock velocity is measured using five flush mounted PCB pressure transducers along the driven section. The minimum response time of these transducers is 2 μs. The signal from the pressure transducers were acquired using a Wavebook 512 data acquisition system sampling at a rate of 140 kHz per channel. The temperature behind the reflected shock is calculated based on normal shock relations using the measured incident shock velocity [27]. The uncertainty in the experimental temperature, calculated based on the uncertainty in the measured shock velocity, is around 14K.

A stainless steel section equipped with three 199 × 15 mm fused quartz windows was attached to the end of the driven section to provide optical access to the experimental area. Methane (99.97% purity) was injected into the shock tube along its axis through a 1.1 mm diameter single nozzle natural gas injector equipped with a magnetostrictive actuator. The response time of the injector is around 250 μs with a standard deviation of 20 μs. The injection was initiated between 100 and 800 μs after the shock reflection by a customized controller unit triggered using the pressure signal sensed at the end plate of the driven section. The total injection duration was 1.5 ms. A Vision Research Phantom high speed CMOS digital camera operated at a rate of 31000 fps was used to capture broad band luminosity during the ignition and combustion process of the methane jet behind the reflected shock wave. The location of initial ignition kernel is defined as the emergence of a non-contiguous flame region, which is able to develop into a fully fledged jet flame. The ignition delay is thus defined as the time delay from the start of gas injection to the emergence of the ignition kernel.

Tailored interface conditions [27] were used to obtain a maximum experimental time of around 5 ms. The calculated contact surface po-

sition when stopped by the reflected shock wave was more than 40 cm away from the end plate of the driven section, which is considerably longer than the maximum penetration length of the methane jet during the experimental period. This ensured that the temperature, pressure and gas composition during the experiment were not affected by the driver gas. At the end of the experimental time, the reaction in the experimental region was quenched due to the arrival of the rarefaction wave that rapidly reduces the temperature and pressure in the test section.

After each experiment, the complete contents of the shock tube were vented through an impacter-type filter into a 400 L carbon-impregnated polyolefin sampling bag. The sample was then analyzed using an API 200E Chemiluminscent NOx analyzer to obtain the concentration of NO and NO_2 in the combustion products.

Table 7.1 summarizes the experimental conditions and main parameters in these experiments.

Table 7.1: Experimental conditions of this work

No. Runs	d_{injector} [mm]	P_i[16] [bar]	P_o[17][bar]	τ_i[18][ms]	T_i[19]	T_o[20]K
28	1.1	75	30	1.5	300	1150-1400

---

[16]Injection pressure
[17]Back pressure (pressure behind reflected shock)
[18]injection duration
[19]Fuel temperature
[20]Temperature behind reflected shock

7.4 Model Formulation and Validation

7.4.1 CFD Model Formulation

For the experimental conditions just described, the jet is choked at the nozzle exit. The flow field in the region close to the nozzle exit has a high Mach number and thus need to be treated as being fully compressible. The Reynolds averaged transport equations for mass, momentum and energy in the cylindrical coordinates with an axisymmetric configuration are

- Continuity

$$\frac{\partial \bar{\rho}}{\partial t} + \frac{1}{r}\frac{\partial}{\partial r}(\bar{\rho} r \widetilde{u}_r) + \frac{\partial}{\partial z}(\bar{\rho} \widetilde{u}_z) = 0. \tag{7.8}$$

Symbol $\sim$ denotes Favre average and $\bar{\rho}$ is the mean of density.

- Momentum

$$\bar{\rho}\left(\frac{\partial \widetilde{u}_r}{\partial t} + \widetilde{u}_r\frac{\partial \widetilde{u}_r}{\partial r} + \widetilde{u}_z\frac{\partial \widetilde{u}_r}{\partial z}\right) = -\frac{\partial \widetilde{p}}{\partial r} + \left(\frac{1}{r}\frac{\partial}{\partial r}(r\tau_{rr}) + \frac{\partial \tau_{rz}}{\partial z}\right) \tag{7.9}$$

$$\bar{\rho}\left(\frac{\partial \widetilde{u}_z}{\partial t} + \widetilde{u}_r\frac{\partial \widetilde{u}_z}{\partial r} + \widetilde{u}_z\frac{\partial \widetilde{u}_z}{\partial z}\right) = -\frac{\partial \widetilde{p}}{\partial z} + \left(\frac{1}{r}\frac{\partial}{\partial z}(r\tau_{rz}) + \frac{\partial \tau_{zz}}{\partial z}\right), \tag{7.10}$$

where τ designates the stress tensor whose components are given by

$$\tau_{rr} = \mu_t\left[2\frac{\partial \widetilde{u}_r}{\partial r} - \frac{2}{3}(\nabla \cdot \mathbf{v})\right] \tag{7.11}$$

$$\tau_{zz} = \mu_t\left[2\frac{\partial \widetilde{u}_z}{\partial z} - \frac{2}{3}(\nabla \cdot \mathbf{v})\right]$$

$$\tau_{zr} = \tau_{rz} = \mu_t\left[2\frac{\partial \widetilde{u}_z}{\partial r} + \frac{\partial \widetilde{u}_r}{\partial z}\right]$$

- Energy

$$\bar{\rho} C_p \left(\frac{\partial \widetilde{T}}{\partial t} + \widetilde{u}_r \frac{\partial \widetilde{T}}{\partial r} + \widetilde{u}_z \frac{\partial \widetilde{T}}{\partial z} \right) - \left(\frac{\partial p}{\partial t} + \widetilde{u}_r \frac{\partial \widetilde{p}}{\partial r} + \widetilde{u}_z \frac{\partial \widetilde{p}}{\partial z} \right) \qquad (7.12)$$

$$= \lambda \left[\frac{1}{r} \frac{\partial}{\partial r} \left(r \frac{\partial \widetilde{T}}{\partial r} \right) + \frac{\partial^2 \widetilde{T}}{\partial z^2} \right] + \mu_t \left\{ 2 \left[\left(\frac{\partial \widetilde{u}_r}{\partial r} \right)^2 + \left(\frac{\widetilde{u}_r}{r} \right)^2 + \left(\frac{\partial \widetilde{u}_z}{\partial z} \right)^2 \right] \right.$$

$$\left. + \left(\frac{\partial \widetilde{u}_r}{\partial z} + \frac{\partial \widetilde{u}_z}{\partial r} \right)^2 - \frac{2}{3} \left(\frac{1}{r} \frac{\partial}{\partial r} (r \widetilde{u}_r) + \frac{\partial \widetilde{u}_z}{\partial z} \right)^2 \right\} + \dot{\omega}$$

Body force and radiation effects have been neglected in these equations. All the chemical species are assumed to diffuse at the same rate and the Lewis number is unity. The turbulent viscosity μ_t is calculated using the standard $k - \epsilon$ model [183]

$$\mu_t = \bar{\rho} C_u \frac{k^2}{\epsilon}, \qquad (7.13)$$

where k is the turbulent kinetic energy; ϵ is the dissipation rate of turbulent kinetic energy; the value of coefficient C_u is 0.09.

7.4.2 Combustion Model Formulation

In the CSE method, a probability density function for mixture fraction is constructed from its local mean and variance. The closure for transport equations for the mean and variance of mixture fraction is achieved by employing a gradient transport hypothesis:

- Mean mixture fraction

$$\bar{\rho} \left(\frac{\partial \langle Z \rangle}{\partial t} + \widetilde{u}_r \frac{\partial \langle Z \rangle}{\partial r} + \widetilde{u}_z \frac{\partial \langle Z \rangle}{\partial z} \right) = \frac{1}{r} \frac{\partial}{\partial r} \left(\frac{\mu}{Sc} \frac{\partial \langle Z \rangle}{\partial r} \right) + \frac{\partial}{\partial z} \left(\frac{\mu}{Sc} \frac{\partial \langle Z \rangle}{\partial z} \right)$$
$$(7.14)$$

- Variance of mixture fraction

$$\bar{\rho} \left(\frac{\partial \langle Z''^2 \rangle}{\partial t} + \widetilde{u}_r \frac{\partial \langle Z''^2 \rangle}{\partial r} + \widetilde{u}_z \frac{\partial \langle Z''^2 \rangle}{\partial z} \right) = \frac{1}{r} \frac{\partial}{\partial r} \left(\frac{\mu}{Sc} \frac{\partial \langle Z''^2 \rangle}{\partial r} \right) \quad (7.15)$$

$$+ \frac{\partial}{\partial z} \left(\frac{\mu}{Sc} \frac{\partial \langle Z''^2 \rangle}{\partial z} \right) + \frac{2\mu}{Sc} \left(\frac{1}{r} \frac{\partial \langle Z \rangle}{\partial r} + \frac{\partial \langle Z \rangle}{\partial z} \right)^2 - \bar{\rho} c_x \frac{\epsilon}{k} \langle Z''^2 \rangle$$

In the above two equations, Sc denotes the Schmidt number. In this study, a value of 0.9 is assigned to Sc, which is identical to that used by Hasse et al. [110]. A standard value of 2.0 has been assigned to the coefficient c_x in the source term of the variance of mixture fraction [96]. To use the two-dimensional TGLDM for the chemical source term, transport equations for two progress variables (Y_{CO_2} and Y_{H_2O} in this work) need to be solved. The basic form of the transport equation for a reaction scalar Y_i is given by

$$\bar{\rho}\left(\frac{\partial Y_i}{\partial t} + \tilde{u}_r\frac{\partial Y_i}{\partial r} + \tilde{u}_z\frac{\partial Y_i}{\partial z}\right) = \frac{1}{r}\frac{\partial}{\partial r}\left(\frac{\mu}{Sc}\frac{\partial Y_i}{\partial r}\right) + \frac{\partial}{\partial z}\left(\frac{\mu}{Sc}\frac{\partial Y_i}{\partial z}\right) + \dot{\omega}_i, \quad (7.16)$$

where $\dot{\omega}_i$ is the rate of change of Y_i due to chemical reaction.

A total ten transport equations are solved in the simulation model. The equations are for continuity ($\times 1$), momentum ($\times 2$), energy ($\times 1$), k-ϵ ($\times 2$), mixture fraction and its variance ($\times 2$), and progress variables for TGLDM ($\times 2$). They were solved numerically using a Flux-Corrected Transport (FCT) algorithm [184] with a finite-volume representation. This algorithm is suitable for dealing with flow fields with large gradients, such as that at the jet exit, which often cause significant numerical dispersion or dissipation in ordinary discretization schemes. A brief description of the fundamental principles of FCT scheme is given in Appendix D. The FCT scheme used in this work is nominally fourth-order accurate in space. A second-order Runge-Kutta time advance scheme was used for the temporal discretization. Since the equations for a fully compressible flow are solved, the coupling between the density and pressure fields was achieved directly through the energy equation in conjunction with the ideal gas state function.

A schematic of the simulation is shown in Fig. 7.2. The instantaneous probability density function is presumed to take on the form of
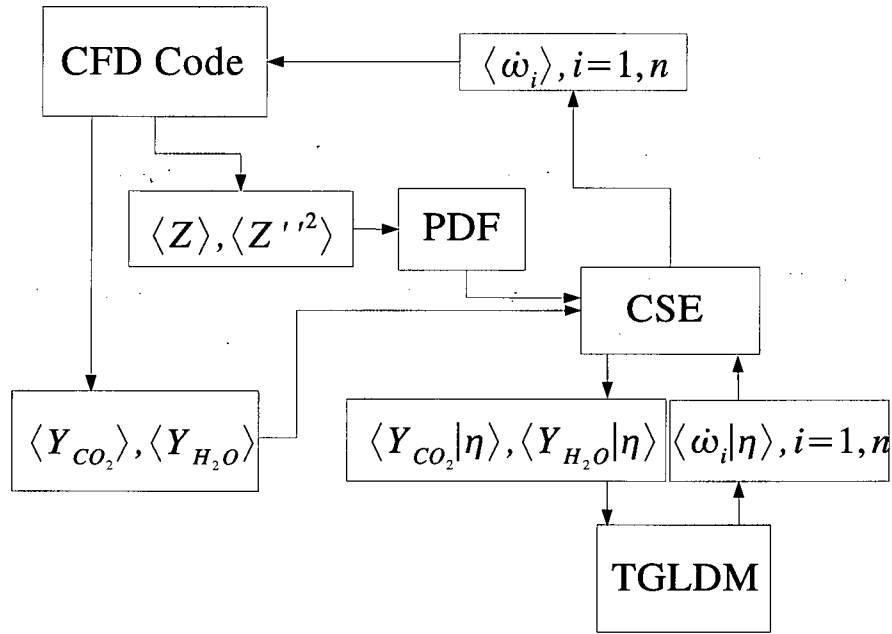
Figure 7.2: Structure of CSE-TGLDM method in the simulation

a β function, which is completely determined by the mean and variance of the mixture fraction. The transport equations for the instantaneous values of the mean and variance of mixture fraction are solved, as are those for the means of the two progress variables, Y_{CO_2} and Y_{H_2O}. The CSE module takes the PDF, $\langle Y_{CO_2} \rangle$ and $\langle Y_{H_2O} \rangle$ and solves for the conditional average of $\langle Y_{CO_2}|\eta \rangle$ and $\langle Y_{H_2O}|\eta \rangle$ using Eq. 7.4. The TGLDM module takes $\langle Y_{CO_2}|\eta \rangle$ and $\langle Y_{H_2O}|\eta \rangle$ as the input and performs an interior point search and interpolation to find the corresponding species mass fractions and reaction rates on the manifold. The conditional mass fractions of reaction scalar $\langle Y_i|\eta \rangle$ is reassembled using the PDF in the CSE module to get the unconditional mean, which is feed back to the CFD code to close the conservation equation.

The computational domain, which is half of the axisymmetric plane cutting through the center line of the shock tube, was discretized using

a 110×220 (radial $\times$ axial) structured grid. The nozzle exit was resolved using six grid points along the radial direction. A relatively fine mesh has been used close to the exit of the nozzle to resolve the sharp gradient locally. For the transient velocity profile at the nozzle exit of the injector, a polytropic expansion from the stagnation pressure was used. The polytropic coefficient was obtained by matching the steady state mass flow rate with the experimentally measured value.

7.5 Results and Discussion

7.5.1 Non-reactive Jet Validation

Prior to adding the combustion model, simulations for a transient non-reactive methane jet were performed to validate the CFD code, particularly the FCT scheme. The results are compared with experimental measurements using Schlieren photography. For the penetration length of a transient turbulent jet, Hill and Ouellette [185] proposed a scaling model based on the vortex-quasi-steady-state assumption of Turner [186] and the mass and momentum entrainment measurements from Ricou and Spalding [187]. For a self-similar transient jet, the model suggests that

$$\left(\frac{Z_t}{d\sqrt{\frac{\rho_i}{\rho_o}}} \right) = \Gamma \sqrt{\frac{\pi}{4}} \left(\frac{U_o t}{d\sqrt{\frac{\rho_i}{\rho_o}}} \right)^{0.5}, \qquad (7.17)$$

where Z_t is the penetration length; d is the nozzle diameter; ρ_i and ρ_o is the density of gas at the nozzle exit and in the ambient respectively; U_o is the jet exit velocity; and Γ is an empirical penetration number, which is assigned a value of 3. They also reported that the self-preserving aspect ratio of the jet for a penetration length over 20 nozzle diameters is in the range of 0.25 ± 0.5. They have shown that the above scaling

model agrees well with various experimental measurements for free jets with length larger than 20 nozzle diameters and with Reynolds number greater than 30,000. Figures 7.3 and 7.4 present the penetration length and aspect ratio of the jet as a function of time as calculated using the current numerical scheme in comparison with the prediction from the scaling model as well as the experimental results. For the validation cases, the injection pressure ratio was varied from 3 to 5. The ambient pressure was kept at 1 atm. The ambient and stagnation fuel temperatures were both round 300K. The experimental data presented are averaged over three independent tests. It can be seen that the agreement for the jet profile between the simulation and experiment is very good for the pressure ratios of 3. At the higher pressure ratios, the simulation overpredicts the jet penetration length by about 15 percent for a long injection duration, but the transient aspect ratio was predicted correctly. The difference in the simulated and measured penetration length for the high pressure ratio case may be related to the uncertainty in the inflow boundary conditions: the assumption of a polytropic expansion may not be suitable for a jet undergoing significant underexpansion at the nozzle exit. In the later reactive jet study, the injection pressure ratio was kept at 2.5, for which the current inflow boundary conditions appear to work well.

Fig. 7.5 shows a Schlieren-like picture obtained from the simulation results which was constructed from the calculated density field (see Appendix E for details), for a methane jet at 200 μs from the start of injection with an injection pressure ratio of 3. By comparing with the experimental results, it can be seen that some important features of the transient jet have been captured by the current numerical scheme. In particular, the simulated Schlieren image shows the vortex structure
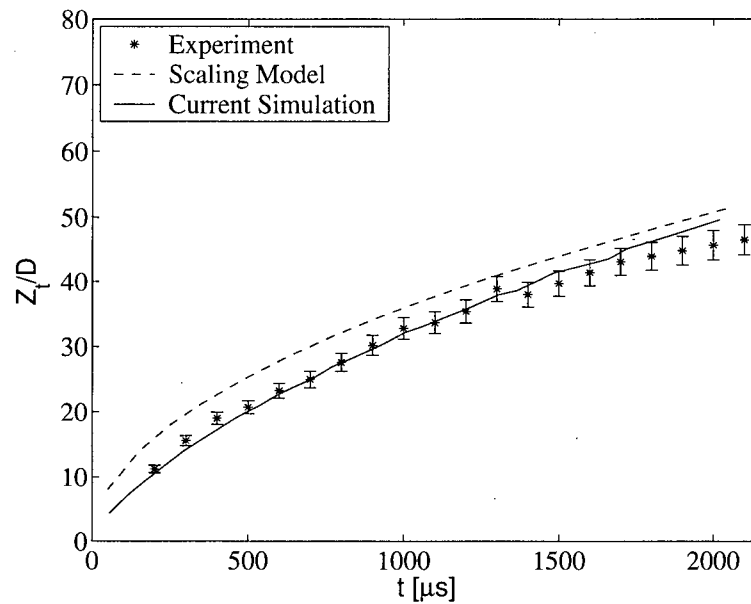
(a) Penetration Length
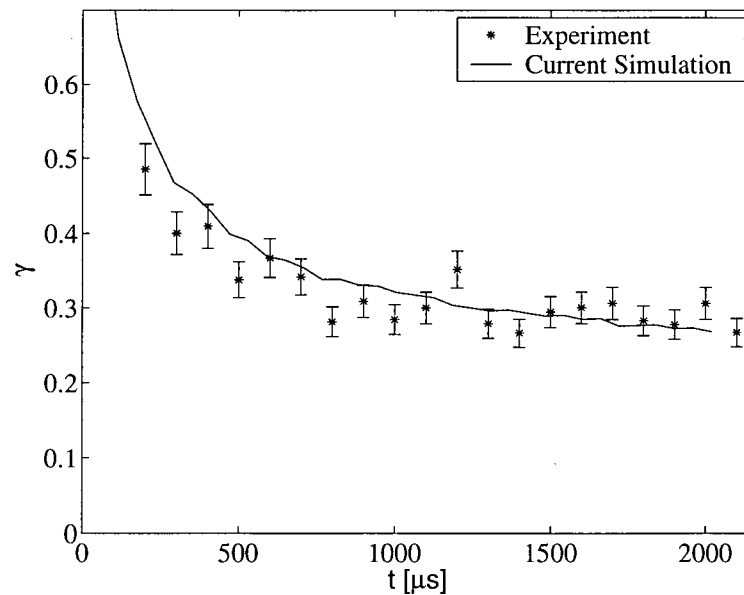
(b) Aspect Ratio

Figure 7.3: Comparison of simulation, scaling model and experimental measurement for the transient profiles of a non-reactive methane jet. The gas from the injector is pure methane and the ambient gas is air. The downstream pressure is 1 atm. The injection pressure ratio is 3.
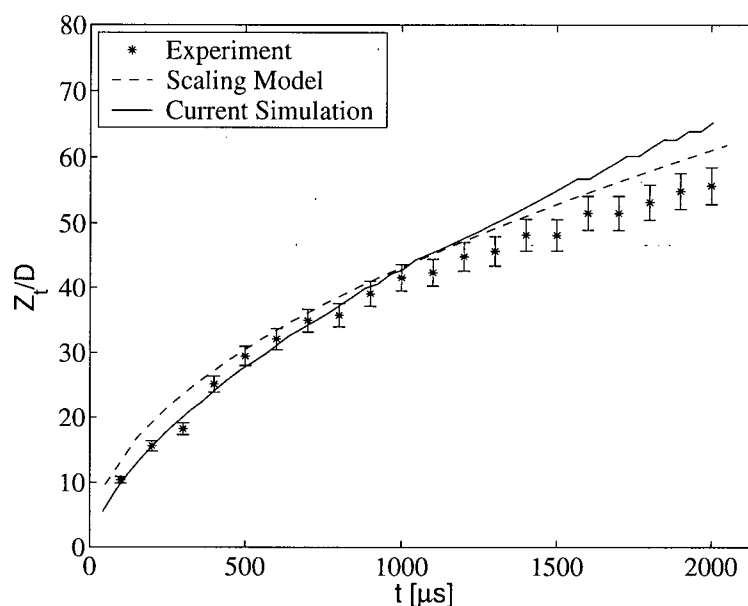
(a) Penetration Length
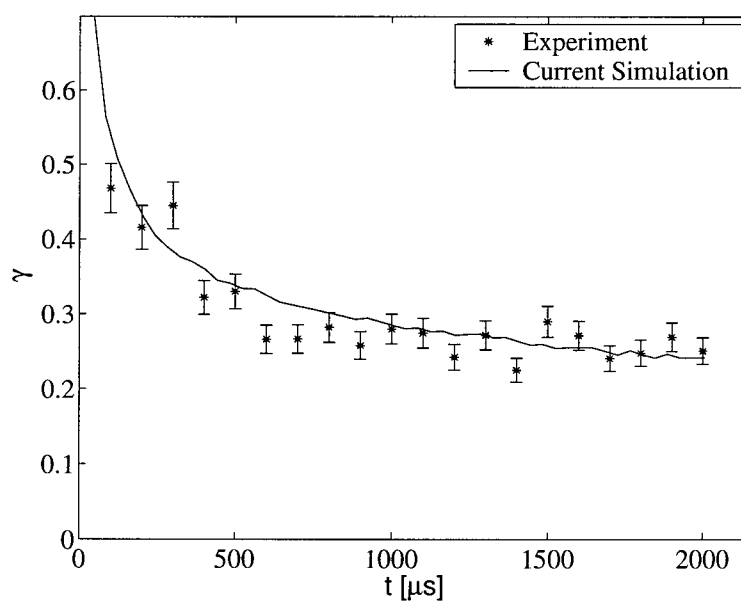
(b) Aspect Ratio

Figure 7.4: Comparison of simulation, scaling model and experimental measurement for the transient profiles of a non-reactive methane jet. The gas from the injector is pure methane and the ambient gas is air. The downstream pressure is 1 atm. The injection pressure ratio is 5.
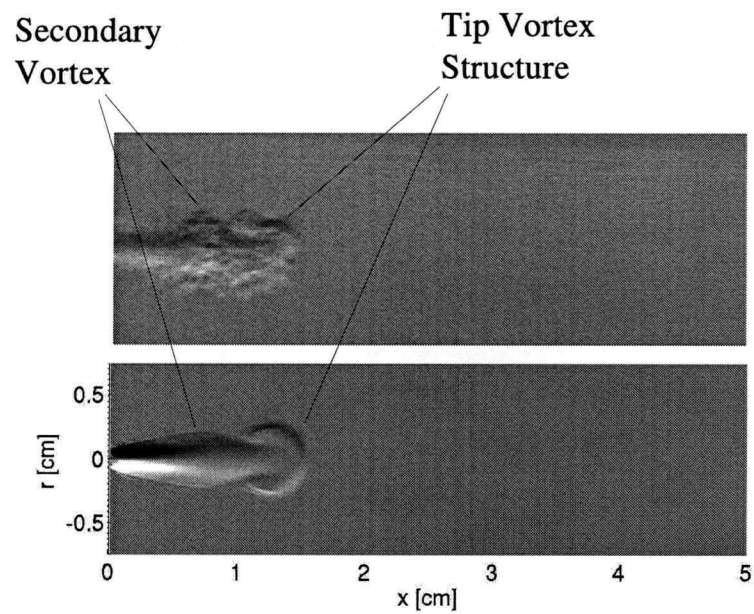
Figure 7.5: Comparison of simulated (bottom) and experimental (top) Schlieren images for a methane jet at $200\mu s$ from the start of injection. The injection pressure ratio is 3 and the ambient pressure is 1 bar.

at the tip of the jet and a forming secondary vortex following the primary vortex, both of which have been observed in the experiment. It is very important that the FCT scheme adopted in the current calculation is able to predict these structures correctly, because, for a reactive jet, the initial mixing field could be critical for determining the ignition delay time, the initial kernal location and subsequently, the spread of the flame.

7.5.2 Shock-tube Ignition

The ignition and combustion for the methane jet under the experimental conditions described in Table 7.1 has been simulated using the CSE-TGLDM combustion model described earlier. In the simulation, ignition delay is found by plotting the maximum mean value of a scalar associated with ignition as a function of time, then extrapolating the maximum slope of a scalar history back to the level at the onset of injection. Fig. 7.6 gives an example of how this procedure is used to calculate the ignition delay based on the maximum temperature trace. The corresponding location at which the ignition starts is recorded as the initial flame kernel.

Figure 7.7 compares the ignition delay obtained from the simulation with the experimental results. Three reaction scalars – temperature, OH and C_2H_2 – are used to establish the ignition delay from the simulation. It can be seen that the ignition delay calculated using the current model agrees well with the experimental measurements. As could be expected, the ignition delay defined based on C_2H_2 profile is considerably longer than that from OH and temperature. This is because C_2H_2 is mainly formed in the fuel rich region whereas the autoignition in a diffusion flame typically starts from the fuel lean side where the tem-
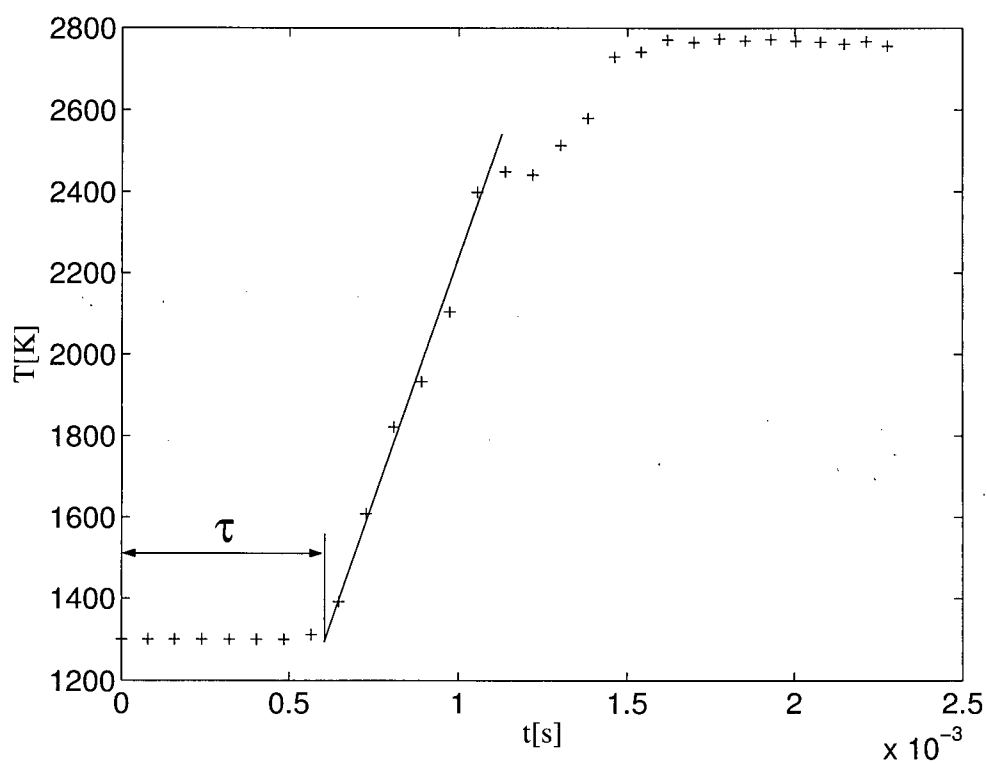
Figure 7.6: Definition of ignition using the scalar history. The symbol in the graph represents the maximum value of temperature in the computational domain at given time.
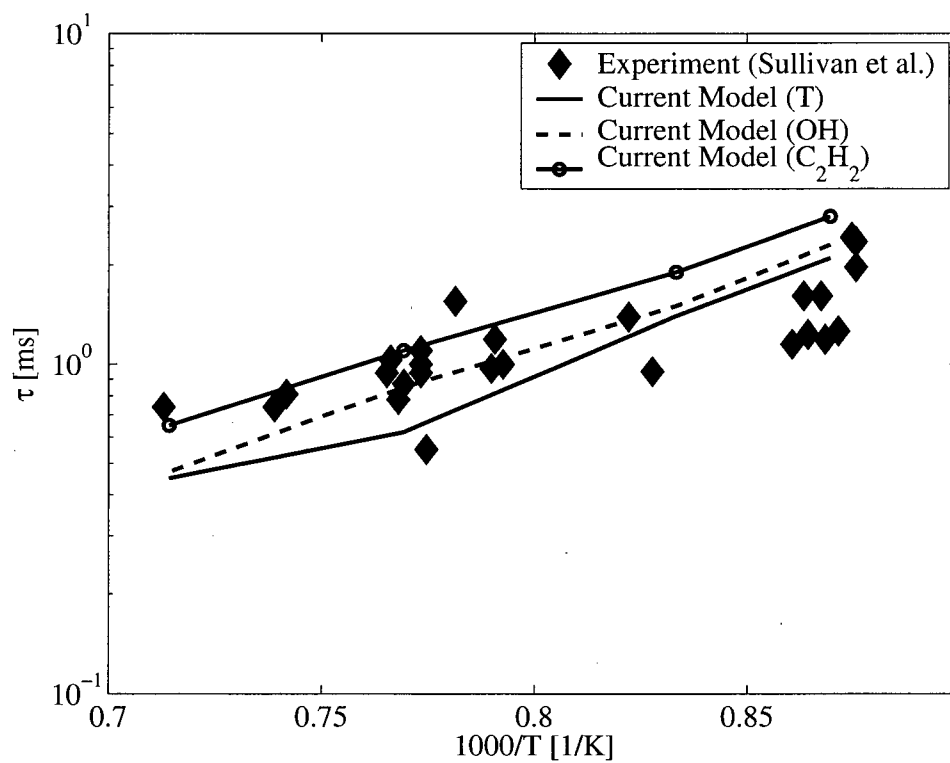
Figure 7.7: Comparison of ignition delay calculated using the CSE-TGLDM combustion model with experimental measurements. Detailed experimental conditions are given in Table 7.1. Experimental data are from Sullivan et al. [182]
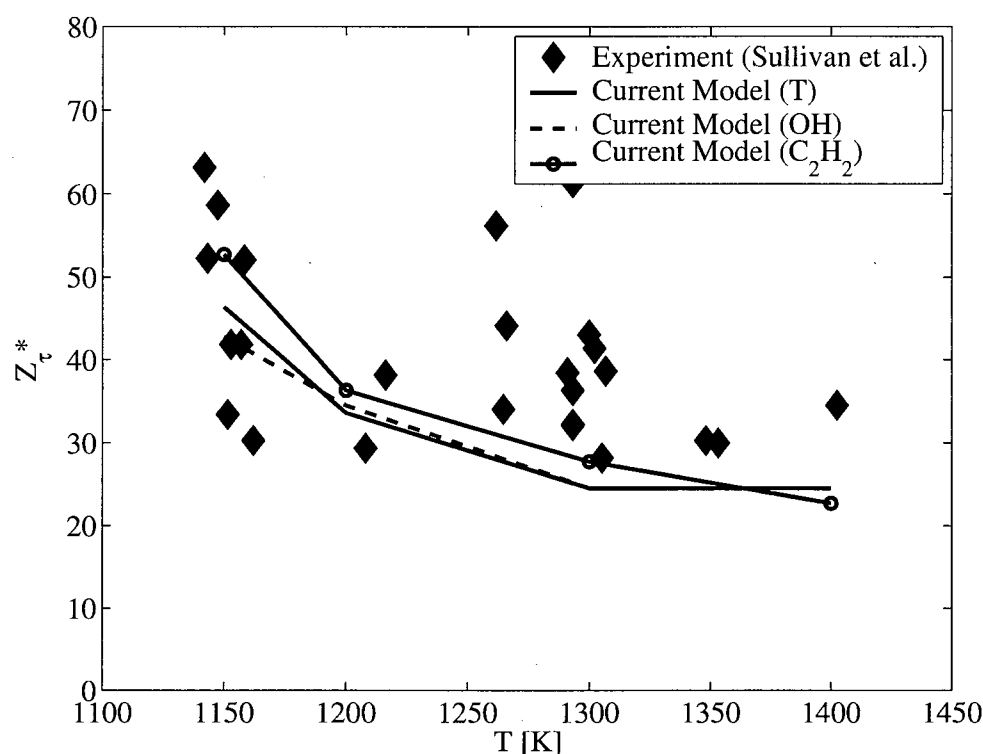
Figure 7.8: Comparison of axial locations of initial ignition kernel from the CSE-TGLDM combustion model with those from the experiment. The location is normalized by the nozzle diameter. The detailed experimental conditions are given in Table 7.1. Experimental data are from Sullivan et al. [182]

perature is higher.

Figure 7.8 shows a comparison of normalized ignition kernel locations. The experimental data shows very large scatter in this case. Nevertheless, the trend is predicted reasonably by the simulation.

Depending on the ambient air temperature and injection duration, two different combustion modes have been observed. The difference is illustrated in Figs. 7.9 to 7.14. When the ambient temperature is high, the ignition starts prior to the end of injection. A clearly defined diffusion flame is observed. The flame is confined to a thin outer layer of the jet, as shown in Figs. 7.9(a) and 7.10(a). It is interesting to notice

that the flame is not able to propagate back to the nozzle exit. This is because the high strain rate, indicated by the high variance of mixture fraction, causes a high rate of mass transport locally. The time scale associated with the physical perturbation is short, which makes ignition and a sustainable flame difficult to achieve in this region. When the fuel injection stops (at 1.5 ms), a drastic reduction of the mixture fraction close to the nozzle exit occurs, as is evident in Fig. 7.10(b). The expansion wave accompanying the end of injection cause a significant entrainment of air at the tail of the jet that leads to a rapid dilution of the jet locally. The regions with enhanced mixing can also be identified by observing the field of the variance of mixture fraction given in Fig. 7.11(b). Figure 7.12 shows the profile of the burning jet shortly after the end of injection. The flame is able to surround the entire jet. An increase of flame thickness was observed with the mixture fraction and the strain conditions (the variance of mixture fraction) close to the core of the jet becoming more favorable to the spread of the flame.

When the ambient temperature is reduced to 1150K, the chemical delay is long and ignition starts long after the end of injection. Significant mixing between the methane and air has already occurred at the moment of ignition. The jet burns in a partially premixed mode. The flame is able to propagate quickly from the edge into the core of the jet where the local stoichiometry is favorable. The combustion then spreads rapidly towards the tip and tail of the jet.

7.5.3 NO Prediction

Adapting CSE-TGLDM Model for NO Chemistry

The prediction of NO formation in the current jet flame presents another challenge to the CSE-TGLDM combustion model, particularly
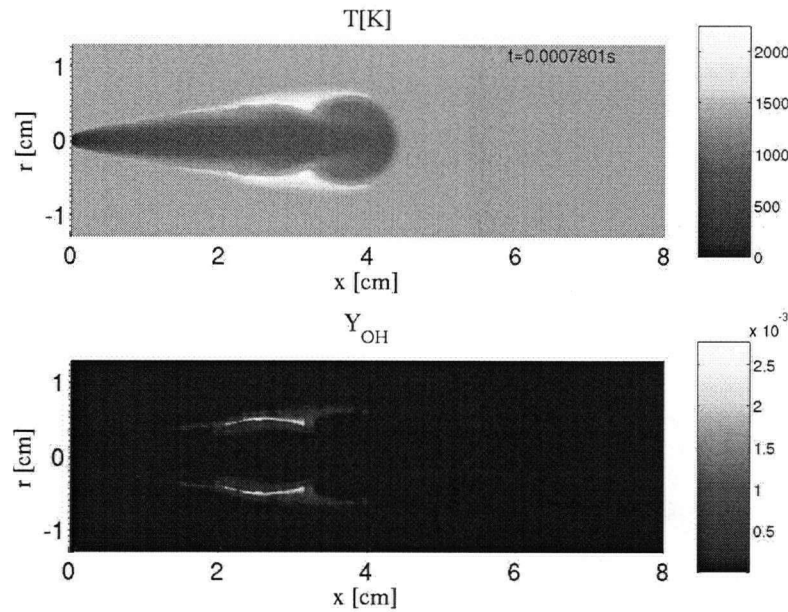
(a) T and OH mass fraction
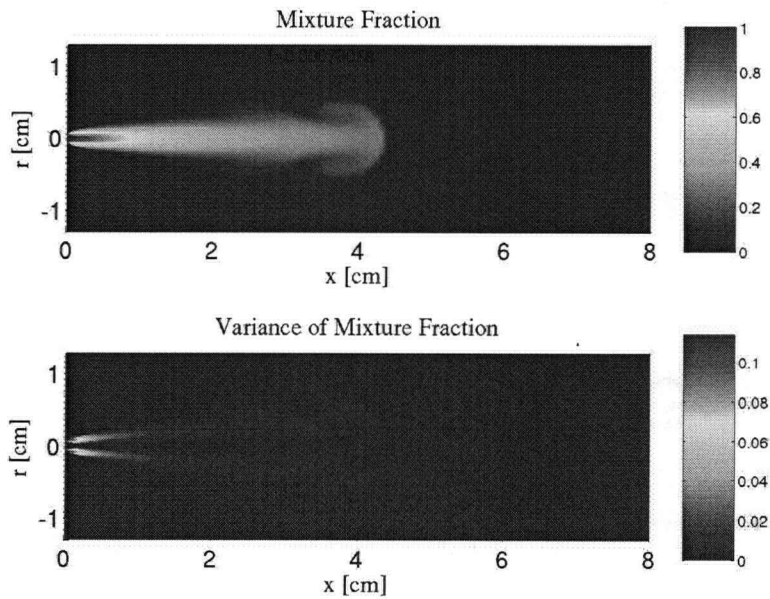
(b) $\langle Z \rangle$ and $\langle Z''^2 \rangle$

Figure 7.9: Profiles of reaction scalars, mixture fraction and its variance in the computational domain shortly after ignition. The ambient temperature is 1400K.
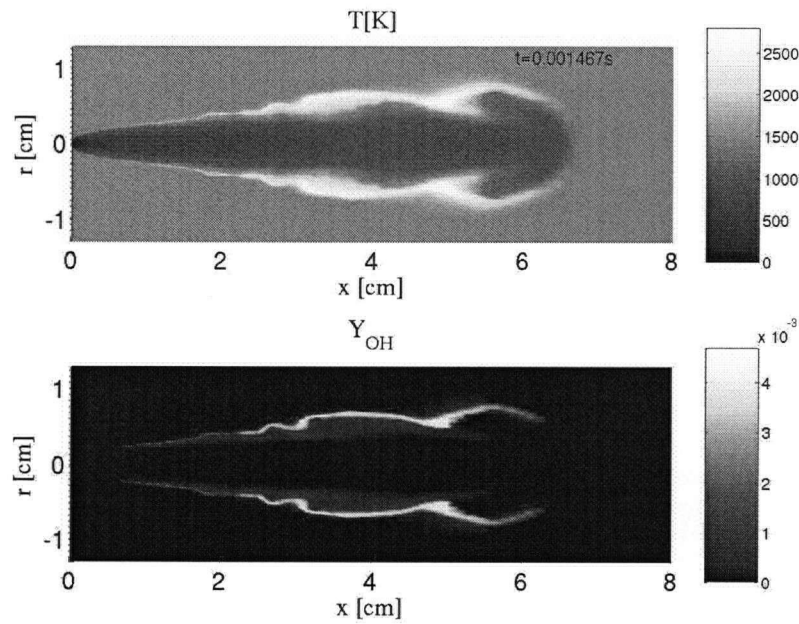
(a) T and OH mass fraction
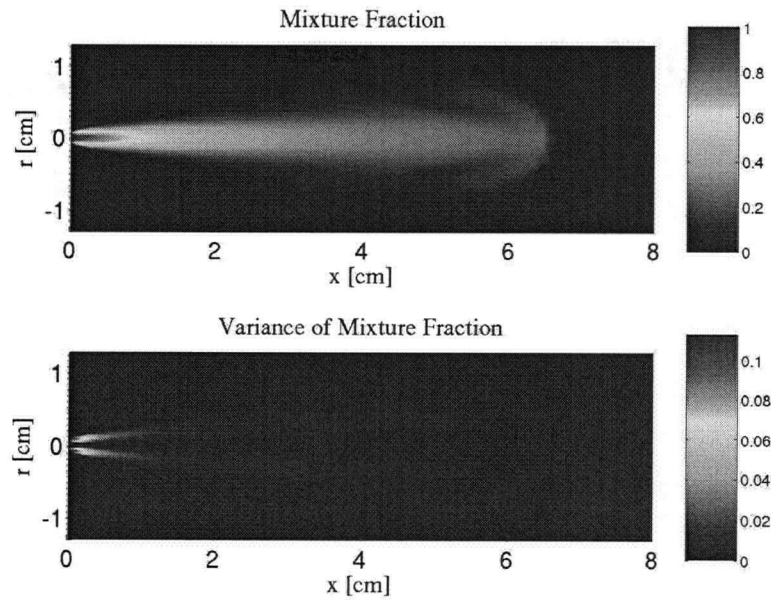
(b) $\langle Z \rangle$ and $\langle Z''^2 \rangle$

Figure 7.10: Profiles of reaction scalars, mixture fraction and its variance in the computational domain before the injection stops. The ambient temperature is 1400K.
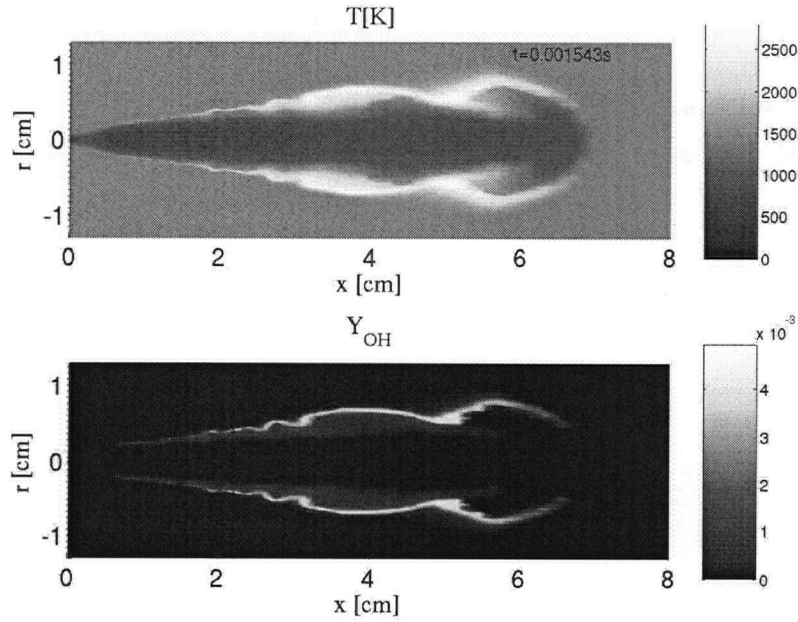
(a) T and OH mass fraction
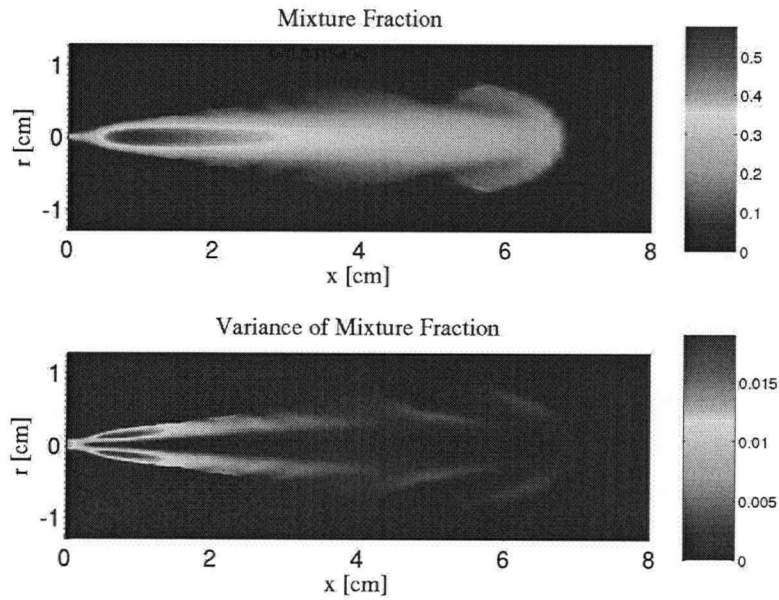
(b) $\langle Z \rangle$ and $\langle Z''^2 \rangle$

Figure 7.11: Profiles of reaction scalars, mixture fraction and its variance in the computational domain shortly after the injection stops. The ambient temperature is 1400K.
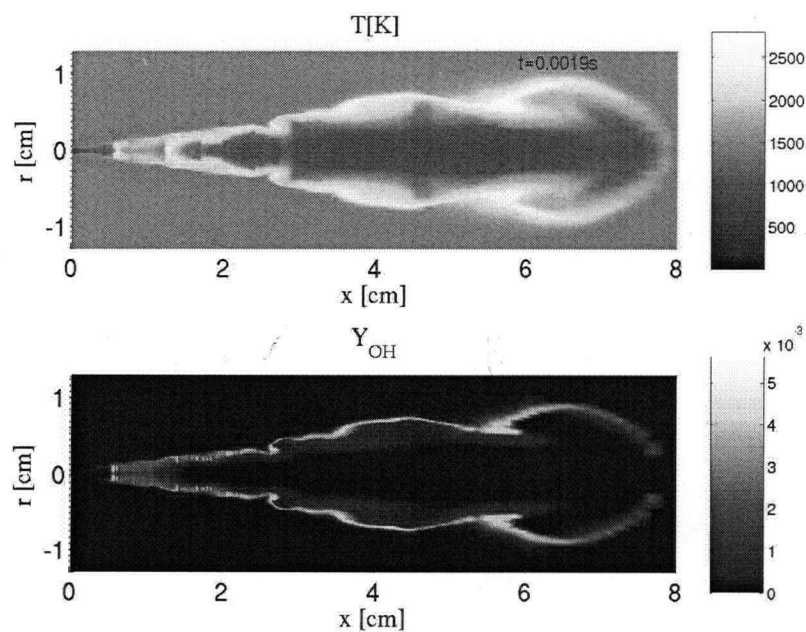
(a) T and OH mass fraction
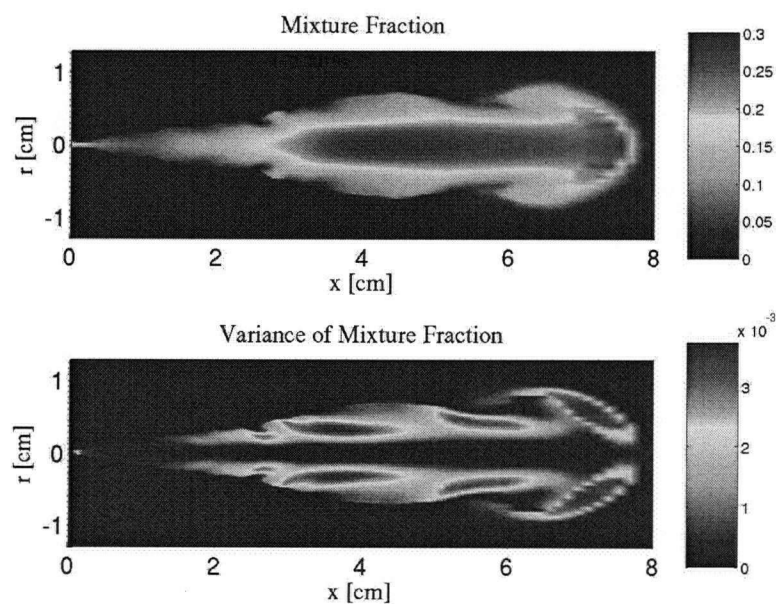
(b) $\langle Z \rangle$ and $\langle Z''^2 \rangle$

Figure 7.12: Profiles of reaction scalars, mixture fraction and its variance in the computational domain after the injection stops. The ambient temperature is 1400K.
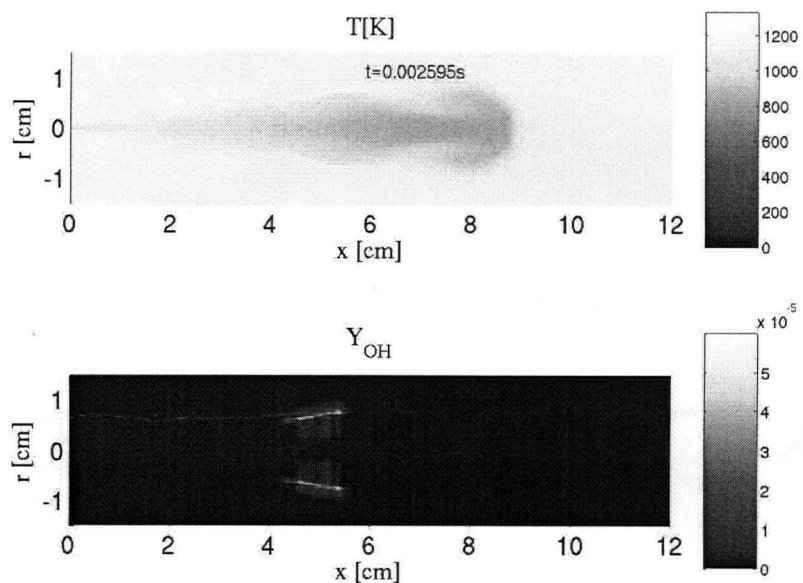
(a) T and OH mass fraction
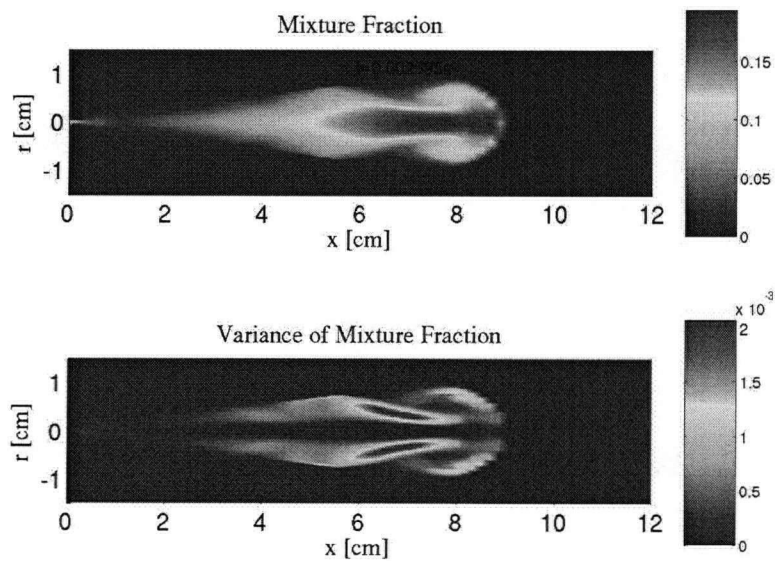
(b) $\langle Z \rangle$ and $\langle Z''^2 \rangle$

Figure 7.13: Profiles of reaction scalars, mixture fraction and its variance in the computational domain during ignition. The ambient temperature is 1150K.
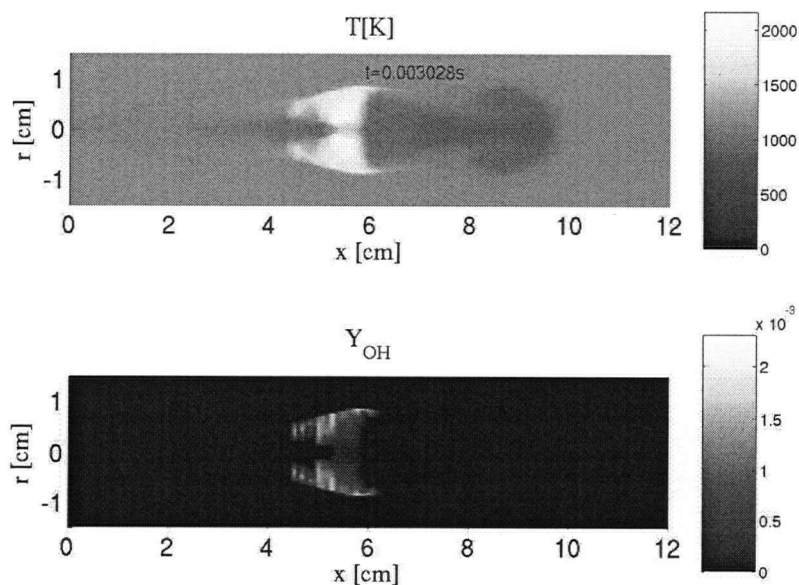
(a) T and OH mass fraction
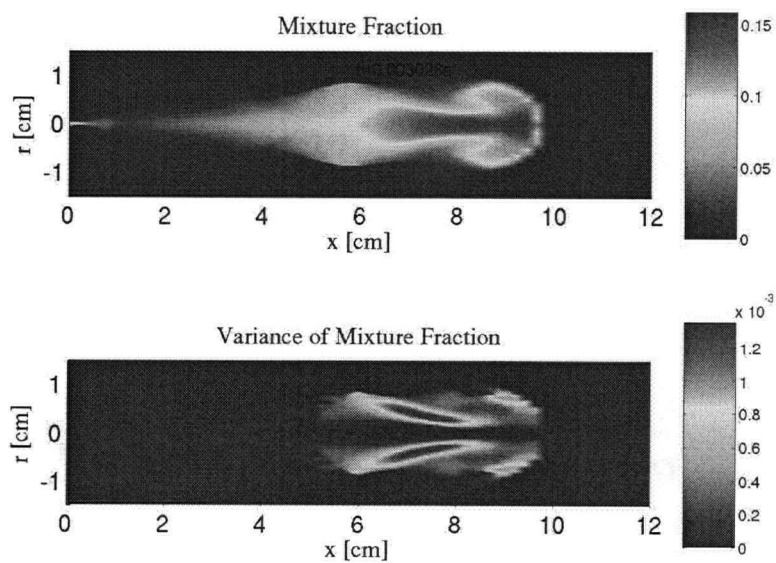
(b) $\langle Z \rangle$ and $\langle Z''^2 \rangle$

Figure 7.14: Profiles of reaction scalars, mixture fraction and its variance in the computational domain shortly after ignition. The ambient temperature is 1150K.

to the TGLDM method. This is because the chemical scale associated with NO is very long, thus its convergence onto the manifold is slow. In other words, the manifold cannot be used to represent the state of species for which the time scale is longer than that of the slow subspace. However, as reported by Nafe and Maas [92], the formation of NO has little effect on the main combustion mechanism of methane. It is thus possible to decouple the NO formation from the manifold and treat it separately. In a transient flame when the concentration of NO is significantly lower than its equilibrium concentration, the rate of NO formation is mainly governed by other reaction scalars such as the mass fractions of N, O, OH and temperature. The values of these scalars converge onto the manifold rapidly in the high temperature region of a flame, which means the rate of NO approaches the rate on manifold significantly faster than does its mass fraction. Thus in the simulation, the CSE-TGLDM model was modified to account for the formation of NO by adopting the following steps

- The transport equation for mean NO mass fraction is solved using the CFD code.

- The CSE module is called to calculated the conditional averages of the progress variables for the TGLDM.

- The conditional value of the production rate of NO, rather than its conditional mass fraction, is obtained from the TGLDM.

- The unconditional mean of the rate of NO is calculated by integrating the conditional average of the production rate with the PDF function.

- The mean source term for NO is returned to the CFD code to close

the transport equation.

Correction of Experimental Time

In the shock tube study, the end of an experiment is marked by the arrival of the rarefaction wave, which should also define the total simulation time. Unlike the shock wave, the rarefaction wave is a continuous wave. The pressure and temperature drops in the experimental region that accompany the arrival of the rarefaction wave occur in a finite time. For many of the experiments, the combustion does not end instantaneously when the rarefaction wave reaches the test section. Although the overall reaction rate drops drastically with decreasing temperature, it is nevertheless important to examine the effect of the cooling process on the overall NO production and adjust the simulation results accordingly. Ideally, it is desirable to simulate the expansion wave which can be realized by modifying the boundary conditions based on the experimental pressure trace. In practice, this leads to a significant increase in the computational time resulting from

1. the largely expanded the computational domain, and

2. higher dimensional TGLDMs required to address the large pressure change.

In this study, the finite-rate cooling process is addressed by extending the experimental time based on a simple thermodynamic model.

Assuming an isotropic expansion of the driven gas as the expansion wave arrives, the temperature drop in the driven gas can be estimated using the formula

$$T = T_o e^{-\lambda t}. \tag{7.18}$$

Here, λ is the inverse of a characteristic time scale, which can be evaluated from

$$\lambda = \frac{\gamma - 1}{\gamma \Delta t_{pc}}, \tag{7.19}$$

where γ is the local specific heat ratio of test gas, and Δt_{pc} is the characteristic time of the pressure drop, which is the time from the arrival of the rarefaction wave to when the pressure drops to 36.8% of its initial value. Assuming the global reaction for NOx formation is of second order and the reaction rate is governed by an Arrhenius expression, the instantaneous reaction rate can be correlated with the initial rate at $T = T_o$ using the formula

$$\frac{\omega}{\omega_o} = \left(\frac{T}{T_o}\right)^{2/(\gamma-1)} \exp\left(E(\frac{1}{T_o} - \frac{1}{T})\right), \tag{7.20}$$

where E is a global activation temperature. For NOx formation under diesel conditions, the value of E reported in the literature falls between 38000 and 45000K [4]. Substituting Eqs. 7.18 and 7.19 into Eq. 7.20, one obtains

$$\frac{\omega}{\omega_o} = \left(\frac{T}{T_o}\right)^{2/(\gamma-1)} \exp\left(\frac{E}{T_o}(1 - e^{\lambda t})\right). \tag{7.21}$$

An equivalent time extension Δt_x can be defined as

$$\omega_o \Delta t_x = \int_0^\infty \omega \, dt. \tag{7.22}$$

Substituting Eq. 7.21 into Eq. 7.22, we get

$$\Delta t_x = \int_0^\infty \exp\left(\frac{E}{T_o}(1 - e^{\lambda t}) - \frac{2\lambda t}{\gamma - 1}\right) dt. \tag{7.23}$$

The total NO formed is corrected using the rate at the end of the experimental time and Δt_x to address the finite cooling rate of the rarefaction wave. A schematic of the correction method is shown in Fig. 7.15. For the experimental conditions in this work, the following values are used: $E = 41,000K$, $T \approx 2800K$ (approximately the adiabatic flame
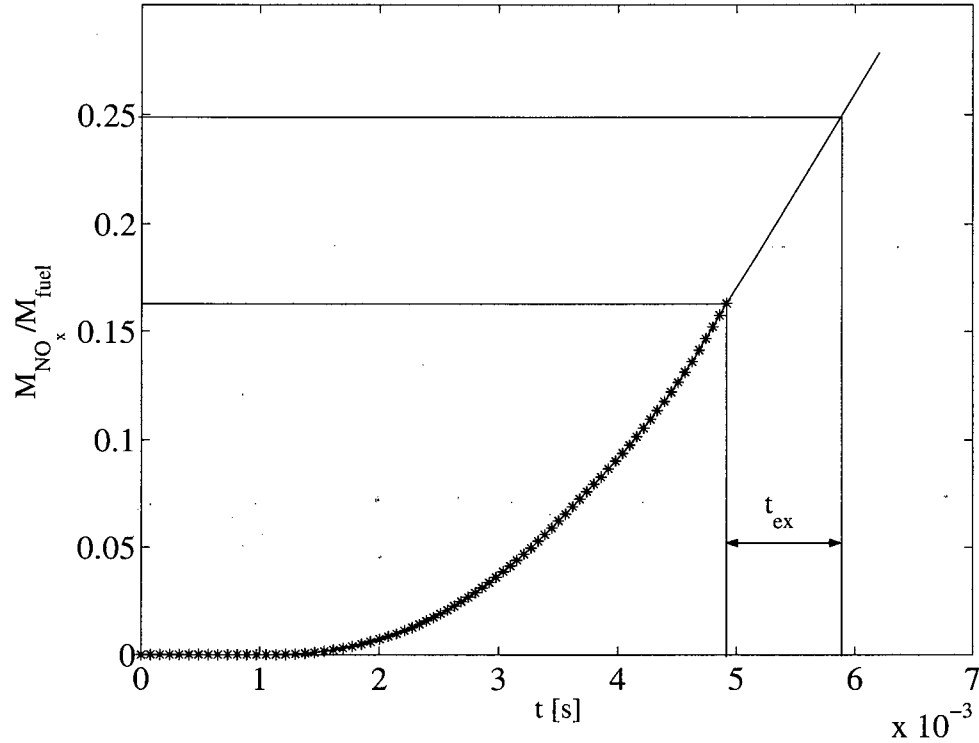
Figure 7.15: Correction of NO mass fraction for the finite cooling rate of rarefaction wave

temperature), $\Delta t_{pc} \approx 5.6$ ms (from the experimental pressure trace). The calculated time extension from Eq. 7.23 is around 0.96 ms, which is nearly 20% of the simulation time prior to applying the adjustment. Fig. 7.16 presents the predicted total mass of NOx (NO + NO$_2$) formed from the combustion of the methane jet in comparison with the experimental measurements. It can be seen that, with the correction, the total NOx from the simulation is brought in line with the experimental data.

7.5.4 Combustion Bomb Ignition

To further examine the performance of the new combustion model in predicting the ignition delay of turbulent methane jets at elevated pressures and moderate temperatures, simulations have been performed
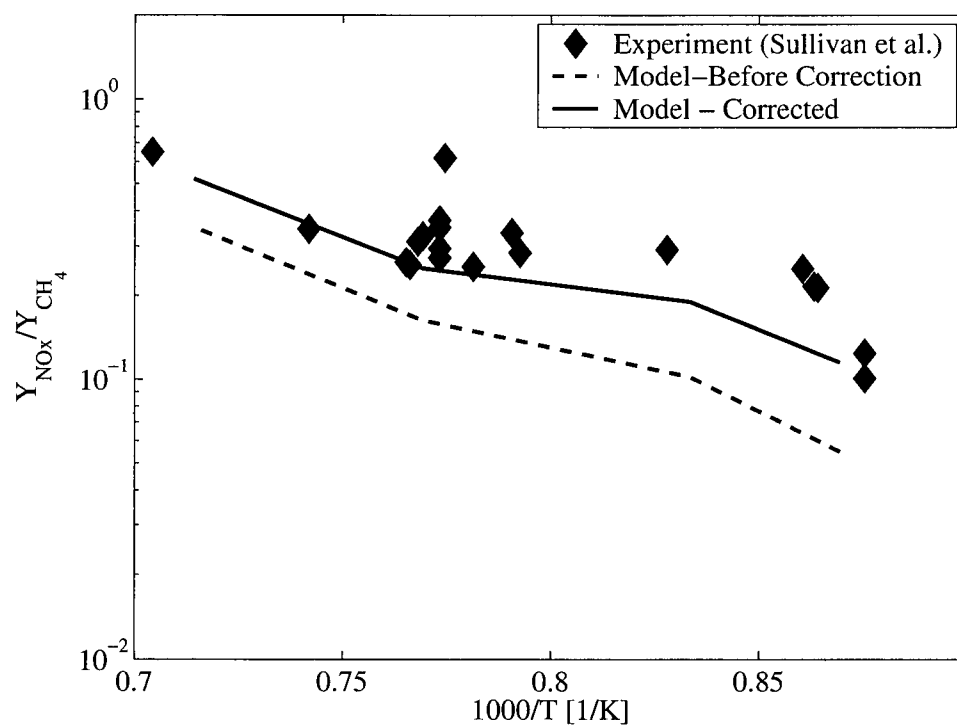
Figure 7.16: Comparison of predicted NOx mass fraction and experimental measurements. The total NOx mass is normalized by the total mass of fuel injected into the shock tube

for the experimental conditions reported by Naber et al. [188]. The experiments were conducted in a constant-volume combustion bomb facility. The experimental conditions and main parameters used as input to the simulation are given in Table 7.2. The TGLDMs were built based on the fuel and oxidizer compositions reported in the same paper. The ignition criterion used by Naber et al. was based on a net increase of pressure over 14 kPa, which corresponds to the heat release from 0.33 mg of methane. The flow velocity in the combustion chamber prior to injection is significantly lower than the jet velocity, which, according to the authors, does not cause a significant perturbation to the jet. In the simulation, the flow in the combustion chamber is treated as quiescent prior to injection. The disk-shaped combustion chamber geometry was not modeled in the simulation; rather, the computational domain was scaled to match the total volume of the experimental chamber. Previous experimental studies have shown that, before the jet impinges on the wall of its enclosure, the shape of the enclosure has little effect on the development of the jet if the initial flow condition in the enclosure is quiescent [189].

Table 7.2: Operating conditions for the experiment of Naber et al. [188]

$d_{injector}$ [mm]	P_i [bar]	P_o [bar]	$\rho_o^{21}[kg/m^3]$	T_i [K]	T_o [K]
0.25	207	63-92	20.4	450	1100-1600

Fig. 7.17 shows a comparison of simulated ignition delay and the experimental data. The ignition in the simulation is defined by the time when the consumption of methane exceeds 3.3 mg. It can be seen that the agreement between the simulation and Naber's experimental data is very good, which further confirms the validity of the model.
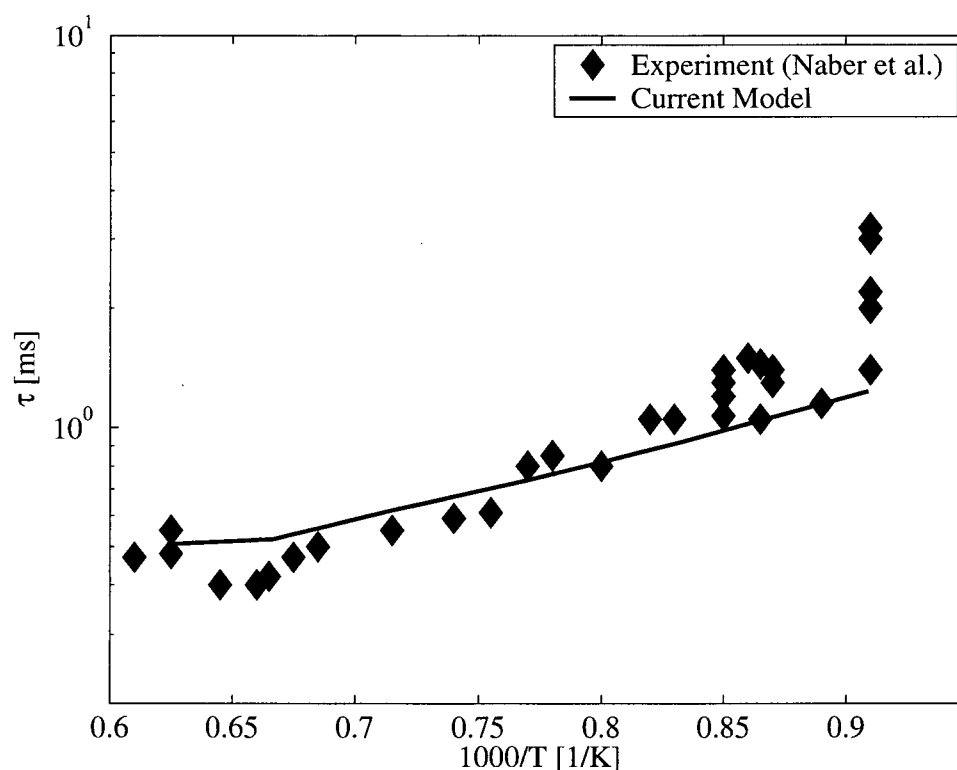
Figure 7.17: Simulation results for the experiment of Naber et al. [188]

---

[21]Ambient Density
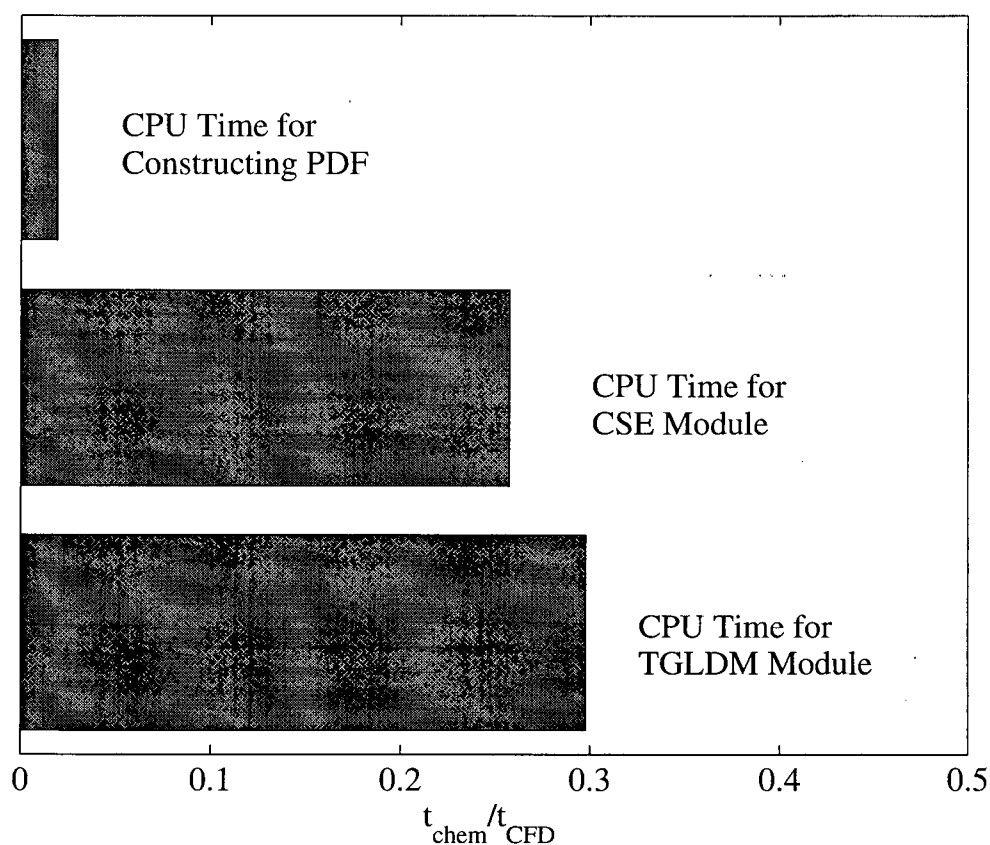
Figure 7.18: Comparison of CPU time on CSE-TGLDM module with that on CFD module in a typical simulation.

7.5.5 Computational Time

A comparison of CPU time for a typical calculation using the CSE-TGLDM model is shown in Fig. 7.18. The time used for calculating the chemical source term is compared with that required for solving the transport equations. It can be seen that the CPU time spent on the CSE-TGLDM combustion module is significantly less than that on the CFD module. Further efficiency improvements of the combustion model might be possible with a more advanced manifold-search algorithm and matrix inversion routine.

7.6 Conclusions

In this work, a CSE-TGLDM combustion model has been used to simulate the ignition and combustion of transient turbulent methane jets under engine-relevant conditions. The model is able to predict the experimental ignition delay and ignition kernel locations measured in this study reasonably well; it also predicts ignition data reported in the literature. A method that allows for calculating the slow formation rate of NO using the CSE-TGLDM model was discussed. The total NOx calculated from the simulation is less than the experimental measurement. The discrepancy could be explained by the finite cooling time of the rarefaction wave which was not reflected in the numerical model.

For the development of the jet flame after ignition, two different modes have been identified based on initial oxidizer temperature. At high temperatures, the ignition starts prior to the end of injection. A thin diffusion flame confined to the outer skin of the jet is observed. During the injection, the strain close to the exit of the jet is high; the diffusion flame is not able to survive in that region. The end of injection leads to a rapid entrainment of air at the tail of the jet and the spread of the diffusion flame locally. At lower temperatures, partially premixed combustion occurs due to significant mixing of fuel and oxidizer prior to ignition. For both combustion modes, the favorable conditions for the propagation or spread of flame are those with the right stoichiometry and low strain-rate.

Chapter 8
Conclusions and Future Work

8.1 Summary and Conclusions

The objective of this thesis work is to address three fundamental questions regarding the study of natural gas combustion under the conditions relevant to internal combustion engines and other practical combustion devices.

- Firstly, what is the chemical kinetic mechanism that governs the combustion of natural gas (methane based fuels) in IC engines? The question involves two parts - one regards to the kinetic mechanism that results in the ignition delay of natural gas or methane–additive mixtures; the other is related to the formation of pollutant emissions, in particular, the formation of nitrogen oxides.

- Secondly, how to use such a detailed chemical kinetic mechanism, which demands excessive CPU time, in modeling reactive flows with limited computational resource. If a reduction method has to be used, what is the most efficient and accurate method for such an application.

- Finally, can we properly represent the interaction between the chemical kinetics of natural gas combustion and turbulence in an engine-like environment using an existing turbulent combustion

214

model in conjunction with detailed chemistry. To what degree can the model reflects the underlining physics and how accurate is the results in comparison with experimental measurements?

In this thesis work, the first and last questions were studied with the experimental investigations followed by numerical studies. The second question was approached using a combination of analytical and numerical methods.

To address the first question, experimental studies have been conducted on the ignition of homogeneous methane-air mixtures enriched with small fraction of ethane and/or propane. The experimental pressure ranges from 16 to 40 atm and temperature ranges from 900 to 1400K. The concentrations of ethane and propane were varied so that the resulting mixtures cover the range of the two non-methane hydrocarbons from typical natural gas sources worldwide. A complex behavior has been observed for the promoting effect of ethane/propane, which varies significantly with temperature and pressure.

The ignition delay results from the experimental study provide a valuable database for developing and validating detailed chemical kinetic mechanisms. The kinetic modeling work started with a GRI Mechanism (Version 1.2) as a base mechanism. It was found that the base mechanism significantly overpredicts the ignition delay time of natural gas mixtures under the conditions of this study. Through literature reviews and kinetic analyses, it was found that the proxy chemistry are important for natural gas ignition for temperatures below 1300K, while elementary reactions related to methylperoxy, ethyl peroxy and propel peroxy radicals are not included in the GRI mechanisms, which was mainly developed based on high temperature kinetic data. With the addition of key reactions related to peroxy chemistry, the new kinetic

mechanism was able to achieve a good agreement with the experimental results in predicting ignition delay of various modeled natural gas mixtures.

The kinetic study based on the new mechanism reveals a switch of the dominant ignition-promoting mechanism for ethane/propane with changing temperature. At high temperature (T>1200K), the H-atom abstraction from ethane and the subsequent decomposition of ethyl radical is very efficient in producing H atoms, which enhance the chain branching and accelerate methane ignition.

The promoting effect of ethane and/or propane at low temperature (T<1100K) is attributed to the increasing significance of methylperoxy and methylhydroperoxide chemistry. In particular, additional ethane and propane was found to increases rate of production of methylhydroperoxide (CH_3O_2H), which subsequently decomposes to generate an OH radical. Since the depletion of OH radical is the main rate-limiting mechanism for methane ignition at temperature below 1100K, the contribution from the above mechanism is more prominent at low temperatures.

To further examine the kinetic interaction between methane and higher alkanes in this study, an analytical solution was obtained for the ignition delay of the test mixtures by systematically reducing the skeletal mechanism identified from the reaction-flow analysis using the steady state assumption. The analytical model agrees well with the detailed-kinetic model for both ignition delay and the concentrations of main intermediate species. Both the analytical model and kinetic analysis of the detailed mechanism show that the addition of ethane-/propane does not change the main reaction path of the methane system. The promotion of ignition is realized through accelerating the ini-

tiation phase in the induction period.

Another fuel of interest, whose ignition mechanism was studied in this work, is hydrogen-enriched methane. This is motivated by the potential of achieving higher combustion efficiency and lower emission level through hydrogen enrichment. Shock tube experiments on the ignition of two stoichiometric CH_4-H_2-air mixtures under high pressure and moderate temperature conditions have been conducted. It has been observed that the promoting effect of hydrogen is, in general, less than that of ethane and propane; it also decreases with decreasing temperature. The difference between pure methane and methane-/hydrogen mixtures is more prominent at 16 atm than that at 40 atm. A low fraction of hydrogen addition shows only weak effects on the ignition delay of methane under the conditions explored.

A numerical study of methane/hydrogen/air ignition under the experimental conditions of this work has been conducted using the detailed chemical kinetic mechanism developed from the work described in Chapter 3. The mechanism was further optimized based on the latest kinetic data from the literature to obtain an improved agreement between the model and experimental results. The effect of hydrogen on methane ignition was mainly related to the generation and consumption of H radicals. At high temperature, the rapid oxidation of hydrogen molecules through R85 ($OH + H_2 \rightleftharpoons O + H_2O$) and the fast branching reaction R39 ($H + O_2 \rightleftharpoons O + OH$) are mainly responsible for the stronger ignition promoting effect. The rates of both R85 and R39 decrease rapidly with decreasing temperature. At lower temperature, reactions between H_2 and CH_3O_2 account for a weak effect of hydrogen on methane ignition due to the production of extra H radicals. The effect of hydrogen in the reaction system exhibits a negative

pressure dependence, which implies that the third-order recombination reactions (R33-R38) are rate-limiting steps under the conditions of this work.

The new mechanism was completed by adding a NOx submechanism selected from the literature. A series of five candidate NOx mechanisms from the literature was added to the new natural gas reaction mechanism developed in this work; they were used to predict experimental NOx data from a stirred reactor [66] and a counterflow diffusion flame [36]. The numerical results using the mechanism proposed by Glarborg et al. [84] and GRI-Mech 2.11 show the best agreement with the experimental data. The reburn of NO by methyl radicals is found to be important in reaction systems at relatively low temperatures (such as those in the experiment of Steele et al. [66]. A consistent trend has been identified between higher predicted NO concentration and higher rate of a key reaction for prompt NO formation, which suggests that the prompt NO mechanism is important under the conditions of this study.

The manifold methods were used to address the second question at the beginning of this chapter, i.e. to find an effective method to use detailed chemistry with the maximum reduction of computational time and reasonable accuracy. While the Intrinsically Low Dimensional Manifold method proposed by Maas and Pope [94] is plausible for its rigorous mathematical derivation, its solution is difficult to achieve due to the highly non-linear implicit construction equation. Furthermore, the fact that ILDM is a non-inertial manifold increases the difficulty of applying the method. The trajectory generated low-dimensional manifold method [94], on the other hand, offers an solution to the above two problems of ILDM. However, the method has never been system-

atically validated or put in direct comparison with ILDM to illustrate the difference. The above issues of TGLDM were addressed in this thesis work.

For a one-dimensional manifold, the TGLDM method with constrained equilibrium states as the onset for the trajectories yields an essentially identical manifold as does the ILDM method. This result supports the concept proposed in this thesis work. That is the trajectory method can be used to reduce the problem of solving for an inertial manifold from a global optimization problem to a local optimization problem by optimizing the onset of trajectories.

The difference between the general TGLDM and the ILDM generated using the method of Maas and Pope [90] has been investigated. Several merits of the TGLDM method have been identified: the construction of the manifold is less mathematically involved than the conventional ILDM method; the reaction vector of a TGLDM is always in the tangent plane of the manifold. An analysis of a hypothetical reaction system showed that if the initial state of the reaction system is known, the TGLDM with optimized initial conditions gives a better approximation to detailed chemistry than the ILDM.

The performance of the TGLDM in predicting reactive scalar profiles for a methane/air mixture has been investigated in modeling laminar premixed flames, laminar flamelets, and the transient processes in a perfectly stirred reactor. In general, reasonable agreement between the results using the TGLDM and those from the detailed chemistry has been reached. When the physical time scales approaches the chemical time scales in the fast subspace, relatively large errors occur using the TGLDM. Combustion systems modeled using the detailed chemical kinetic mechanism appears to be more resilient to large perturba-

tions than those modeled with the TGLDM method.

Finally, to address the last question as one of the objectives of this thesis work, a CSE-TGLDM combustion model has been proposed. The model was used in simulating transient turbulent natural gas combustion under engine-relevant conditions to examine the performance of TGLDM derived from the new reaction mechanism in conjunction with a turbulence closure method . The model is able to predict correctly the experimental ignition delay and ignition kernel locations measured in this study as well as ignition data reported in the literature.

The formation of NO, which is a slow process, was decoupled from the main combustion process. The fact that the concentration of NO approaches equilibrium at a rate significantly slower than most of the species related to NO formation suggests that the formation rate of NO converges significantly faster than its mass fraction on a manifold. The CSE-TGLDM model is then adjusted to calculate the unconditional rate of NO rather than the unconditional mass fraction as was used for other species. The total NOx calculated from the simulation is less than the experimental measurement. The discrepancy could be explained by the finite cooling time of the rarefaction wave which was not reflected in the numerical model.

For the development of the jet flame after ignition, two different modes have been identified based on temperature. At high temperature, the ignition starts prior to the end of injection. A thin diffusion flame confined to the outer skin of the jet was observed. During the injection, the strain close to the exit of the jet is high; the diffusion flame is not able to survive in that area. The end of injection leads to a rapid entrainment of air at the tail of the jet, and the spread of the diffu-

sion flame locally. At lower temperature, a partially premixed mode combustion due to a significant mixing of fuel and oxidizer prior to ignition was found. The flame is able to propagate rapidly through the core of the jet that leads the jet to expand rapidly. For both combustion modes, the favorable conditions for the propagation or spread of flame are those with the right stoichiometry and low strain-rate.

Through the course of this thesis work, the three fundamental questions regarding the natures of natural gas combustion under engine-relevant conditions and the methods of exploring these natures have been addressed consecutively. The study of chemical kinetics for methane – additive ignition and NOx formation increased our knowledge regarding the governing factors which can be used to control the combustion of natural gas. In particular, a better understanding have been obtained regarding the effects of the environmental factors such as temperature and pressure as well as the effects from the fuel constituents on the ignition characteristics of natural gas. The development of TGLDM method and CSE-TGLDM model provides a powerful tool for applying the knowledge of combustion chemistry in detailed modeling of a turbulent combustion process. This study has shown that the TGLDM method, although being relatively simple in its formulation, can provide a reasonable approximation to detailed chemistry in modeling many reactive flow problems with significantly reduced computational cost. Such modeling work in conjunction with experimental investigations offers a promising approach for obtaining critical information regarding the combustion process in natural gas engines, and can eventually be used to direct engine designs and improve combustion control strategies.

8.2 Future Work

Further experimental and kinetic studies are necessary to improve our understanding of the ignition characteristics of methane+additive mixtures under high-pressure and intermediate-temperature conditions. There are still a significant number of elementary reactions in the detailed reaction mechanism whose rate constants are less well studied. Some of these rate constants are essential for determining the overall reaction rate of the system. There is a high priority to obtain reliable experimental or theoretical data on the rate constants of these reactions.

Given the need to achieve accurate NOx predictions in modeling practical combustion devices, detailed reaction flow and sensitivity analyses are warranted to understand the major factors contributing to the NOx formation under various operating conditions. In particular, there are strong interests in understanding the reason behind the high NO_2 measurement from a directly-injected natural gas engine under high EGR conditions.

It is important to further our study on improving the performance of manifold methods in the regions where the physical time scale are comparable with the time scale in the fast subspace. There is also an urgent need to study the generation of manifolds that can be used in the combustion simulation for internal combustion engines. The current manifolds are generated subject to a constrain of constant pressure and adiabatic boundary conditions, while in an IC engine, the pressure varies constantly and the heat transfer to the wall of the combustion chamber is significant. A higher dimensional manifold is thus necessary to account for these factors. With the increase of dimensions of manifold, the storage and retrieving methods soon becomes a critical

issue. One possible solution to this problem is to use *in situ* tabulation of the manifold that eliminates the requirement of storing manifolds or sections of manifold that are never used by a specific problem. While the method in its concept is very attractive, its realization, limitation, efficiency and accuracy needs to be carefully studied before it can be applied to turbulent combustion modeling for IC engines.

Bibliography

[1] S. Soylu, Examination of combustion characteristics and phasing strategies of a natural gas hcci engine, Energy Conservation and Management 46 (2005) 101–119.

[2] A. Ishida, A. Nishimura, M. Uranishi, R. Kihara, A. Nakamura, P. Newman, The development of the ecos-ddf natural gas engine for medium-duty trucks: Exhaust emission reduction against base diesel engine, JSAE Review 22 (2001) 237–243.

[3] P. Ouellette, High-pressure direct injection of natural gas in diesel engines, proceeding of ngv 2000: Ngv- transportation for the new century, Seventh International Conference and Exhibition on Natural Gas Vehicles, International Association For Natural Gas Vehicles, Inc., Yokohama, Japan (2000) 235–241.

[4] G. McTaggart-Cowan, S. Rogak, P. Hill, W. Bushe, S. Munshi, Effects of operating condition on particulate matter and nitrogen oxides emissions from a heavy-duty direct injection natural gas engine using cooled exhaust gas recirculation, International Journal of Engine Research 5 (2004) 499–511.

[5] G. McTaggart-Cowan, W. Bushe, P. Hill, S. Munshi, The application of exhaust gas recirculation to a heavy duty direct injection of natural gas engine, International Journal of Engine Research 5 (2004) 175–191.

[6] G. McTaggart-Cowan, W. Bushe, S. Rogak, P. Hill, S. Munshi, The effects of varying egr test conditions on a direct injection of natural gas heavy-duty engine with high egr levels, SAE Technical Paper 2004-01-2955. SAE Transactions, Journal of Engines 113 (2004) 1500–1509.

[7] G. McTaggart-Cowan, W. Bushe, P. Hill, S. A. Munshi, Supercharged single cylinder heavy duty engine for high pressure direct injection of natural gas, International Journal of Engine Research 4 (2004) 315–329.

[8] G. McTaggart-Cowan, W. Bushe, S. Rogak, P. Hill, S. Munshi, Injection parameter effects on a direct injected, pilot ignited, heavy duty natural gas engine with egr, SAE Technical Paper 2003-01-3089. SAE Transactions, Journal of Fuels and Lubricants 112 (2003) 2103–2109.

[9] D. J. Seery, C. T. Bowman, An experimental and analytical study of methane oxidation behind shock wave, Combustion and Flame 14 (1970) 37–47.

[10] A. Lifshitz, k. Scheller, A. Burcat, G. B. Skinner, Shock-tube investigation of ignition in methane-oxygen-argon mixtures, Combustion and Flame 16 (1971) 331.

[11] T. Tsuboi, H. G. Wagner, Homogeneous thermal oxidation of methane in reflected shock waves, Proceedings of the Combustion Institute 15 (1974) 883.

[12] A. K. Cheng, R. K. and Oppenheim, Autoignition in methane-hydrogen mixtures, Combustion and Flame 58 (1984) 125–139.

[13] A. Grillo, M. W. Slack, Shock tube study of ignition delay times in methane-oxygen-nitrogen-argon mixtures, Combustion and Flame. 27 (1976) 377–381.

[14] D. W. Walker, L. H. Diehl, W. A. Strauss, R. Edse, Investigation of ignition properties of flowing combustible gas mixtures, Report No. AFAPL-TR-69-82, USAF Report.

[15] A. Turbiez, A. ElBakali, J. F. Pauwels, A. Rida, P. Meunier, Experimental study of a low pressure stoichiometric premixed methane, methane/ethane, methane/ethane/propane and synthetic natural gas flames, Fuel 83 (2004) 933–941.

[16] M. Mbarawa, E. W. Mureithi, Modelling the effects of natural gas composition on dual-fuel combustion under constant-volume conditions, Journal of the Institute of Energy 76 (2003) 2–9.

[17] J. Hiltner, R. Agama, F. Mauss, B. Johansson, M. Christensen, Homogeneous charge compression ignition operation with natural gas: Fuel composition implications, Journal of Engineering for Gas Turbine and Power-Transaction of ASME 125 (2003) 837–844.

[18] E. B. Khalil, G. A. Karim, A kinetic investigation of the role of changes in the composition of natural gas in engine applications, Journal of Engineering for Gas Turbine and Power-Transaction of ASME 124 (2002) 404–411.

[19] A. Burcat, K. Scheller, A. Lifshitz, Shock-tube investigation of comparative ignition delay times for c1-c5 alkanes, Combustion and Flame 16 (1971) 29.

[20] R. W. Crossley, E. A. Dorko, K. Scheller, A. Burcat, The effect of higher alkanes on the ignition of methane-oxygen-argon mixtures in shock waves, Combustion and Flame 19 (1972) 373–378.

[21] C. K. Westbrook, W. J. Pitz, Effects of propane on ignition of methane-ethane-air mixtures, Combustion Science and Technology 33 (1983) 315–319.

[22] M. Frenklach, D. E. Bornside, Shock-ignition in methane-propane mixture, Combustion and Flame 56 (1984) 1–27.

[23] L. J. Spadaccini, M. B. Colket III, Ignition delay characteristics of methane fuels, Progress in Energy and Combustion Science 20 (1994) 431–460.

[24] A. El Bakali, P. Dagaut, L. Pillier, P. Desgroux, J. F. Pauwels, A. Rida, P. Meunier, Experimental and modeling study of the oxidation of natural gas in a premixed flame, shock tube, and jet-stirred reactor, Combustion and Flame 137 (2004) 109–128.

[25] N. Lamoureux, C. E. Paillard, Natural gas ignition delay times behind reflected shock waves: Application to modeling and safety, Shock Waves 13 (2003) 57–68.

[26] Annual energy outlook 2006 with projections to 2030, Energy Information Administration Report DOE/EIA-0383(2006), http : //www.eia.doe.gov/oiaf/aeo/.

[27] A. G. Gaydon, I. R. Hurle, The shock tube in high temperature chemical physics, Chapman and Hall Ltd., 1963.

[28] J. Huang, P. G. Hill, W. K. Bushe, S. R. Munshi, Shock-tube study of methane ignition under engine-relevant conditions: experiments and modeling, Combustion and Flame 136 (2004) 25–42.

[29] E. L. Petersen, D. F. Davidson, R. K. Hanson, Kinetics modeling of shock-induced ignition in low-dilution $ch4/o2$ mixtures at high pressures and intermediate temperatures, Combustion and Flame 117 (1999) 272–290.

[30] E. Petersen, D. Davidson, R. Rohrig, M. and Hanson, High-pressure shock-tube measurements of ignition times in stoichiometric $h2/o2/ar$ mixtures, In 20th Symp. Int. Shock Waves (1996) 941–946.

[31] D. C. Bull, J. E. Elsworth, G. Hooper, Susceptibility of methane-ethane mixtures to gaseous detonation in air, Combustion and Flame. 34 (1979) 327.

[32] C. S. Eubank, M. J. Rabinowitz, W. C. J. Gardiner, R. E. Zellner, Shock initiated ignition of natural gas-air mixtures, Eighteenth Symposium (International) on Combustion. The Combustion Institute, Pittsburgh (1981) 1767.

[33] R. M. R. Higgin, A. Williams, A shock-tube investigation of the ignition of lean methane and n-butane mixtures with oxygen, Sixteenth Symposium (International) on Combustion. The Combustion Institute, Pittsburgh (1968) 579.

[34] R. Zellner, K. J. Niemitz, J. Warnatz, W. C. J. Gardiner, C. S. Eubank, J. M. Simmif, Prog. in Astro and Aero 88 (1981) 252.

[35] J. R. Griffiths, D. Coopersthwaite, C. H. Philips, C. K. Westbrook, Auto-ignition temperature of binary mixtures of alkane in a closed vessel: Comparisons between experimental measurements and numerical predictions, 23rd Symposium (international) on Combustion (1990) 1745.

[36] S. C. Li, F. A. Williams, Nox formation in two-stage methane-air flames, Combustion and Flame 118 (1999) 399–414.

[37] K. Hughes, T. Turnyi, A. Clague, P. M. J., Development and testing of a comprehensive chemical mechanism for the oxidation of methane, International Journal of Chemical Kinetics 33 (2001) 513–538.

[38] T. B. Hunter, H. Wang, L. T. A., F. M., The oxidation of methane at elevated pressure: experiments and modeling, Combustion and Flame 87 (1991) 365–370.

[39] M. Frenklach, H. Wang, M. Goldenberg, G. P. Smith, D. M. Golden, B. C. T., R. K. Hanson, W. C. Gardiner, V. Lissianski, Gri-mech–an optimized detailed chemical reaction mechanism for methane combustion, Report No. GRI-95/0058.

[40] C. T. Bowman, R. K. Hanson, D. F. Davidson, W. C. J. Gardiner, V. Lissianski, G. P. Smith, D. M. Golden, F. M., M. Goldenberg, Gri-mech 2.11, $http : //www.me.berkeley.edu/grimech/$.

[41] G. P. Smith, D. M. Golden, M. Frenklach, N. W. Moriarty, B. Eiteneer, M. Goldenberg, C. T. Bowman, R. K. Hanson, S. S. Song, W. C. Gardiner, V. V. Lissianski, Z. Qin, Gri-mech3.0, $http : //www.me.berkeley.edu/grimech/..$

[42] E. Ranzi, A. Sogaro, P. Gaffuri, C. Pennati, C. K. Westbrook, W. J. Pitz, A new comprehensive reaction mechanism for combustion of hydrocarbon fuels, Combustion and Flame 99 (1994) 201–211.

[43] C. K. Westbrook, An analytical study of the shock tube ignition of methane and ethane, Combustion Science and Technology 20 (1979) 5.

[44] T. B. Hunter, T. A. Litzinger, H. Wang, M. Frenklach, Ethane oxidation at elevated pressures in the intermediate temperature regime: Experiments and modeling, Combustion and Flame 104 (1996) 505–523.

[45] I. R. Roger, Natural gas/hydrogen mixtures for low noxious emissions, Journal of Scientific and Industrial Research 62 (2003) 64–70.

[46] A. Raju, B. Ramesh, A. and Nagalingam, Effect of hydrogen induction on the performance of a natural-gas-fueled lean-burn si engine, Journal of the Institute of Energy 73 (2000) 143–148.

[47] C. G. a. F. T. W. Bauer, Effect of hydrogen addition on the performance of methane-fueled vehicles. part i, effect on si engine performance, International Journal of Hydrogen Energy 26 (2001) 55–70.

[48] R. Sierens, E. Rosseel, Variable composition hydrogen/natural gas mixtures for increased engine efficiency and decreased emissions, Journal of Engineering for Gas Turbines and Power-Transactions of the ASME 122 (2000) 135–140.

[49] S. Allenby, A. Chang W. C. and Megaritis, M. L. Wyszynski, Hydrogen enrichment: a way to maintain combustion stability in a natural gas fueled engine with exhaust gas recirculation, the potential of fuel reforming, proceedings of the institution of mechanical engineers, part d, Journal of Automobile Engineering 215 (2001) 405–418.

[50] J. L. Gauducheau, B. Denet, G. Searby, A numerical study of lean ch4/h2/air premixed flames at high pressure, Combustion Science and Technology. 137 (1998) 81–99.

[51] Y. Ju, T. Niioka, Ignition simulation of methane/hydrogen mixtures in a supersonic mixing layer, Combustion and Flame 102 (1995) 462–470.

[52] J. Y. Ren, T. T. Egolfopoulos, F. N. and Tsotsis, Nox emission control of lean methane-air combustion with addition of methane reforming products, Combustion Science and Technology 174 (2002) 181–205.

[53] C. G. Fotache, G. Dreutz, T, C. K. Law, Ignition of hydrogen enriched methane by heated air, Combustion and Flame 110 (1997) 429–440.

[54] D. Davidson, M. DiRosa, A. Chang, R. Hanson, C. Bowman, A shock tube study of methane decomposition using laser absorption by ch3, Twenty-fourth Symposium (International) on Combustion, The Combustion Institute (1992) 589–596.

[55] C. L. Yu, C. Wang, M. Frenklach, Chemical kinetics of methyl oxidation by molecular oxygen, Journal of Physical Chemistry 99 (1995) 14377 – 14387.

[56] R. A. Marcus, Unimolecular dissociation and free radical recombination reactions, Journal of Chemical Physics 20 (1952) 359–364.

[57] K. K. Kuo, Principles of combustion, John Wiley and Son, New York, 2005.

[58] E. F.N., P. Cho, C. Law, Laminar flame speeds of methane-air mixtures under reduced and elevated pressures, Combustion and Flame 76 (1989) 375.

[59] A. Garforth, C. Rallis, Laminar burning velocity of stoichiometric methane-air: pressure and temperature dependence, Combustion and Flame 31 (1978) 53.

[60] G. Andrews, D. Bradley, Burning velocity of methane/air mixtures, Combustion and Flame 19 (1972) 275.

[61] T. Iijima, T. Takeno, Effects of temperature and pressure on burning velocity, Combustion and Flame 65 (1986) 35.

[62] J. Warnatz, U. Maas, W. Dibble, R, Combustion, 2nd Edition, Springer-Verlag, New York, 1999.

[63] Y. B. Zeldovich, The oxidation of nitrogen in combustion and explosives, Acta Physicochim USSR 21 (1946) 577.

[64] J. S. Bernstein, A. Fein, J. B. Choi, C. Terrill, A. Sausa, S. L. Howard, R. J. Locke, A. W. Miziolek, Laser-based flame species profile measurements: A comparison with flame model predictions, Combustion and Flame 92 (1993) 85–105.

[65] D. Heard, J. Jeffries, G. Smith, D. Crosley, Lif measurements in methane/air flames of radicals important in prompt-no formation, Combustion and Flame 88 (1992) 137.

[66] R. Steele, P. Malte, D. Nichol, J. Kramlich, Nox and n2o in lean-premixed jet-stirred flames, Combustion and Flame 100 (1995) 440.

[67] W. Bartok, V. Engleman, R. Goldstein, E. delValle, Basic kinetic studies and modeling of nitrogen oxide formation in combustion processes, AIChE Symposium Series 68 (1972) 30–38.

[68] B. Williams, J. Fleming, Comparative species concentrations in ch4/o2/ar flames doped with n2o, no and no2, Combustion and Flame 98 (1994) 93.

[69] T. Etzkorn, S. Muris, J. Wolfrum, C. Dembny, H. Bockhorn, P. Nelson, A. Attia-Shahin, J. Warnatz, Destruction and formation of no in low pressure stoichiometric ch4/o2 flames, Twenty-fourth Symposium (International) on Combustion, The Combustion Institute (1992) 925–932.

[70] D. L. Baulch, C. J. Cobos, R. A. Cox, P. Frank, G. Hayman, T. Just, J. A. Kerr, T. Murrells, M. J. Pilling, J. Troe, J. Walker, R. W. and Warnatz, Evaluated kinetic data for combustion modeling, supplement i, ref. data, Journal of Physical Chemistry 23 (1994) 847–1033.

[71] J. B. Heywood, Internal Combustion Engine Fundmentals, McGraw-Hill, 1988.

[72] C. P. Fenimore, Studies of fuel-nitrogen species in rich flame gases, 17th Symposium (intl) on combustion, the combustion institute, Pittsburgh (1979) 661–670.

[73] C. P. Fenimore, Formation of nitro oxide in premixed hydrocarbon flames, 13th Symposium (intl) on combustion, the combustion institute, Pittsburgh (1970) 373–380.

[74] P. Glarborg, J. A. Miller, R. J. Kee, Kinetic modeling and sensitivity analysis of nitrogen oxide formation in well-stirred reactors, Combustion and Flame 65 (1986) 177–202.

[75] Y. Matsui, A. Yuuki, Radical concentrations and prompt no formation in hydrocarbon-air premixed flames, Jpn. J. Appl. Phys. 24.

[76] D. Lindackers, M. Burmeister, P. Roth, Perturbation studies of high temperature c and ch reactions with n2 and no, Symp. Int. Combust. Proc. 23 (1991) 251 – 257.

[77] J. Miller, S. Walch, Prompt no: theoretical prediction of the high-temperature rate coefficient for $ch + n_2 \rightarrow hcn + n$, International Journal of Chemical Kinetics 29 (1997) 253 – 259.

[78] J. A. Miller, C. T. Bowman, Mechanism and modeling of nitrogen chemistry in combustion, Progress in Energy and Combustion Science 15 (1989) 287–338.

[79] A. H. Lefebvre, The role of fuel preparation in low-emission combustion, Journal of Engineering for Gas Turbine and Power-Transaction of ASME 117 (1995) 617–654.

[80] S. C. Li, I. N., F. A. Williams, Reduction of nox formation by water sprays in strained two-stage flames, Journal of Engineering for Gas Turbines and Power-Transactions of the ASME 119 (1997) 836–843.

[81] M. U. Alzueta, P. Glarborg, K. Dam-Johansen, Low temperature interactions between hydrocarbons and nitric oxide: An experimental study, Combustion and Flame 109 (1997) 25–36.

[82] P. G. Kristensen, P. Glarborg, K. Dam-Johansen, Nitrogen chemistry during burnout in fuel-staged combustion, Combustion and Flame 107 (1996) 211–222.

[83] P. Glarborg, P. G. Kristensen, S. H. Jensen, A flow reactor study of hnco oxidation chemistry, Combustion and Flame 98 (1994) 241–258.

[84] P. Glarborg, M. U. Alzueta, K. Dam-Johansen, A flow reactor study of hnco oxidation chemistry, Combustion and Flame 115 (1998) 1–27.

[85] M. Frenklach, Complex chemical reaction systems, mathematical modeling and simulation, Springer series in chemical physics 47 (1987) 2–16.

[86] H. Wang, M. Frenklach, Detailed reduction of reaction mechanism for flame modeling, Combustion and Flame 87 (1991) 365–370.

[87] S. Lam, D. A. Goussis, Research on computational singular perturbation, Progress Report #1, Report #1749(a)-MAE, Department of Mechanical and Aerospace Engineering, Princeton University, 1987.

[88] S. Lam, D. A. Goussis, The csp method for simplifying kinetics, International Journal of Chemical Kinetics 26 (1994) 461–486.

[89] T. Lu, Y. Ju, C. K. Law, Complex csp for chemistry reduction and analysis, Combustion and Flame 126 (2001) 1445–1455.

[90] U. Maas, S. B. Pope, Simplifying chemical kinetics: Intrinsic low-dimensional manifolds in composition space, Combustion and Flame 88 (1992) 239–264.

[91] W. Press, B. Flannery, S. Teukolsky, W. Vetterling, Numerical recipes: The art of scientific computing, Cambridge University Press, New York, NY, 1986.

[92] J. Nafe, U. Maas, Modeling of no formation based on ildm reduced chemistry, Proceeding of the Combustion Institute 29 (2002) 1379–1385.

[93] S. J. Fraser, The steady and equilibrium approximation: a geometrical picture, Journal of Chemical Physics 88 (1988) 4732.

[94] S. B. Pope, U. Maas, Simplifying chemical kinetics: trajectory-generated low-dimensional manifolds, FDA 93-11.

[95] J. P. Ignizio, T. M. Cavalier, Linear programming, Prentice Hall International Series in Industrial and Systems Engineering, Prentice Hall, Englewood Cliffs, NJ, 1994.

[96] P. N., Laminar diffusion flamelet models in non-premixed turbulent combustion, Progress in Energy and Combustion Science 10 (1982) 369–399.

[97] A. Y. Klimenko, R. W. Bilger, Conditional moment closure for turbulent combustion, Progress in energy and combustion science 25 (1999) 595–687.

[98] S. B. Pope, Pdf methods for turbulent reactive flow, Progress in Energy and Combustion Science 11 (1985) 119–192.

[99] A. R. Masri, S. B. Pope, Pdf calculations of piloted turbulent non-premixed flames of methane, Combustion and Flame 81 (1990) 13–29.

[100] A. T. Norris, S. B. Pope, Modeling of extinction in turbulent-diffusion flames by the velocity-dissipation-composition pdf method, Combustion and Flame 100 (1996) 211–220.

[101] V. Saxena, S. B. Pope, Pdf calculation of major and minor species in a turbulent piloted jet flame, Twenty-Seventh Symposium (International) on Combustion, the Combustion Institute (1998) 1081–1086.

[102] C. K. Law, Steady-state diffusion flame structure with lewis number variation, Combustion Science and Technology 29 (1982) 129–145.

[103] W. P. Jones, W. J. H, Calculation methods for reacting turbulent flows: A review, Combustion and Flame 48 (1982) 1–26.

[104] T. Saitoh, O. Y., Unsteady behavior of diffusion flames and pre-mixed flames for counter flow geometry, Combustion Science and Technology 12 (1976) 135.

[105] F. MauB, D. Keller, N. Peters, A lagrangian simulation of flamelet extinction and re-ignition in turbulent jet diffusion flames, Twenty-third symposium (Int.) on combustion, the combustion institute (1990) 693–698.

[106] N. Peters, Turbulent combustion, Cambridge University Press, Cambridge, 2000.

[107] P. J. Coelho, N. Peters, Unsteady modeling of a piloted methane/air jet flame based on the eulerian particle flamelet model, Combustion and Flame 124 (2001) 444–465.

[108] H. Barths, C. Antoni, N. Peters, Three-dimensional simulation of pollutant formation in a di diesel engine using multiple interactive flamelets, SAE technical paper, No. 982459.

[109] C. A. Hergart, H. Barths, N. Peters, Modeling the combustion in a small-bore diesel engine using a method based on representative interactive flamelets, SAE technical paper, No. 1999-01-3550.

[110] C. Hasse, H. Barths, P. N., Modeling the effect of split injections in diesel engines using representative interactive flamelets, SAE technical paper, No. 1999-01-3547.

[111] H. Barths, C. Hasse, P. N., Computational fluid dynamics mod-elling of non-premixed combustion in direct injection diesel en-gines, International Journal of Engine Research 1 (2000) 249–267.

[112] S. Rao, C. J. Rutland, A flamelet time scale model for non-premixed combustion including chemical kinetic effects, Com-bustion and Flame 133 (2003) 189–191.

[113] N. Swaminathan, Flamelet regime in non-premixed combustion, Combustion and Flame 129 (2002) 217–219.

[114] A. Y. Klimenko, Multicomponent diffusion of various admixtures in turbulent flow, Fluid Dynamics 25 (1990) 327–334.

[115] R. W. Bilger, Conditional moment methods for turbulent reacting flow using crocco variable conditions, Report TN F-99, Department of Mechanical Engineering, University of Sydney.

[116] R. Lee, J. H. Whitelaw, T. S. Wung (Eds.), Aerothermodynamics in combustion, Springer, Berlin, 1991.

[117] N. Smith, R. Bilger, C. Carter, A comparison of cmc and pdf modeling predictions with experimental nitric oxide lif/raman measurements in a turbulent h-2 jet flame, Combustion Science and Technology 105 (1995) 357–375.

[118] M. Roomina, R. Bilger, Conditional moment closure modeling of turbulent methanol jet flames, Combustion Theory and Modeling 3 (1999) 689–708.

[119] M. Roomina, R. W. Bilger, Conditional moment closure (cmc) prediction of a turbulent methane-air jet flames, Combustion and Flame 125 (2001) 1176–1195.

[120] M. Fairweather, R. M. Woolley, First-order conditional moment closure modeling of turbulent, non-premixed methane flames, Combustion and Flame 138 (2004) 3–19.

[121] C. Devaud, K. N. C. Bray, Assessment of the applicability of conditional moment closure to a lifted turbulent flame: first order model, Combustion and Flame 132 (2003) 102–114.

[122] S. Kim, K. Y. Huh, L. Tao, Application of the elliptic conditional moment closure model to a two-dimensional nonpremixed methanol bluff-body flame, Combustion and Flame 120 (2000) 75–90.

[123] S. Kim, K. Y. Huh, Use of the conditional moment closure model to predict no formation in a turbulent ch4/h-2 flame over a bluff-body, Combustion and Flame 130 (2002) 94–111.

[124] A. Kronenburg, R. Bilger, J. Kent, Modeling soot formation in turbulent methane-air jet diffusion flames, Combustion and Flame 121 (2000) 24–40.

[125] D. Bradley, D. Emerson, P. Gaskell, Mathematical modeling of turbulent non-premixed piloted-jet flames with local extinction, Proceedings of the combustion institute 29 (2002) 2155–2162.

[126] E. Mastorakos, R. Bilger, Second-order conditional moment closure for the autoignition of turbulent flows, Physics of Fluids 10 (1998) 1246–1248.

[127] W. Bushe, H. Steiner, Conditional moment closure for large eddy simulation of nonpremixed turbulent reacting flows, Physics of Fluids 11 (1999) 1896–1906.

[128] H. Steiner, W. K. Bushe, Large eddy simulation of a turbulent reacting jet with conditional source-term estimation, Physics of Fluids 13 (2001) 754–769.

[129] W. Bushe, H. Steiner, Laminar flamelet decomposition for conditional source-term estimation, Physics of Fluids 15 (2003) 1564–1575.

[130] C. Blair, Implementation of conditional source term estimation for prediction of methane ignition, Master Thesis, Department of Mechanical Engineering, University of British Columbia, 2003.

[131] R. Grout, Combustion modeling with conditional source term estimation and laminar flamelet decomposition, Master Thesis, Department of Mechanical Engineering, University of British Columbia, 2004.

[132] D. Flowers, S. Aceves, C. K. Westbrook, J. R. Smith, D. R., Detailed chemical kinetic simulation of natural gas hcci combustion: Gas composition effects and investigation of control strategies, Journal of Engineering for Gas Turbine and Power-Transaction of ASME 123 (2001) 433–439.

[133] G. Ben-Dor, O. Igra, T. Elperin, In Handbook of Shock Waves, Vol. 1, Academic Press, New York, 2001.

[134] J. E. G. Lapworth, K. C. and Townsend, Temperature and pressure studies in the reservoir of a reflected-shock hypersonic tunnel, A.R.C 26 (1964) 100.

[135] H. Mark, The interaction of a reflected shock wave with the boundary layer in a shock tube, NSCA TM (1958) 1418.

[136] L. Davies, The interaction of the reflected shock with the boundary layer in a shock tube and its influence on the duration of hot flow in the reflected-shock tunnel, A.R.C (1967) 880–881.

[137] G. H. Markstein, Flow disturbances induced near a slightly wavy contact surface or flame front traversed by a shock wave, J. Aeronautic Sci. 24 (1957) 238–239.

[138] G. I. Taylor, The instability of liquid surface when accelerated in a direction perpendicular to their planes 1, Proc. Roy. Soc. (1950) A 201.

[139] J. P. Holman, Experimental methods for engineers, seventh Edition, McGraw-Hill, New York, 2001.

[140] G. B. Skinner, Limitation of the reflected shock technique for studying fast chemical reactions, Journal of Chemical Physics 31 (1959) 268.

[141] W. Tsang, R. Hampson, Chemical kinetic data base for combustion chemistry. part i. methane and related compounds, Journal of Chemical Physics: Reference Data 15 (1986) 1087.

[142] H. J. Curran, P. Gaffuri, W. J. Pitz, C. K. Westbrook, A comprehensive modeling study of iso-octane oxidation, Combustion and Flame 129 (2002) 253–280.

[143] D. L. Baulch, C. J. Cobos, R. A. Cox, C. Esser, P. Frank, T. Just, J. A. Kerr, M. J. Pilling, J. Troe, R. W. Walker, J. Warnatz, Evaluated kinetic data for combustion modeling, Journal of Physical Chemistry 21 (1992) 411–429.

[144] N. Cohen, Are reaction rate coefficients additive? revised transition state theory calculations for oh + alkane reactions, Journal of Chemical Kinetics 23 (1991) 239–417.

[145] A. Burcat, B. McBride, 1994 ideal gas thermodynamic data for combustion and air-pollution use, Technion Aerospace Engineering Report No. TAE 697.

[146] A. Burcat, Third millennium ideal gas and condensed phase thermochemical database for combustion, technion aerospace engineering report no. tae 867.

[147] R. J. Kee, F. M. Rupley, J. A. Miller, Chemkin-II: A fortran chemical kinetics package for the analysis of gas phase chemical kinetics, SAND89-8009, UC401.

[148] P. N. Brown, G. D. Byme, H. A. C., Vode: a variable coefficient ode solver, SIAM J. Sci. Stat. Comput. 10 (1988) 1038–1051.

[149] W. C. Gardiner, V. Lissianski, V, M. Zamanski, V, Reduced chemical reaction mechanism of shock-initiated ignition of methane and ethane mixtures with oxygen, 19th International Symposium on Shock Waves, Marseille (1993) 154–159.

[150] C. K. Westbrook, W. J. Pitz, H. C. Curran, J. Boercker, Chemical kinetic modelling study of shock tube ignition of heptane isomers, International Journal of Chemical Kinetics 33 (2001) 868–877.

[151] V. M. Zamansky, A. A. Borisov, Promotion of high-temperature self-ignition, Energy Combust. Sci 18 (1992) 297–235.

[152] S. C. Li, F. A. Williams, Reaction mechanisms for methane ignition, Journal of Engineering for Gas Turbine and Power - Transaction of ASME 124 (2002) 471–480.

[153] D. F. Cooke, A. Wiliams, Shock-tube study of the ignition delay and combustion of ethane and slightly rich methane mixtures with oxygen, 13th Symposium (Int) on Combustion, The Combustion Institute (1970) 757–765.

[154] R. Akbar, M. Kaneshige, E. Schultz, J. E. Shepherd, Detonations in $h_2-n_2o-ch_4-nh_3-o_2-n_2$ mixtures, Technical Report FM97-3, GALCIT.

[155] J. W. Sutherland, M. C. Su, J. V. Michael, Rate constants for $h + ch_4, ch_3 + h_2$, and ch_4 dissociation at high temperature, International Journal of Chemical Kinetics 33 (2001) 669–684.

[156] A. D., Isaacson, Harmonic and anharmonic rate constants and transmission coefficients obtained from ab initio data, Journal of Chemical Physics 107 (1997) 3832–3839.

[157] S. I. W. M. and Crim F. F., The chemical kinetics and dynamics of the prototypical reaction: $oh + h_2 \rightarrow h_2o + h$, Journal of Physical Chemistry Chemical Physics 4 (2002) 3543–3551.

[158] H. J. Curran, W. J. Pitz, N. M. Marinov, C. K. Westbrook, P. Dagaut, M. Boettner, J-C. and Cathonnet, A wide range modeling study of dimethyl ether oxidation, Journal of Chemical Kinetics 30 (1998) 229–241.

[159] R. Craig, A shock tube study of the ignition delay of hydrogen-air mixtures near the second, explosion limit, Technical Report, AFAPL-TR-66-74, Air Force Aero-Propulsion Lab, Wright-Patterson.

[160] G. Skinner, G. and Ringrose, Ignition delays of a hydrogen-oxygen-argon mixture at relatively low temperature, Journal of Chemical Physics 42 (1966) 2190–2192.

[161] R. Blumenthal, K. Fieweger, K. Komp, G. Adomeit, B. Gelfand, Self-ignition of h_2-air mixtures at high pressure and low temperature, In 20th Symp. Int. Shock Waves (1996) 935–940.

[162] A. B. Bendtsen, P. Glarborg, K. Dam-Johansen, Chemometric analysis of a detailed chemical reaction mechanism for methane oxidation, Chemometric and intelligent laboratory systems 44 (1998) 353–361.

[163] C. Mansour, A. Bounif, A. Aris, F. Gaillard, Gas-diesel (dual-fuel) modeling in diesel engine environment, International Journal of Thermal Sciences 40 (2001) 409–424.

[164] Q. P. Zheng, H. M. Zhang, D. F. Zhang, A computational study of combustion in compression ignition natural gas engine with separated chamber, Fuel 84 (2005) 12–13.

[165] J. Huang, W. K. Bushe, Experimental and kinetic study of autoignition in methane/ethane/air and methane/propane/air mixtures under engine-relevant conditions, Combustion and Flame.

[166] H. Pitsch, Flamemaster v3.1: a c++ computer program for 0d combustion and 1d laminar flame calculations, available from http://www.stanford.edu/ hpitsch.

[167] O. Gicquel, D. Thevenin, M. Hilka, Direct numerical simulation of turbulent premixed flames using intrinsic low-dimensional manifolds, Combustion Theory and Modelling 3 (1999) 479–502.

[168] D. Thevenin, Three-dimensional direct simulations and structure of expanding turbulent methane flames, Proceedings of the Combustion Institute 30 (2005) 629–637.

[169] P. Nooren, H. Wouters, T. W. J. Peeters, Monte carlo pdf modeling of a turbulent natural-gas diffusion flame, Combustion Theory and Modeling 1 (1997) 79–96.

[170] H. Bongers, J. A. Van Oijen, L. De Goey, Intrinsic low-dimensional manifold method extended with diffusion, Proceedings of the Combustion Institute 29 (2002) 1371–1378.

[171] J. A. VanOijen, L. De Goey, Modelling of premixed laminar flames using flamelet-generated manifolds, Combustion Science and Technology 161 (2000) 113–137.

[172] B. Fiorina, O. Gicquel, L. Vervisch, Premixed turbulent combustion modeling using tabulated detailed chemistry and pdf, Proceeding of the Combustion Institute 30 (2005) 867–874.

[173] S. Singh, J. Powers, S. Paolucci, On slow manifolds of chemically reactive systems, Journal of Chemical Physics 117 (2002) 1482–1496.

[174] M. Davis, R. Skodje, Geometric investigation of low-dimensional manifolds in systems approaching equilibrium, Journal of Chemical Physics 111 (1999) 859–874.

[175] S. Gordon, B. J. McBride, Computer program for calculation of complex chemical equilibrium compositions and applications, NASA Reference Publication 1311.

[176] W. C. Reynolds, The element potential method for chemical equilibrium analysis: implementation in the interactive program stanjan, Stanford University Report ME 270 HO No.7.

[177] S. B. Pope, Gibbs function continuation for the stable computation of chemical equilibrium, Combustion and Flame 139 (2004) 222–226.

[178] R. Renka, Algorithm 751: Tripack: A constrained two-dimensional delaunay triangulation package, ACM Transactions on Mathematical Software 22 (1996) 1–8.

[179] G. Strang, On construction and comparison of differential schemes, SIAM Journal of Numerical Analysis 5 (1968) 506.

[180] S. S. H., R. W. Bilger, K. M. Lyons, J. H. Frank, M. B. Long, Conserved scalar measurements in turbulent-diffusion flames by a raman and rayleigh ribbon imaging method, Combustion and Flame 99 (1994) 347–354.

[181] Y. Chen, M. S. Mansour, Measurements of scalar dissipation in turbulent hydrogen diffusion flames and some implications on combustion modeling, Combustion Science and Technology 126 (1997) 291–313.

[182] G. D. Sullivan, J. Huang, T. X. Wang, W. K. Bushe, S. N. Rogak, Emissions variability in gas fuel direct injection compression ignition combustion, SAE Technical Paper No. 2005-01-0917.

[183] B. E. Launder, D. B. Spalding, Mathematical model of turbulence, Academic Press, 1972.

[184] B. J. P., D. L. Book, Flux-corrected transport i. shasta, a fluid transport algorithm that works, Journal of Computational Physics 11 (1973) 38–69.

[185] P. G. Hill, P. Ouellette, Transient turbulent gaseous fuel jets for diesel engine, Journal of Fluid Engineering 121 (1999) 93–101.

[186] J. S. Turner, The 'starting plum' in neutral surrounding, Journal of Fluid Mechanics 13 (1962) 356–368.

[187] F. P. Ricou, D. B. Spalding, Measurement of entrainment by asymmetrical turbulent jets, Journal of Fluid Mechanics 11 (1961) 21–32.

[188] J. D. Naber, D. L. Siebers, J. A. Caton, C. K. Westbrook, S. S. Di Julio, Natural gas autoignition under diesel conditions: experiments and chemical kinetic modeling, SAE Paper No. 942034.

[189] J. Iaconis, An investigation of methane autoignition behavior under diesel engine-relevant conditions, Master Thesis, Department of Mechanical Engineering, University of British Columbia.

[190] D. C. Lay, Linear algebra and its applications, Addison-Wesley, 2003.

Appendix A
Derivations of Key Equations in CSP

For a reaction system involving N species and K elementary reactions, the rates in which the mass fractions of species change are given by

$$\mathbf{G}_i = \frac{d\mathbf{y}_i}{dt} = \mathbf{S}_{i,j}\mathbf{F}_j, \tag{A.1}$$

where $\mathbf{y}$ is the array of mass fraction of N species; $i = 1...N$; $\mathbf{S}$ is a $N \times K$ matrix of stoichiometric coefficient; $j = 1...K$, and $\mathbf{F}$ is the rate array of K reactions.

In the Computational Singular Perturbation (CSP) method [87, 88], the composition space, $\Re^N$, is split into a fast subspace, $\mathbf{G}_{fast}^m$, and a slow subspaces, $\mathbf{G}_{slow}^n$

$$< \mathbf{G}_{fast}^m \cup \mathbf{G}_{slow}^n > \equiv \mathrm{Span}(\mathbf{G}_{fast}^m \cup \mathbf{G}_{slow}^n) = \Re^N \tag{A.2}$$

$$< \mathbf{G}_{fast}^m \cap \mathbf{G}_{slow}^n > \equiv \mathbf{0}.$$

The superscripts m and n denote the dimensions of the fast subspace and slow subspace respectively. Let $\mathbf{a}_j$ be a set of basis vectors spanning $\mathbf{G}_{fast}^m$; let $\mathbf{b}^i$ be the dual vectors of $\mathbf{a}_j$ that satisfy the orthonormal relation

$$\mathbf{b}^i \mathbf{a}_j = \delta_j^i, \tag{A.3}$$

in which δ is the Kronecker delta. The basis-vector matrix, $\mathbf{A}$, whose columns are the basis vectors of $\mathbf{G}_{fast}^m$, defines a linear transformation

(projection) onto the fast subspace.

$$\mathbf{G}_{fast}^{m} \equiv \mathbf{Af}, \qquad (A.4)$$

where $\mathbf{f}$ is a vector whose elements represent the magnitude of fast reactions. Multiply both sides of Eq. A.4 by a dual-vector matrix, $\mathbf{B}$, whose rows are $\mathbf{b}_i$. One get

$$\mathbf{BG}_{fast}^{m} = \delta\mathbf{f} \Rightarrow \qquad (A.5)$$

$$\mathbf{BAf} = \mathbf{f}.$$

By definition, the null space (or kernel) of transformation $\mathbf{B}$ is the slow subspace

$$\mathbf{BG}_{slow}^{n} = 0. \qquad (A.6)$$

The CSP method reduces the computational time for solving stiff ODEs by examining the contribution of $\mathbf{G}_{fast}^{m}$, which is represented by the magnitude of $\mathbf{f}$. When the contribution of $\mathbf{G}_{fast}^{m}$ becomes trivial compared with that of $\mathbf{G}_{s}^{n}low$, the processes in the fast subspace is in quasi-steady state. Large time steps is then used to speed up the numerical integration of Eq. A.1 because the system is now governed only by the slow processes. The equation governing the change of $\mathbf{f}$ can be obtained by differentiating Eq. A.5

$$\begin{aligned}
\frac{d\mathbf{f}}{dt} &= \mathbf{B}\frac{d\mathbf{G}_{fast}^{m}}{dt} + \mathbf{G}_{fast}^{m}\frac{d\mathbf{B}}{dt} \qquad (A.7)\\
&= \mathbf{B}\frac{d\mathbf{G}}{dt} + \mathbf{G}_{fast}^{m}\frac{d\mathbf{B}}{dt}\\
&= \mathbf{B}\frac{d\mathbf{G}}{d\mathbf{y}}\frac{d\mathbf{y}}{dt} + \mathbf{G}_{fast}^{m}\frac{d\mathbf{B}}{dt}\\
&= \mathbf{B}\frac{d\mathbf{G}}{d\mathbf{y}}(\mathbf{G}_{fast}^{m} + \mathbf{G}_{slow}^{n}) + \mathbf{G}_{fast}^{m}\frac{d\mathbf{B}}{dt}\\
&= (\mathbf{BJA} + \frac{d\mathbf{B}}{dt}\mathbf{A})\mathbf{f},
\end{aligned}$$

in which $\mathbf{J} \equiv d\mathbf{G}/d\mathbf{y}$ is the Jacobian matrix. Note that Eq. A.6 was used to derive the second step in the above equation.

Appendix B
Eigen Decomposition and Schur Decomposition

For a n × n square matrix [22] A, if A has non-degenerative eigenvalues, there exists a decomposition of A so that

$$\mathbf{A} = \mathbf{PDP}^{-1},\qquad\qquad (B.1)$$

where $\mathbf{P}$ is a matrix of right eigenvectors, $\mathbf{D}$ is a diagonal matrix whose diagonal entries are the eigenvalues of $\mathbf{A}$. The matrix decomposition of Eq. B.1 is called eigen decomposition.

By definition, a general eigenvalue problem regarding a linear system $\mathbf{A}$ can be written as

$$\mathbf{A}x = \lambda x,\qquad\qquad (B.2)$$

where x is the right eigenvector corresponding to eigenvalue λ. Equation B.2 can be rearranged into

$$(\mathbf{A} - \mathbf{I})x = 0,\qquad\qquad (B.3)$$

were $\mathbf{I}$ is an n × n identity matrix. Analytically, the eigenvalues of A can be computed from

$$det(\mathbf{A} - \mathbf{I}) = 0,\qquad\qquad (B.4)$$

---

[22] A matrix whose vertical and horizontal dimensions are the same

243

which requires solving a polynomial of nth order. Numerically, to solve Eq. B.4 is highly inefficient especially for high-dimensional problems. In practice, A is usually transformed into a Hessenberg matrix through a similarity transformation [190] (e.g. householder transformation)

$$\mathbf{SAS}^{-1}\mathbf{S}x = \lambda \mathbf{S}x \qquad (B.5)$$

$$\mathbf{B}y = \lambda y.$$

Matrix **B** is a Hessenberg matrix, which is subsequently decomposed to

$$\mathbf{B} = \mathbf{V}\boldsymbol{\Lambda}\mathbf{V}^T, \qquad (B.6)$$

where **V** is a unitary matrix, $\boldsymbol{\Lambda}$ is an upper triangular matrix whose diagonal entries are the eigenvalues of **B** (which shares the same eigenvalues as **A**). The decomposition given in Eq. B.6 is called Schur decomposition and the resulting matrix **V** contains a set of orthonormal basis vectors of **A**, which are called Schur vectors [190]. Given the eigenvalues, the eigenvectors of **A** can be computed using the iterative QR factorization method.

In many occasions, the Jacobian matrix of a reaction system does not have a full rank as a result of nearly liner dependence among the rows in the Jacobian matrix. Consequently, the eigenvalue decomposition may not be computed, but a Schur decomposition always exists. For this reason, Maas and Pope [90] proposed using Schur vectors instead of eigenvectors to form the basis of the Jacobian matrix.

Appendix C
Solution of Ricatti's Differential Equation

The Ricatti's equation with constant coefficients is given by

$$\frac{dy}{dt} = m + ny + py^2.$$
(C.1)

The initial condition for the current problem is $y_{t=0} = 0$. Namely, no methyl radical appears in the initial mixture before reaction. To solve Eq. C.1, we rewrite the equation as

$$\frac{d(y + s)}{dt} = a(y + s) + b(y + s)^2,$$
(C.2)

where

$$m = as + bs^2$$
(C.3)

$$n = a + 2bs$$

$$p = b.$$

Solving the equation system C.3, we get

$$s = \frac{n \pm \sqrt{n^2 - 4pm}}{2p}$$
(C.4)

$$a = \mp \sqrt{n^2 - 4pm}$$

$$b = p.$$

Let $y + s = u$, Eq. C.2 can be rewritten as

$$\frac{du}{dt} = au + bu^2. \tag{C.5}$$

Rearranging Eq. C.5, we get

$$\frac{d\frac{1}{u}}{dt} = -a\frac{1}{u} - b. \tag{C.6}$$

Let $z = \frac{1}{u}$, we rewrite Eq C.6 as

$$\frac{dz}{dt} + az + b = 0. \tag{C.7}$$

This is a first-order homogeneous equation, which can be readily solved to get

$$z = -\frac{b}{a} + ce^{-at}. \tag{C.8}$$

where c is an integral constant, which need to be determined from the initial condition of the problem. Given $y_{t=0} = 0$, we get

$$z_{t=0} = \frac{1}{s} = -\frac{b}{a} + c, \tag{C.9}$$

or

$$c = \frac{1}{s} + \frac{b}{a}. \tag{C.10}$$

The final form of z can be obtained by substituting Eq. C.10 into Eq C.8 to get

$$z = -\frac{b}{a} + \left(\frac{1}{s} + \frac{b}{a}\right)e^{-at}. \tag{C.11}$$

Thus the solution for y is given by

$$y = \frac{1}{-\frac{b}{a} + \left(\frac{1}{s} + \frac{b}{a}\right)e^{-at}} - s. \tag{C.12}$$

The current analytical model determines the ignition delay time based on extrapolation of the slope at the inflection point on the $y - t$ curve.

The slope is determined by the first derivative of y with respect to t, given by

$$y' = \frac{-a(\frac{1}{s} + \frac{b}{a})e^{-at}}{\left[-\frac{b}{a} + [(\frac{1}{s} + \frac{b}{a})e^{-at}]^2 \right]}.$$ (C.13)

The second derivative of y with respect to t is

$$y'' = \frac{a^2(\frac{1}{s} + \frac{b}{a})e^{-at}}{\left[-\frac{b}{a} + (\frac{1}{s} + \frac{b}{a})e^{-at} \right]^2} - 2\frac{\left[a^2(\frac{1}{s} + \frac{b}{a})e^{-at} \right]^2}{\left[-\frac{b}{a} + (\frac{1}{s} + \frac{b}{a})e^{-at} \right]^3}.$$ (C.14)

The inflection point can be calculated by setting $y'' = 0$, which yields

$$t_i = \frac{-ln-\frac{b}{a}(\frac{1}{s} + \frac{b}{a})}{a}.$$ (C.15)

The equilibrium value of y can be obtained at $t \to \infty$ from Eq. C.12

$$y_{equi} = -\frac{a}{b} - s.$$ (C.16)

The time from the inflection point to the intersection of extrapolated slope and equilibrium value of y can be calculated from

$$t_{ex} = \frac{y_{equi} - y_{t=t_i}}{y'_{t=t_i}}.$$ (C.17)

Substituting Eqs. C.15,C.13 and C.12 into Eq. C.17 and solve for t_{ex}, we get

$$t_{ex} = \frac{2}{a}.$$ (C.18)

Finally, the ignition delay is calculated by combining t_{ex} with t_i

$$\tau = \frac{2 - ln-\frac{b}{a}(\frac{1}{s} + \frac{b}{a})}{a}.$$ (C.19)

Appendix D
Flux Corrected Transport

Flux-Corrected Transport (FCT) [184] is a conservative, monotone technique for integrating generalized continuity and hydromagnetic equations. It is especially useful for solving compressible-flow problems, particularly those involving shock and rarefaction waves and contact discontinuities. FCT accomplishes this objective by combining integration schemes with low and high orders of spatial accuracy. The low-order scheme provides a monotone solution, usually by the introduction of diffusive numerical fluxes, while the high-order scheme provides high accuracy in regions of smooth flow and shallow gradients. The high-order solution is obtained by "antidiffusing" the low-order, monotone solution, but only to such an extent that no new extrema are created and no existing extrema are accentuated. This is done by limiting, or "correcting," the antidiffusive fluxes of the high-order scheme, hence the name Flux-Corrected Transport. A key feature of the FCT scheme is to use flux limiters to remove non-physical extremes. We use the Euler equations to illustrate the application of such flux limiters.

$$\frac{\partial \rho \psi}{\partial t} + \frac{\partial \mathbf{F}_{x_1}}{\partial x_1} + \frac{\partial \mathbf{F}_{x_2}}{\partial x_2} + \frac{\partial \mathbf{F}_{x_3}}{\partial x_3} = \mathbf{S}(x_1, x_2, x_3) \tag{D.1}$$

Using a second-order central time advance scheme, Eq. D.1 can be discretized temporally into

$$\frac{\rho \psi^{t+\Delta t}}{2\Delta t} = \frac{\rho \psi^{t-\Delta t}}{2\Delta t} - \sum_{i=1}^{3} \frac{\partial \mathbf{F}_i^t}{\partial x_i} \qquad (D.2)$$

For a Courant-Friedrichs-Lewy (CFL) number less than unity, the lower limit of updated scalar ψ must satisfy

$$\psi_{min}^{t+\Delta t} \leq \psi^{t+\Delta t} = \frac{-2\Delta t}{\Delta x_i \rho} \int_{cv} \mathbf{F} + \psi^{t-\Delta t} \qquad (D.3)$$

where ψ_{min} is the local minimum of the transported scalar. A sufficient condition that satisfies Eq. D.3 is

$$\psi^{t+\Delta t} - \psi_{min}^{t+\Delta t} \geq \frac{2\Delta t}{\Delta x_i \rho} \int_{cv} \mathbf{F}_{out} + \psi^{t-\Delta t} \qquad (D.4)$$

where $\int_{cv} \mathbf{F}_{out}$ is the total flux leaving the control volume. The flux limiter ratio is thus defined as

$$\beta^{out} = \frac{\psi^{t+\Delta t} - \psi_{min}^{t+\Delta t}}{\frac{2\Delta t}{\Delta x_i \rho} \int_{cv} \mathbf{F}_{out} + \psi^{t-\Delta t}} \qquad (D.5)$$

If β^{out} is greater than 1, then no flux correction is necessary; otherwise, the flux limiter should be applied to the out flux

$$\mathbf{F}_i = min(1, \beta_{i-1}^{out}) max(0, F_i) + min(1, \beta_i^{out}) min(0, F_i) \qquad (D.6)$$

where i is the node at which β^{out} is evaluated. In the current study, the FCT scheme is used to resolve the fine structures of the flow field as well as to enhance the numerical stability - the existence of a large pressure drop at the nozzle exit and non-linear nature of the chemical reaction may lead to large local gradients of reaction scalars, which may cause non-physical oscillations due to the numerical dispersion with ordinary second-order schemes.

Appendix E
Numerical Schlieren

The Schlieren image represents the density gradient integrated along the transverse direction of the test section. In a cylindrical coordinates, the transverse-direction density gradient can be obtained from

$$\frac{d\rho(r,\theta)}{dx} = \frac{\partial \rho}{\partial r}\frac{\partial r}{\partial x} + \frac{\partial \rho}{\partial \theta}\frac{\partial \theta}{\partial x}. \tag{E.1}$$

The differential term with respect to θ drops due to the axisymmetry of the flow field. We integrate Eq. E.1 along the transverse direction of the test section

$$I(r_0) = 2k \int_{r=R}^{r=r_0} \frac{\partial \rho}{\partial r}\frac{\partial r}{\partial x}dx = 2k \int_{r=R}^{r=r_0} \frac{\partial \rho(r,z)}{\partial r}dr, \tag{E.2}$$

where I is proportional to the light intensity of the Schlieren image. Note that we only integrate $d\rho$ in first quadrant to take advantage of the symmetry of the round jet.